Self-propelled active droplets : a short story of their interactions.

Kevin Lippera

To cite this version:

Kevin Lippera. Self-propelled active droplets : a short story of their interactions.. Fluid mechanics [physics.class-ph]. Institut Polytechnique de Paris, 2020. English. NNT : 2020IPPAX067 . tel-03379891

HAL Id: tel-03379891
https://theses.hal.science/tel-03379891

Submitted on 15 Oct 2021

INSTITUT
POLYTECHNIQUE
DE PARIS

NNT : 2020IPPAX067

Thèse de doctorat

Gouttes actives auto-propulsées : une histoire d'interactions

Thèse de doctorat de l'Institut Polytechnique de Paris
préparée à l'École polytechnique

École doctorale n°626 École Doctorale de
l'Institut polytechnique de Paris (ED IP Paris)

Spécialité de doctorat : Mécanique des Fluides

Thèse présentée et soutenue à Paris, le 15 Octobre 2020, par

KEVIN LIPPERA

Composition du Jury :

John Hinch Professeur, DAMPT, University of Cambridge	Examinateur
Cécile Cottin-Bizonne Directrice de Recherche, Institut Lumière Matière	Rapporteuse
Benjamin Dollet Directeur de Recherche, LiPhy, Université Grenoble Alpes	Rapporteur
Denis Bartolo Professeur, Laboratoire Matière & Complexité, ENS de Lyon	Président du jury
Sébastien Michelin Directeur de Recherche, LadHyX, École polytechnique	Directeur de thèse
Michael Benzaquen Directeur de Recherche, LadHyX, École polytechnique	Co-directeur de thèse

Contents

À mes parents et ma soeur bubu,

Remerciement

Mes premières pensées vont à Thierry Ondarcuhu qui m'a fait découvrir en 2015 le monde de la recherche académique et la physique du mouillage à l'échelle nanométrique au sein de son équipe au CEMES. C'est sa passion pour la science, sa générosité et sa bienveillance qui ont fait naître en moi l'envie de poursuivre dans le monde de la recherche.
Je voudrais ensuite remercier chaleureusement Olivier Dauchot – avec qui j'ai pu travailler sur des sujets de lévitation acoustique – pour son caractère inspirant, moteur, pour son aide, ses précieux conseils et enfin pour les bons moments passés aux alentours de la rue Mouffetard ou encore face au Mont Blanc à l'Ecole des Houches.
Je voudrais maintenant remercier avec une attention particulière mes deux directeurs de thèse Sébastien Michelin et Michael Benzaquen. Merci, Michael, pour m'avoir toujours soutenu pendant les périodes difficiles de ma thèse ainsi que pour tes nombreuses idées partagées pour m'aider à débloquer certains problèmes de physique. Merci, Sébastien, d'avoir eu cette pédagogie et tout ce temps disponible pour me faire découvrir ce que voulait vraiment dire le mot rigueur. Merci d'avoir toujours eu la patience de me pousser à faire mieux, de me pousser à comprendre d'avantage. Merci de m'avoir fait grandir, et ce bien au-delà des questions scientifiques.
Merci à Mathilde Reyssat et Charlotte de Blois d'avoir été disponibles pour discuter de nombreuses fois des expériences de gouttes actives au laboratoire Gulliver et à Adrien Saint-Sardos, Gabriel Amselem et Charles Baroud pour avoir permis de travailler ensemble à l'Institut Pasteur et m'avoir fait découvrir le monde de la biologie et la légendaire crème brulée du vendredi.
Je souhaiterais également remercier Cécile Cottin-Bizonne et Benjamin Dollet pour avoir accepté de rapporter ce manuscrit et aussi pour leurs nombreuses questions très intéressantes lors de la soutenance. Merci beaucoup à John Hinch et Denis Bartolo pour avoir accepté d'être examinateurs et pour vos apports, questions et discussions très enrichissantes au moment de la soutenance de thèse.
Merci beaucoup à toutes les personnes que j'ai pu rencontrer au LadHyX et aux très bonnes amitiés que j'ai eu la chance de nouer, avec lesquelles j'ai partagé beaucoup de rires, de cafés et de musique. Merci donc à Tom, Thibaut, Juliette, Francesco, Alexandra, Ambre, Adrien, Pierre, Benjamin, Caroline, Matvey, Akhil, Blaise, Gabriel, Graham, Tulio et Antoine.
Merci à mes amis proches du Lycée, de l'Ecole des Ponts ou d'ailleurs qui m'ont beaucoup soutenu pendant ces trois ans et notamment à Marie, Omar, Lucas, Sarah, Bouch, Diane, Eliot, Emilien, Racca et James pour leur générosité et leur patience concernant la relecture des fautes d'anglais de ce manuscrit.
Enfin, un immense merci à mes parents et ma grande soeur pour leur soutien et leur présence sans faille depuis maintenant près de 28 ans.

Foreword

I discovered low Reynolds fluid mechanics and the world of research during an experimental internship at CEMES in 2016 under the supervision of Thierry Ondarçuhu. The research project tackles the issue of wetting at the nanoscale and specifically aims to understand dissipation phenomena that occur when a needle of a 10nm radius oscillates at the surface of a liquid. Thanks to this internship, I had the opportunity to meet other researchers, amongst which Michael Benzaquen. After a Master's degree in Aeronautical Engineering at the Imperial College of London, I decided to dive deeper into fluid mechanics at small scale during my Master's internship under the supervision of Michael Benzaquen at LadHyX (École polytechnique) and Olivier Dauchot at GULLIVER (ESPCI Paris). The project was dedicated to the study of acoustically levitating nanoparticles, which display spontaneous rigid body motions. In particular, we focused on acoustic streaming around a nearly-spherical particle to look for an explanation of such spontaneous motions (see Appendix C).

I started my PhD at the end of this internship, in October 2017, under the supervision of Sébastien Michelin and Michael Benzaquen. The main topic of this PhD was to study autonomous micro-metric systems, called *active droplets*, which self-propel in liquids as the result of Marangoni stresses on their surface. The origin of these Marangoni flows is explained by surface tension gradients induced by complex interactions between chemical species in the outer fluid with the interface of the droplet. In addition to industrial or medical applications such as drug delivery or new water treatment processes, such self-propelled active droplets represent a promising system to study active matter. More specifically, the main goal of the PhD was to accurately study collisions of one droplet against a boundary, or interactions between several active droplets.

During this PhD, I had the opportunity to collaborate with Matvey Morozov, who provided useful asymptotic computations to gain insights into the physics involved in the head-on collision of two active droplets. Besides, Sébastien Michelin and I were able to take part in a research project at Institut-Pasteur carried out by Adrien Saint-Sardos, Gabriel Amselem, Sébastien Sart, Elodie Brient-Litzler and Charles Baroud. This project aimed to study the dynamics of human Mesenchymal Stem Cells spheroid secretions inside a droplet. Sébastien and I provided theoretical and numerical results regarding the diffusive VEGF transport inside the droplet that is captured by magnetic beads. Finally, Olivier Dauchot introduced me to Charlotte de Blois, at that time finishing her PhD at GULLIVER (ESPCI Paris), who was studying active droplets under his supervision and the one of Mathilde Reyssat. Fruitful discussions with them enabled me to discuss the similarities and differences between their experimental observations and our theoretical predictions.

The manuscript is organised as follows: in the first chapter, we introduce some key aspects of low Reynolds number fluid mechanics and describe the physical system of interest, namely active droplets like those used in recent experiments. The mathematical framework employed to model the self-propulsion of active droplets is presented in chapter two, together with a preliminary discussion of the hydro-chemical interactions involved in the presence of multiple droplets and generic boundaries. In chapter three we provide the exact derivation of the hydro-chemical interactions involved for a droplet colliding against a rigid wall, or with another active droplet. In the fourth chapter, we study the influence of the size-ratio on head-on collisions of two droplets. Here we show that collision dynamics are highly dependent on the droplet's size-ratio, leading to three different regimes, i.e. rebound, chasing and pausing. In chapter five we introduce a simplified framework for modelling the behaviour of active droplets' dynamics, which is then employed to study the general case of oblique collisions. While we notice a significant alignment of the droplets when initial conditions are symmetric, we show that the system can become highly asymmetric with the introduction of a misalignment in the droplets' initial conditions. In the sixth and final chapter, we provide several perspectives regarding the study of active droplet interactions.

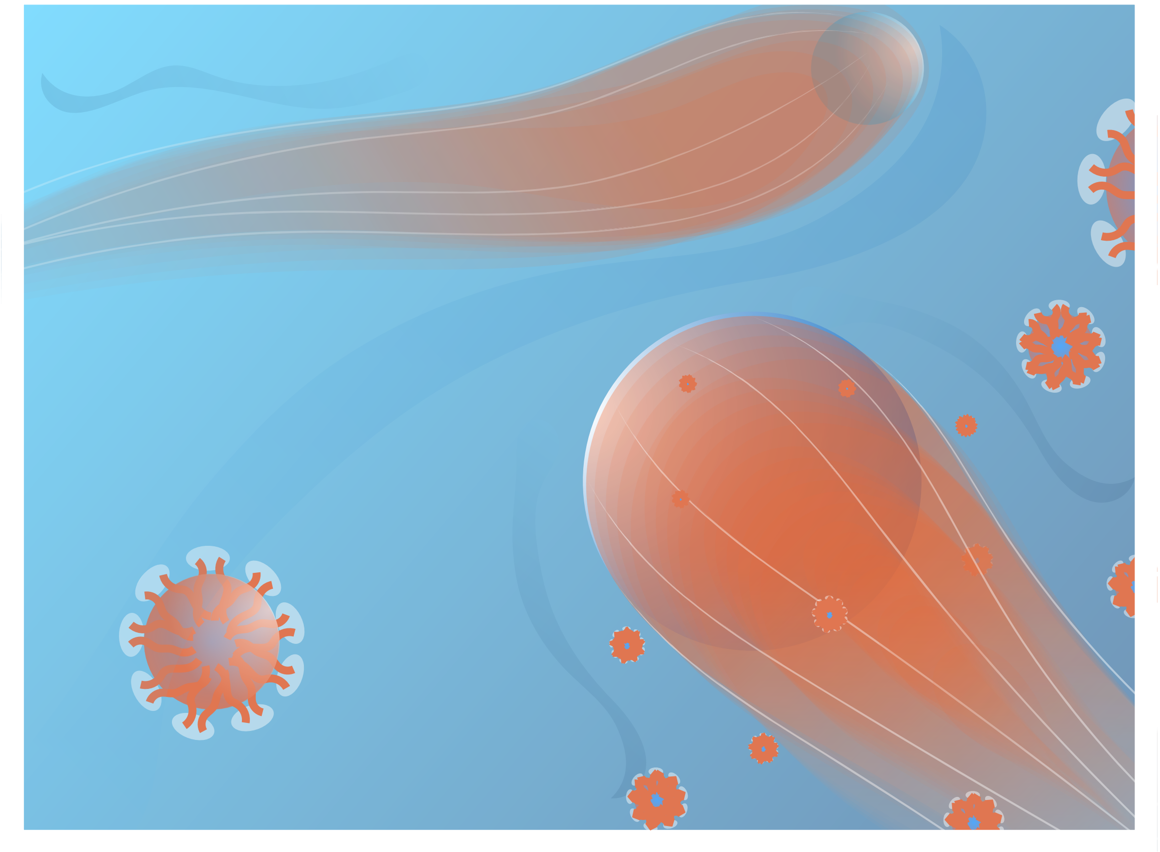

Intuition has to lead knowledge, but it can't be out there alone.

Bill Evans

Résumé substantiel

La Nature témoigne d'un grand nombre de comportements collectifs : un banc de poissons formant un tourbillon en présence d'un prédateur, un ensemble d'oiseaux volant de manière structurée ou encore un mouvement d'une foule d'humains. Si ces comportements sont souvent observés à l'échelle macroscopique, des dynamiques similaires existent parmi les microorganismes comme des bactéries, micro-algues ou même des filaments d'actine. À cette échelle, les systèmes cognitifs y sont absents et le mouvement des individus survient sans inertie. On peut alors se demander si ces mouvements collectifs peuvent être expliqués par des interactions physiques ou biologiques. Comprendre le comportement de systèmes microscopiques s'avère important à la fois d'un point de vue de physique fondamentale, mais présente également un intérêt pour le développement de technologies micro-chirurgicales, de nouvelles méthodes de traitement de l'eau ou encore de systèmes d'administration de médicaments. Pour caractériser la coordination au sein d'une multitude d'agents actifs, une approche populaire consiste à analyser les effets du couplage physico-chimique dans l'interaction d'une paire de ces agents. Cependant, comprendre le comportement collectif d'organismes biologiques est une tache complexe du fait de la multiplicité de phénomènes pouvant être à leur l'origine. Le développement de systèmes artificiels offre alors une bonne alternative. Parmi les candidats prometteurs, on peut citer les gouttes actives. Ces gouttes d'huile ou d'eau mesurant quelques dizaines de microns s'auto-propulsent à une vitesse de quelques rayons par seconde lorsqu'elles sont immergées dans un autre liquide saturé en surfactants.

L'approche combinée d'expériences et de travaux théoriques a permis d'identifier que la dissolution des gouttes dans leur milieu est à l'origine de leur mouvement. Une goutte active peut alors être vue comme la source d'une espèce chimique modifiant la tension de surface à son interface avec le liquide qui l'entoure. Ainsi, une distribution non-homogène de l'espèce chimique génère un écoulement Marangoni qui déplace la goutte vers des zones où la concentration en espèce chimique est la plus basse. Le couplage non-linéaire entre la dynamique de transport de l'espèce chimique et le mouvement du fluide a alors un rôle central dans l'instabilité à l'origine de l'auto-propulsion des gouttes. De plus, en raison de leurs signatures chimique et hydrodynamique, ces gouttes actives modifient la trajectoire de leurs voisines, ouvrant ainsi la possibilité à des mouvements collectifs de se développer. Comprendre l'origine et la physique des interactions entre ces gouttes ou avec des parois est primordial pour expliquer les comportements observés expérimentalement. Cette problématique constitue l'objectif principal de cette thèse. La première question abordée est la suivante : laquelle des deux types d'interactions (hydrodynamique ou chimique) est prédominante lorsque deux gouttes actives interagissent ? Répondre à cette question est un challenge technique, car ce problème à deux corps implique la résolution d'équations différentielles instationnaires et non-linéaires décrivant le couplage entre transport chimique et le mouvement du fluide en géométrie complexe.

La première contribution de cette thèse concerne le développement du premier modèle théorique exact décrivant l'interaction entre deux gouttes actives ainsi que celle d'une goutte active avec un mur passif. On propose alors une approche analytique nouvelle, basée sur une grille bi-spherique dynamique fournissant un système de coordonnées toujours parfaitement adapté à la géométrie du problème. Cette approche permet la résolution complète du problème hydro-chimique quelque soit la distance relative entre les gouttes à la différence de la plupart des modèles existant qui se focalisent sur des interactions en champ lointain.

Lorsque deux gouttes actives s'approchent, la concentration en espèce chimique augmente dans la région entre les gouttes. En conséquence, la tension de surface augmente également dans cette zone. Il arrive un moment où la concentration à l'avant des gouttes dépasse celle à l'arrière, provoquant alors leur répulsion. Les résultats obtenus montrent que pour des effets advectifs modérés (en comparaison aux effets diffusifs), les interactions chimiques sont prédominantes lors d'une collision frontale entre deux gouttes actives et que les interactions hydrodynamiques sont quant à elles négligeables. Dans ce cas, une collision frontale peut être décrite en considérant uniquement les forces Marangoni générées par la variation de la tension de surface à l'interface des gouttes. En revanche, les interactions hydrodynamiques ne sont plus négligeables lorsque les effets advectifs deviennent significatifs (dans le cas d'une diffusion lente). Dans cette situation, l'espèce chimique à l'arrière d'une goutte, à l'origine de sa propulsion, s'oppose à la répulsion chimique due à la présence de l'autre goutte. Les deux gouttes restent alors proches pendant un certain temps, ce qui ralentit leur dynamique de rebond. Le couplage entre le transport chimique et le mouvement du fluide est ici crucial et ne peut être capturé que par une résolution complète du problème.

La deuxième contribution de cette thèse aborde le rôle d'une différence de rayon lors de l'interaction entre deux gouttes. Cette étude a permis de montrer que la dynamique de collision est fortement sensible à la différence de rayons et conduit à deux régimes fondamentalement différents en plus du rebond symétrique constaté pour des gouttes de même taille : premièrement, un régime de chasse survient et dans lequel la plus grosse goutte suit la plus petite à la suite de leur collision. Dans ce cas, les gouttes finissent par adopter un état d'équilibre où elles se propulsent dans le même sens avec des vitesses identiques. Le second régime est encore moins intuitif et appelé le régime de pause. Dans ce cas, la grosse goutte s'arrête de nager juste après la collision avec la plus petite. Un écoulement quadripolaire se forme alors autour de la grosse goutte, permettant de maintenir une accumulation en espèce chimique à l'avant et à l'arrière de cette dernière. L'analyse de ces deux régimes semble prometteuse notamment pour décrire théoriquement de récentes observations expérimentales dans lesquelles des trains de gouttes se forment spontanément lorsque ces dernières évoluent dans un capillaire.

La troisième et finale contribution de cette thèse concerne le développement d'un modèle théorique simplifié appelé modèle de singularité dynamique. Ce modèle est suffisamment simple pour permettre l'analyse de situations plus complexes incluant des collisions générales entre deux ou un ensemble de gouttes actives. Le modèle exact présenté précédemment a permis de conclure que les effets hydrodynamiques peuvent raisonnablement être négligés lorsque l'advection est modérée. Le présent modèle simplifié néglige alors la dynamique complète de l'advection autour des gouttes. Néanmoins, il retient la caractéristique fondamentale de l'asymétrie avant-arrière en espèce chimique à l'origine de la propulsion d'une goutte active. La signature chimique d'une goutte active est alors représentée par la superposition d'un monopôle et d'un dipôle positionnés en son centre. Lorsque les effets advectifs sont modérés, le modèle de singularité dynamique est alors capable de reproduire de façon très proche la dynamique de collision frontale obtenue en utilisant le modèle exact. Ce résultat fournit alors une validation quantitative du modèle réduit. Si l'approche exacte s'est focalisée sur des problèmes de collisions frontales, le modèle réduit est utilisé pour traiter des interactions plus génériques telles que des collisions obliques. De façon surprenante, on constate alors un alignement significatif des gouttes lors de telles collisions obliques. De plus, une fois que les gouttes ont retrouvé une trajectoire rectiligne après leur collision, l'angle relatif entre leur direction est le même pour une grande gamme de directions initiales. Ce résultat remarquable résulte de la dynamique du sillage chimique à l'arrière des gouttes. Enfin, cette thèse a montré que l'interaction entre des gouttes actives peuvent conduire à une dispersion importante de leur trajectoire lorsqu'une des deux est en retard par rapport à l'autre et interagit avec son sillage chimique.

En conclusion, cette thèse a permis de remplir deux objectifs différents : premièrement, elle constitue une étape clef dans la compréhension des gouttes actives en fournissant le premier modèle exacte d'interaction entre deux gouttes actives. Deuxièmement, elle suggère un modèle numérique simplifié robuste permettant d'étudier des collisions génériques au sein d'un ensemble de gouttes actives. En particulier, ce modèle est facilement adaptable pour prendre en compte la variation du rayon des gouttes au cours du temps du fait de leur dissolution ou même pour décrire l'influence chimique de murs passifs sur leur dynamique.

1

ACTIVE MATTER AND ACTIVE DROPLETS

Active matter is a branch of physics that yearns to study the behaviour of an assembly of active systems such as birds, bacteria or microtubules that may develop collective motion in response to external stimuli (like the presence of a predator in the vicinity of a school of fish), or even spontaneously. In this chapter, we suggest how studying the interactions between such active agents may highlight some of the mechanisms at the origin of the observed collective behaviour. After providing the reader with the hydrodynamical framework that governs fluids at small scales, we introduce artificial micro-swimmers of particular interest: the active droplets. This swimmers happen to spontaneously swim in a liquid under specific conditions, making them promising autonomous systems to mimic living microorganisms.

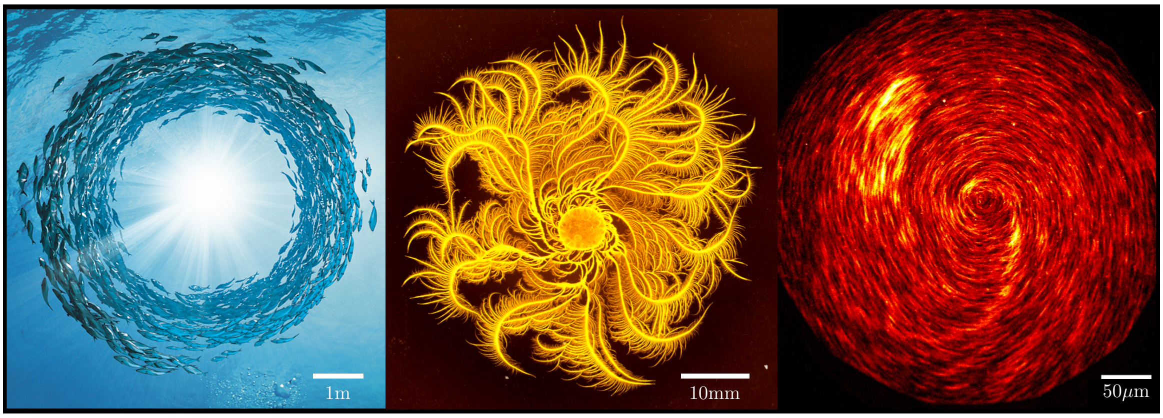

Left: fish school, Simon Tuckett, http://simontucket.com, 2009. Centre: colony generated by the chiral morphotype bacteria of P. dendritiformis, Eshel Ben-Jacob, 2011. Right: collective swirling motion of actin filaments [1]

Contents

1.1 Collective motion and interactions

We may be both intrigued and astonished by some persisting patterns and ordered motions which are appearing in the animal world. If army ants sometimes perform fast-rotating circles [2] (panel (a) of Fig. 1.1) some humans may also adopt such collective dynamics when attending some musical festivities (panel (b) of Fig. 1.1). Herds of sheep, traffic jams and bird flocks are some of many examples of the collective dynamics we can observe in nature [3]. The following questions may then arise: *Is the intelligence of each individual necessary in such spontaneous collective dynamics? How does the motion of each individual synchronise with the rest of the group?*

If any would argue that one leader orders the motion of everyone in the group, such an assertion seems hard to believe when the number of individuals increases drastically, forcing each of them to interact only with few others that surround it. In particular, it is not rare to observe that schools of fish adopt milling dynamics in the presence of predators (panel (f) of Fig. 1.1). Some decades ago, Ref. [4] showed that such collective motion occurs without the help of any leader. Instead, both behavioural rules and hydrodynamic interactions between the fish lead to such a circular pattern when alignment and attraction between the fish are comparable in magnitude (panel (g) of Fig. 1.1) [5]. This particular example gives the feeling that studying interactions between individuals in a group enables to highlight the necessary ingredients to observe collective dynamics, and therefore to learn more about their origin. Such an approach has already proven to be useful in providing physical explanations of the diamond pattern whales adopt when swimming together [6], in giving interpretations of the intermittent collective motion observed in sheep herds [7] and even in quantifying jammed dynamics when too many people aim to exit a room as fast as possible while using the same door [8].

If social interactions or planned collective organisations were possible at the macroscale, they would become much more unlikely to justify group patterns as we focus on the micrometric scales, where we still observe collective dynamics: swarming of actin filaments [1] (panel (h) of Fig. 1.1), swarming of bacteria [9] (panel (i) of Fig. 1.1) or even bacteria combat strategies [10] (panel (j) of Fig. 1.1). Keeping the same approach based on the study of interactions, researchers have developed artificial devices called *microswimmers*, which happen to share similarities with propulsion and dynamics of living microorganisms. If the collective dynamics observed for microorganisms also happen to occur for artificial swimmers, we may hope to identify the minimal ingredients at their origin. In the following sections, we first introduce the framework called *low-Reynolds fluid mechanics* that governs any fluid's motion at such small scales. In a second stage, starting from the example of the paramecia, we show how tangential velocity at the surface of a body may lead to its propulsion. This swimming mechanism has inspired the design of artificial microswimmers such as *active droplets*, which are the last focus of this chapter and the main topic of this manuscript.

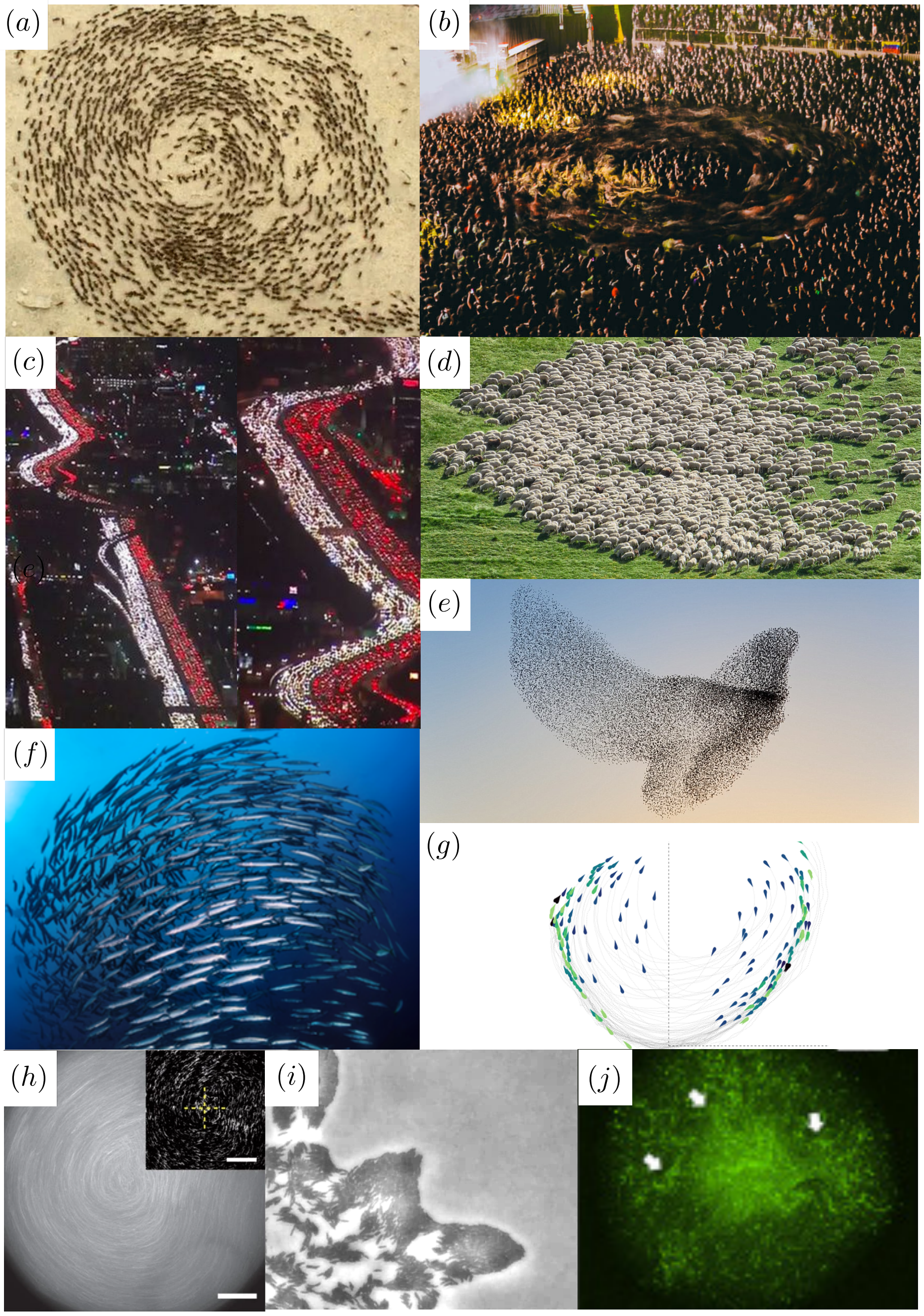

Figure 1.1: Pictures of collective dynamics illustrating the possible existence of very general behavioural patterns: (a) A rotating colony of army ants from *https://onedio.com* (b) Pogo circle pit in a concert, Sebastian Dominguez Urzua-2011 (c) Traffic jam in Los Angeles, credit: californiadreamin (d) A herd of sheep, www.unsplash.com (e) Birds flocks, credit: Robert Wolstenholme (f): Milling motion for fish schools, iStock.com/armiblue (g): Numerical simulations of fish schooling [5]. (h): Swarming of actin filament [1]. (i): Bacteria swarming [9]. (j): Bacteria combat strategy [10].

1.2 Propulsion of microorganisms

Microswimmers, either biological or synthetic, swim at the microscale using different locomotion strategies. Aiming to study their interactions, we first need to know how they swim. We suggest in this section a brief overview of the microscale world, to introduce some of the existing natural propulsion mechanisms.

While visiting a warm-blooded organism body, we may encounter an Escherichia coli [11], a rodlike bacterium 2μm long and 0.2 to $1\mu m$ in diameter that uses several rotating rigid and helical flagella to propel up to 35 body lengths per second (panel (*a*) of Fig. 1.2). While lingering into the human body, we may also witness the frantic race of spermatozoa [12] performing fast oscillations of their single 50μm long whip-like tail to swim about 40 to 100μm/s in the direction of the ovum (panel (*b*) of Fig. 1.2). Pursuing our journey in freshwater basins, we may have the chance to come across a Chlamydomonas reinhardtii [13], a single-cell microalgae of about 10μm. The latter achieves propulsion in steering through the fluid in a breaststroke movement enabled by its two flagella, except for the fact it performs 50 motions per second and reaches a velocity close to 70μm/s (panel (*c*) of Fig. 1.2). Finally, in the same aqueous environment, we may notice the presence of a paramecium [14], a cell of 50-300μm, which takes advantage of the coordinated action of thousands of cilia that lie at its surface to propel up to 500μm/s (panel (*d*) of Fig. 1.2).

However, such a journey in the microscopic world may be exhausting since all these propulsion mechanisms are far from being energetically efficient. Let us choose the definition of efficiency according to Lighthill [15], which compares the work of the net propulsive force to all the dissipated energy. We realise the maximum propulsion efficiency of a microorganism is about 3% regarding cilia-based propulsion [16] and only 2% for an Escherichia Coli bacterium and its rotating helixes [17]. Indeed, swimming at those scales is quite a feat due to the absence of inertia, a framework for which the next section aims to provide more in-depth details.

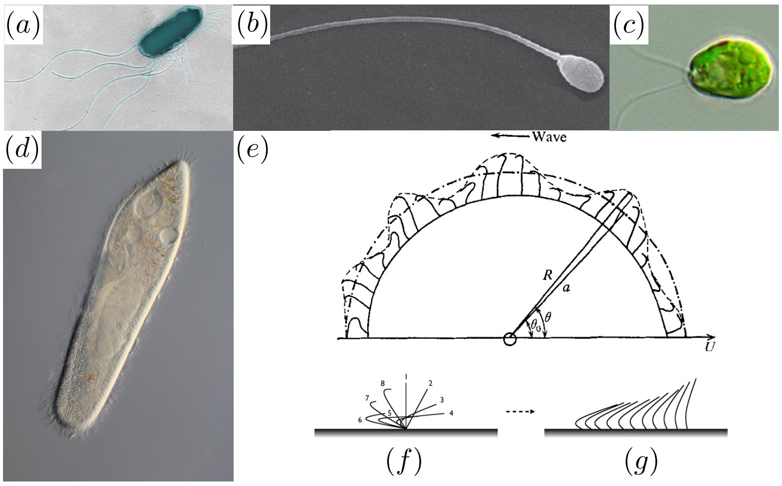

Figure 1.2: Propulsion strategies at the microscale: (*a*): Microscope picture of a Escherichia coli bacterium from *microbiologybytes.com.* (*b*): Spermatozoon as seen under the scanning electron microscope, adapted from [18] (*c*): Microscope picture of a Chlamydomonas Reinhardtii algae from Ref. *AlgaeIndustryMagazine.com* (*d*): Photomicrograph of a paramecium, www.micropia.nl. (*e*): Enveloppe model of ciliary propulsion from Ref. [19]. (*f*): Schematic of one cilia dynamics from 1 to 8 from Ref. [20]. (*g*): Schematic of a metachronal wave which arises from the coordinated beating of cilia drawn from Ref. [20].

1.3 Fluid mechanics at vanishing Reynolds number

Unsurprisingly, swimming in a pool can be achieved through the action of our arms and legs that expell water in the direction opposed to our motion. We then expect that swimming in honey should be more exhausting due to the surge of viscous dissipation that we should overcome to move. At the microscale, it is quite the opposite. Microorganisms move thanks to the drag forces that result from fluid viscosity. To understand such a surprising assertion, we can start by considering that a liquid flows in response to external forces such as gravity or electromagnetic fields, and is also driven among other things by pressure forces, density gradients or viscous interactions. Within the framework of classical mechanics, we consider that two quantities are conserved: (*i*) the mass and (*ii*) the momentum, which thus provides two local relations:

$$\frac{\partial \rho}{\partial t} + \boldsymbol{\nabla} \cdot (\rho \boldsymbol{u}) = 0, \tag{1.1}$$

$$\rho \left(\frac{\partial \boldsymbol{u}}{\partial t} + \boldsymbol{\nabla} \boldsymbol{u} \cdot \boldsymbol{u} \right) = \boldsymbol{\nabla} \cdot \boldsymbol{\sigma} + \boldsymbol{f}, \tag{1.2}$$

where ρ is the fluid density, $\boldsymbol{u}$ the Eulerian velocity field, $\boldsymbol{f}$ an external body force and $\boldsymbol{\sigma}$ the Cauchy stress tensor. In the particular case of an incompressible and Newtonian fluid, we may write:

$$\boldsymbol{\sigma} = -p\boldsymbol{I} + \eta \left(\boldsymbol{\nabla} \boldsymbol{u} + \boldsymbol{\nabla}^T \boldsymbol{u} \right), \tag{1.3}$$

where η is the fluid viscosity and p the pressure field. The fluid flow dynamics is then described by the *Navier-Stokes* and *continuity* equations:

$$\rho \left(\frac{\partial \boldsymbol{u}}{\partial t} + \boldsymbol{\nabla} \boldsymbol{u} \cdot \boldsymbol{u} \right) = -\boldsymbol{\nabla} p + \eta \boldsymbol{\nabla}^2 \boldsymbol{u} + \boldsymbol{f}, \tag{1.4}$$

$$\boldsymbol{\nabla} \cdot \boldsymbol{u} = 0. \tag{1.5}$$

To assess the significance of the fluid's inertia in comparison to its viscosity, we consider a dimensionless number called Reynolds number (noted Re) which reads:

$$\mathrm{Re} = \frac{V^* L^*}{\nu^*} \sim \frac{\text{Inertial terms}}{\text{Viscous terms}} \sim \frac{|\rho \boldsymbol{\nabla} \boldsymbol{u} \cdot \boldsymbol{u}|}{|\eta \boldsymbol{\nabla}^2 \boldsymbol{u}|}, \tag{1.6}$$

where V^*, L^* and ν^* are the characteristic velocity, length and kinematic viscosity of the considered problem. While $\mathrm{Re} \sim 10^6$ for a human swimming in a pool, it collapses to $\mathrm{Re} \sim 10^{-4}$ in the case of swimming bacteria. We then expect that if inertia seems crucial for a human to swim, viscous contributions are essential for microorganisms' motion. The Reynolds number may also be seen differently as the ratio of the diffusive time (driven by viscosity) to convective one (driven by inertia). In the case of vanishing Reynolds number, any perturbation in the flow diffuses in a very short time, and thus any action appears to have almost immediate consequences. Focusing on the case of microorganisms, we can reasonably simplify the Navier-Stokes equation by removing the inertial terms. In the absence of an external body force, we obtain the Stokes equation [21]:

$$\boldsymbol{\nabla} p = \eta \boldsymbol{\nabla}^2 \boldsymbol{u}, \quad \boldsymbol{\nabla} \cdot \boldsymbol{u} = 0. \tag{1.7}$$

The Stokes equation also neglects what is sometimes called the unsteady Reynolds number $\mathrm{Re}_\omega = \rho L^* \omega^2 / \eta$, where ω is the characteristic frequency that arises in unsteady situations like beating flagella or waving cilia for instance. Such a simplified version of the Navier-Stokes equation has several specific features that deserve to be noted.

First, the Stokes' equation is linear, which implies that the force $\boldsymbol{F}$ and torque $\boldsymbol{T}$ experienced by a swimmer are linear functions of its angular and linear velocities, $\boldsymbol{\Omega}$ and $\boldsymbol{V}$ respectively:

$$\begin{bmatrix} \boldsymbol{F} \\ \boldsymbol{T} \end{bmatrix} = \eta \boldsymbol{\mathcal{R}} \cdot \begin{bmatrix} \boldsymbol{V} \\ \boldsymbol{\Omega} \end{bmatrix}, \tag{1.8}$$

where $\boldsymbol{\mathcal{R}}$, called the *resistance matrix*, is only function of the swimmer's geometrical properties such as its size, shape or orientation with the flow [22, 23].

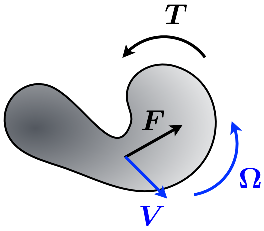

Figure 1.3: Schematic of the rigid body motion $(\boldsymbol{V}, \boldsymbol{\Omega})$ experienced by an object subjected to a force $\boldsymbol{F}$ and a torque $\boldsymbol{T}$. The directions and magnitudes of the resulting velocities depend on the resistance matrix $\boldsymbol{\mathcal{R}}$ of the object [22, 23].

Secondly, neglecting the swimmer's inertia implies the total forces and total torques it experiences vanish exactly. By noting $\mathcal{S}$ its surface, we obtain the *force-free* and *torque-free* relations:

$$\int_{\mathcal{S}} \boldsymbol{\sigma} \cdot \boldsymbol{n} \mathrm{d}\mathcal{S} = \boldsymbol{0}, \quad \int_{\mathcal{S}} \boldsymbol{r} \times \boldsymbol{\sigma} \cdot \boldsymbol{n} \mathrm{d}\mathcal{S} = \boldsymbol{0}, \tag{1.9}$$

where $\boldsymbol{r}$ is the position vector on its surface. Those relations tell us that viscous drag forces dissipate any propulsion work. In the case of an E. Coli bacterium, its rotating helixes generate an amount of work entirely dissipated by the drag forces experienced by the rest of its body.

Finally, the absence of a time-derivative in the Stokes equation implies the flow solution depends on time only through its boundary conditions. Any variation of the flow field propagates with an infinite speed everywhere in the medium. In particular, the time-reversed Stokes flow and associated pressure field solve the same equation. As a result, if a microorganism performs a time-reciprocal stroke (like a human does by flapping his legs in a pool for instance), the drag force it experiences in the second half of the motion is then exactly the opposite of the one it has experienced during the first half. As a result, the microorganism comes back to its initial position and therefore remains, on average, at the same location. Such a result, which we owe to Purcell (1977) [24], is called the *Scallop theorem* and remains valid for Newtonian fluids in the limit of vanishing Reynolds numbers. Microorganisms have then adopted specific strategies, briefly mentioned in section 1.2, which break the necessary spatiotemporal symmetry to achieve a net motion.

1.4 Propulsion induced by surface velocity

In this section, we focus on one particular propulsion strategy, which enables the swimmer to generate tangential velocities at its surface. First of all, we provide the reader with a convenient method specific to the low Reynolds fluid mechanics, called the *Lorentz reciprocal theorem*, which enables us to compute a system's net motion from the knowledge of the velocity field at its surface. We then consider the particularly enlightening case of a swimming paramecium before focusing on some artificial microswimmers that also use such a propulsion strategy.

1.4.1 Lorentz' reciprocal theorem

Let us consider a swimmer (called 1) that generates a tangential velocity $\boldsymbol{u}_s$ at its surface $\mathcal{S}$. The goal of this approach is to compute its resulting velocity $\boldsymbol{V}_1$. To do this, we consider an auxiliary problem (called 2) involving a passive and rigid object of same geometry that experiences a rigid body motion $(\boldsymbol{V}_2, \boldsymbol{\Omega}_2)$ in reaction to an imposed external force taken in the same direction as $\boldsymbol{V}_1$. We may note that while the swimmer 1 is force-free and satisfies Eq. (1.9), the swimmer 2 is not, since an external force drags it. The velocity field in each problem satisfies the Stokes equation. Considering both flow problems in the lab frame, it comes:

$$\boldsymbol{\nabla}\cdot\boldsymbol{\sigma}_1 = \boldsymbol{0}, \qquad \boldsymbol{\nabla}\cdot\boldsymbol{\sigma}_2 = \boldsymbol{0}, \tag{1.10}$$

$$\boldsymbol{\nabla}\cdot\boldsymbol{u}_1 = 0, \qquad \boldsymbol{\nabla}\cdot\boldsymbol{u}_2 = 0, \tag{1.11}$$

$$\boldsymbol{u}_1|_{\mathcal{S}} = \boldsymbol{u}_s + \boldsymbol{V}_1 + \boldsymbol{\Omega}_1\times\boldsymbol{r}, \qquad \boldsymbol{u}_2|_{\mathcal{S}} = \boldsymbol{V}_2 + \boldsymbol{\Omega}_2\times\boldsymbol{r}, \tag{1.12}$$

$$\boldsymbol{u}_1|_{\boldsymbol{r}\to\infty} = \boldsymbol{0}, \qquad \boldsymbol{u}_2|_{\boldsymbol{r}\to\infty} = \boldsymbol{0}, \tag{1.13}$$

$$\int_{\mathcal{S}} \boldsymbol{\sigma}_1\cdot\boldsymbol{n}\,\mathrm{d}\mathcal{S} = \boldsymbol{0}, \qquad \int_{\mathcal{S}} \boldsymbol{\sigma}_2\cdot\boldsymbol{n}\,\mathrm{d}\mathcal{S} = \boldsymbol{F}_2, \tag{1.14}$$

$$\int_{\mathcal{S}} \boldsymbol{r}\times\boldsymbol{\sigma}_1\cdot\boldsymbol{n}\,\mathrm{d}\mathcal{S} = \boldsymbol{0}, \qquad \int_{\mathcal{S}} \boldsymbol{r}\times\boldsymbol{\sigma}_2\cdot\boldsymbol{n}\,\mathrm{d}\mathcal{S} = \boldsymbol{0}. \tag{1.15}$$

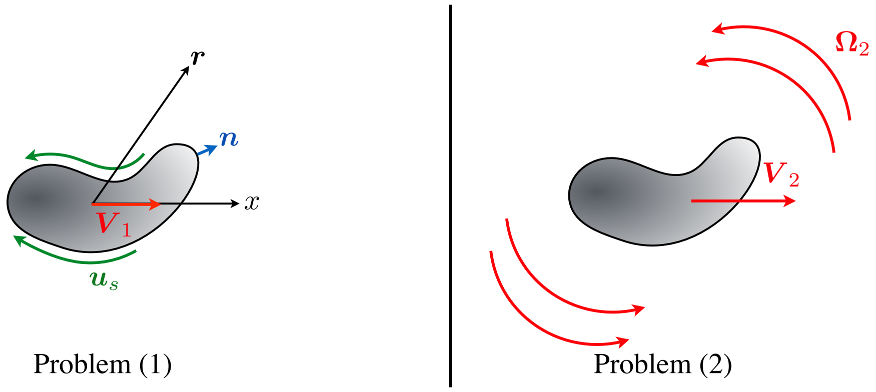

Figure 1.4: Schematic of the flow problems used in the Lorentz reciprocal theorem. (1): Force-free swimmer that moves at the velocity $\boldsymbol{V}_1$ (to determine) resulting from known tangential velocities $\boldsymbol{u}_s$. (2): Object of same geometry that experiences a rigid body motion $(\boldsymbol{V}_2, \boldsymbol{\Omega}_2)$ resulting from an external force taken in the same direction as $\boldsymbol{V}_1$.

Contracting the Stokes equation of each problem against the Eulerian velocity field of the dual problem and integrating the result over the outer volume $\mathcal{V}$, we obtain the Lorentz reciprocal theorem [25]:

$$\int_{\mathcal{V}} \Big[(\boldsymbol{\nabla}\cdot\boldsymbol{\sigma}_1)\cdot\boldsymbol{u}_2 - (\boldsymbol{\nabla}\cdot\boldsymbol{\sigma}_2)\cdot\boldsymbol{u}_1\Big]\mathrm{d}\mathcal{V} = 0. \tag{1.16}$$

Using the incompressibility condition Eq. (1.11), the divergence theorem, the force-free conditions Eq. (1.14) and Eq. (1.14) and finally the boundary conditions Eq. (1.12) and Eq. (1.13), Eq. (1.16) becomes:

$$\boldsymbol{V}_1 \cdot \boldsymbol{F}_2 + \int_{\mathcal{S}} \boldsymbol{u}_s \cdot \boldsymbol{\sigma}_2 \cdot \boldsymbol{n} \mathrm{d}\mathcal{S} = 0. \tag{1.17}$$

Knowing the flow field around the steadily translating object of the problem (2) at vanishing Reynolds [22], we are then able to determine the swimmer's velocity:

$$V_1 = -\frac{1}{\boldsymbol{F}_2 \cdot \boldsymbol{e}_x} \int_{\mathcal{S}} \boldsymbol{u}_s \cdot \boldsymbol{\sigma}_2 \cdot \boldsymbol{n} \mathrm{d}\mathcal{S}. \tag{1.18}$$

We notice from Eq. (1.18) that we do not need to know the velocity field of the problem (1) everywhere in the medium but only at the surface $\mathcal{S}$ to compute the propulsion velocity $\boldsymbol{V}_1$.

1.4.2 Paramecia

Let us now go back to the example of the paramecium, observed for the first time in 1645 by Dutch microscopist Leeuwenhoek, who used the term *cilia* to describe the "*incredibly thin feet or little legs by which a small animal can propel itself through water*". We can indeed represent a paramecium approximately as an elongated body (panel (*d*) of Fig. 1.2) with a multitude of ciliary hairs. Two cilia beating side by side tend to synchronise their motion [26]. However, metachronal waves occur spontaneously when several of them are involved (thousands in the case of a paramecium), which generate a net flow at the surface of the paramecium (panel (*g*) of Fig. 1.2).

If full numerical models of ciliary propulsion have been carried out [27, 28, 29], we focus here on the pioneering work of Lighthill (1952) [30] and Blake (1971) [19], who considered a simplified approach also known as the *squirmer model*, which approximates the paramecium as a sphere and the cilia as a small and unsteady deformation of the body. Following their approach and taking advantage of the axial symmetry of the problem, the radius R and angle θ that characterise the surface geometry (panel (*e*) of Fig. 1.2) are decomposed in Legendre modes:

$$\begin{aligned} R(\theta_0, t) &= a\left(1 + \epsilon \sum_{n=2}^{N} \alpha_n(t) P_n(\cos\theta_0)\right), && (1.19)\\ \theta &= \theta_0 + \epsilon \sum_{n=1}^{N} \beta_n(t) V_n(\cos\theta_0), && (1.20) \end{aligned}$$

where $\epsilon \ll 1$, a the average radius of the envelope composed of the cilia and the paramecium body, α_n and β_n are periodic functions of time, P_n the n-th Legendre polynomial and $V_n = -2/(n(n+1))P_n^1$. If Blake computed the entire velocity field solution, we may notice the cilia coordinated motions provide a non-zero value regarding the tangential velocity at the vicinity of the paramecium body. Such an apparent slip-velocity may be approximated at the leading order by:

$$\boldsymbol{u}_\theta\big|_{|\boldsymbol{r}|=a} = -a\epsilon\dot{\beta}_1 \sin\theta_0 \boldsymbol{e}_\theta. \tag{1.21}$$

By a direct application of the Lorentz-reciprocal theorem on the sphere of radius a, we may determine the paramecium propulsion speed which results from the tangential velocity induced by the ciliary motion.

1.4.3 Interfacial microswimmers

If nature has found ways to generate slip-velocities, it has also inspired researchers in the design of microswimmers. According to Eq. (1.18), a body experiencing appropriate tangential velocities at its surface can self-propel in a viscous fluid. In particular, some swimmers can generate a surface tension imbalance at their surface that induces a stress jump. The latter is balanced by viscous dissipations and create a tangential flow. While section 1.5 gives more physical details, the goal of this section is to provide the reader with a global overview of several experimental systems that use interfacial stresses to self-propel in their medium. In the following, we first introduce swimmers which exploit interactions with a surface to achieve self-propulsion. In a second stage, we draw our attention to droplets, which swim as the result of chemical reactions that modify the *surface activity of their surfactant coverage*. Finally, we focus on droplets that propel as a result of micellar interactions with the outer fluid that alter the *surfactant distribution* at their surface.

First, let us consider swimmers that self-propel on a surface. The experiments carried out in Ref. [31] involve a pure oil droplet of about 2mm radius, placed on a glass plate covered with surfactants and partially pre-treated with acid. As the droplet moves, it modifies the surfactant distribution on the plate and thus experiences surface tension stresses (panel (*a*) of Fig. 1.5). Experiencing interfacial forces, the droplet reaches a velocity of about 60mm/s within the zones delimited by the acid boundaries. Differently, droplets containing surfactants and deposited on a clean plate may also self-propel. The study from Ref. [32] presents water droplets containing surface-active agents and put on a glass plate. Initially pushed, the droplet is destabilised and self-propels at a velocity of a few centimetres per second (panel (*b*) of Fig. 1.5). In this case, the droplet uses interfacial stresses coming from the trace of surface-active agent it leaves on its path, which imposes a front-back force difference. We should note the droplet is either dragged or pushed by surface tension stresses that result from a non-uniform surface tension on the rigid plate.

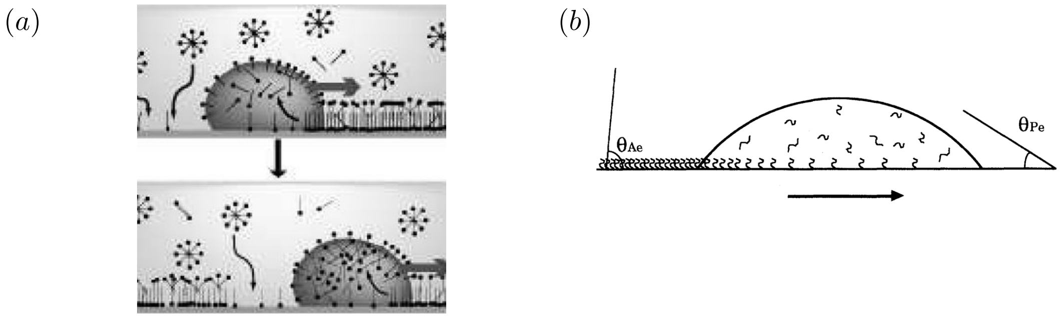

Figure 1.5: Swimmers that self-propel in reaction to interfacial stresses with a surface. (*a*): Schematic of an oil droplet that propels on a glass plate partially covered with surfactant molecules [31]. (*b*): Schematic of a water droplet containing surface active agent that moves on a glass plate due to the trace it leaves on its path, which imposes a front-back force difference [32].

Recent experiments have shown that droplets can spontaneously swim using comparable mechanisms without needing any interaction with a boundary. In the following, we distinguish two kinds of self-propelled droplets: (*i*) the ones that take advantage of chemical reactions to induce variations of the surface tension activity along their surface, and (*ii*) the ones that experience a solubilisation process with the outer fluid which modifies the surfactant distribution on their surface.

About 15 years ago, the study from Ref. [33] and Ref. [34] showed that an oil droplet with a radius of between 50 and 120μm, deposited in an aqueous micellar solution can swim autonomously at a maximal speed of 11μm/s. In its motion, the droplet emits giant vesicles at its back. The study claims that interactions between the micelles present in the solution and the droplet's surface lead to the dehydrocondensation of the oil into vesicular amphiphile. As a consequence, the presence of two different species in the vicinity of the droplet (the surfactant molecules and the vesicles) alters the surface tension activity along with its interface, generating interfacial stresses that trigger its propulsion.

Another possibility has been explored in Ref. [35] and involves an oil droplet of nitrobenzene floating in an aqueous phase containing oleic acid. The pH of the aqueous phase is set sufficiently high so that oleate molecules act as surfactants. The spontaneous propulsion mechanism depicted on the panel (*b*) of Fig. 1.6 is observed as follows: (*i*) Initially, the droplet has a uniform distribution of oleate molecules on its surface. (*ii*) It experiences a hydrolysis reaction which distorts its coverage of oleate molecules. As a consequence, the droplet becomes turbid and performs jerky motions. (*iii*) The symmetry is finally broken and internal convection flows provide the leading edge with new anhydride molecules. The latter rolls thus sustain a front-back surface tension difference that enables the droplet to swim.

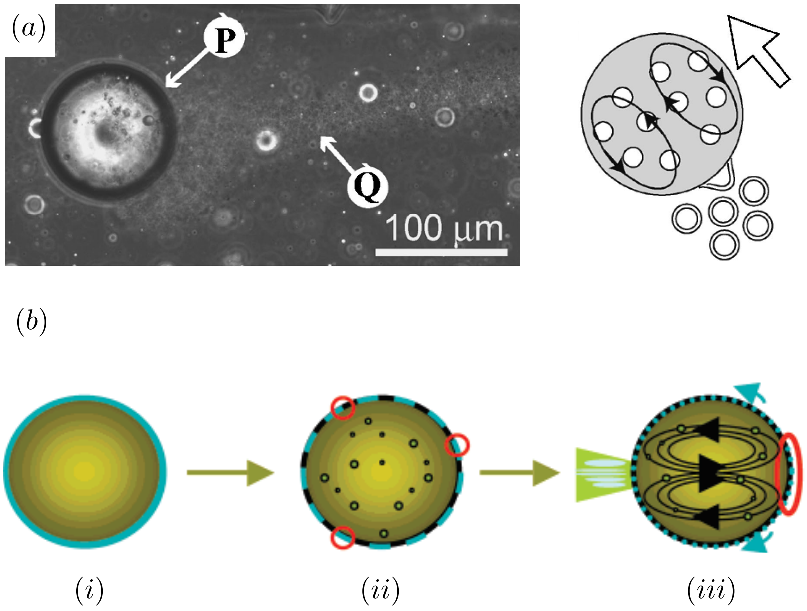

Figure 1.6: (*a*) figure drawn from Ref. [33]. Left: Phase-contrast microscopic images on self-propelled motion of an oil emulsion droplet (site P) with a trail of giant vesicles (site Q). Right: Schematic of the dynamics. (*b*): Schematic model of the initial stages in oil droplet movement drawn from Ref. [35]. (*i*): A fresh oil droplet (amber sphere) is introduced to the aqueous phase. The droplet appears symmetric and is coated in surfactant (blue line), and the oil phase is clear. (*ii*): Internal structures form within the oil droplet and begin to move as spontaneous oscillations exposing precursor to the water phase. Potential sites of hydrolysis are shown in red. The oil droplet now appears turbid. (*iii*): Symmetry is broken, convection begins (arrows within the oil), surfactant (blue) moves to the anterior pole (blue arrows), and hydrolysis of the precursor is localised (red circle). The blue lines behind the droplet represent surfactant coming off the interface. The green zone indicates a zone of low pH.

In the previous situations, specific chemical reactions happen to modify the surface activity of the droplets' surfactant coverage, leading to interfacial stresses and self-propulsion. Besides, solubilisation processes occurring at the droplet's interface may result in a non-uniform distribution of the surfactants on the droplet's surface, leading to similar interfacial stresses and propulsion.

Let us consider the swimming water droplets from Ref. [36], which evolve in an organic phase composed of a solution of nonionic surfactants. While the droplets' radii range between 20 and 60μm, they reach a velocity between 10 and 50μm/s. It can be noticed that (*i*) the droplets shrink over time and (*ii*) they slow down as well (see panel (*g*) of Fig. 1.7). Besides, each droplet's velocity appears to evolve proportionally to its radius, as reported on the left of the panel (*g*) of Fig. 1.7. However, the droplets do not both self-propel in situations where the solution is already saturated in water or if the surfactant concentration is too low (the reader may refer to the section 1.5 for more details about surfactant molecules and CMC). Actually, the droplet solubilises as a result of the interactions with the micelles present in the outer fluid. Such a solubilisation process creates depletion zones on the droplet's surfactant coverage, which generate interfacial stresses that propel the droplet (see section 1.5 for more details). Additionally, we may refer to the recent experiments of Ref. [37], which provide an example of the reversed system: oil droplets, with radii ranging between 25 and 35μm, immersed in a water reservoir containing surfactants. Their self-propulsion velocities may reach up to 450μm/s and are thus almost ten times higher than the ones recorded in Ref. [36].

On the other hand, an active droplet may consist of liquid crystals and be immersed in an aqueous medium containing surfactants [38]. It is important to note its nematic state does not happen to play any role in the droplet's self-propulsion mechanism but is convenient in the experiments to visualise its direction of motion by looking at the position of the topological defect. However, active nematic droplets may exhibit specific swimming regimes at high advection-to-diffusion ratio (see section 1.6.3 for more details). Such nematic droplets self-propel at a velocity between 5 and 25μm/s in the case where the surfactant concentration lies above 5wt%. Besides, in a similar way as in Ref. [36], we witness a linear decrease of the droplet size and velocity over time, indicating the presence of a solubilisation process. Finally, both shrinking rate and velocity magnitude tend to increase with the surfactant concentration [38, 37] as reported on the panel (*b*) of Fig. 1.7 drawn from Ref. [38].

Let us consider a spherical active droplet undergoing a solubilisation process and evolving far from any boundary. The solubilisation is then isotropic and does not breaks any spatio-temporal symmetry. It appears thus very surprising that active droplets self-propel since the scallop theorem prevents any swimmer that does not break such a symmetry to have a net displacement. The answer to this apparent paradox lies in the coupling between the solubilisation process and the flow field around the droplet (see section 1.6).

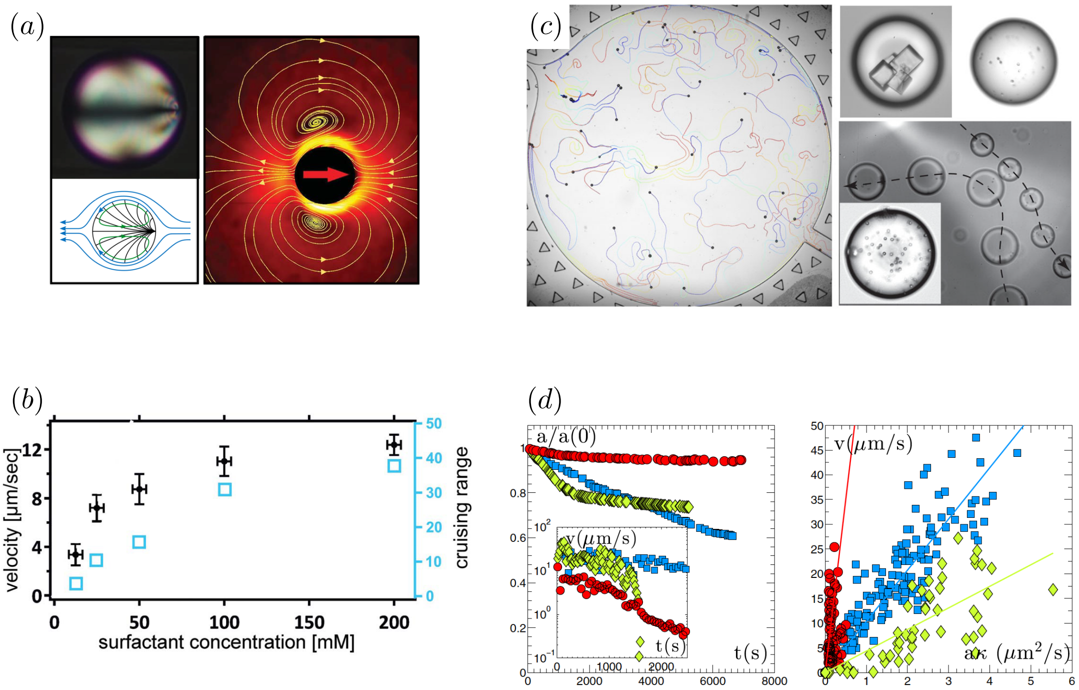

Figure 1.7: (a) single active droplet swimming. Upper left: Picture from Ref. [39] representing a liquid crystal droplet of radius approximately of 25μm that moves from left to right. Lower left: Schematic from Ref. [39] illustrating the flow field (arrow) inside and outside of the droplet and distorted nematic director field (black lines). Right: Velocity field (in laboratory frame) around a liquid crystal droplet as revealed by PIV [38]. The yellow lines are streamlines of the flow. (b): Velocity of a liquid crystal droplet as function of the surfactant concentration in the medium [38] (c)-left: Trajectories of approximately 50 pure water droplets in the observation room of length 0.5cm recorded during $500s$ [36]. Each droplet trajectory is color-coded with the time preceding its present location. (c)-right: Transport of salt crystals and colloids from Ref. [36]. (d)-left: Velocity v and relative diameter $a/a(0)$ versus time for three droplets under different conditions: water in Sq-MO (blue squares), water in Td-MO (green diamonds), water$-$26wt%NaCl in Sq-MO (red circles) [36]. (d)-right: Velocity as function of κa (where a is the droplet diameter and $\kappa = 5 \times 10^{-3} \mu m/s$ the characteristic radius rate of decay) from Ref. [36].

1.5 Surface tension and Marangoni flows

In this section, we introduce surface tension and explain how the presence of surfactant molecules influence it. In a second stage, we provide the reader with a physical description of Marangoni flows which appear in the presence of surface tension gradients at an interface.

Figure 1.8: (*a*) Image of a *Gerris remigis* on water, credit: Deep Look. (*b*) Bug trapped in a spherical water droplet, credit: Paul Jones. (*c*) Pin floating upturned on water, image drawn from Ref. [40]

1.5.1 Surface tension

While observing flows in our daily life, we may wonder why a droplet is almost spherical? Why some insects successfully run across water surface? Why soap bubbles in a bathtub attract each other and finally merge into a bigger one? All these effects involve *surface tension*, briefly introduced below.

Let us consider a liquid-vapour interface such as water and air. The water molecules exert electrostatic forces between each other, and while most are located in the bulk, surrounded everywhere by other molecules, others lie at the water-air interface and only interact with molecules on their side or below them (see Fig. 1.9). This anisotropy of interactions causes the liquid surface to be attracted towards the interior region. At the equilibrium, the surface area at the interface is minimal and the surface contraction balances the interactions with other molecules.

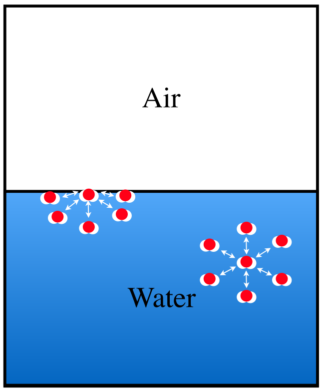

Figure 1.9: Schematic of the water-air interface: other molecules well surround the molecules of water in the bulk, unlike the ones at the interface.

1.5.2 Surfactant molecules

As schematised in the panel (*a*) of Fig. 1.10, a surfactant molecule consists of a hydrophilic head and a hydrophobic tail. In a mixture of oil and water, the water-oil interface adsorbs surfactant molecules where they can satisfy both head and tail affinities. The interactions between surfactants and water molecules are much lower than between two water ones. As a result, the energy of the interface decreases, which leads to a lower surface tension value. These local variations of surface tension are not without consequence on the flow, as detailed in the following section.

If adding surfactant molecules reduces the surface tension of the interface, there is a critical surfactant concentration called CMC (critical micelle concentration), above which the surfactant molecules spontaneously gather and form micelles. This phenomanon occurs in the bulk and does not depend on the interface but is instead a specificity of the surfactant molecule itself (see panel (*b*) and (*d*) of Fig. 1.10). A surfactant molecule may not be adsorbed at the interface but gathers with other molecules to gain in stability instead. As a result, the surface tension at the interface remains approximately constant above the CMC.

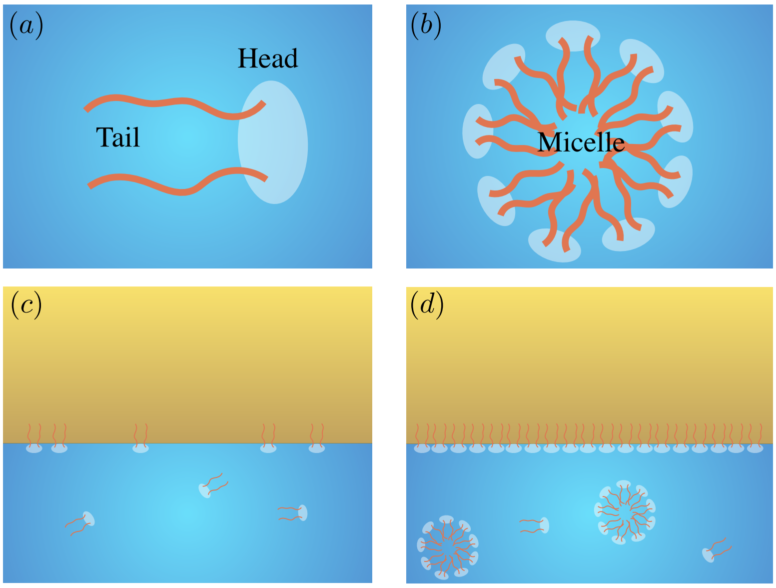

Figure 1.10: (*a*) Schematic of a surfactant molecule with a hydrophilic head and a hydrophobic tail. (*b*) Schematic of a micelle composed of several surfactant molecules. (*c*) Schematic illustrating a situation below the CMC, where surfactant molecules are still adsorbed at the interface. (*d*) Schematic illustrating a situation above the CMC, where micelles are spontaneously formed.

1.5.3 Marangoni effect

When observing the robe of a wine containing a high alcohol content, we may notice the interface between wine, glass and air – called the triple line – has a wavy shape (panel (a) of Fig. 1.11). Moreover, we often hear that the stronger the wine, the larger the oscillation amplitude. This phenomenon is known as the *tears of wine*, phenomenon first discovered by James Thomson in 1855 [41] and then studied in more details by Carlo Marangoni during its PhD in 1865 [42].

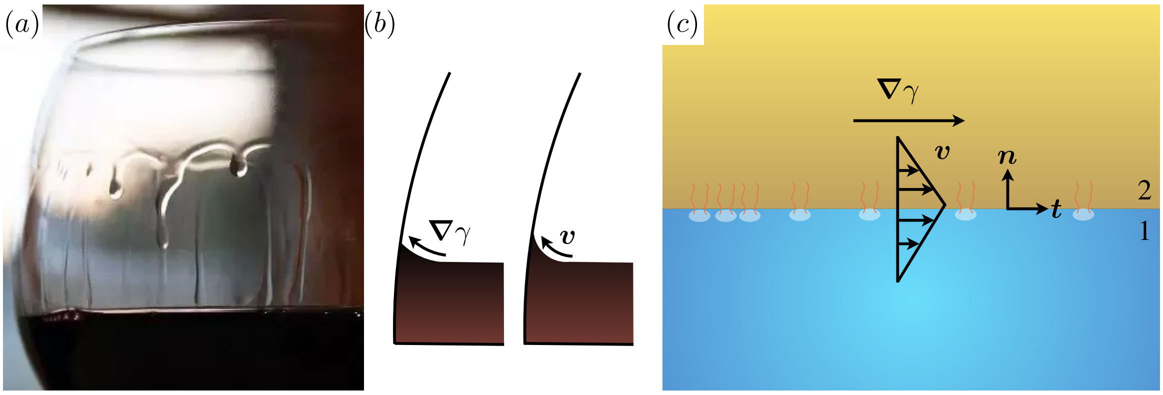

Figure 1.11: (a): Picture of a glass of wine which illustrates the *tears of wine* effect, credit: Wikipedia (b): Schematic of the meniscus created at the interface between the air, glass and wine. The meniscus moves up in reaction to a surface tension gradient $\boldsymbol{\nabla}\gamma$. ($c$): Schematic of the Marangoni flows induced by the presence of a surface tension gradient $\boldsymbol{\nabla}\gamma$ at the interface of two fluids. The figure illustrates one possible origin of such a gradient with a non-uniform distribution of surfactant molecules at the interface.

Without wishing to offend wine amateurs, we can consider that wine is simply a mixture of water and alcohol. The surface tension differences between the three phases lead to higher adhesion forces between glass and wine compared to the cohesive forces within the wine. As a result, a concave meniscus appears on the edge of the glass [43] (panel (b) of Fig. 1.11). Alcohol evaporates faster than water due to its lower vapour pressure value. Since alcohol also has a lower surface tension, its evaporation induces a local surface tension gradient. The latter generates a flow, called *Marangoni flow*, towards the evaporation zone. As a result, the height of the wine meniscus increases. Besides, this old problem has recently been revisited, and the regular wavy pattern of wine tear formation happens to result from a Rayleigh-Plateau instability. The interested reader may thus consult Ref. [44] for more information.

If we notice Marangoni flows in the case of alcohol evaporation, they may also result from many other events such as a lack of temperature homogeneity or a non-uniform distribution of surfactants. Willing to remain general, let us consider the interface between two fluids noted 1 and 2, where we denote by $\boldsymbol{\sigma}^{(1,2)}$ the Cauchy stress tensors in each fluid and by $\mathcal{S}$ the surface of the interface. Neglecting inertia, the balance of stresses at the interface reads [45]:

$$\boldsymbol{n} \cdot \left(\boldsymbol{\sigma}^{(2)} - \boldsymbol{\sigma}^{(1)}\right)\Big|_{\mathcal{S}} \cdot \boldsymbol{t} = - \left.\boldsymbol{\nabla}\gamma\right|_{\mathcal{S}} \cdot \boldsymbol{t}, \tag{1.22}$$

where $\boldsymbol{n}$ and $\boldsymbol{t}$ are normal and tangential vectors to the interface (panel (c) of Fig. 1.11). The fluid is hence not at the equilibrium, and a flow arises in response to the viscous stress jump at the interface. Let us consider a droplet of radius R and viscosity $\eta^{(i)}$ immersed in another liquid of viscosity $\eta^{(o)}$, in the presence of an external surface tension gradient $\boldsymbol{\nabla}\gamma$. This gradient leads to Marangoni flows at the interface of the droplet, which therefore swims towards the zone of lower surface tension. Following the work of Hadamard (1911) [46] and Young (1959) [47], we can derive the velocity $\boldsymbol{V}$ of the droplet:

$$\boldsymbol{V} = \frac{-R}{2\eta^{(o)} + 3\eta^{(i)}} \boldsymbol{\nabla}\gamma. \tag{1.23}$$

Let us consider a chemical solute of concentration C, composed of molecules, which linearly modifies the surface tension of the droplet via the relation:

$$\gamma = \gamma_0 + \gamma_1 C, \tag{1.24}$$

where $\gamma_1 > 0$. The presence of the solute then increases the surface tension of the fluid. Let us consider a droplet immersed in a liquid in the presence of an external uniform solute gradient $\boldsymbol{\nabla}C = -\mathcal{A}/D\boldsymbol{e}$, where $\mathcal{A}$ denotes the external flux of solute whose diffusion coefficient is noted D. Using Eq. (1.23) together with Eq. (1.24), the droplet's velocity finally follows [48]:

$$\boldsymbol{V} = \frac{\mathcal{A}R\gamma_1}{(2\eta^{(o)} + 3\eta^{(i)})D} \boldsymbol{e} = V^* \boldsymbol{e}. \tag{1.25}$$

In the following, the drift velocity V^* is chosen as a reference velocity with which the self-propulsion velocity of the active droplets introduced in section 1.4.3 may be compared.

1.6 Active droplets

In this section, we first introduce the notion of *activity* and *mobility* specific to an active droplet. Then, we provide a physical explanation of an active droplet's spontaneous self-propulsion, which results from their coupling. The second part tackles the issue of solute dynamics and provides the general transport equations used in this manuscript. Finally, the third part presents some observed behaviours displayed by a single active droplet in addition to collective dynamics manifested by an assembly of active droplets in the presence of boundaries.

1.6.1 Activity, mobility and self-propulsion

Let us consider a droplet immersed in a liquid medium saturated with surfactants. We consider the concentration of surfactant in the bulk phase to be sufficiently high so that the average concentration is above the CMC. This implies that micelles (called *empty micelles*) spontaneously form in the outer fluid. Complex interactions between the droplet and the micelles lead to the production of *swollen micelles* and the consumption of free-surfactant molecules (see Fig. 1.12). Such physicochemical phenomena deplete the surfactant coverage at the droplet interface. In the following, we consider an effective solute of concentration C, produced at the droplet's surface, which increases the surface tension at the interface of the droplet.

In the so-called *molecular pathway* framework [38], the effective solute concentration may refer to $C = C_\infty - C_s$, where C_s is the concentration of free-surfactant molecules that tends to C_∞ infinitely far from the droplet. C has a positive value in the vicinity of the droplet as the result of the consumption of free-surfactant molecules and vanishes far from the droplet. Besides, since any increase of C is related to a decrease in the number of free-surfactant molecules, the zones of high concentration represent the regions with high surface tension.

On the other hand, in the framework called *micellar pathway* [36], the effective solute concentration C may be directly identified as the concentration of swollen micelles produced at the droplet's surface. The micelles deplete the surfactant coverage of the droplet as they get swollen. As a result, a local increase of C in the vicinity of the droplet leads to a local increase of surface tension.

In particular, within the case of small concentration variation, we assume the link between such an effective solute and surface tension γ to follow a linear relation:

$$\gamma = \gamma_0 + \gamma_1 C, \tag{1.26}$$

where γ_1 is a positive constant. A reader willing to get more information of the physico-chemical dynamics may consult the very recent theoretical work of Ref. [49], which derives both the advection-diffusion dynamics of the swollen micelles in the bulk and surfactant molecules motion at the droplet's surface.

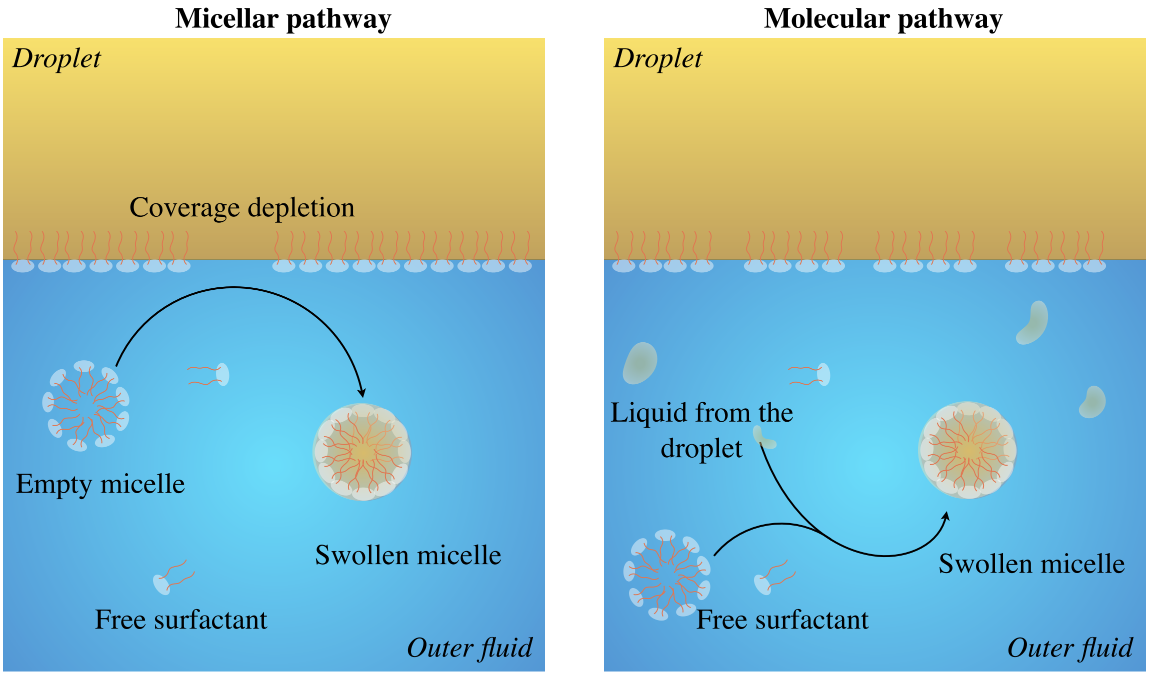

Figure 1.12: Overview of two possible interfacial mechanisms at the origin of the droplet's self-propulsion. Left: Micellar pathway in which empty micelles get swollen in interacting with the surface of the droplet. Right: Molecular pathway in which the droplet solubilises in the outer fluid. As a consequence, empty micelles get swollen without interacting with the interface.

In the activity mechanism previously introduced, the interactions of micelles and surfactant molecules with the droplet surface results in an increase of the surface tension in the region of high effective solute concentration C. As a consequence, any solute gradient in the vicinity of the droplet causes a gradient of surface tension. The latter then generates Marangoni flows towards the zone of high concentration. This mechanism, which converts solute imbalance in a flow, is called *mobility*.

Gathering *activity* and *mobility* enables us finally to provide a physical explanation of the instability at the origin of an active droplet's self-propulsion (see Fig. 1.13): (*i*) Initially, let us consider an active droplet with a uniform solute distribution on its surface. In this situation, the droplet remains immobile and generates no flow. (*ii*) A small motion of the droplet induces a flow, which transports the solute by advection at its back. As a consequence, solute gradients arise at the droplet's surface. (*iii*) Since the solute locally increases the surface tension of the interface, Marangoni flows are generated and transport even more solute towards the back of the droplet. (*iv*) The enhanced solute gradient thus reinforces the Marangoni flows as well as the droplet's velocity. In that way, solute advection plays a crucial role since it consists of a positive feedback loop of solute at the back of the droplet. The latter sustains Marangoni flows at the surface of the droplet, which hence keeps swimming. Previously, the steps (*ii*) and (*iii*) coincide but we have split them apart solely for pedagogical reasons.

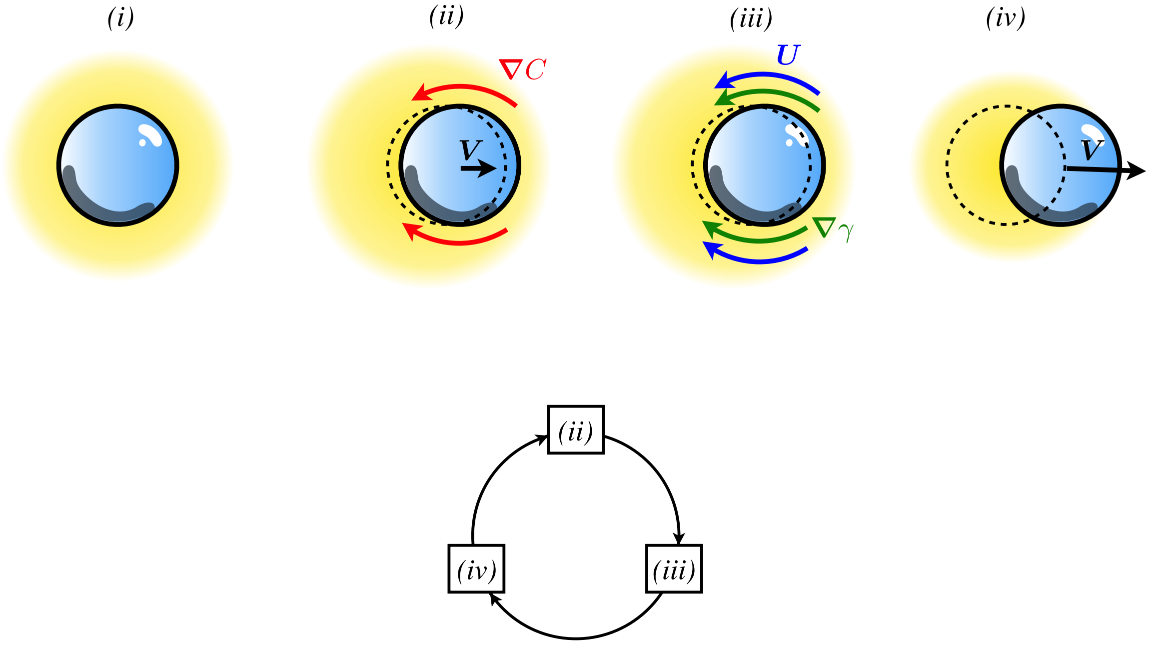

Figure 1.13: Schematic of the instability phenomenon at the origin of the spontaneous propulsion of an active droplet. (*i*): Uniform solute distribution around an immobile droplet in a quiescent fluid. (*ii*): Small velocity perturbation that induces a solute gradient $\boldsymbol{\nabla} C$ towards the back of the droplet. (*iii*): Induced surface tension gradient $\boldsymbol{\nabla}\gamma$ and Marangoni flows $\boldsymbol{U}$ that transports even more solute at the back of the droplet. (*iv*): Enhanced propulsion of the droplet resulting from the solute gradients reinforced by advection.

1.6.2 Solute transport at the microscale

We have learnt from the previous section that micelles and surfactants dynamics are critical to understand the behaviour of active droplets. In this section, we provide the necessary mathematical framework regarding transport phenomena. The latter will be very useful in the following chapters to compute droplets' self-propulsion as well as their interactions.

1.6.2.1 Brownian diffusion

The name of Brownian diffusion is a tribute to the work of Robert Brown (1827) who was the first to observe a diffusion process in studying the random walk of pollen seeds in water [50]. Later, the theoretical work of Einstein (1905) [51], Sutherland (1905) [52], Smoluchowski (1906) [53], in addition to experimental studies by Jean Perrin in 1909 [54] were carried out. Let us consider N particles immersed in a fluid of viscosity η, which perform a random motion: each particle has an equal probability of moving towards any direction in space. We define the mean squared displacement (MSD) of the assembly:

$$\langle \Delta x^2 \rangle = \frac{1}{N} \sum_{i=1}^{N} |\boldsymbol{x}^i(t) - \boldsymbol{x}^i(0)|^2, \tag{1.27}$$

where $\boldsymbol{x}^i(t)$ stands for the position of the particle i at the time t. After computations, it turns out the MSD follows the relation:

$$\frac{\langle \Delta x^2 \rangle}{2t} = D = \mu k_B T, \tag{1.28}$$

where D is a constant called *diffusion coefficient* proper to the particles, T the absolute temperature, k_B the Boltzmann constant and μ the thermal mobility which reads:

$$\mu = \frac{\text{Drift velocity}}{\text{Applied force}}. \tag{1.29}$$

For spherical particles of radius R, Eq. (1.29) simplifies to $\mu = (6\pi\eta R)^{-1}$. In particular, we can find $D = 10^{-10}$-$10^{-9}\text{m}^2/\text{s}$ for stationary bacteria and $D = 10^{-10}\text{m}^2/\text{s}$ for typical surfactant molecules.

1.6.2.2 Transport equations

Considering a sufficiently large number of particles, we may adopt a point of view from larger length scales. To do so, we consider a continuous description of the particles we now call *solute*, which volume's concentration is denoted by C. Diffusion is a phenomenon that tends to homogenise the solute distribution, and Adolf Fick developed a phenomenological law in 1855, which describes the tendency of the particles to travel from zones of higher concentration towards zones of lower ones [55]. Denoting by $\boldsymbol{j}_d$ the diffusion flux that represents the amount of particles per unit area and per unit time that travels in the medium through diffusive processes, *Fick's law* reads:

$$\boldsymbol{j}_d = -D\boldsymbol{\nabla} C, \tag{1.30}$$

where D is the previously defined diffusion coefficient relative to the solute. In addition to the diffusive flux, the fluid transports the solute by advection. We define the advective flux $\boldsymbol{j}_a$:

$$\boldsymbol{j}_a = \boldsymbol{U} C, \tag{1.31}$$

where $\boldsymbol{U}$ stands for the Eulerian velocity field. The local solute concentration thus varies (i) as a result of fluxes (either of advective or diffusive nature) and (ii) because of the presence of local sources (chemical reactions in the medium for instance). In other words, the solute concentration C satisfies the local partial differential equation:

$$\frac{\partial C}{\partial t} + \boldsymbol{\nabla} \cdot \boldsymbol{j} = \mathcal{Q}, \tag{1.32}$$

where $\mathcal{Q}$ is a solute source and $\boldsymbol{j} = \boldsymbol{j}_a + \boldsymbol{j}_d$ the total flux of solute. Combining Eq. (1.30) and Eq. (1.31) together with Eq. (1.32), we obtain the advection-diffusion equation:

$$\frac{\partial C}{\partial t} + \boldsymbol{U} \cdot \boldsymbol{\nabla} C = D\nabla^2 C + \mathcal{Q}. \tag{1.33}$$

Denoting by L^*, V^* and C^* the characteristic length, velocity and concentration of the problem respectively, we define $\boldsymbol{u} = \boldsymbol{U}/V^*$, $c = C/C^*$ and $q = \mathcal{Q}L^*/(V^*C^*)$ as dimensionless Eulerian velocity field, solute concentration and source intensity respectively. Finally, we obtain a dimensionless version of Eq. (1.33):

$$\mathrm{Pe}\left(\frac{\partial c}{\partial t} + \boldsymbol{u} \cdot \boldsymbol{\nabla} c\right) = \nabla^2 c + s, \tag{1.34}$$

where Pe is a dimensionless number called Péclet number, which gauges the contribution of advective transport compared to diffusive ones and is defined as:

$$\mathrm{Pe} = \frac{V^* L^*}{D}. \tag{1.35}$$

Since advection of micelles appears crucial for an active droplet to sustain its propulsion, we expect Pe to be finite in the solute transport dynamics involving active droplets. In particular, the experiments of Ref. [56] provide $R \sim 40\mu$m and $V \sim 40 \times \mu$m/s as typical values for a droplet radius and velocity. We thus estimate Pe ~ 16 using typical diffusivity of surfactants $D = 10^{-10} m^2/s$. Besides, as mentioned in section 1.4.3, radius and velocity both decrease throughout the length of the experiments. Using the minimum droplet size for self-propulsion reported in Ref. [57], the estimate becomes Pe ~ 10.

Choosing the radius R and the drift velocity V^* computed in equation Eq. (1.25) as characteristic radius and velocity respectively, we can find the following expression for Pe:

$$\mathrm{Pe} = \frac{\mathcal{A} R^2 \gamma_1}{(2\eta^{(o)} + 3\eta^{(i)})D^2}. \tag{1.36}$$

We thus may adopt various strategies to modify Pe: (i) changing the droplet's activity $\mathcal{A}$, in varying the surfactant concentration for instance [37], (ii) changing viscosity ratio $\eta^{(i)}/\eta^{(o)}$ [58] or changing the droplet's size [57].

1.6.3 Self-propulsion of active droplets

In this section, we first briefly present various behaviours that may be adopted by a single active droplet. In a second stage, we will focus on collective dynamics exhibited by an assembly of active droplets in the presence of boundaries. This last part raises the question of interactions between active droplets and boundaries, an issue further detailed in chapter 2.

Convinced of the crucial role of advection in an active droplet's self-propulsion mechanism, we can wonder the effect of the Péclet number has on its dynamics. In the following, we make a distinction between liquid crystal droplets in a nematic state and the isotropic active droplets made of oil (resp. made of water) and immersed in an aqueous medium (resp. in an oil medium). We remind that an active droplet shrinks and slows down over time as the result of the solubilisation process it experiences. As a consequence, Pe being proportional to V^*L^*, it will necessarily decrease over time. In the particular case of nematic droplets, Ref. [57] reports three different regimes adopted by a droplet as it shrinks (see Fig. 1.14): (*i*) chaotic motions at early stages when the droplet has a diameter of 110μm, (*ii*) helicoidal trajectories at intermediate times when the droplet's diameter has reduced to approximately 50μm and finally (*iii*) straight motions when the droplet is small (which diameter being approximatively 20μm). Besides, we can note the helicoidal regime is specific to the nematic nature of the droplet as shown in Ref. [39]. Theoretically, Ref. [59] provides a reduced model of nematic droplets. This model informs that in addition to its self-propulsion instability, a nematic active droplet may experience a second one resulting from the coupling between surfactant transport (through advection) and nematic orientation. Indeed, a small concentration disturbance on one side of the droplet makes it rotate, which enhances the initial concentration perturbation and reinforces the rotation of the liquid crystal droplet. Besides, a transition to chaos at sufficiently high Pe is predicted in Ref. [59].

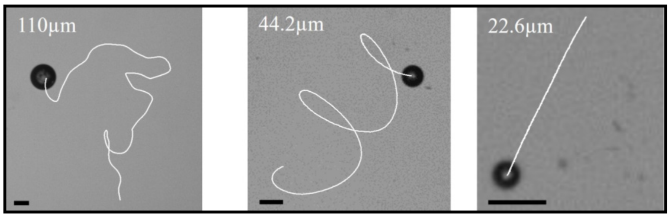

Figure 1.14: Trajectories of a nematic droplet over 30s drawn from Ref. [57]. The shrinking of an active droplet over time leads to a succession of three regimes: random, helical, straight. The scale bars represent 50μm.

In the case of isotropic active droplets, we no longer notice helicoidal trajectories but still witness chaotic ones. The droplet's liquid and outer fluid have distinct viscosities. It is possible to modify the Péclet number of the problem in varying such a viscosity difference (see Eq. (1.36)) as done in Ref. [58] for an active droplet confined in a Hele-Shaw cell. In the latter, we notice first that for Pe close to the instability threshold $\mathrm{Pe}_c = 4$, the droplet performs a ballistic regime where it swims in a straight line. Secondly, at higher Pe (when advection contributes much greater than diffusion in the surfactants transport dynamics), the droplet loses its directionality and performs sudden reorientations. If we may think such erratic reorientations are of thermal nature, we realise this would be very unlikely when comparing the thermal contribution $k_BT/(2R) \sim 10^{-16}$N, with the typically involved drag forces $6\pi\eta^{(o)}RV \sim 10^{-10}$N. Instead, as a result of the non-linear coupling between the solute transport and flow field, higher-order instabilities arise when increasing Pe. While at low Pe the flow field around a droplet appears mainly dipolar, at larger Pe, a quadrupolar structure arises and results in an extensile flow field around the droplet. The droplet then experiences frequent reorientations and thus a chaotic behaviour. Finally, increasing the surfactant concentration in the medium enhances the shrinking rate of the oil droplet considered in Ref. [37]. The enhanced activity thus increases the Péclet number, which results in a transition from a ballistic to an anomalous diffusive regime [37]. In addition to such experimental evidences of chaotic behaviour, theoretical and numerical approaches based on reduced models have recently confirmed the transition from ballistic to chaotic behaviour experienced by an active droplet as Pe is increased [60, 61].

To conclude this chapter, we provide some recently observed collective dynamics, which appear for active droplets in specific geometries. First, let us consider the situation where we place an assembly of nematic active droplets in a reservoir of water containing the right amount of surfactants so that the droplets exhibit self-propulsion. In doing so, clusters spontaneously form at a finite distance from the bottom of the tank (panel (*b*) of Fig. 1.15) [39]. Even if the droplets remain fixed in the cluster, they pump some flow, leading to the formation of large convection rolls. Such rolls are suspected of stabilising the cluster in bringing a constant flux of droplets at its centre. In increasing the confinement by reducing the distance between the top and bottom walls, the clusters break and become long lines of droplets that swim side by side [62]. Finally, in a Hele-Shaw cell, those lines become metastable and break after some time [62] (panel (*a*) of Fig. 1.15). Finally, the study from Ref. [63] considers several water active droplets placed in a microfluidic serpentine full of oil and surfactants. After some time, spontaneous one-dimensional collective motion emerges. In such lines, called trains, the droplets are separated by a fix distance and swim in the same direction (panel (*c*) of Fig. 1.15). The velocity difference between two colliding active droplets appears essential for a train to form. We may thus wonder if a size difference among the droplets would be sufficient to observe such trains (see chapter 4).

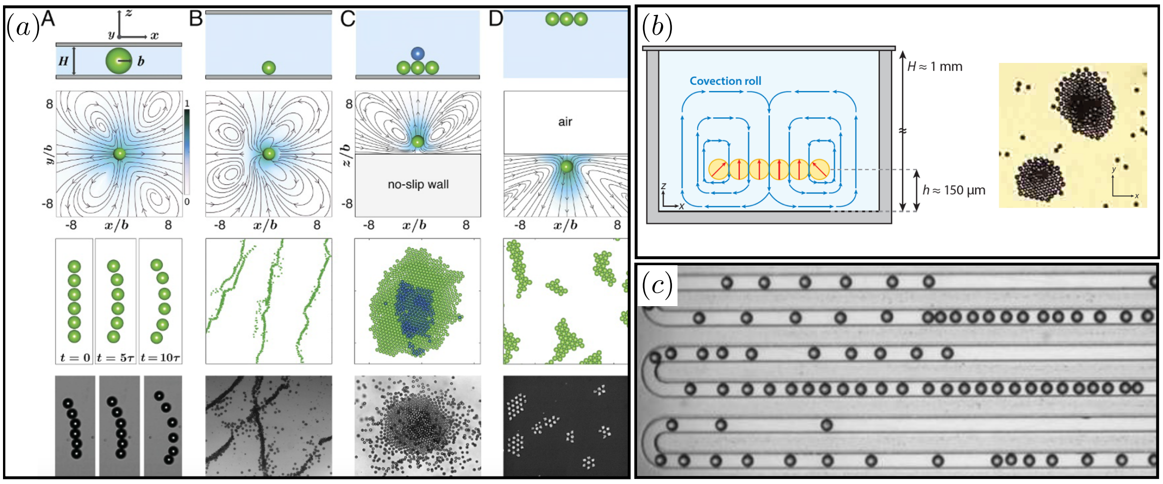

Figure 1.15: (a): Figure drawn from Ref. [62]. (Top) Schematic of confinement. (Upper Middle) The exterior flow field produced by the active particles (of radius b) in each boundary condition considered. Lower Middle and Bottom contain snapshots from simulations and experiments, respectively. Different boundary conditions: A Hele-Shaw ($H/b \approx 2$), B two planar walls ($H/b \approx 8$), C a single planar wall ($H/b \approx 400$) and finally D an air-water interface ($H/b \approx 400$). Here $\tau = b/v_0$ is the time in which the active droplet moves a distance equal to its radius. (b): Clustering in a liquid crystal droplet system in a three-dimensional sample chamber, figure from Ref. [64]. (left) Micrograph of two stable clusters in a three-dimensional reservoir but without buoyancy matching. The diameter of the droplets is 50μm. (right) Schematic of emerging convection roll around a stable cluster. H: reservoir height, h: distance between cluster and reservoir bottom. The red arrows indicate the symmetry axis of the droplets (i.e., the direction in which they try to self-propel), and blue arrows indicate the convection roll. (c): Collective dynamics of swimming droplets in a microfluidic serpentine from Ref. [63]

1.7 Conclusion and discussion

Assemblies of active systems such as bird flocks, human crowds or bacterium colonies happen to perform complex and sometimes spectacular collective motion. In this chapter, we put forth the idea that studying interactions between them may be the first step to decipher their collective dynamics. If artificial swimmers have gained a renewed interest within the scientific community as promising systems to mimic microorganisms, we casted a particular one in this manuscript under the spotlight: *active droplets*. For those experiencing a solubilisation process, the micelles present in the outer fluid induce surface tension gradients, which generate Marangoni flows. The resulting advection of micelles and surfactants appears therefore essential in the droplet's self-propulsion as it sustains a front-back surface tension difference on the droplets.

Studying active droplets (and more generally microswimmers) enables us to put aside the complexity of living organisms and to retain only a few physical ingredients that enable them to self-propel autonomously in a liquid. As claimed in this chapter, the first step to better understand the collective dynamics of active droplets is to accurately describe elementary interactions such as collisions of an active droplet against a flat wall or another droplet. In doing so, we aim to quantify the role of hydrodynamic and chemical interactions, and in particular to determine if one is dominant or negligible during a collision. Providing an accurate description of theses interactions may also be used to build more approximate models, maybe more adapted (especially in terms of numerical cost) to deal with numerous droplets and boundaries. For active systems such as Janus particles [65], that are intrinsically asymmetric, it is not necessary to include advection in the solute transport dynamics to provide accurate self-propulsion or interaction models. On the contrary, active droplets are isotropic at rest, and advection is then essential to explain their propulsion. On the one hand, such a non-linearity introduced in the effective solute transport dynamics leads to non-trivial regimes where a single droplet may exhibit helicoidal and chaotic trajectories. We thus expect complex but exciting dynamics to emerge from the interactions between active droplets. On the other hand, such a non-linearity introduces a significant mathematical challenge since it prevents the use of superposition methods and imposes the treatment of the full coupled hydro-chemical problem. Interested in the modelling of those interactions, we introduce in the next chapter a mathematical model regarding the self-propulsion of a single active droplet in addition to qualitative insights regarding the hydro-chemical interactions between several active droplets.

Take home message of Chapter 1

1. Scallop theorem and propulsion: At the microscale, the Reynolds number vanishes. As a consequence, a swimmer performing a time-reciprocal stroke in a Newtonian fluid cannot achieve a net displacement. To propel, it should break a spatio-temporal symmetry, for example by generating tangential flows at its surface.

2. Droplet's activity: A complex chemical interplay between surfactant molecules, micelles and the surface of a droplet leads to a situation where the droplet appears to emit an effective solute that increases the surface tension locally.

3. Marangoni flows: Any surface tension gradient at the interface of two fluids leads to a stress jump that induces a flow. In particular, a depletion in the surfactant coverage of an active droplet generates Marangoni flows towards the depletion zone.

4. Spontaneous swimming of active droplets: An active droplet spontaneously swims as a result of the coupling between flow field and solute transport. Indeed, an increase of the solute concentration on one side of the droplet induces Marangoni flows that advect even more solute towards the zone of high concentration. As a result of this positive feedback loop, the droplet swims spontaneously and autonomously. We should remember that solute advection is crucial in the droplet's propulsion, which arises only if the solute advection is strong enough.

2

THEORETICAL MODELLING OF SINGLE AND INTERACTING ACTIVE DROPLETS

In the previous chapter, we discovered that Marangoni flows and the resulting solute dynamics are essential in the self-propulsion of an active droplet. The first part of this chapter provides the reader with a spectral decomposition method that mathematically models the phenomenon of instability at the origin of the droplet's spontaneous motion. The aim of this section is to introduce a typical procedure that will be adapted in chapter 3 and 4 to compute the full dynamics of two colliding active droplets. The second part focuses on hydrodynamic interactions between active droplets. In particular, we present a singularity approach drawn from the literature that can be used to estimate far-field hydrodynamic interactions between several active droplets or in the presence of boundaries. Finally, the third part is dedicated to chemical interactions between two active droplets or in the presence of boundaries.

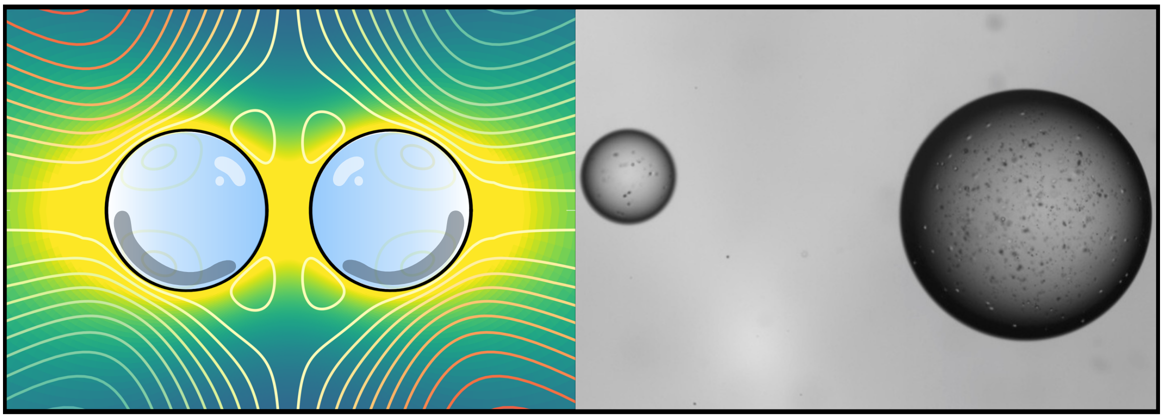

Left: simulation of the concentration field and streamlines involved in the collision between two active droplets (from chapter 3). Right: picture of active droplets from Ref. [36]

Contents

2.1 Self-propulsion of a single active droplet

In this section, we will focus on the behaviour of a single active droplet in bulk and show how both activity and Marangoni flows work hand in hand and lead, if the advection-to-diffusion ratio (Pe) is large enough, to the droplet's self-propulsion. Sections 2.1.1, 2.1.2, 2.1.4 and 2.1.5 are based on derivations drawn from Ref. [66] and Ref. [36] and aim to provide the reader with a guideline using spectral decomposition to solve the coupled hydro-chemical problem at the origin of the droplet's motion. The same approach will be adapted in chapters 3 and 4 to compute exact interactions between a pair of active droplets.

2.1.1 Mathematical description

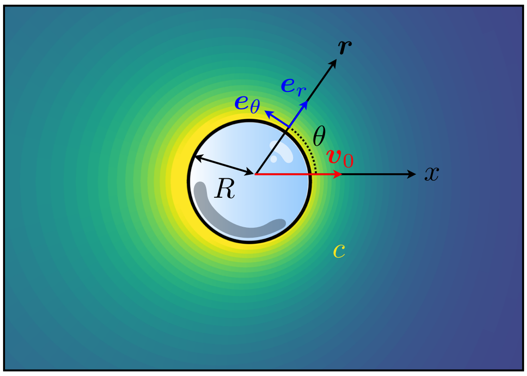

Figure 2.1: Schematic of an active droplet of radius R, which generates a concentration field c and swims at the self-propulsion velocity $v_0\boldsymbol{e}_x$.

Let us consider a spherical droplet of radius R composed of a Newtonian fluid of viscosity $\eta^{(i)}$ and density $\rho^{(i)}$, which swims at a velocity $\boldsymbol{V}$ in another Newtonian fluid of viscosity $\eta^{(o)}$ and density $\rho^{(o)}$. Without privileging any particular physicochemical mechanism introduced in section 1.5, the droplet appears to emit a given solute at its surface $\mathcal{S}$. We denote by $\mathcal{A}$ the flux of solute. Within the limit of small variations, C is assumed to linearly modify the surface tension of the fluid and thus satisfies Eq. (1.26), reminded below for convenience:

$$\gamma = \gamma_0 + \gamma_1 C, \tag{2.1}$$

Besides, computing the capillary number $\mathrm{Ca} = \eta V/\gamma$ for typical experimental viscosity, velocity and surface tension values ($\eta = 10^{-2}\mathrm{m}^2.\mathrm{s}$, $V = 10 - 50\mu\mathrm{m/s}$, $\gamma = 2\mathrm{mN/m}$), we obtain $\mathrm{Ca} \sim 10^{-5} - 10^{-4}$, which thus confirms the droplet's deformation can indeed be neglected. Since the solute both diffuses and is transported by advection, denoting by $\boldsymbol{U}^{(i,o)}$ the Eulerian velocity field either inside or outside the droplet, we consider the following advection-diffusion problem:

$$\frac{\partial C}{\partial t} + \boldsymbol{U}^{(o)} \cdot \boldsymbol{\nabla} C = D\nabla^2 C, \quad \boldsymbol{\nabla} C \cdot \boldsymbol{n}|_{\mathcal{S}} = -\frac{\mathcal{A}}{D}, \quad C|_{\boldsymbol{r}\to\infty} = 0, \tag{2.2}$$

where D denotes the solute diffusion coefficient. Using typical radii and velocities involved in experiments ($R \sim 20\mu$m and $V \sim 50\mu\mathrm{m}/s$), we can realise that at such scales, inertia is negligible (i.e. characteristic Reynolds number is $\mathrm{Re} = \rho^{(o)}VR/\eta^{(o)} \sim 10^{-3}$). The flow field satisfies therefore the Stokes equation:

$$\boldsymbol{\nabla} \cdot \boldsymbol{\sigma}^{(i,o)} = \boldsymbol{0}, \quad \boldsymbol{\nabla} \cdot \boldsymbol{U}^{(i,o)} = 0, \tag{2.3}$$

where $\boldsymbol{\sigma}^{(i,o)}$ denotes the Cauchy stress tensor either inside or outside the droplet. While the velocity field satisfies the impermeability condition, it is continuous at the droplet's interface (phoretic effects are indeed considered negligible compared to Marangoni ones [36]). In the frame of reference of the droplet, such boundary conditions read:

$$\boldsymbol{U}^{(i)}\Big|_{\mathcal{S}} = \boldsymbol{U}^{(o)}\Big|_{\mathcal{S}}, \quad \boldsymbol{U}^{(o)}|_{\boldsymbol{r}\to\infty} = -\boldsymbol{V}. \tag{2.4}$$

In reaction to surface tension gradients, the fluid experiences a stress jump at the droplet's interface expressed by the Marangoni condition:

$$\boldsymbol{n}\cdot\left(\boldsymbol{\sigma}^{(o)} - \boldsymbol{\sigma}^{(i)}\right)\Big|_{\mathcal{S}} \cdot (\boldsymbol{I} - \boldsymbol{nn}) = -\gamma_1 \left(\boldsymbol{I} - \boldsymbol{nn}\right) \cdot \boldsymbol{\nabla} C|_{\mathcal{S}}\,, \tag{2.5}$$

where equation 2.1 was used to link surface tension gradients with solute ones. Finally, neglecting the droplet's inertia enables to obtain the *force-free condition*:

$$\int_{\mathcal{S}} \boldsymbol{\sigma}^{(o)} \cdot \boldsymbol{n}\mathrm{d}\mathcal{S} = \boldsymbol{0}, \quad \int_{\mathcal{S}} \boldsymbol{r} \times \boldsymbol{\sigma}^{(o)} \cdot \boldsymbol{n}\mathrm{d}\mathcal{S} = \boldsymbol{0}. \tag{2.6}$$

In order to compute the flow field, we define the streamfunction $\psi^{(i,o)}$ (inside or outside the droplet) that satisfies:

$$\boldsymbol{U}^{(i,o)} = -\frac{1}{r^2}\frac{\partial \psi^{(i,o)}}{\partial \mu}\boldsymbol{e}_r - \frac{1}{r\sqrt{1-\mu^2}}\frac{\partial \psi^{(i,o)}}{\partial r}\boldsymbol{e}_\theta, \tag{2.7}$$

with $\mu = \cos\theta$, and where radial and azimuthal vectors $\boldsymbol{e}_r$ and $\boldsymbol{e}_\theta$ are defined in figure 2.1.

2.1.2 Spectral decomposition of ψ and C

Taking advantage of the axial symmetry of the problem, $\psi^{(i,o)}$ is decomposed in Legendre modes:

$$\begin{aligned}
\psi^{(i,o)}(r,\mu,t) &= \sum_{n=1}^{\infty} \frac{2n+1}{n(n+1)} \alpha_n^{(i,o)}(t)\psi_n^{(i,o)}(r)(1-\mu^2)L_n'(\mu), && (2.8)\\
\psi_n^{(i,o)}(r) &= E_n^{(i,o)} r^{n+3} + F_n^{(i,o)} r^{n+1} + G_n^{(i,o)} r^{2-n} + H_n^{(i,o)} r^{-n}, && (2.9)
\end{aligned}$$

where $E_n^{(i,o)}$, $F_n^{(i,o)}$, $G_n^{(i,o)}$ and $H_n^{(i,o)}$ are constants to determine, and the prime symbol stands for the derivative of L_n (Legendre polynomial of order n, see appendix A.1) with μ. Using the boundary conditions on the droplet's surface and at infinity Eq. (2.4) together with the force-free condition Eq. (2.6), we obtain:

$$\psi_1^{(o)} = \frac{R^3}{3r} - \frac{r^2}{3}, \quad \psi_n^{(o)} = \frac{1}{2}\left(\frac{R^{n+2}}{r^n} - \frac{R^n}{r^{n-2}}\right) \quad \text{for } n>1 \tag{2.10}$$

$$\psi_n^{(i)} = \frac{1}{2}\left(\frac{r^{n+1}}{R^{n-1}} - \frac{r^{n+3}}{R^{n+1}}\right) \quad \text{for } n>0. \tag{2.11}$$

In the same manner, we decompose the concentration field c in Legendre modes:

$$C(r,\mu,t) = \sum_{p=0}^{\infty} C_p(r,t)L_p(\mu), \tag{2.12}$$

which enables to express the diffusion advection equation 2.2 projected on each mode $p \geq 0$:

$$\begin{aligned} &\frac{\partial C_p}{\partial t} + \frac{1}{r^2}\sum_{m=0}^{\infty}\sum_{n=1}^{\infty}\alpha_n^{(o)}(t)\left(A_{mnp}\frac{\partial C_m}{\partial r}\psi_n^{(o)} + B_{mnp}C_m\frac{\partial \psi_n^{(o)}}{\partial r}\right) \\ = \; &\frac{D}{r^2}\left(\frac{\partial}{\partial r}\left(r^2\frac{\partial C_p}{\partial r}\right) - p(p+1)C_p\right), \end{aligned} \tag{2.13}$$

where A_{mnp} and B_{mnp} are defined as follow:

$$A_{mnp} = \frac{(2n+1)(2p+1)}{2}\int_{-1}^{1} L_m(\mu)L_m(\mu)L_p(\mu)\mathrm{d}\mu, \tag{2.14}$$

$$B_{mnp} = \frac{(2n+1)(2p+1)}{2n(n+1)}\int_{-1}^{1}(1-\mu^2)L'_m(\mu)L'_m(\mu)L_p(\mu)\mathrm{d}\mu. \tag{2.15}$$

In addition, the projection of Eq. (2.4), provides:

$$\alpha_p^{(o)} = \alpha_p^{(i)} \quad \text{for } p > 0, \tag{2.16}$$

while we use the expression of the shear stress:

$$\begin{aligned} \sigma_{r,\theta}^{(i,o)} &= \eta^{(i,o)}\left(r\frac{\partial}{\partial r}\left(\frac{u_\theta^{(i,o)}}{r}\right) - \frac{\sqrt{1-\mu^2}}{r}\frac{\partial u_r^{(i,o)}}{\partial \mu}\right) \\ &= -\eta^{(i,o)}\sqrt{1-\mu^2}\sum_{n=1}^{\infty}\frac{2n+1}{n(n+1)}\alpha_n^{(i,o)}L'_n(t)\left(r\frac{d}{dr}\left(\frac{1}{r^2}\frac{d\psi_n^{(i,o)}}{dr}\right) + \frac{n(n+1)}{r^2}\psi_n^{(i,o)}\right), \end{aligned} \tag{2.17}$$

together with the Marangoni condition Eq. (2.5) to obtain:

$$3\eta^{(o)}\alpha_1^{(o)} + \frac{9\eta^{(i)}}{2}\alpha_1^{(i)} = -\gamma_1 C_1|_{r=R}, \tag{2.18}$$

$$\eta^{(o)}\alpha_p^{(o)} + \eta^{(i)}\alpha_p^{(i)} = -\frac{p(p+1)}{(2p+1)^2}\gamma_1 C_p|_{r=R} \quad \text{for } p > 1. \tag{2.19}$$

Using Eq. (2.16), Eq. (2.18) and Eq. (2.19) leads to the following relations for $\alpha_p^{(o)}$:

$$\alpha_1^{(o)} = -\frac{2\gamma_1}{3(2\eta^{(o)} + 3\eta^{(i)})}C_1|_{r=R}, \tag{2.20}$$

$$\alpha_p^{(o)} = -\frac{p(p+1)\gamma_1}{(\eta^{(o)} + \eta^{(i)})(2p+1)^2}C_p|_{r=R} \quad \text{for } p > 1. \tag{2.21}$$

In order to get access to the unsteady dynamics of the droplet, we may consider a truncated concentration field composed of the N first modes. Eq. (2.13) then provides N partial differential equations for each mode, which could be numerically solved using for instance a finite difference scheme. In addition, the resulting flow field is directly computed as the instantaneous and linear response to the concentration field moments C_p via Eq. (2.20) and Eq. (2.21).

2.1.3 Solute polarity and droplet velocity

In this part, we suggest an extended version of the Lorentz reciprocal theorem of section 1.4.1 to the case of an active droplet. The aim of this derivation is to establish a direct relation between the droplet's velocity and the solute distribution at its surface.

In a similar manner as introduced in section 2.1, we consider a force-free active droplet that self-propels at a velocity $\boldsymbol{V}$ in reaction to Marangoni stresses at its surface $\mathcal{S}$. In the following, $\mathcal{V}^{(i)}$ (resp. $\mathcal{V}^{(o)}$) denotes the inner volume (resp. outer volume) of the droplet. In the lab-frame, the flow problem is thus described by the following system of equations:

$$\boldsymbol{\nabla}\cdot\boldsymbol{\sigma}^{(i,o)}=\boldsymbol{0},\quad \boldsymbol{\nabla}\cdot\boldsymbol{U}^{(i,o)}=0, \tag{2.22}$$

$$\boldsymbol{U}^{(i)}\Big|_{\mathcal{S}}=\boldsymbol{U}^{(o)}\Big|_{\mathcal{S}},\quad \boldsymbol{U}^{(i)}\Big|_{\mathcal{S}}\cdot\boldsymbol{n}=0,\quad \boldsymbol{U}^{(o)}|_{\boldsymbol{r}\to\infty}=-\boldsymbol{V}, \tag{2.23}$$

$$\boldsymbol{n}\cdot\left(\boldsymbol{\sigma}^{(o)}-\boldsymbol{\sigma}^{(i)}\right)\Big|_{\mathcal{S}}\cdot(\boldsymbol{I}-\boldsymbol{nn})=-\gamma_1\,(\boldsymbol{I}-\boldsymbol{nn})\cdot\boldsymbol{\nabla}C|_{\mathcal{S}}\,. \tag{2.24}$$

$$\boldsymbol{F}=\int_{\mathcal{S}}\boldsymbol{\sigma}^{(o)}\cdot\boldsymbol{n}\mathrm{d}\mathcal{S}=\boldsymbol{0}. \tag{2.25}$$

In addition, we consider an auxiliary problem involving a passive droplet, of same geometry, that swims at the velocity $\hat{\boldsymbol{V}}$ in reaction to an external force $\hat{\boldsymbol{F}}$. A similar system of equations characterising the auxiliary flow problem reads:

$$\boldsymbol{\nabla}\cdot\hat{\boldsymbol{\sigma}}^{(i,o)}=\boldsymbol{0},\quad \boldsymbol{\nabla}\cdot\hat{\boldsymbol{U}}^{(i,o)}=0, \tag{2.26}$$

$$\hat{\boldsymbol{U}}^{(i)}\Big|_{\mathcal{S}}=\hat{\boldsymbol{U}}^{(o)}\Big|_{\mathcal{S}},\quad \hat{\boldsymbol{U}}^{(i)}\Big|_{\mathcal{S}}\cdot\boldsymbol{n}=0,\quad \hat{\boldsymbol{U}}^{(o)}|_{\boldsymbol{r}\to\infty}=-\hat{\boldsymbol{V}}, \tag{2.27}$$

$$\boldsymbol{n}\cdot\left(\hat{\boldsymbol{\sigma}}^{(o)}-\hat{\boldsymbol{\sigma}}^{(i)}\right)\Big|_{\mathcal{S}}\cdot(\boldsymbol{I}-\boldsymbol{nn})=\boldsymbol{0}, \tag{2.28}$$

$$\hat{\boldsymbol{F}}=\int_{\mathcal{S}}\hat{\boldsymbol{\sigma}}^{(o)}\cdot\boldsymbol{n}\mathrm{d}\mathcal{S}. \tag{2.29}$$

In the same manner as in section 1.4.1, contracting the Stokes equation of each problem with the dual Eulerian velocity field gives two relations respectively inside and outside the droplets:

$$\int_{\mathcal{V}^{(o)}}\left[\left(\boldsymbol{\nabla}\cdot\boldsymbol{\sigma}^{(o)}\right)\cdot\hat{\boldsymbol{U}}^{(o)}-\left(\boldsymbol{\nabla}\cdot\hat{\boldsymbol{\sigma}}^{(o)}\right)\cdot\boldsymbol{U}^{(o)}\right]\mathrm{d}\mathcal{V}^{(o)}=0, \tag{2.30}$$

$$\int_{\mathcal{V}^{(i)}}\left[\left(\boldsymbol{\nabla}\cdot\boldsymbol{\sigma}^{(i)}\right)\cdot\hat{\boldsymbol{U}}^{(i)}-\left(\boldsymbol{\nabla}\cdot\hat{\boldsymbol{\sigma}}^{(i)}\right)\cdot\boldsymbol{U}^{(i)}\right]\mathrm{d}\mathcal{V}^{(i)}=0. \tag{2.31}$$

Using the incompressibility relations together with the divergence theorem provides:

$$\int_{\mathcal{S}^{\infty}-\mathcal{S}}\left(\boldsymbol{n}\cdot\boldsymbol{\sigma}^{(o)}\cdot\hat{\boldsymbol{U}}^{(o)}-\boldsymbol{n}\cdot\hat{\boldsymbol{\sigma}}^{(o)}\cdot\boldsymbol{U}^{(o)}\right)\mathrm{d}\mathcal{S}=0, \tag{2.32}$$

$$\int_{\mathcal{S}}\left(\boldsymbol{n}\cdot\boldsymbol{\sigma}^{(i)}\cdot\hat{\boldsymbol{U}}^{(i)}-\boldsymbol{n}\cdot\hat{\boldsymbol{\sigma}}^{(i)}\cdot\boldsymbol{U}^{(i)}\right)\mathrm{d}\mathcal{S}=0, \tag{2.33}$$

where $\mathcal{S}^{\infty}$ denotes the surface infinitely far from the droplet. Using the boundary conditions of each problem, Eq. (2.32) becomes:

$$-\hat{\boldsymbol{V}}\cdot\int_{\mathcal{S}^{\infty}}\boldsymbol{\sigma}^{(o)}\cdot\boldsymbol{n}\mathrm{d}\mathcal{S}+\boldsymbol{V}\cdot\int_{\mathcal{S}^{\infty}}\hat{\boldsymbol{\sigma}}^{(o)}\cdot\boldsymbol{n}\mathrm{d}\mathcal{S}-\int_{\mathcal{S}}\left(\boldsymbol{n}\cdot\boldsymbol{\sigma}^{(o)}\cdot\hat{\boldsymbol{U}}^{(o)}-\boldsymbol{n}\cdot\hat{\boldsymbol{\sigma}}^{(o)}\cdot\boldsymbol{U}^{(o)}\right)\mathrm{d}\mathcal{S}=0. \tag{2.34}$$

Since $\boldsymbol{\nabla}\cdot\boldsymbol{\sigma}^{(o)}=\boldsymbol{0}$ and $\boldsymbol{\nabla}\cdot\hat{\boldsymbol{\sigma}}^{(o)}=\boldsymbol{0}$, using the divergence theorem enables us to identify the first two integrals in Eq. (2.34) to $\boldsymbol{F}$ and $\hat{\boldsymbol{F}}$ respectively. Then, summing Eq. (2.33) with

Eq. (2.34) and using the continuity of the velocity field at the interface of the droplet for each problem Eq. (2.23) and Eq. (2.27), we get:

$$-\hat{\boldsymbol{V}}\cdot\boldsymbol{F}+\boldsymbol{V}\cdot\hat{\boldsymbol{F}}-\int_{\mathcal{S}}\left[\boldsymbol{n}\cdot\left(\boldsymbol{\sigma}^{(o)}-\boldsymbol{\sigma}^{(i)}\right)\cdot\hat{\boldsymbol{U}}^{(o)}-\boldsymbol{n}\cdot\left(\hat{\boldsymbol{\sigma}}^{(o)}-\hat{\boldsymbol{\sigma}}^{(i)}\right)\cdot\boldsymbol{U}^{(o)}\right]\mathrm{d}\mathcal{S}=0. \quad (2.35)$$

The first term of Eq. (2.35) vanishes according to the force-free condition Eq. (2.25). Using the impermeability condition of the velocity field in each problem together with the continuity of the tangential stress (resp. Marangoni condition) at the interface of the droplet in the auxiliary problem (resp. main problem) Eq. (2.28) (resp. Eq. (2.24)), Eq. (2.35):

$$\boldsymbol{V}\cdot\hat{\boldsymbol{F}}+\gamma_1\int_{\mathcal{S}}\boldsymbol{\nabla}C\cdot(\boldsymbol{I}-\boldsymbol{nn})\cdot\hat{\boldsymbol{U}}^{(o)}\mathrm{d}\mathcal{S}=0. \quad (2.36)$$

Choosing $\hat{\boldsymbol{V}}$ in the same direction as $\boldsymbol{V}$, the classical results from Ref. [46] provide:

$$\hat{\boldsymbol{U}}^{(o)}|_{\mathcal{S}}\cdot(\boldsymbol{I}-\boldsymbol{nn}) = -\frac{\hat{\boldsymbol{V}}\cdot(\boldsymbol{I}-\boldsymbol{nn})}{2(\tilde{\eta}+1)}, \quad (2.37)$$

$$\hat{\boldsymbol{F}} = -\frac{4\pi\eta^{(o)}R(3\tilde{\eta}+2)}{2(1+\tilde{\eta})}\hat{\boldsymbol{V}}. \quad (2.38)$$

Finally, integrating by part the right-hand-side of Eq. (2.36) leads to:

$$\boldsymbol{V}=-\frac{\gamma_1}{2\pi(2\eta^{(o)}+3\eta^{(i)})R^2}\int_{\mathcal{S}}C\boldsymbol{n}\mathrm{d}\mathcal{S}. \quad (2.39)$$

Eq. (2.39) therefore establishes a direct link between the velocity of the droplet and the solute distribution at its surface. It specifically informs the droplet moves in reaction to any imbalance of solute at its surface. Nevertheless, we should remind that Eq. (2.39) is only valid for a single active hydrodynamically isolated droplet.

Choosing R, $C^*=\mathcal{A}R/D$ and $V^*=\mathcal{A}R\gamma_1/D(2\eta^{(o)}+3\eta^{(i)})$ as resp. characteristic length, concentration and velocity (see section 1.5 for more details about these scales) enables to write a dimensionless relation between the solute distribution and droplet's velocity:

$$\boldsymbol{v}=-\frac{1}{2\pi}\int_{\mathcal{S}}c\boldsymbol{n}\mathrm{d}\mathcal{S}=\boldsymbol{\Pi}, \quad (2.40)$$

where $\boldsymbol{v}=\boldsymbol{V}/V^*$, $c=C/C^*$ and $\boldsymbol{\Pi}$ is called the *solute polarity.*

2.1.4 Spontaneous propulsion

Refocusing on the single droplet problem, we present the results from Ref. [66] and Ref. [36] regarding the instability phenomenon at the origin of the droplet's self-propulsion. In the following, we only deal with the dimensionless quantities $c = C/C^*$ and $\boldsymbol{u}^{(i,o)} = \boldsymbol{U}^{(i,o)}/V^*$, while keeping the same other notations to ease the reading. Besides, we denote by $\tilde{\eta} = \eta^{(i)}/\eta^{(o)}$ the viscosity ratio. The advection-diffusion problem Eq. (2.2) thus becomes:

$$\mathrm{Pe}\left(\frac{\partial c}{\partial t} + \boldsymbol{u}^{(o)} \cdot \boldsymbol{\nabla} c\right) = \nabla^2 c, \quad \boldsymbol{\nabla} c \cdot \boldsymbol{n}|_{\mathcal{S}} = -1, \quad c|_{\boldsymbol{r}\to\infty} = 0, \tag{2.41}$$

where $\mathrm{Pe} = \mathcal{A}R^2\gamma_1/((2\eta^{(o)} + 3\eta^{(i)})D^2)$ as defined in section 1.6.2. Then, considering a small perturbation $\tilde{c}$ from the quiescent state $\bar{c}(r) = 1/r$, where the droplet is fixed in space and generates no flow. At the leading order, the first azimuthal mode $\tilde{c}_1$ satisfies:

$$\mathrm{Pe}\frac{\partial \tilde{c}_1}{\partial t} - \frac{1}{r^2}\left(\frac{\partial}{\partial r}\left(r^2\frac{\partial \tilde{c}_1}{\partial r}\right) - 2\tilde{c}_1\right) = -\mathrm{Pe}\frac{2\tilde{c}_1|_{r=R}}{3r^2}\left(\frac{1}{r^3} - 1\right), \tag{2.42}$$

$$\left.\frac{\partial \tilde{c}_1}{\partial r}\right|_{r=R} = 0, \quad \tilde{c}_1(r \to \infty, t) = 0. \tag{2.43}$$

The linear stability analysis provides that for $\mathrm{Pe} > \mathrm{Pe}_c = 4$, advection effects are sufficient to amplify the initial perturbation [66, 36]. Consequently, we may remember that an active droplet spontaneously swim when Pe is above this threshold.

2.1.5 Self-propulsion velocity of a single active droplet

Finally, we provide the self-propulsion velocity $v_0(\mathrm{Pe})$ of a single active droplet, numerically computed in Ref. [36]. Fig. 2.2 shows the evolution of v_0 as function of Pe. We notice that v_0 promptly grows from the critical threshold $\mathrm{Pe}_c = 4$, then reaches a maximal value around Pe = 12 before finally decaying slowly for even greater Pe.

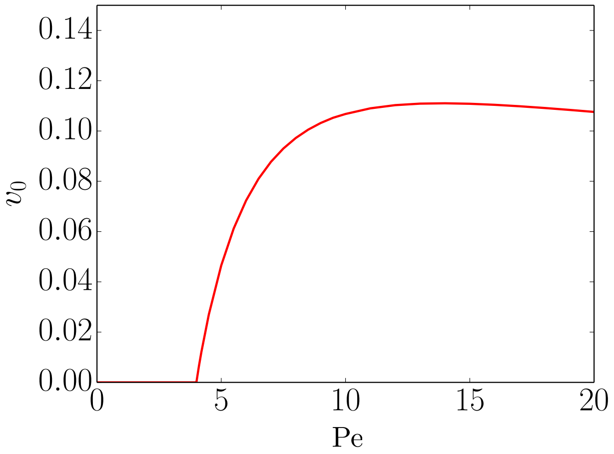

Figure 2.2: Active droplet's self-propulsion velocity v_0 as function of Pe taken from Ref. [36].

2.2 Hydrodynamic interactions

As seen previously, an imbalance of solute at the surface of an active droplet induces Marangoni flows. Therefore, a swimming droplet locally steers the fluid. Since the Stokes equation drives the flow problem, the flow field generated by the droplet propagates at an infinite speed in the outer fluid. We thus expect that a second droplet (or a boundary) would instantaneously feel the hydrodynamic signature coming from the first one. The flow field induced by each droplet alters the viscous stresses and thus the drag forces experienced by the other droplet. Finally, we expect hydrodynamic interactions between several droplets (or in the presence of a boundary) to decay with the separation distance.

This section will be dedicated to hydrodynamic interactions between active droplets. First, we will examine the leading order hydrodynamic signature generated by an active droplet and determine its far-field approximation. In a second stage, we will provide a qualitative discussion of the expected hydrodynamic interactions between two active droplets. Finally, we will introduce briefly the method of images that enables to estimate quantitatively far-field hydrodynamic interactions between several active droplets or in the presence of a boundary.

2.2.1 Singularities expansion

Let us start from the flow field solution of the single droplet problem of section 2.1. Using the expression of the streamfunction $\psi^{(i,o)}$ expressed in Eq. (2.9) and using the relation Eq. (2.7), we find that *in the lab frame*, the far-field leading order of the flow generated by an active droplet follows:

$$\boldsymbol{U}^{(o)} \sim \frac{5\alpha_2^{(o)} R^2}{4r^2}(1-3\mu^2)\boldsymbol{e}_r. \tag{2.44}$$

The intensity of the flow is driven by the coefficient $\alpha_2^{(o)}$ that may be expressed as function of the solute distribution at the surface of the droplet via the relation Eq. (2.21). Consequently, we get:

$$\boldsymbol{U}^{(o)} \sim \frac{3\gamma_1 R^2 C_2|_{r=R}}{10\left(\eta^{(i)}+\eta^{(o)}\right) r^2}(3\mu^2-1)\boldsymbol{e}_r. \tag{2.45}$$

Seen from a far distance, the leading hydrodynamic signature of an active droplet is then radial, scales as $1/r^2$ and is proportional to the second moment of the concentration field $C_2|_{(r=R)}$.

To understand why such a behaviour is expected from an active droplet, we can start by computing the flow field created by a point force $F\boldsymbol{e}$ located at the origin of the coordinates system for convenience. Dropping the exponent (o) for convenience, the flow problem then reads:

$$\begin{aligned} \boldsymbol{\nabla}\cdot\boldsymbol{\sigma} + F\delta(\boldsymbol{x})\boldsymbol{e} &= \boldsymbol{0}, && (2.46)\\ \boldsymbol{\nabla}\cdot\boldsymbol{U} &= 0, && (2.47)\end{aligned}$$

where δ is the Dirac function and $\boldsymbol{x}$ denotes the position in the fluid relative to the point force location. Eq. (2.46) and Eq. (2.47) are solved using the Green function $\boldsymbol{G}$ [67]:

$$\boldsymbol{U}_s = \frac{F}{8\pi\eta^{(o)}}\boldsymbol{G} = \frac{F}{8\pi\eta^{(o)}}\left(\frac{\boldsymbol{e}}{|\boldsymbol{x}|} + \frac{(\boldsymbol{e}\cdot\boldsymbol{x})\boldsymbol{x}}{|\boldsymbol{x}|^3}\right). \tag{2.48}$$

This flow field, called a *Stokeslet* [68], slowly decays from the droplet's position as $\sim 1/|\boldsymbol{x}|$. However, because the droplet is force-free, such a singularity naturally does not appear in Eq. (2.45). Since the Stokes equation is linear, any derivative of a Stokeslet is also a solution. Taking the derivative of $\boldsymbol{U}_s^{(o)}$ along the direction $\boldsymbol{e}_d$ provides the solution called *Stokes dipole* [68]:

$$\boldsymbol{U}_{sd} = -\boldsymbol{e}_d \cdot \boldsymbol{\nabla} \boldsymbol{U}_s = \frac{F}{8\pi\eta^{(o)}} \boldsymbol{G}_D \tag{2.49}$$

$$\boldsymbol{G}_D = \frac{1}{|\boldsymbol{x}|^2} \left(\frac{(\boldsymbol{e}_d \cdot \boldsymbol{x})\boldsymbol{e} - (\boldsymbol{e} \cdot \boldsymbol{x})\boldsymbol{e}_d - (\boldsymbol{e}_d \cdot \boldsymbol{e})\boldsymbol{x}}{|\boldsymbol{x}|} + \frac{3(\boldsymbol{e} \cdot \boldsymbol{x})(\boldsymbol{e}_d \cdot \boldsymbol{x})\boldsymbol{x}}{|x|^3} \right). \tag{2.50}$$

In the particular situation of axial symmetry (which is the case for a single active droplet), the *Stokes dipole solution* is called a *Stresslet solution*:

$$\boldsymbol{U}_{sd} = \frac{F}{8\pi\eta^{(o)}} \left(-\frac{\boldsymbol{x}}{|\boldsymbol{x}|^3} + \frac{3(\boldsymbol{e} \cdot \boldsymbol{x})^2 \boldsymbol{x}}{|x|^5} \right). \tag{2.51}$$

where $\boldsymbol{e}$ represents the swimming direction of the droplet. The expression obtained in Eq. (2.51) echoes the far-field leading order of an active droplet obtained in Eq. (2.45). Because the droplet's inertia is negligible, we realise that the induced flow field decays faster than the one generated by a droplet dragged by an external force [69, 70]. Physically, the propulsion force resulting from Marangoni stresses at the droplet's surface is exactly balanced by the drag forces it experiences, a situation already encountered in Eq. (1.9).

In coming back to Eq. (2.45), we notice that C_2 may be computed using the orthogonal properties of the Legendre modes by:

$$C_2(t) = \frac{5}{4} \int_{-1}^{1} (3\mu^2 - 1) C(R, \mu, t) \mathrm{d}\mu. \tag{2.52}$$

C_2 turns out to be positive for a self-propelling active droplet. As a consequence, an active droplet belongs to the *pusher* kind of swimmers [71, 20] and expels the flow at its head and tail ($\mu = -1, \mu = 1$) while pumping it for its sides ($\mu = 0$) (see Fig. 2.3) [72, 73].

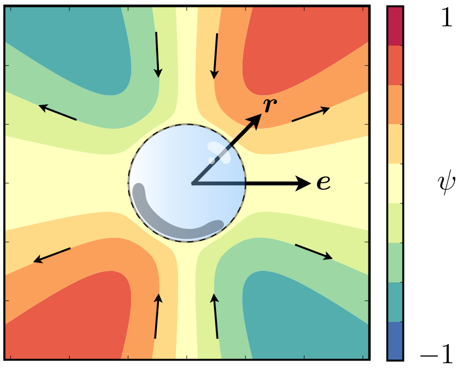

Figure 2.3: Streamlines relative to the streamfunction $\psi = -2\mu(1-\mu^2)(1/r^2-1)$. While the second part : $2\mu(1-\mu^2)$ is associated to a stresslet velocity field, the first one: $-2\mu(1-\mu^2)/r^2$, is associated to a source quadrupole that enables the flow to satisfy the impermeability condition at the surface of the droplet. The vector $\boldsymbol{e}$ represents the velocity direction of the droplet.

2.2.2 Hydrodynamic interactions between active droplets or boundaries

First, let us qualitatively describe the expected hydrodynamic interactions experienced by an active droplet in the presence of a second one. According to the last section, the leading order flow field generated by an active droplet is a *Stresslet solution*, where the flow is pumped on the side of the droplet while is expelled at its back and front. We thus expect two droplets to repel each other if their centre-to-centre axis is collinear to their swimming direction [74, 69] (see panel (a) of Fig. 2.4). Besides, two droplets swimming side-by-side are expected to experience attraction [74] as depicted in the panel (b) of Fig. 2.4. Furthermore, denoting by d the separation distance between the droplets, such repulsion and attraction interactions result from the stresslet intensity of each droplet, which is expected to decay as $1/d^2$.

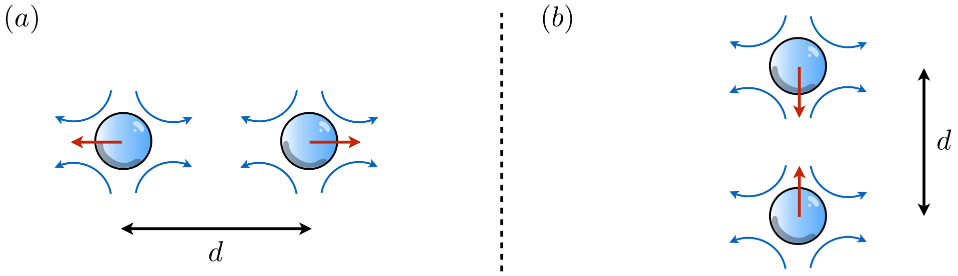

Figure 2.4: Schematic of the far-field hydrodynamic interactions between two active droplets separated by a distance d (a): Two colliding active droplets experiencing repulsive hydrodynamic forces. (b): Two side-by-side active droplets experiencing attractive hydrodynamic forces. The red arrows in both panels represent the directions of the hydrodynamic force experienced by each droplet while the blue arrows represent the flow field they generate.

Besides, the presence of boundaries in the vicinity of an active droplet is not without consequence on its dynamics [75, 62, 64]. Several methods are available to compute hydrodynamic interactions between bodies, and among other, one can think of the method of reflections suggested by Smoluchowski (1911) [76] or the exact treatment in bi-spherical coordinates in the case of axisymmetric problems provided by Stimson & Jeffrey (1926) [77]. Willing to provide the reader with a physical understanding and scaling laws regarding the hydrodynamic influence of a boundary on a swimmer, we briefly provide a method we owe to Blake (1974) [78] and later revisited in Refs. [69, 79, 62] to compute hydrodynamic interactions of a swimmer with a rigid wall or a free-surface.

From Eq. (2.45) and Eq. (2.51) we remind the far-field signature of an active droplet located in $\boldsymbol{x}_0$ may be written as:

$$\boldsymbol{U} = K\boldsymbol{G}_D(\boldsymbol{x}-\boldsymbol{x}_0, \boldsymbol{e}, \boldsymbol{e}) \tag{2.53}$$

where K is a positive constant and $\boldsymbol{e}$ the droplet's swimming direction. To compute the hydrodynamic influence of a rigid wall at a distance d_c from the droplet, we add a set of singularities $K\boldsymbol{G}_D^*$ located on $\boldsymbol{x}_0^*$, symmetric point of $\boldsymbol{x}_0$ about the wall (see Fig. 2.5):

$$\begin{aligned}\boldsymbol{G}_D^*(\boldsymbol{x}-\boldsymbol{x}_0^*) &= -\boldsymbol{G}_D(\boldsymbol{x}-\boldsymbol{x}_0^*, \boldsymbol{n}, \boldsymbol{n}) + 4h\boldsymbol{D}(\boldsymbol{x}-\boldsymbol{x}_0^*, \boldsymbol{n}) \\ &+ 2h\boldsymbol{G}_Q(\boldsymbol{x}-\boldsymbol{x}_0^*, \boldsymbol{n}, \boldsymbol{n}, \boldsymbol{n}) - 2h^2\boldsymbol{Q}(\boldsymbol{x}-\boldsymbol{x}_0^*, \boldsymbol{n}, \boldsymbol{n}),\end{aligned} \tag{2.54}$$

where $\boldsymbol{n}$ denotes the normal unit vector on the boundary that points toward the fluid region (see figure 2.5). The Stokes quadrupole $\boldsymbol{G}_Q$, source dipole $\boldsymbol{D}$ and source quadrupole $\boldsymbol{Q}$ involved in equation (2.54) follow:

$$\begin{aligned}
\boldsymbol{G}_Q(\boldsymbol{x}) &= \frac{1}{|\boldsymbol{x}|^3}\left(\boldsymbol{n} - \frac{3(\boldsymbol{x}\cdot\boldsymbol{n})}{|\boldsymbol{x}|^2}\left(3\boldsymbol{x} + (\boldsymbol{x}\cdot\boldsymbol{n})^2\boldsymbol{n}\right) + \frac{15(\boldsymbol{x}\cdot\boldsymbol{n})^3\boldsymbol{x}}{|\boldsymbol{x}|^4}\right), && (2.55)\\
\boldsymbol{D}(\boldsymbol{x}) &= \frac{1}{|\boldsymbol{x}|^3}\left(-\boldsymbol{n} + \frac{3(\boldsymbol{x}\cdot\boldsymbol{n})\boldsymbol{x}}{|\boldsymbol{x}|^2}\right), && (2.56)\\
\boldsymbol{Q}(\boldsymbol{x}) &= -\frac{3}{|\boldsymbol{x}|^4}\left(\frac{3(\boldsymbol{x}\cdot\boldsymbol{n})\boldsymbol{n}}{|\boldsymbol{x}|} - \frac{5(\boldsymbol{x}\cdot\boldsymbol{n})^2\boldsymbol{x}}{|\boldsymbol{x}|^3}\right). && (2.57)
\end{aligned}$$

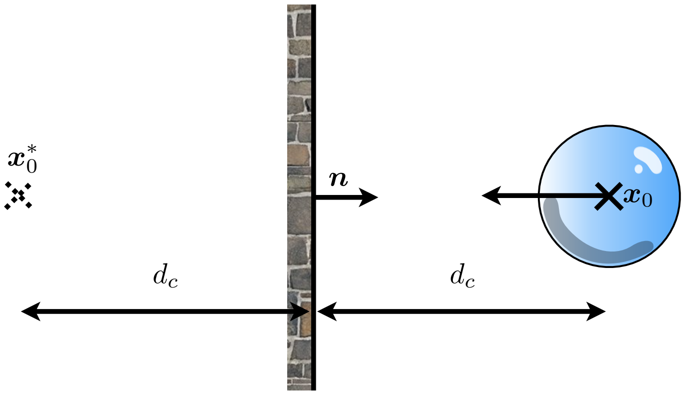

Figure 2.5: Schematic of the method of images considering a droplet located at a distance d_c from a wall of normal $\boldsymbol{n}$.

Let us assume for a moment that the propulsion mechanism of the droplet is not modified by the presence of the wall (i.e the solute concentration around the droplet is not modified the presence of the wall). Using an adapted version of the Faxén's law [80], we can compute the leading order of the velocity correction experienced by a droplet in the presence of a rigid wall located at a distance d_c:

$$\boldsymbol{v}_+^{\text{wall}} = \frac{3K}{4d_c^2}\boldsymbol{n}. \qquad (2.58)$$

We may notice the hydrodynamic influence of the wall on the droplet scales as $1/d_c^2$ in a similar way to the case of the active droplets pair seen previously. The same derivation may be performed in the case of a free surface [69, 62], which is hydrodynamically equivalent to the situation of two identical droplets separated by a distance $2d_c$. In that particular situation, the leading order velocity correction reads:

$$\boldsymbol{v}_+^{\text{free-surf}} = \frac{K}{2d_c^2}\boldsymbol{n}. \qquad (2.59)$$

If the scaling of the velocity correction is identical for both kinds of boundary, we however notice the pre-factor is smaller in the case of a free-surface. Consequently, we expect a droplet swimming towards a rigid wall to be slowed down sooner than two droplets involved in a head-on collision. Such a singularity approach has been used to deal with hydrodynamic interactions between active droplets and boundaries [62].

Finally, we find essential to stress that an active droplet induces a flow field as the result of the solute distribution at its surface (see Eq. (2.45)). Consequently, the flow field generated by one droplet alters the solute distribution around the second, which thus modifies its hydrodynamic signature. Besides, recent experiments presented in Ref. [75] have shown that the hydrodynamic flow field induced by an active droplet in the vicinity of a rigid wall may indeed be accurately approximated by few hydrodynamic modes. However the presence of the wall induces an accumulation of the solute (i.e swollen micelles in that case) emitted by the droplet that generates a significant dipolar flow field in a direction orthogonal to the wall. Because an active droplet self-propels and stirs the flow as a result of the solute dynamics, in the next section, we discuss about the expected chemical interactions involving several active droplets or in the presence of boundaries.

2.3 Chemical interactions

In this section, we will focus on the chemical aspect of the interactions between active droplets. First, in a similar way as for the hydrodynamic flow field, we will briefly introduce the multipole expansion that may be used to approximate the far-field chemical signature induced by an active droplet. In the second part, we will provide a qualitative discussion regarding the expected chemical influence of an active droplet (or boundary) on the dynamics of a second one. Finally, we will provide a derivation of the far-field chemical interactions between two active particles in the purely diffusive limit. The aim of this last part is first to provide an expression of the drift velocity experienced by one particle as the result of the concentration field emitted by the second one. Having in mind such leading order results for two active particles may thus enable us to note the differences with the full interaction model for active droplets provided in chapters 3 and 4. Besides, this example is a convenient opportunity to stress the fundamental differences between active droplets and active particles and the role of advection in the swimmers' dynamics in particular.

2.3.1 Multipole expansion of the concentration field

First, let us briefly mention that in the same way as for the flow field of section 2.2.1, an observer that looks at an active droplet from a far distance may approximate the concentration field it creates as a superimposition of singularities located at the position of the droplet $\boldsymbol{x}_0$. In this situation, an active droplet reduces to a point where the solute is emitted. The resulting transport problem reads [81]:

$$\mathrm{Pe}\left(\frac{\partial c}{\partial t}+\boldsymbol{u}\cdot\boldsymbol{\nabla}c\right)=\nabla^2 c+a_0\delta(\boldsymbol{x}-\boldsymbol{x}_0)+\boldsymbol{a}_1\cdot\boldsymbol{\nabla}\delta(\boldsymbol{x}-\boldsymbol{x}_0)+\boldsymbol{a}_2:\boldsymbol{\nabla\nabla}\delta(\boldsymbol{x}-\boldsymbol{x}_0)+...,\quad(2.60)$$

where δ is the Dirac function and a_0, $\boldsymbol{a}_1$ and $\boldsymbol{a}_2$ are tensors of increasing order named *monopole, dipole and quadrupole* intensities, which are illustrated on Fig. 2.6 in the case of purely diffusive regimes ($\mathrm{Pe} = 0$). Approximating the chemical signature of an active droplet by a superposition of few singularities may thus significantly simplify the solving of the solute dynamics [82, 83]. This approach will be used in chapter 5 to derive a *moving singularity model* that approximates an active droplet as the superposition of a source and a source-dipole.

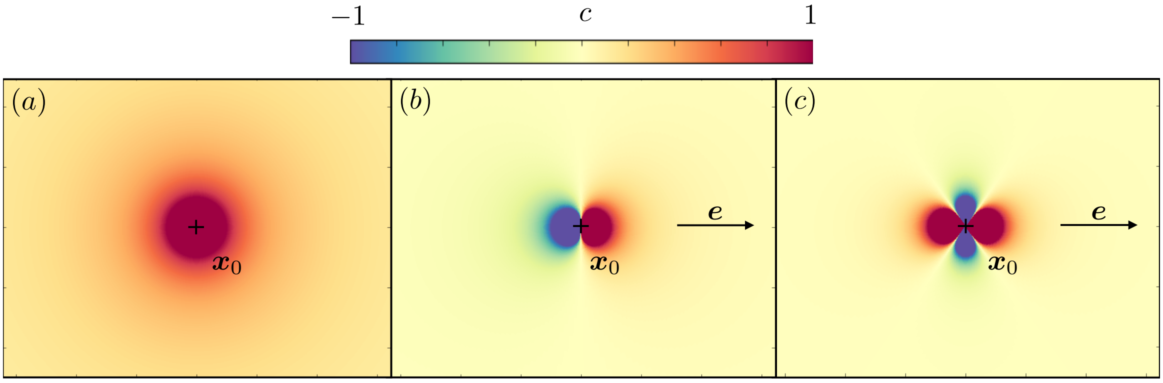

Figure 2.6: Concentration field generated by a monopole of intensity $a_0 = 4\pi$ (a), a dipole of intensity $\boldsymbol{a}_1 = 4\pi\boldsymbol{e}$ (b) and a quadrupole of intensity $\boldsymbol{a}_2 = 4\pi\boldsymbol{ee}$ (c).

2.3.2 Qualitative discussion regarding chemical interactions

We remind from section 2.1 that an active droplet emits at its surface a constant flux of solute that increases the surface tension of the outer-fluid. Consequently, any solute imbalance induces a surface tension gradient that generates Marangoni flows towards the zone where the solute concentration is the highest. The active droplet thus swims towards the zone of lower concentration in reaction to the Marangoni stresses exerted on its surface. Active droplets are said to be *antichemotactic*, as they swim in the direction opposite to solute gradients.

Let us consider two active droplets initially motionless and separated by a distance d_c. Since the droplets emit a flux of solute at their surface, the solute concentration increases in the region between them. The resulting increase of surface tension induces Marangoni flows at their surface that are directed towards the region between the droplets (see panel (a) of Fig. 2.7). As a consequence, each droplet swims away from the other one. The motion of a droplet resulting from the perturbation of the solute distribution around it and due to the presence of a second is called a *chemical interaction*, which is thus expected to be repulsive. The repelling dynamics previously described have been investigated recently in Ref. [56], where two oil active droplets of approximately 30μm radius are initially placed side-by-side for various separation distances d_c. The droplets then swim away from each other at a velocity that decreases with the separation distance. More precisely, such an escaping velocity is noticed to scales in $1/d_c^2$ [56].

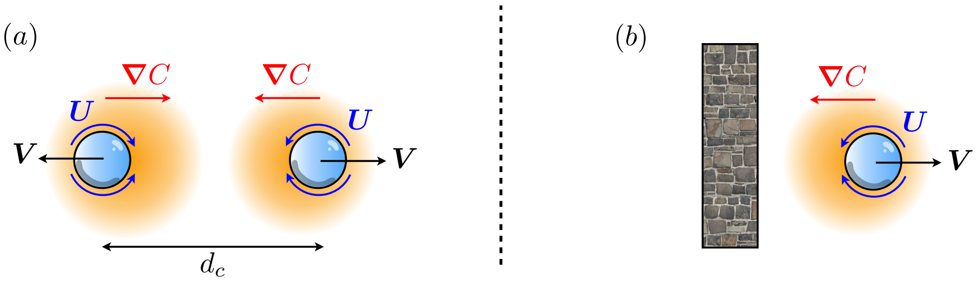

Figure 2.7: Schematic of the repulsion experienced by an active droplet in the presence of a second one (a) or a boundary (b). The presence of a second droplet or a boundary induces solute gradient $\boldsymbol{\nabla}C$ (red arrows) that generate tangential Marangoni flows $\boldsymbol{U}$ (blue arrows) towards the zone of higher concentration. Consequently, the droplets swim away at the velocity $\boldsymbol{V}$ (black arrows).

Besides, we have seen in section 2.1 that the solute distribution and swimming velocity are directly proportional in the case of a single active droplet hydrodynamically isolated (see Eq. (2.40)). This means that a swimming droplet has more solute at its back (called the solute wake) than at its front. In other words, a swimming droplet maintains a self-induced gradient of solute towards its back. Due to the repulsive nature of the chemical interactions, we would expect two active droplets that swim towards each other to slow down as they get closer. Eventually, each droplet will stop as the increase of solute concentration at its front resulting from the presence of the other one balances its self-induced gradient. If the droplets are identical, they will stop simultaneously, and we find the case discussed in the previous paragraph. Finally, we then expect that two colliding droplets would experience a rebound as the result of (*i*) their constant emission of solute (i.e. their activity) and (*ii*) the induced Marangoni flows (i.e their mobility).

Similarly, let us consider an active droplet close to a boundary impermeable to the solute. The confinement imposed by the boundary induces a rise in solute concentration in the confined region (see panel (*b*) of Fig. 2.7). Consequently, we expect a similar rebound dynamic to occur in the presence of a rigid wall or a free-surface. Experimentally, when an active droplet is more dense than the outer fluid it may sediment towards the bottom of the tank that contains the medium [56, 64]. As a consequence of the chemical repulsion with the boundary, the droplet is observed to hover at a finite distance from it [75, 56]. Besides, we remind that increasing the surfactant concentration in the outer fluid provides the droplet with a stronger activity. Interestingly, the experimental results of Ref. [56] show that the hovering distance from the wall increases for higher surfactant concentration, which evidences the chemical nature of the repulsion.

2.3.3 Far-field chemical interactions of two active particles in the purely diffusive limit

In the present paragraph, we find enlightening to consider the situation of two interacting active particles at $\mathrm{Pe} = 0$. The purpose of the following derivation is to quantitatively provide the resulting drift velocity experienced by one active particle in the presence of the concentration field generated by another one. This situation constitutes a reference case that should be kept in mind when dealing with exact interactions between active droplets presented in chapters 3 and 4. The absence of advection in the present situation suggests that the concentration field C is not influenced by the flow. In that way, the chemical and hydrodynamical problems are fully decoupled and we can focus here on chemical interactions only.

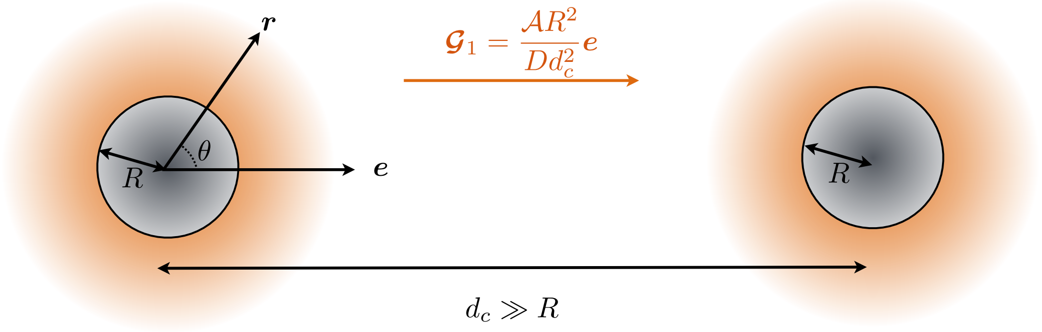

Figure 2.8: Schematic of two active particles separated by a distance $d_c \gg R$ that interact chemically via the concentration field generated at their surfaces.

First, let us examine the problem of a single force-free active particle of radius R, fixed in a quiescent fluid. We consider the particle emits a constant flux of solute $\mathcal{A}$ at its surface $\mathcal{S}$. In the purely diffusive limit, the solute transport dynamics satisfies the following diffusion problem:

$$\nabla^2 C = 0, \quad \boldsymbol{\nabla} C \cdot \boldsymbol{n}|_{\mathcal{S}} = -\mathcal{A}/D \quad , \quad C|_{\boldsymbol{r}\to\infty} = 0. \tag{2.61}$$

Similary to the case of active droplets, the flow problem is described by the Stokes equation:

$$\boldsymbol{\nabla} \cdot \boldsymbol{\sigma} = \boldsymbol{0}, \quad \boldsymbol{\nabla} \cdot \boldsymbol{U} = 0, \tag{2.62}$$

where $\boldsymbol{U}$ denotes the Eulerian velocity field in the surrounding fluid. Besides, the mobility mechanism considered for an active particle is slightly different from the one of an active droplet. Indeed, the flow generated by an imbalance of solute in the vicinity of the particle does not result from Marangoni stresses but comes from phoretic effects instead, which induces a slip velocity at the surface of the particle proportional to tangential solute gradients [84, 48]:

$$\boldsymbol{U}|_{\mathcal{S}} \cdot (\boldsymbol{I} - \boldsymbol{nn}) = M \boldsymbol{\nabla} C|_{\mathcal{S}} \cdot (\boldsymbol{I} - \boldsymbol{nn}), \tag{2.63}$$

where M is a positive coefficient called *mobility*. We note that for both active particles and active droplets, the induced flow in the vicinity of the swimmer is oriented towards positive solute gradients. The sphericity of the particle surface enables to easily compute the concentration field solution of Eq. (2.61):

$$C(\boldsymbol{r}) = \frac{\mathcal{A}R^2}{Dr}. \tag{2.64}$$

In this case, the concentration field is uniform around the particle. Consequently, Eq. (2.62) together with Eq. (2.63) imply $\boldsymbol{U} = \boldsymbol{0}$.

Adding a second identical active particle in the medium disturbs the concentration field of Eq. (2.64). Using the linearity of the Laplace equation and considering the limit where $d_c \gg R$, the concentration field felt by the first particle in the presence of the second can be reasonably approximated by the superposition of (*i*) a uniform increase of the solute concentration, $\mathcal{A}R^2/(Dd_c)$, and (*ii*) a uniform solute gradient whose intensity is denoted by $\boldsymbol{\mathcal{G}}_1 = \mathcal{A}R^2/(Dd_c^2)\boldsymbol{e} = \mathcal{G}_1 \boldsymbol{e}$ (see Fig. 2.8). While the uniform contribution does not impact the particle dynamics (according to Eq. (2.63)), we may focus on the influence of the external solute gradient $\boldsymbol{\mathcal{G}}_1$. In the presence of $\boldsymbol{\mathcal{G}}_1$, the solute transport problem Eq. (2.61) becomes:

$$\nabla^2 C = 0, \quad \boldsymbol{\nabla} C \cdot \boldsymbol{n}|_{\mathcal{S}} = -\mathcal{A}/D, \quad C|_{\boldsymbol{r}\to\infty} = r\boldsymbol{\mathcal{G}}_1 \cdot \boldsymbol{e} + C_\infty, \tag{2.65}$$

where C_∞ is a constant set to zero in the following since it corresponds to a uniform concentration field variation. Besides, taking advantage of the axial symmetry of the problem, we may decompose the concentration field solution of equation Eq. (2.65) in Legendre modes:

$$C(\boldsymbol{r}) = \sum_{k=0}^{\infty} c_k(r) L_k(\theta), \tag{2.66}$$

where c_k are coefficients to be determined and θ the azimuthal angle (see Fig. 2.8). Limiting the study to the first three modes enables to find a concentration field solution of the form:

$$C(\boldsymbol{r}) = \lambda_0 + \frac{\lambda_1}{r} + \left(\lambda_3 r + \frac{\lambda_4}{r^2}\right) \boldsymbol{\mathcal{G}}_1 \cdot \boldsymbol{e}, \tag{2.67}$$

where λ_i ($i \in \{0,1,2,3\}$) are constants to determine. Using the boundary conditions Eq. (2.65) we finally get:

$$C(\boldsymbol{r}) = \frac{\mathcal{A}R^2}{Dr} + \left(r + \frac{R^3}{2r^2}\right) \boldsymbol{\mathcal{G}}_1 \cdot \boldsymbol{e}. \tag{2.68}$$

First, the concentration field at the surface of the first particle is no longer uniform. Indeed, in addition to the concentration field solution of the single-particle case Eq. (2.64), the additional term proportional to $\mathcal{G}_1$ induces an azimuthal variation. According to Eq. (2.63), any solute gradient at the surface of the particle generates a flow. Using the Lorentz reciprocal theorem Eq. (1.18) in the case of a force-free particle, we obtain the velocity of the first droplet $\boldsymbol{V}_1$ [25]:

$$\boldsymbol{V}_1 = -\frac{1}{4\pi R^2} \int_{\mathcal{S}} \boldsymbol{U} \cdot (\boldsymbol{I} - \boldsymbol{nn})\, \mathrm{d}\mathcal{S}. \tag{2.69}$$

Then, using Eq. (2.63) provides a relation similar to Eq. (2.40) in the case of an active particle:

$$\boldsymbol{V}_1 = -\frac{M}{2\pi R^3} \int_{\mathcal{S}} C\boldsymbol{n} \mathrm{d}\mathcal{S}. \tag{2.70}$$

Finally, using Eq. (2.68) together with Eq. (2.70) provides:

$$\boldsymbol{V}_1 = -M\mathcal{G}_1\boldsymbol{e} = -\frac{M\mathcal{A}R^2}{Dd_c^2}\boldsymbol{e}. \tag{2.71}$$

First, the minus sign on the right-hand side of Eq. (2.71) informs that we recover the antichemotactic feature both shared by active particles and active droplets. Besides, we notice that the drift velocity of the first particle in the presence of the other scales in $1/d_c^2$. This scaling echoes the result obtained in the previous section regarding far-field hydrodynamic interactions. Consequently, we may expect both hydrodynamic and chemical interactions to play comparable roles in the presence of two active droplets.

2.4 Conclusion

In this chapter, we have first provided the reader with a useful spectral decomposition method regarding the exact model of a single self-propelled active droplet. This approach shows that an active droplet self-propels as the result of an instability phenomenon that occurs above a critical Péclet number ($\mathrm{Pe}_c = 4$). In this case the induced Marangoni flows transport a sufficient amount of solute at the back of the droplet to sustain its net propulsion. After a brief qualitative discussion of the hydrodynamic interactions between two active droplets (or in the presence of a boundary), we have provided a singularity approach that enables to estimate their far-field hydrodynamic interactions. Then, we have stressed the antichemotactic nature of active droplets and suggested the expected dynamics resulting from chemical interactions between two of them (or in the presence of a boundary). Finally, we have derived a canonic example of far-field chemical interactions between two active particles in the purely diffusive limit.

The far-field chemical interactions presented in the last part of this section allows reminding a fundamental difference with the case of active droplets. Experimentally, the self-propulsion of a phoretic active particle is often driven by an intrinsic asymmetry. Indeed, non-uniform mobility or activity on the particle surface are convenient strategies (adopted among others by Janus particles [65]) to achieve propulsion. Consequently, the leading order mechanism at the origin of the self-propulsion is predominantly diffusive. Within that framework, the linearity of Laplace and Stokes equations enable the use of superposition methods to compute hydro-chemical interactions among an assembly of active particles [79] or the influence of a boundary [85]. However, as seen at the beginning of this chapter, advection is essential for an active droplet to self-propel. The resulting non-linearity in the transport dynamics prevents the use of the previously mentioned methods to describe the interactions between several active droplets and boundaries. Due to the mathematical complexity of the coupled hydro-chemical interactions, existing models in the literature estimate them by making approximations. While some consider the sole effect of chemical interactions [56], others focus on hydrodynamic interactions only [86, 62] or suggest far-field models that remain valid only when the droplets are far from each other [87, 88, 83]. In the next chapter, we suggest a new approach to compute exact hydro-chemical interactions at finite Pe between two active droplets.

Take home message of Chapter 2

1. Self-propulsion of active droplets: An instability phenomenon resulting from the coupling between flow field and solute transport leads to the spontaneous self-propulsion of an active droplet for $\text{Pe} > \text{Pe}_c = 4$.

2. Solute polarity and droplet's velocity: The solute polarity quantifies the solute distribution on the droplet's surface. We can show that in the particular case of a single hydrodynamically isolated droplet, the dimensionless velocity and solute polarity are equal. Consequently, an active droplet swims as a result of any solute imbalance at its surface.

3. Hydrodynamic interactions: The leading order far-field hydrodynamic signature of an active droplet is called a stresslet and scales as $1/r^2$. Hydrodynamic interactions between two active droplets swimming side by side are attractive, whereas they become repulsive when the droplets swim on the same axis. Superposition methods are helpful to compute far-fields hydrodynamic interactions between several swimmers and boundaries.

4. Chemical interactions: From a far distance, an active droplet may be approximated by a source of solute. Due to the antichemotactic nature of active droplets, chemical interactions between active droplets (or in the presence of a boundary) are repulsive and scale as $1/r^2$.

5. Active droplets and active particles: Advection phenomena are inseparable from active droplets' self-propulsion. As a result of the non-linearity introduced in the transport dynamics, the usual superposition methods employed to compute interactions between active particles cannot be used in the case of active droplets.

3

HEAD-ON COLLISION OF AN ACTIVE DROPLET WITH A FLAT SURFACE

In this chapter, we will present a novel approach based on a moving body-fitted bi-spherical grid to solve exactly the fully-coupled nonlinear dynamics of the chemical solute and flow fields. This method will then be used to characterise in detail the axisymmetric collision of an active droplet with a rigid wall (or with a second droplet). The results of this chapter were published in the Journal of Fluid Mechanics [89].

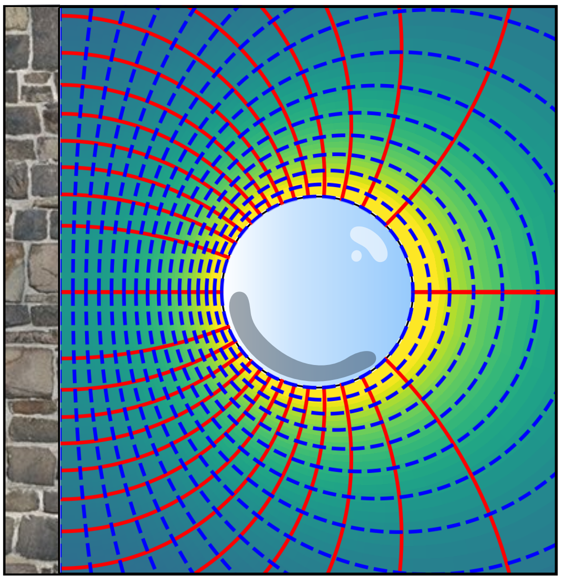

Concentration field around an active droplet which collide a rigid and passive wall frontally. The bi-spherical grid used for the computation is represented by the solid red (iso-μ) and dashed blue (iso-ξ) lines.

Contents

3.1 Motivations for a full interaction model

Most models available so far for both phoretic particles and active droplets consider a single micro-swimmer in an unbounded fluid medium (i.e. far from any confining boundary). Yet, most experiments involve many swimmers. Furthermore, the density of the particles or droplets does not match that of the surrounding fluid, and as a consequence, many if not most of them swim close to a bottom rigid wall or a free surface [90, 91, 64]. This interaction and collective dynamics of multiple swimmers is the focus of an increasing attention from the modelling point of view to understand the formation of clusters of particles [92, 93], in particular as a result of the multiple interaction routes available [94, 79] or of the effect of the walls on their interactions [95, 62]. The dynamics of a rigid phoretic particle close to a rigid wall has become a canonical problem to analyse such interactions and the resulting complex dynamics [96, 85, 97, 98]. It was also shown that interaction and self-assembly of active but individually non-motile particles may also lead to self-propulsion at the collective level [99, 100]. In most experimental systems, the chemical dynamics leading to the self-propulsion of phoretic particles is dominantly diffusive, and most of the models discussed above exploit the resulting linearity of the underlying Laplace and Stokes' problems.

However, advection and the non-linear coupling it introduces between the chemical and hydrodynamic fields, play a critical role in the emergence of self-propulsion for active droplets and thus can not be simply neglected. Yet, accounting for this full non-linear coupling in a model or a numerical simulation is no easy task. Several studies have attempted to model the interactions of active droplets, at least within a simplifying limit. The approach of Ref. [56] focused on a purely diffusive limit with no hydrodynamic interactions. Ref. [87] considered the influence of both chemical and hydrodynamic interactions during the collision of two self-propelled droplets, but the approach, which relies on the linear superposition of the hydrodynamic and chemical signature of each droplet, is intrinsically limited to the case of far-field interactions (i.e. when the relative distance of the droplets is large compared to their radii) and to the vicinity of the self-propulsion threshold. Numerically, Ref. [86] proposed a simulation of the collision problem using a Lattice-Boltzmann framework focusing on the velocity field generated by the two droplets; yet, the solute chemical dynamics and its coupling to the flows it produces, as well as the impact of the proximity of the two droplets, remain elusive at this point.

In contrast with existing modelling efforts on the interaction of two self-propelled droplets (or the interaction of a droplet with a confining wall), this chapter aims at the full description of the nonlinearly coupled hydrodynamic and chemical dynamics involved during a head-on (normal) collision. The present approach takes advantage of the axisymmetric setting of the problem but does not require any restrictive assumption regarding either the relative distance of the droplet and the wall (or between the droplets), the origin of the Marangoni flow which is entirely driven by solute concentration gradients at the droplet's surface or the magnitude of the convective transport with respect to diffusion (finite Péclet number Pe). The goal is twofold: (i) provide an in-depth physical insight into the chemical and fluid dynamics involved during the interaction, in particular to understand how the relative magnitude of advection and diffusion may modify or condition the droplets' collision and rebound; (ii) establish a benchmark study for the collision dynamics, to which reduced model used to analyse the collective behaviour of many droplets could be confronted and validated.

To this end, we develop a novel framework to analyse the unsteady dynamics of non-linearly coupled hydrodynamic and physicochemical systems using a semi-analytical treatment of both problems using bi-spherical harmonic decompositions on a moving conformal grid, which could be used for the treatment of more generic problems (e.g. bubble dynamics). For simplicity and clarity, because of the strong physical and mathematical similarity between the droplet-droplet and droplet-wall collisions, we focus specifically in the following on the latter problem (i.e. the canonical droplet-wall interaction, Fig. 3.1-a) before extending the simulation framework and results to the droplet-droplet collision (Fig. 3.1-b, § 3.6.2). We provide in section 3.3.1 the coupled hydrodynamic and chemical problems involved in the interaction, together with the governing equations. In § 3.3.2 and 3.3.3, a novel treatment of the problem using a spectral decomposition of the fields onto a moving bi-spherical grid is presented. This approach is used in § 3.4 and 3.5 to analyse in detail the interaction and rebound of a droplet onto a rigid wall, above the self-propulsion threshold, and the different behaviours observed depending on the advection-to-diffusion ratio. The results for a droplet-droplet collision are also presented and discussed. To provide further insight into the behaviour of the system in the vicinity of the self-propulsion threshold (i.e. for small velocity magnitude), a rigorous asymptotic treatment of the interaction performed by Matvey Morozov a former postdoctoral researcher at LadHyX is presented in § 3.7. The numerical and asymptotic results are then used to propose a quantitatively-accurate effective model of the rebound in § 3.8, and the findings are finally summarised and discussed in § 3.9.

3.2 Modelling the interactions between an active droplet and a rigid wall

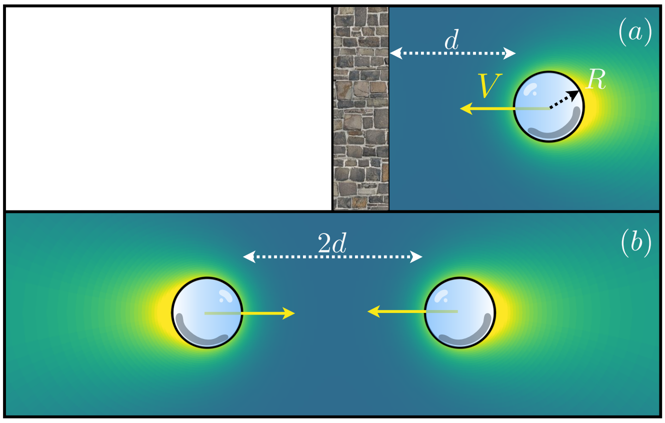

Figure 3.1: (a): Collision between an active droplet and a rigid and passive wall. (b): Collision between two active droplets of same size.

Let us study a spherical active droplet immersed in another fluid, both characterized as Newtonian. The droplet frontally swims toward a rigid and passive wall ($z = 0$) at a velocity $\boldsymbol{V} = V(t)\boldsymbol{e}_z$. The droplet being active, it releases a net flux $\mathcal{A} > 0$ of a chemical solute from its surface. As seen in the first chapter, due to their low shrinking rate [36], we can assume (i) that an active droplet has a constant radius and (ii) that the flux $\mathcal{A}$ remains constant over time. We also remind the solute (which concentration is denoted by C) modifies the fluid's surface tension locally and satisfies for small enough concentration differences the linear relation Eq. (1.26), reminded below for convenience:

$$\gamma = \gamma_0 + \gamma_1 C, \tag{3.1}$$

where γ_0 and γ_1 are two positive constants [36, 101].

In the following, and unless stated otherwise, we focus primarily on the droplet-wall interactions, and briefly analyse the case of two colliding identical active droplets in section 3.6.2. We denote by d the distance between the droplet's surface and the wall (Fig. 3.1). In the following we keep the same characteristic length, concentration and velocity scales as in section 2.1, so that all quantities of interest are made dimensionless.

3.2.1 Chemical problem

The droplet steers some flow as it swims and we thus expect the solute it emits at its surface to both diffuse and be advected by the fluid's motion. In a similar manner as in the single droplet case, we note $\boldsymbol{u}^{(i,o)}$ the Eulerian velocity field in the outer and inner fluids measured in the fixed laboratory frame and in order to describe the solute dynamics we consider the dimensionless concentration c satisfies the advection-diffusion equation:

$$\mathrm{Pe}\left(\frac{\partial c}{\partial t}+\boldsymbol{u}^{(o)}\cdot\boldsymbol{\nabla}c\right)=\nabla^2 c \qquad \text{with} \qquad \mathrm{Pe}=\frac{V^*R}{D}=\frac{\mathcal{A}R^2\gamma_1}{(2\eta^{(o)}+3\eta^{(i)})D^2}\cdot \tag{3.2}$$

A critical parameter in the study is the Péclet number. If Pe = 0, the solute would diffuse instantaneously in the medium whereas if Pe $\gg 1$ its transport results only from the flow motion. Besides, the solute is emitted via a fixed chemical flux from the droplet's surface and we further assume that the rigid wall is unable to exchange any solute with the fluid. Boundary conditions for the solute concentration c are therefore obtained as:

$$\boldsymbol{\nabla}c|_{\mathcal{S}}\cdot\boldsymbol{n} \;=\; -1, \qquad \boldsymbol{\nabla}c|_{W}\cdot\boldsymbol{n}=0, \tag{3.3}$$

$$c|_{r\to\infty} \;=\; 0, \tag{3.4}$$

where $\mathcal{S}$ (resp. W) denotes the surface of the droplet (resp. the wall) and $\boldsymbol{n}$ the unit normal vector pointing into the outer fluid domain.

3.2.2 Hydrodynamic problem

Inertia being negligible as such scales, the flow velocity and pressure satisfy a steady Stokes equation in both phases:

$$\boldsymbol{\nabla}^2\boldsymbol{u}^{(i,o)}=\boldsymbol{\nabla}p^{(i,o)}, \qquad \boldsymbol{\nabla}\cdot\boldsymbol{u}^{(i,o)}=0. \tag{3.5}$$

In the labframe, $\boldsymbol{u}^{(o)}$ vanishes far away from the droplet. At the droplet's interface, the velocity field is continuous and Marangoni stresses result in a jump in tangential hydrodynamic stresses. Additionally, a no-slip condition is imposed at the wall surface. Noting $\boldsymbol{\sigma}^{(i,o)}$, the Cauchy stress tensor in each fluid and $\tilde{\eta}=\eta^{(i)}/\eta^{(o)}$ the viscosity ratio, the boundary conditions for the hydrodynamic problem are therefore obtained as

$$(\boldsymbol{I}-\boldsymbol{nn})\cdot(\boldsymbol{\sigma}^{(o)}-\tilde{\eta}\boldsymbol{\sigma}^{(i)})\Big|_{\mathcal{S}}\cdot\boldsymbol{n}=-(\boldsymbol{I}-\boldsymbol{nn})\cdot(2+3\tilde{\eta})\,\boldsymbol{\nabla}c|_{\mathcal{S}}\,, \tag{3.6}$$

$$\boldsymbol{u}^{(o)}\Big|_{\mathcal{S}}=\boldsymbol{u}^{(i)}\Big|_{\mathcal{S}}, \qquad \boldsymbol{u}^{(o)}\Big|_{W}=\boldsymbol{0}, \qquad \boldsymbol{u}^{(o)}\Big|_{r\to\infty}=\boldsymbol{0}, \tag{3.7}$$

and recalling that $\boldsymbol{v}$ is the dimensionless droplet's velocity, the impermeability condition further imposes:

$$(\boldsymbol{u}^{(o)}\cdot\boldsymbol{n})\Big|_{\mathcal{S}}=\boldsymbol{v}\cdot\boldsymbol{n}, \tag{3.8}$$

Neglecting inertia, the droplet must remain force-free, imposing Eq. (1.9) to be satisfied (reminded below for convenience), which provides an additional implicit relation to determine $\boldsymbol{v}$:

$$\boldsymbol{F} = \int_{\mathcal{S}} \boldsymbol{\sigma}^{(o)} \cdot \boldsymbol{n}\, \mathrm{d}S = \boldsymbol{0}, \quad \boldsymbol{T} = \int_{\mathcal{S}} \boldsymbol{r} \times \boldsymbol{\sigma}^{(o)} \cdot \boldsymbol{n} \mathrm{d}S = \boldsymbol{0}. \tag{3.9}$$

Invoking the linearity of the Stokes equation, one can split the total hydrodynamic force $\boldsymbol{F}$ into the Marangoni forces $\boldsymbol{F_m}$ experienced by a fixed droplet and the drag forces $\boldsymbol{F_d}$ resulting from its translation. Because of the presence of the rigid wall the drag experienced by the droplet follows $\boldsymbol{F_d} = -\boldsymbol{R}_d \cdot \boldsymbol{v}$ with $\boldsymbol{R}_d$ the resistance matrix which is a function only of the geometry of the problem (i.e. the droplet radius and its distance to the wall). As a direct consequence of Eq. (3.9),

$$\boldsymbol{v} = -\boldsymbol{R}_d^{-1} \cdot \boldsymbol{F_m}. \tag{3.10}$$

While we expect $\boldsymbol{R}_d$ to significantly vary with d when the droplet is close to the wall, we remind that $\boldsymbol{R}_d = 2\pi(3\tilde{\eta} + 2)/(\tilde{\eta} + 1)$ when the droplet is infinitely far from it. Fig. 3.2 reports in solid red line the evolution of the drag coefficient C_d experienced by the droplet as function of its distance to the wall d. In order to track the front-back concentration asymmetry along the collision, we keep the same definition of the polarity $\boldsymbol{\Pi}$ introduced in section 2.1, and remind that $\boldsymbol{\Pi} = \boldsymbol{v}$ for any Pe in the case of the single active droplet isolated hydrodynamically.

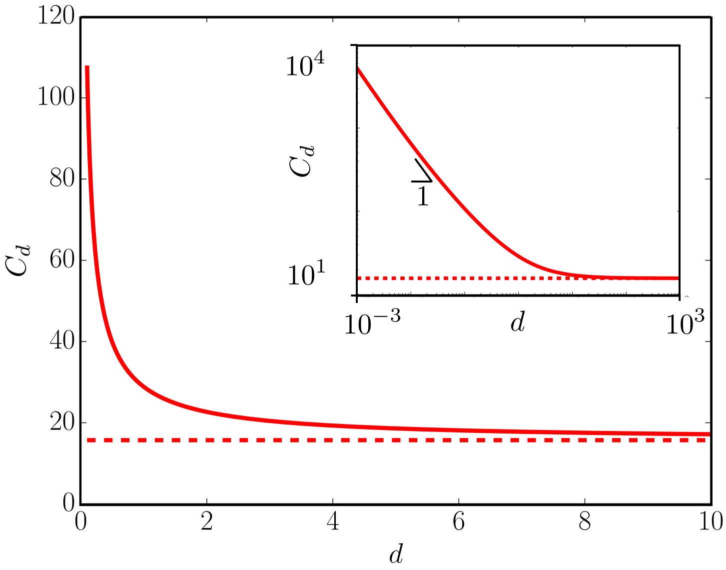

Figure 3.2: Drag coefficient evolution $C_d = \boldsymbol{R}_d : \boldsymbol{e_z e_z}$ of a passive droplet of unit radius moving toward a rigid wall as function of the separation distance d and for $\tilde{\eta} = 1$ (solid red line). The figure also reports in dashed red line the drag coefficient value of the single droplet in bulk: $C_d = 5\pi$.

3.3 Solving for the coupled hydrodynamic and chemical fields

The physical effect of the wall on the approaching droplet is *a priori* two-fold: hydrodynamically, the confinement of the fluid between the droplet and the bounding wall modifies the viscous stresses (and droplet's resistance matrix $\boldsymbol{R}_d$); furthermore, the chemically-inert wall reduces the effective solute diffusion away from the droplet resulting in an accumulation of solute in front of the approaching droplet. Because the active droplet is anti-chemotactic (it swims down the solute concentration gradient), such accumulation is expected to repel the droplet away. To account in details for these two effects and their coupling, a novel analytical and numerical framework is proposed and detailed here to solve exactly for the non-linearly coupled dynamics of the flow field and solute advection-diffusion using a moving bi-spherical coordinate system matching the moving droplet's boundary.

Cartesian coordinates are well-adapted to describe fluid motion or solute transport above a flat wall, yet spherical coordinates are typically more convenient to describe the flow and solute dynamics near a droplet surface. A body-fitted mesh is thus defined to describe simply both boundaries using bi-spherical coordinates, an approach that is convenient to apply boundary conditions (Fig. 3.3). In contrast with many studies using such coordinates [77, 102, 103, 104], the droplet is not fixed with respect to the wall so that the bi-spherical system needs to be modified at each time to match the evolving boundaries.

3.3.1 Bi-spherical grid adaptation for unsteady problems

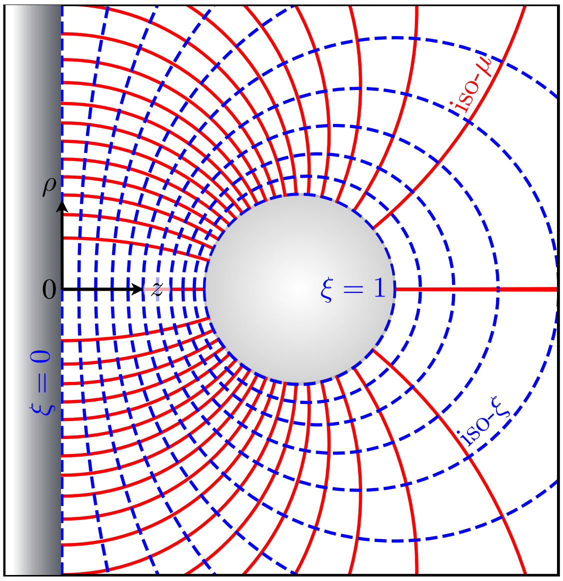

Figure 3.3: Bi-spherical coordinate system. Contours of fixed μ (solid-red) and fixed ξ (dashed blue) are shown at a given time t. The surfaces of the wall and droplet are given by $\xi = 0$ and $\xi = 1$, respectively.

At a given time t, a point located at (z, ρ, ϕ) in the fixed cylindrical coordinate system (with $\boldsymbol{e}_z$ the axis of symmetry of the problem and the origin located on the wall) has bi-spherical coordinates (ξ, μ, ϕ) defined by:

$$\rho = \frac{a(t)\sqrt{1-\mu^2}}{\Gamma}, \qquad z = \frac{a(t)\sinh(\lambda(t)\xi)}{\Gamma} \qquad \text{with } \Gamma(\xi,\mu,t) = \cosh(\lambda(t)\xi) - \mu, \tag{3.11}$$

where $a(t)$ and $\lambda(t)$ are functions of time to account for the time-dependent stretching of the grid. Surfaces of constant ξ represent a set of non-intersecting spheres (see Fig. 3.3). At any time t, the wall and droplet's surfaces correspond to $\xi = 0$ and $\xi = 1$, respectively. The functions $a(t)$ and $\lambda(t)$ are determined uniquely from the droplet's radius and distance to the wall:

$$\lambda(t) = \cosh^{-1}\left(\frac{d(t)}{R} + 1\right), \qquad a(t) = R\sqrt{d(t)(d(t) + 2R)}. \tag{3.12}$$

In addition, the unit vectors of the bi-spherical basis are defined as $(\boldsymbol{e}_\xi, \boldsymbol{e}_\mu, \boldsymbol{e}_\phi)$ with:

$$\begin{aligned} \boldsymbol{e}_\xi &= \frac{1 - \mu\cosh(\lambda\xi)}{\Gamma}\boldsymbol{e}_z - \frac{\sqrt{1-\mu^2}\sinh(\lambda\xi)}{\Gamma}\boldsymbol{e}_\rho, & (3.13)\\ \boldsymbol{e}_\mu &= \frac{\sqrt{1-\mu^2}\sinh(\lambda\xi)}{\Gamma}\boldsymbol{e}_z + \frac{1 - \mu\cosh(\lambda\xi)}{\Gamma}\boldsymbol{e}_\rho. & (3.14) \end{aligned}$$

and the corresponding metric coefficients are:

$$h_\xi = \frac{a\lambda}{\Gamma}, \qquad h_\mu = \frac{a}{\Gamma\sqrt{1-\mu^2}}, \qquad h_\phi = \frac{a\sqrt{1-\mu^2}}{\Gamma}. \tag{3.15}$$

Because of the motion of the droplet (and resulting grid adaption depicted in Fig. 3.4), a point of fixed (ξ, μ, ϕ) is not fixed in the labframe, i.e. it has time-dependent (ρ, z)-coordinates. This has consequences when solving time-dependent equations such as Eq. (3.2). Indeed, considering the local change in time of the concentration field c at a *fixed* point (ρ, z) now introduces a material derivative when considering c as a function of (ξ, μ, t), and we must thus replace:

$$\left.\frac{\partial c}{\partial t}\right|_{\rho,z} = \left.\frac{\partial c}{\partial t}\right|_{\xi,\mu} - \boldsymbol{\chi}\cdot\boldsymbol{\nabla}c, \tag{3.16}$$

where $\boldsymbol{\chi}$ is the velocity of a point with fixed (ξ, μ) in the physical space, and is obtained from Eq. (3.11). The advection-diffusion equation for $c(\xi, \mu, t)$ is therefore obtained as

$$\left.\frac{\partial c}{\partial t}\right|_{\xi,\mu} + (\boldsymbol{u} - \boldsymbol{\chi})\cdot\boldsymbol{\nabla}c = \frac{1}{\mathrm{Pe}}\nabla^2 c, \tag{3.17}$$

where, noting time derivatives of single-variable functions with a dot symbol (see Appendix A for calculation details),

$$\boldsymbol{\chi}\cdot\boldsymbol{\nabla}c = \left(\frac{\dot{\lambda}\xi}{\lambda} - \frac{\dot{a}\mu\sinh(\lambda\xi)}{\lambda a}\right)\frac{\partial c}{\partial\xi} + \frac{\dot{a}}{a}(1-\mu^2)\cosh(\lambda\xi)\frac{\partial c}{\partial\mu}. \tag{3.18}$$

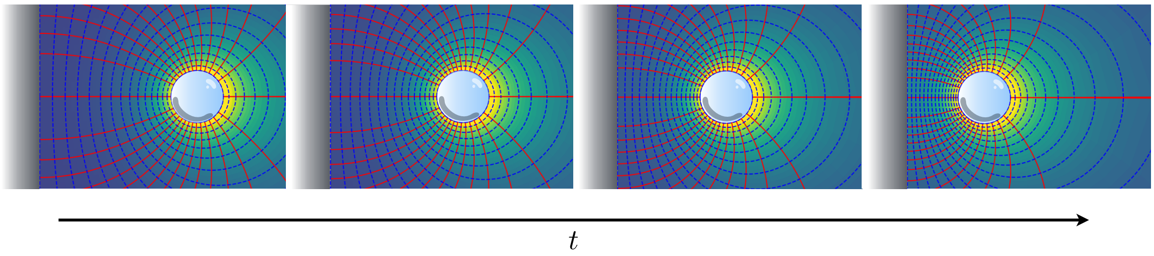

Figure 3.4: Distortion of the bi-spherical grid as the droplet gets closer to the wall. Solid red lines: contours of fixed μ, dashed blue lines: contours of fixed ξ.

3.3.2 Hydrodynamic problem

Solving the transport equation Eq. (3.17) requires knowing the velocity field $\boldsymbol{u}$. As noted before, the hydrodynamic (Stokes) problem is instantaneous and linear and the classical method to obtain Stokes flow solutions in bi-spherical geometries can be used [77]. The (inner and outer) flow fields are obtained in terms of streamfunctions $\psi^{(i,o)}$ [103]:

$$u_\xi^{(i,o)} = \frac{\Gamma^2}{a^2}\frac{\partial \psi^{(i,o)}}{\partial \mu}, \qquad u_\mu^{(i,o)} = -\frac{\Gamma^2}{a^2\lambda\sqrt{1-\mu^2}}\frac{\partial \psi^{(i,o)}}{\partial \xi}, \tag{3.19}$$

which can be written for an axisymmetric problem as [77]:

$$\psi^{(i,o)}(\xi,\mu,t) = \Gamma^{-3/2}\sum_{n=1}^{\infty}(1-\mu^2)L_n'(\mu)U_n^{i,o}(\xi,t), \tag{3.20}$$

where L_n' is the first derivative of L_n, the Legendre polynomial of degree n, and the functions $U_n^{i,o}$ are given by:

$$\begin{aligned} U_n^{i,o}(\xi,t) &= \alpha_n \cosh\left[\left(n+\frac{3}{2}\right)\lambda\xi\right] + \beta_n \sinh\left[\left(n+\frac{3}{2}\right)\lambda\xi\right] + \gamma_n \cosh\left[\left(n-\frac{1}{2}\right)\lambda\xi\right] \\ &\quad +\delta_n \sinh\left[\left(n-\frac{1}{2}\right)\lambda\xi\right], & (3.21) \\ U_n^{i}(\xi,t) &= \tilde{\alpha}_n e^{-(n+3/2)\lambda|\xi|} + \tilde{\beta}_n e^{-(n-1/2)\lambda|\xi|}, & (3.22) \end{aligned}$$

where α_n, β_n, γ_n, δ_n, $\tilde{\alpha}_n$ and $\tilde{\beta}_n$ are determined independently at each instant t from the kinematic and dynamic boundary conditions on the droplet and the wall surfaces. The continuity and impermeability conditions at the droplet's boundary, Eqs. (3.7) and (3.8), become using both Eq. (3.19) and Eq. (3.13):

$$\left.\frac{\partial \psi^{(i)}}{\partial \mu}\right|_{\xi=1} = \left.\frac{\partial \psi^{(o)}}{\partial \mu}\right|_{\xi=1} = \frac{a^2(1-\mu\cosh\lambda)}{(\cosh\lambda-\mu)^3}v. \tag{3.23}$$

Integrating with respect to μ along the droplet's boundary (and imposing $\psi^{(i)} = \psi^{(o)} = 0$ on the axis of symmetry which is a streamline of the problem) we obtain:

$$\left.\psi^{(i)}\right|_{\xi=1} = \left.\psi^{(o)}\right|_{\xi=1} = \frac{(1-\mu^2)a^2}{2(\cosh\lambda-\mu)^2}V. \tag{3.24}$$

The continuity of the velocity field at the droplet's boundary further imposes:

$$\left.\frac{\partial \psi^{(o)}}{\partial \xi}\right|_{\xi=1} = \left.\frac{\partial \psi^{(i)}}{\partial \xi}\right|_{\xi=1}, \tag{3.25}$$

and the Marangoni condition in Eq. (3.6) at the surface of the droplet becomes:

$$\left.(\sigma_{\xi\mu}^{(o)} - \tilde{\eta}\sigma_{\xi\mu}^{(i)})\right|_{\xi=1} = -\frac{(2+3\tilde{\eta})(\cosh\lambda-\mu)\sqrt{1-\mu^2}}{a}\left.\frac{\partial c}{\partial \mu}\right|_{\xi=1}. \tag{3.26}$$

Finally, the no-slip boundary condition at the wall, Eq. (3.7), becomes:

$$\left.\psi^{(o)}\right|_{\xi=0} = 0, \qquad \left.\frac{\partial \psi^{(o)}}{\partial \xi}\right|_{\xi=0} = 0. \tag{3.27}$$

Eqs. (3.24)–(3.27) projected in the polar direction along the n-th Legendre polynomial provide n sets of 6 linear equations. In each one, α_n, β_n, γ_n, δ_n, $\tilde{\alpha}_n$ and $\tilde{\beta}_n$ (and thus the streamfunction) only involve terms related to the surface concentration.

3.3.3 Transport problem

To solve the transport equation Eq. (3.17), we also exploit the spectral decomposition of c along the Legendre polynomials in the polar direction. Inspired by the separated form of the solution for Laplace's equation in bi-spherical coordinates, the relative concentration field c (which vanishes at infinity here) is thus decomposed as:

$$c(\xi,\mu,t) \quad = \quad \Gamma^{1/2}\sum_{n=0}^{\infty} c_n(\xi,t)L_n(\mu), \tag{3.28}$$

where the $c_n(\xi,t)$ functions are yet to be determined. One difficult aspect of the bi-spherical coordinates system is its distortion with the separation distance d (directly linked to λ). In the case of a single active droplet, after a transient regime, the droplet swims at its constant self-propulsion speed. In this situation, the solute dynamic reaches a steady state and the concentration field around the droplet remains constant over time. Consequently, using the spherical coordinates system, the coefficients C_n that characterise the concentration field from the Legendre expansion Eq. (2.12) remain constant over time. On the other hand, in the bi-spherical coordinates system, the coefficients c_n relative to the bi-spherical expansion Eq. (3.28) vary significantly as the droplet moves. Indeed, even if the concentration field around the droplet remains constant, the term $\Gamma^{1/2}$ in the concentration field expansion of Eq. (3.28) depends on the separation distance d and thus distorts the coordinates system as the droplet gets closer to the wall.

Using Eqs. (3.15) and (3.19), the advection-diffusion equation Eq. (3.17) is written:

$$\begin{aligned}&\left.\frac{\partial c}{\partial t}\right|_{\xi,\mu} + \left[\frac{\dot{a}\mu\sinh(\lambda\xi)}{\lambda a} - \frac{\dot{\lambda}\xi}{\lambda} + \frac{\Gamma^3}{\lambda a^3}\frac{\partial\psi^{(o)}}{\partial\mu}\right]\frac{\partial c}{\partial\xi} - \left[\frac{\dot{a}}{a}(1-\mu^2)\cosh(\lambda\xi) + \frac{\Gamma^3}{\lambda a^3}\frac{\partial\psi^{(o)}}{\partial\xi}\right]\frac{\partial c}{\partial\mu}\\ &= \frac{1}{\mathrm{Pe}}\frac{\Gamma^3}{\lambda a^2}\left[\frac{1}{\lambda}\frac{\partial}{\partial\xi}\left(\frac{1}{\Gamma}\frac{\partial c}{\partial\xi}\right) + \frac{\partial}{\partial\mu}\left(\frac{(1-\mu^2)}{\Gamma}\frac{\partial c}{\partial\mu}\right)\right],\end{aligned} \tag{3.29}$$

and substituting ψ and c from Eqs. (3.20) and (3.28) yields:

$$\begin{aligned}&\sum_{n=0}^{\infty}\Bigg\{\frac{L_n}{\Gamma^{1/2}}\frac{\partial c_n}{\partial t} + \frac{\dot{a}}{a}\left[\frac{(1+\mu\cosh(\lambda\xi))L_n - 2\cosh(\lambda\xi)(1-\mu^2)L_n'}{2\Gamma^{1/2}}\right]c_n\\ &+\left(\frac{\dot{a}\mu\sinh(\lambda\xi) - \dot{\lambda}\xi a}{\lambda a}\right)\frac{L_n}{\Gamma^{1/2}}\frac{\partial c_n}{\partial\xi} + \frac{1}{\lambda a^3}\sum_{k=1}^{\infty}\Bigg[\left(\frac{3}{2}(1-\mu^2)L_k'L_n - k(k+1)\Gamma L_kL_n\right)U_k\frac{\partial c_n}{\partial\xi}\\ &+\frac{\lambda\sinh(\lambda\xi)}{2}\left[3(1-\mu^2)L_k'L_n' - k(k+1)L_nL_k\right]U_kc_n + (1-\mu^2)L_k'\left(\frac{L_n}{2} - \Gamma L_n'\right)\frac{\partial U_k}{\partial\xi}c_n\Bigg]\\ &= \frac{\Gamma^{3/2}}{a^2\mathrm{Pe}}\sum_{n=0}^{\infty}\left(\frac{1}{\lambda^2}\frac{\partial^2 c_n}{\partial\xi^2} - \left(n+\frac{1}{2}\right)^2 c_n\right)L_n.\end{aligned} \tag{3.30}$$

Projecting the advection-diffusion equation, Eq. (3.30), onto $L_p(\mu)$ provides a set of coupled partial differential equations for $\tilde{\boldsymbol{C}}(\xi,t) = [c_0(\xi,t), c_1(\xi,t), ..., c_N(\xi,t)]$ (see Appendix

A) which can be formally written as:

$$\boldsymbol{H}\cdot\frac{\partial\tilde{\boldsymbol{C}}}{\partial t}+\left(\boldsymbol{B}^1\cdot\boldsymbol{U}+\boldsymbol{B}^2\cdot\frac{\partial\boldsymbol{U}}{\partial\xi}+\boldsymbol{G}^1\right)\cdot\tilde{\boldsymbol{C}}$$
$$+\left(\boldsymbol{B}^3\cdot\boldsymbol{U}+\boldsymbol{G}^2\right)\cdot\frac{\partial\tilde{\boldsymbol{C}}}{\partial\xi}=\frac{1}{\mathrm{Pe}}\left(\boldsymbol{A}^1\cdot\tilde{\boldsymbol{C}}+\boldsymbol{A}^2\cdot\frac{\partial^2\tilde{\boldsymbol{C}}}{\partial\xi^2}\right),\qquad(3.31)$$

where the second-order tensors $\boldsymbol{H}$, $\boldsymbol{A}^i$, $\boldsymbol{G}^i$ $(i=1,2)$ and the third-order tensor $\boldsymbol{B}^j$ $(j=1,2,3)$ have coefficients that are obtained in terms of integrals of appropriate combinations of Legendre polynomials and depend on ξ (see Appendix A). Physically, terms in $\boldsymbol{H}$, $\boldsymbol{G}^i$, $\boldsymbol{B}^j$ and $\boldsymbol{A}^i$ are related to the local time-derivative (for fixed ξ and μ), the grid adaptation, convection by the Marangoni flow and diffusion, respectively. Besides, $\boldsymbol{U}(\xi,t)=[U_1^o(\xi,t),U_2^o(\xi,t),...,U_N^o(\xi,t)]$ is a linear and instantaneous function of $\tilde{\boldsymbol{C}}$ (see § 3.3.2).

Finally, this set of evolution equations for $c_n(\xi,t)$, Eq. (3.31), which are second-order in space, must be complemented by appropriate boundary conditions. After substitution of Eq. (3.28), and projection onto the n-th Legendre polynomial the flux conditions, Eqs. (3.3), at the droplet's $(\xi=1)$ and wall's $(\xi=0)$ surfaces become:

$$\left.\left(\frac{\lambda\sinh\lambda}{2}c_n+\cosh\lambda\frac{\partial c_n}{\partial\xi}-\frac{n+1}{2n+3}\frac{\partial c_{n+1}}{\partial\xi}-\frac{n}{2n-1}\frac{\partial c_{n-1}}{\partial\xi}\right)\right|_{\xi=1}=\sqrt{2}a\lambda e^{-(n+1/2)|\lambda|},\qquad(3.32)$$

$$\left.\left(\frac{\partial c_n}{\partial\xi}-\frac{n+1}{2n+3}\frac{\partial c_{n+1}}{\partial\xi}-\frac{n}{2n-1}\frac{\partial c_{n-1}}{\partial\xi}\right)\right|_{\xi=0}=0.\qquad(3.33)$$

At each time-step, the functions $(U_n^o)_n$ are obtained from $(c_n)_n$ following the results of Section 3.3.2. Note that only the outer flow needs to be known explicitly. The set of non-linear partial differential equations Eq. (3.31) is then solved using finite differences and a uniform grid of N_ξ points with $0\leq\xi\leq1$. Advective terms, i.e. those involving $U_n^o(\xi)$, are treated explicitly while a Crank-Nicholson scheme is used to account for the diffusive terms. In addition we use a Richardson extrapolation method to get an adaptative time step. We show on Fig. 3.5 the concentration field and streamlines in the lab-frame that one can obtaine by the present derivation.

To clearly identify the hydro-chemical interactions experienced by an active droplet in the presence of a wall, the droplet should reach its self-propelling steady state before it feels any influence form it. Therefore, in the case of a head-on collision, the droplet must begin its journey sufficiently far away from the wall. As the droplet swims, the bi-spherical grid experiences distortions (see Fig. 3.4). Consequently, the farther the droplet, the coarser the spatial resolution. Furthermore, we expect that the solute azimuthal distribution at the droplet surface will significantly vary when the droplet approaches the wall. Therefore, to grasp the physics of the collision, the sufficient number of bi-spherical modes one needs to consider increases as the droplet gets closer to the wall. Finally, for the collision dynamics to be accurately resolved we chose both a sufficiently large number of modes and grid points to reach a numerical convergence (in practice by examining the velocity and the solute polarity for different modal and spatial resolutions).

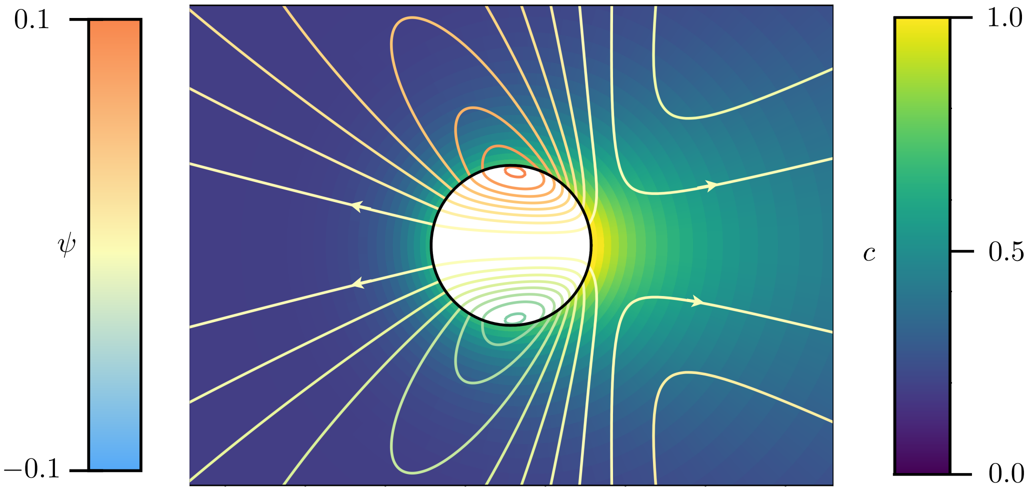

Figure 3.5: Concentration field and streamlines in the lab-frame around an active droplet that swims toward a wall

Finally, it should be noted the present framework can easily be adapted to consider the collision of two droplets rather than a droplet with a wall: for two symmetric droplets, the ξ-grid is simply extended to $-1 \leq \xi \leq 1$ with the boundary conditions at the wall ($\xi = 0$) being replaced by appropriate conditions on the second droplet ($\xi = -1$). Alternatively, for a purely symmetric situation (see section 3.6.2), we only need to solve the right-half plane problem by imposing the symmetry of the concentration and velocity field on $\xi = 0$.

3.3.4 Validation of the numerical model

The validity and accuracy of the present approach are tested by comparison with the case of a single self-propelled droplet considered by Ref. [36]. To this end, we consider the case of two droplets initially separated by a distance $d = 48$, i.e. far enough that one expects their interaction to be only weak and to recover the single-droplet results. The concentration field is initialised using the purely-diffusive solution (Pe = 0) of two droplets, for which an analytical solution can be computed using the same approach of [103]. At $t > 0$, the previous simulation framework is used for a fixed non-zero value of Pe; both droplets are initially forced to move at a fixed positive velocity $v = 0.1$ until $t = 2$ and are let to evolve force-free for $t > 2$; after a transient regime, their velocity relaxes toward a fixed and common value identified as their self-propulsion velocity v_0 when isolated.

The mean long-time velocity of the droplets is measured at $t = 3000$; it is reported on Fig. 3.6 and compared to the results of Ref. [36] for a single droplet. The results are in excellent agreement and validate the present framework: the maximum relative errors obtained are around 2% for $6 \leq \text{Pe} \leq 20$, when using $N = 60$ polar modes and $N_\xi = 100$ regularly-spaced grid points in ξ, a resolution precise enough to guarantee the accurate description of the physical processes, yet light enough to analyse the time-dependent rebound dynamics of the droplet as well as the influence of Pe on the detailed chemo-hydrodynamic interaction between the droplet and the wall.

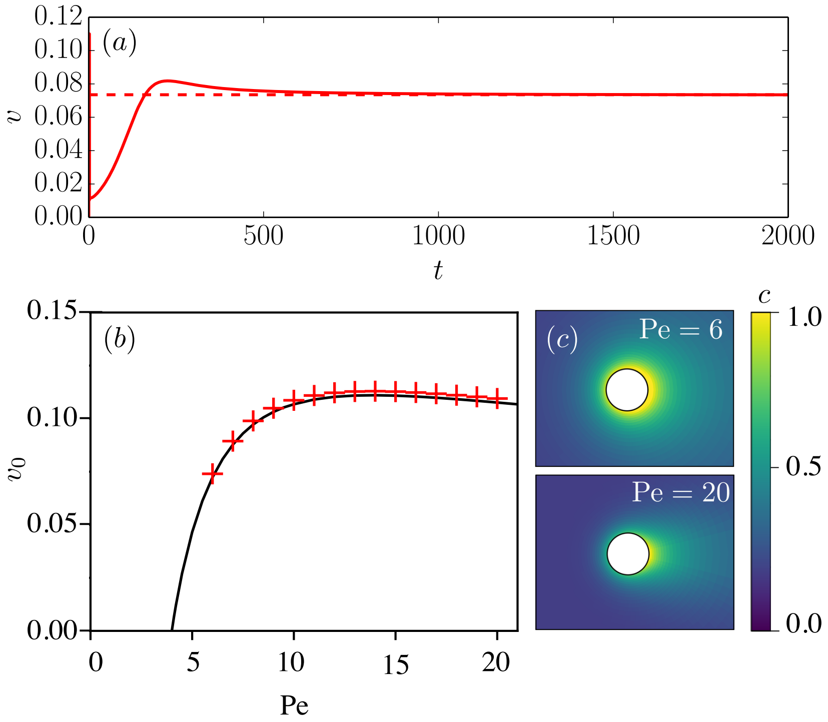

Figure 3.6: (*a*) Mean velocity of two active droplets initially located at $d = 48$ from each other and moving in the same direction at Pe $= 6$ and $\tilde{\eta} = 1/36$ (red solid line). The self-propulsion velocity v_0 for a single active droplet drawn from Ref. [36] (same viscosity ratio and Pe) is also reported by a red dashed line. (*b*) Mean self-propulsion velocity v_0 of two active droplets for Pe $= 6$ and $\tilde{\eta} = 1/36$ (red crosses). The results of Ref. [36] for a single active droplet with the same viscosity ratio are also reported (black solid line). (*c*) concentration field around an active droplet for Pe $= 6$ and Pe $= 20$.

3.4 Collision at moderate Péclet number

We first analyse the collision dynamics for moderate advection, i.e. for Pe slightly above the instability threshold (Pe $= 6$ is chosen here). For simplicity, the inner and outer fluid viscosities are assumed identical from now on ($\tilde{\eta} = 1$). The motion of the droplet as well as the front-back asymmetry of the concentration field, i.e. the motion's primary driving mechanism, are monitored by the droplet's velocity $\boldsymbol{v}$ and the polarity of the surface concentration $\boldsymbol{\Pi}$ defined in section 2.1. Fig. 3.7 displays the evolution of $v = \boldsymbol{v} \cdot \boldsymbol{e}_z$ and $\Pi = \boldsymbol{\Pi} \cdot \boldsymbol{e}_z$ with the distance between the droplet and the wall d. Initially, the droplet swims toward the wall with a constant self-propulsion velocity $-v_0$, where $v_0(\text{Pe})$ is the magnitude of self-propulsion of an isolated droplet. As it approaches the wall, it decelerates and reverses direction ($v = 0$) at a finite distance $d_{\text{min}}(\text{Pe})$ from the wall ($d_{\text{min}} = 1.4$ for Pe $= 6$). In a second phase, the droplet accelerates away from the wall and eventually reaches again its self-propulsion velocity v_0. A main observation of Fig. 3.7 is that the velocity and polarity are almost equal throughout the collision and the consequence of this is discussed in more depth below. In the following, we analyse each sequence of the interaction to identify the roles of the different mechanisms.

3.4.1 Far-field interactions

The droplet is expected to respond to the wall's influence on both the chemical and hydrodynamic fields. Chemically, the droplet acts as a source of solute. The no-flux boundary condition prevents the diffusion of solute through it which essentially amounts to an elevation of the solute content in the wall's vicinity. When the droplet is far enough from the wall, this amounts to an effective image source of chemical located in the $z < 0$ half-plane creating a $1/d^2$ chemical gradient and repulsive Marangoni force on the droplet (see section 2.3). When the droplet is close enough, this repulsion eventually dominates the self-propulsion maintained by the chemical polarity at the droplet's surface.

Hydrodynamically, the wall modifies the drag coefficient on the droplet but also modifies the swimming velocity resulting from a given traction applied at the droplet's surface (here Marangoni stress). Fig. 3.7 shows that the polarity and velocity remain almost identical throughout the collision, as for a single isolated droplet, although both quantities evolve in time due to the modification of the concentration field. The equality of v and Π for a single isolated droplet, Eq. (2.40), solely stems from the hydrodynamic problem, which suggests that the hydrodynamic influence of the wall is weak here; in other words, changes in the droplet velocity result mainly from the modification of the concentration distribution at its surface (i.e. chemical interactions) and not from hydrodynamic interactions with the wall which appear subdominant.

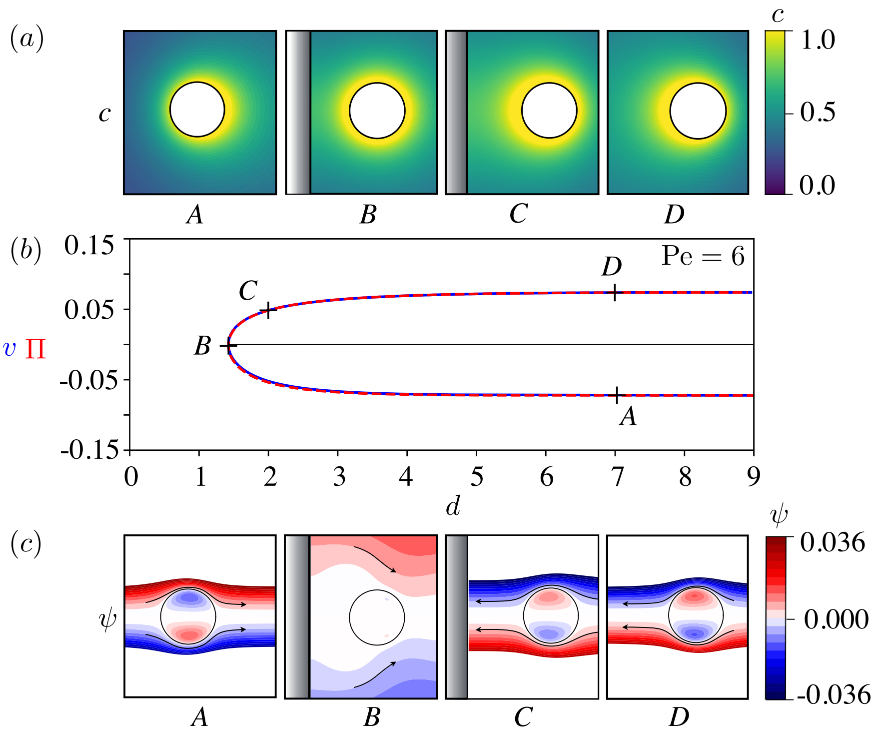

Figure 3.7: Collision of an active droplet with a rigid wall at Pe = 6. The evolution of the droplet velocity v (solid blue) and polarity Π (dashed red) during the collision are reported in terms of the distance d between the droplet's surface and the wall (*b*). Snapshots of the concentration (*a*) and stream-function (*c*) are also shown for four representative positions indicated as (A-D) on panel (*b*).

3.4.2 Near field and re-acceleration toward self-propulsion

When the droplet velocity vanishes (see Fig. 3.7b), the polarity of the concentration field also comes close to zero. A closer look at the distribution of chemical on the surface at that instant in fact reveals that the concentration distribution is almost homogeneous (its variance is reduced by an order of magnitude, when compared to the initial self-propelling state): this results in the droplet's arrest as there is no longer a Marangoni effect acting on the surface of the droplet and the fluid is at rest.

However, this equilibrium is only ephemeral as the presence of the wall promptly breaks this uniform distribution: the chemical flux at the droplet's surface being spatially uniform, the confinement on the side of the wall leads to an increased solute concentration there. As a result, a repelling Marangoni effect forces the droplet to drift away from the wall.

Because Pe is greater than the instability threshold, this perturbation of the concentration field simultaneously leads to the development of the same instability phenomenon that conferred the droplet its initial velocity, until it reaches v_0 as the droplet moves far away from the wall. In order to study the influence of the wall in the droplet "forced" re-acceleration, Fig. 3.8 compares this second phase of the motion with the situation of a single isolated droplet initially pushed at a finite velocity in the positive z direction before left force-free. The acceleration is initially greater in the second part of the droplet collision with the wall than in the reference isolated droplet case. Indeed, the presence of the wall reinforces the droplet acceleration (by accumulating more solute at its back) than in the case where the solute is able to diffuse freely.

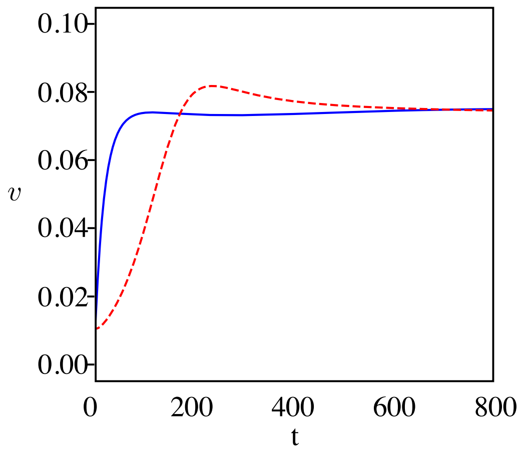

Figure 3.8: Evolution in time of the droplet's velocity for Pe = 6 during its re-acceleration after its collision with the wall (solid blue). This evolution is compared to the acceleration of an isolated droplet initially forced with a positive velocity $v = 0.1$ before being released force free at $t = 0$ (dashed red).

3.5 Collision at higher Péclet number

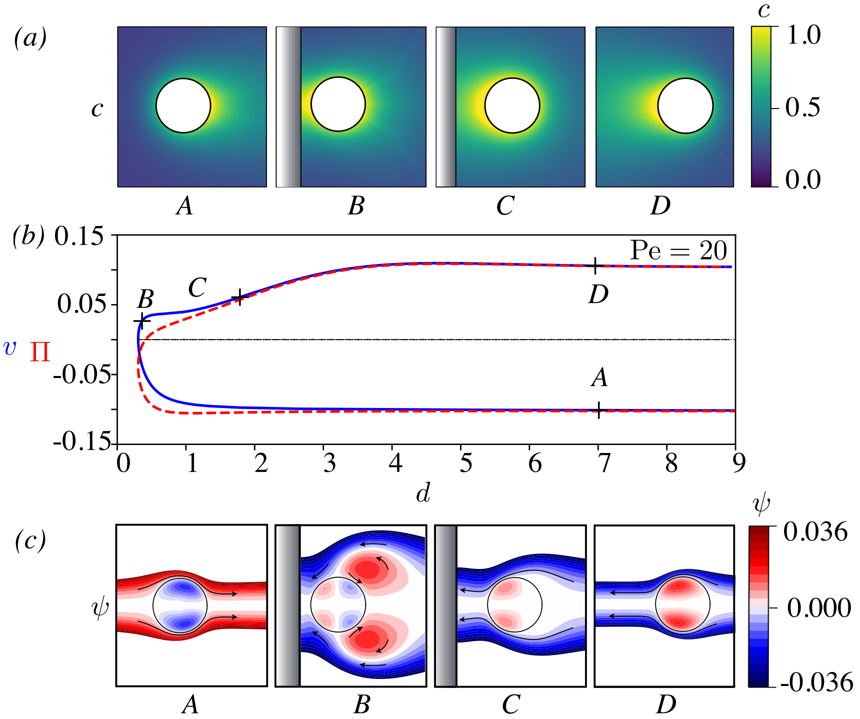

Figure 3.9: Collision of an active droplet with a rigid wall at $\mathrm{Pe} = 20$. The evolution of the droplet velocity v (blue solide) and polarity Π (red dashed) during the collision are reported in terms of the distance d between the droplet's surface and the wall (*b*). Snapshots of the concentration (*a*) and streamfunction (*c*) are also shown for four representative positions indicated as (A-D) on panel (*b*).

The results obtained for moderate Pe presented a rather simple picture of the collision dynamics: dominated by the chemical interactions with the wall, it amounts to a slowing down and repulsion of the droplet under the effect of the accumulating chemical solute in front of it due the confining presence of the wall, the wall's hydrodynamic effect being mostly subdominant. The picture becomes however much more complex as the importance of convection of solute vs. diffusion is increased, and the focus of this section is to analyse how wall interactions and collision dynamics are modified as Pe is increased.

Fig. 3.9 presents the evolution of velocity and polarity throughout the collision for $\mathrm{Pe} = 20$. As for $\mathrm{Pe} = 6$, the droplet initially propels at $-v_0$ toward the wall and decelerates up to a stopping point. This minimum rebound distance, $d_{\min}$ is however much lower, e.g. $d_{\min} = 0.3$ for $\mathrm{Pe} = 20$. Also, unlike for moderate Pe, the re-acceleration of the droplet is not a smooth process. In particular it displays a clear velocity plateau right after the rebound during which the droplet velocity remains almost constant. Eventually, and as expected, the droplet reaches once again its self-propulsion velocity as it moves away from the wall whose influence becomes negligible. In contrast with the moderate-Pe collision (Fig. 3.7), we note that the polarity and velocity do not match one another anymore during most of the near-field interactions with the wall, suggesting a stronger hydrodynamic influence of the confinement.

3.5.1 Early interactions and droplet deceleration

In contrast with the case of moderate advection (Pe = 6) for which the droplet starts to slow down at a distance $d \approx 4.5$ away from the wall, the velocity of the droplet remains relatively unchanged for larger Pe (e.g. down to a distance $d \approx 3$ for Pe = 20, Fig. 3.9). This slowing down of the droplet was identified as predominantly associated with the chemical repulsion resulting from the confinement of its own chemical signature. This approach of the droplet closer to the wall is therefore consistent with the faster (exponential) decay of the concentration field in front of the droplet as a result of the solute advection, while the decay is only algebraic in its wake [105, 106, 101]. The asymmetric structure of the concentration field can be observed by comparing the instant A of each panel (a) relative to the Figs. 3.7 and 3.9. As a result, the direct influence of the wall on the concentration field arises belatedly during the interaction for larger Pe.

One already noted that v and Π do not match one another anymore, contrary to the moderate Pe regime, indicating a direct hydrodynamic influence of the wall. Strikingly, and contrary to the intuition that chemical confinement would reduce the front-back concentration contrast at the droplet's surface, we also note that the polarity of the surface concentration $|\Pi|$ is increased as the droplet approaches the wall, and reaches its maximal value close to $d = 1$ before sharply reversing as the droplet stops. To understand this phenomenon in greater depth, the front-back concentration difference at the surface $\Delta c = c_{\text{front}} - c_{\text{back}}$ is represented on Fig. 3.10. Note that Δc is a second measure of the asymmetry in surface concentration which evolves in the same manner as $|\Pi|$ during the first part of the motion. During the approach of the droplet, both back and front concentrations are observed to increase (down to a distance $d = 3$). In a second phase, v starts to decrease under the effect of hydrodynamic interactions. Yet, the Marangoni flow is not stopped, and in fact contributes to maintain the concentration contrast responsible for a net pumping flow toward the back of the droplet effectively expelling more solute toward the droplet's wake (illustrated by the decrease of c_{front}), which therefore explains the increase of $|\Pi|$. As in the moderate-Pe case, solute accumulates between the wall and the droplet as they get closer to each other, but the minimum distance d_{min} of the droplet surface to the wall is now significantly smaller as a result of the sharper decay of the surface concentration ahead of the droplet during the approaching phase. This induces a sharper increase of the concentration between the wall and droplet, resulting in the fast inversion of v observed in Fig. 3.9. In addition, Fig. 3.10 shows how the inversion of v can directly be correlated to the increase of Π.

3.5.2 Rebound and velocity plateau

A distinguishing feature of the collision dynamics for higher Pe is the existence, shortly after the rebound of the droplet (Fig. 3.9b), of a velocity plateau during which the droplet's velocity remains relatively constant, and significantly smaller than v_0, while the droplet moves away from the wall by about one radius.

To understand its origin, Fig. 3.7 and Fig. 3.9 provide the evolution of the flow field (streamlines) in the frame of reference of the droplet for Pe = 6 and Pe = 20. For Pe = 6, the flow field is very weak at the instant of rebound, a consequence of the homogeneity of the surface concentration and resulting absence of Marangoni forcing. In contrast, at that same instant for Pe = 20, a strong flow in and around the droplet is observed to persist as a consequence of the surface concentration inhomogeneity (Fig. 3.9b). Within the present Stokesian approach, this flow field is an instantaneous response to the concentration distribution at the droplet surface. This flow helps sustain the polarity of the arrested

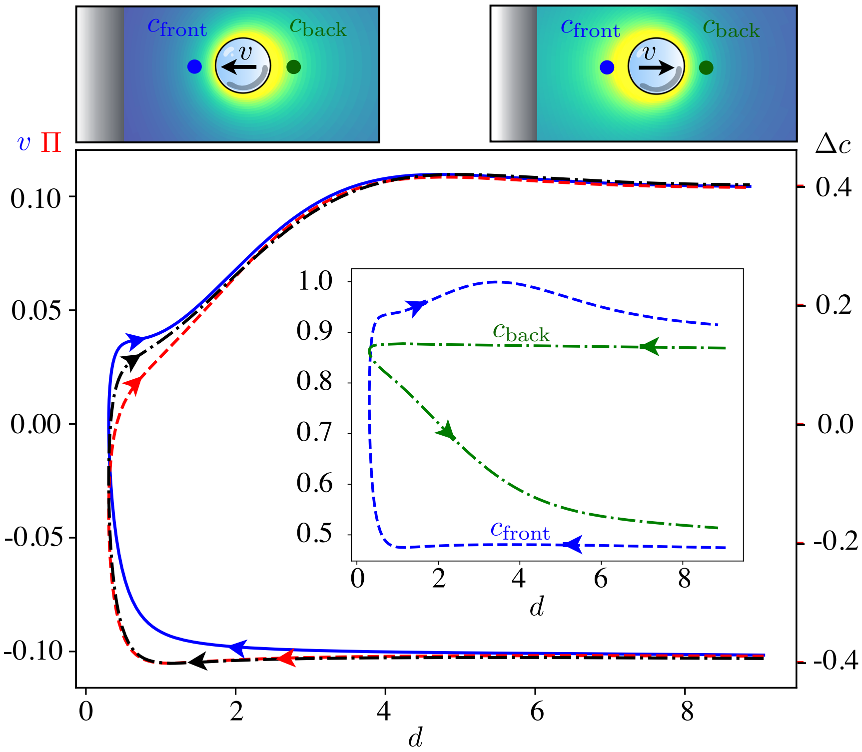

Figure 3.10: Evolution as a function of the droplet-wall distance d of the velocity v (solid blue) the polarity (red dashed) and front-back surface concentration contrast $\Delta c = c_{\mathrm{front}} - c_{\mathrm{back}}$ (black dashed-dotted) at Pe = 20. The inset shows the evolution of c_{back} and c_{front} with d individually and the definition of these two quantities is given at the top of the figure.

droplet while balancing the chemical repulsion introduced by the wall; as a result, a velocity plateau develops until the flow within the droplet reverses. The structure of the flow within the droplet is quadrupolar (in contrast with the dipolar flow observed during self-propulsion) and is a direct result of the surface concentration distribution, whose slow relaxation for larger Pe introduces a delay before the instability leading to the droplet's self-propulsion away from the wall may develop again. The evolution of c_{back} in Fig. 3.10 illustrates the mitigation of the residual amount of solute at the back of the droplet during the second part of the rebound.

3.5.3 Re-acceleration toward self-propulsion

Since d_{min} is lower at higher Pe, one would expect an enhanced repulsion from the wall and therefore an even faster re-acceleration of the droplet (when compared to the development of the self-propulsion instability for an isolated droplet) than was observed for moderate Pe (Fig. 3.8). This is however not the case: strikingly, and in contrast with the moderate-Pe situation, the droplet actually takes more time to recover its propulsion velocity v_0 after the rebound than if it was alone (Fig. 3.11). This effect is a direct consequence of the persistence of an excess of solute in the droplet's wake after its approach to the wall, which was already shown to create a pumping flow that holds the droplet back.

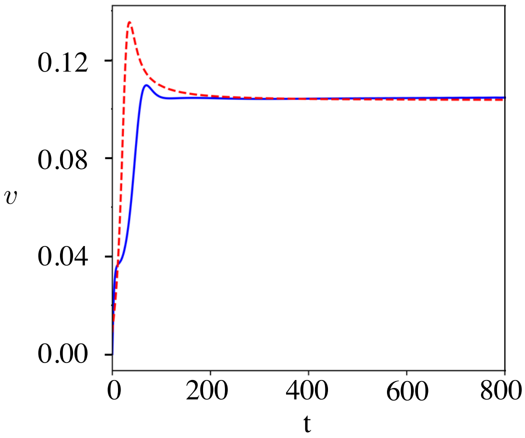

Figure 3.11: Evolution in time of the droplet's velocity for Pe $= 20$ during its re-acceleration after its collision with the wall (solid blue). This evolution is compared to the acceleration of an isolated droplet initially forced with a positive velocity $v = 0.1$ before being released force free at $t = 0$ (dashed red).

3.6 Rebound distance and two-droplet collision

In the previous sections, the droplet-wall interaction was analysed in details for two different values of Pe. One key feature was that, due to the structure of the concentration field ahead of the moving droplet, the rebound distance (i.e. the minimum distance of approach of the droplet to the wall) is reduced when advection plays a more important role in the solute transport. The goal of this section is to provide a more complete characterisation of this phenomenon and we thus now focus on the evolution with Pe of the distance d_{min} between the wall and the front of the droplet at the time it reverses direction (Fig. 3.12).

3.6.1 Rebound distance with varying Pe

A monotonic decrease of d_{min} is observed, as expected from the structure of the concentration field ahead of the moving droplet (see top panels of Fig. 3.12). We also note the existence of two distinct regimes in this decrease. For moderate Pe, and as Pe approaches the minimum value for self-propulsion $\text{Pe}_c = 4$ [66, 36, 101], d_{min} diverges as $(\text{Pe} - \text{Pe}_c)^{-1}$: close to the self-propulsion threshold, the droplet is more sensitive to the wall's influence and is repelled at much greater distances. For larger Pe (typically Pe $\gtrsim 10$), a slower decrease is observed as $(\text{Pe} - \text{Pe}_c)^{-1/2}$. The asymptotic analysis of the collision near Pe_c, presented in section 3.7, confirms the former scaling and provides more depth on the interaction and rebound dynamics.

3.6.2 Two-droplet collision

The interaction of a droplet with a chemically-inert wall shares many similarities to the symmetric interaction of two identical droplets. Mathematically, the chemical problem is in fact identical, the no-flux condition at the wall in Eq. (3.3) being strictly equivalent to a perfect symmetry of the concentration field as for the case of two symmetric droplets. The only difference therefore lies in the hydrodynamic problem and resulting flow field: a no-slip condition is applied for the case of rebound on a wall, Eq. (3.7), while symmetry conditions on the velocity field would hold on $z = 0$ for the case of two droplets (effectively amounting to the presence of a free surface rather than a rigid wall). The modification

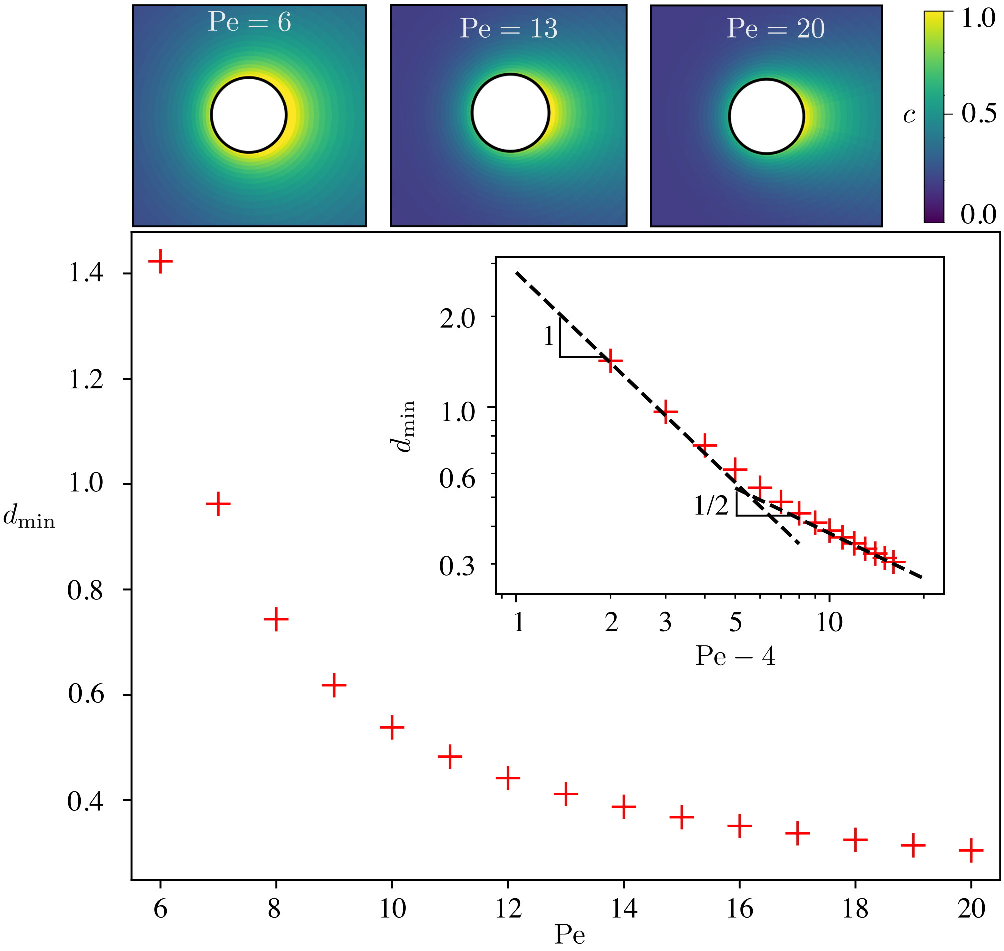

Figure 3.12: Evolution of the rebound distance $d_{\min}$ (measured when $v = 0$) for the droplet-wall collision (red crosses). The inset reproduces the same data in log-log scales to identify the asymptotic scaling for near critical and large Pe. The concentration fields around an active droplet approaching the wall (i.e. propelling to the left) are also shown for three representative Péclet numbers Pe = 6, 13 and 20.

of the hydrodynamic field may nevertheless have significant consequences, in particular at larger Pe due to the importance of advection by this flow field on the solute dynamics.

Before closing this section, we therefore briefly analyse the difference between the two situations in more details. Defining $2d$ the minimum distance between the surfaces of the two droplets (Fig. 3.1b), and performing the same numerical approach as for the droplet-wall interaction, one reports in Fig. 3.13 the evolution with d of the velocity and polarity of the right-hand droplet for moderate and higher Pe, and compare those results to that obtained for the wall collision. Both configurations lead to the same dynamics except in the immediate vicinity of the stopping point where some small variations can be identified. These differences are more pronounced for larger Pe, which is likely due to the closer proximity to the wall.

Indeed, the free-surface boundary condition for the velocity field in the plane $z = 0$ has two main consequences. First, consistent with the asymptotic results of section 2.2, Fig. 3.15 shows the drag coefficient experienced by each droplet is lower in the two-droplet collision when compared to the droplet-wall situation for the same separation distance d [22, 107].

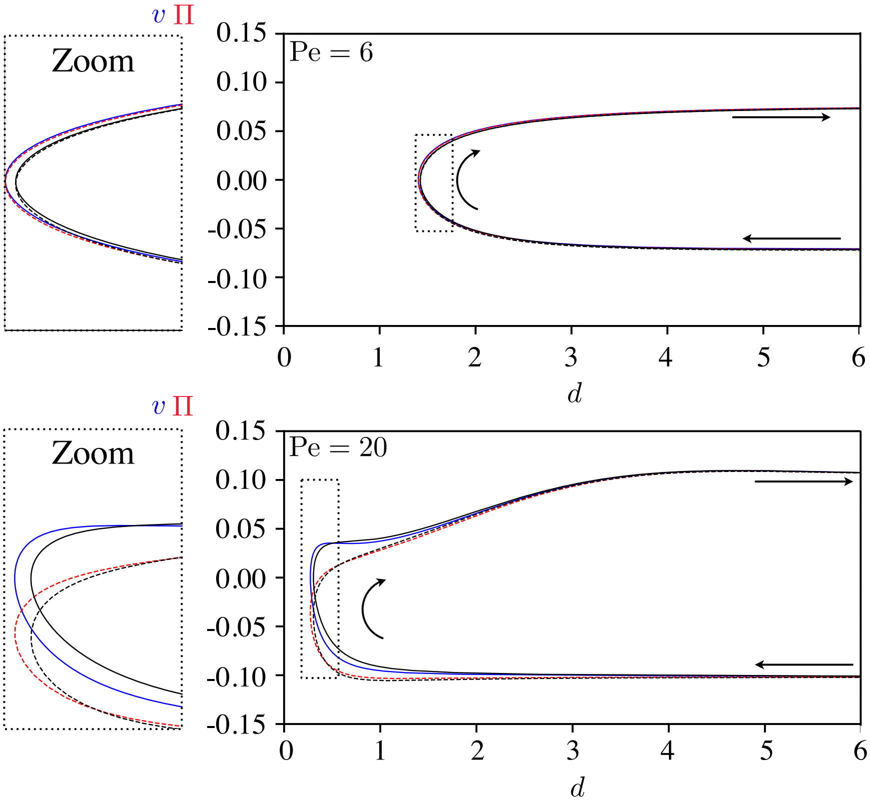

Figure 3.13: Collision between two active droplets at Pe = 6 (top) and Pe = 20 (bottom). In each case, the evolution with d, the half-distance between the two droplets, of the droplet velocity v (solid blue) and polarity Π (dashed red) is shown. For reference the corresponding results for the collision of a single droplet with a no-slip wall are also shown for the velocity (solid black) and polarity (dashed black).

Indeed, in the case of the symmetric collision of two droplets, the free-surface at $z = 0$ is mobile and does not generate additional viscous dissipation as in the case of a rigid wall which imposes the flow to vanish. Having a lower drag coefficient, Eq. (3.10) implies directly that the same solute distribution around the droplet's surface leads to a greater propulsion velocity. Besides, the solute is evacuated by advection more easily from the zone between the droplets, since the flow field have a component along $\boldsymbol{e}_y$ on the $z = 0$ plan. The latter results in the mitigation of the solute concentration in the region between the droplets, which therefore approach closer before experiencing a rebound. Fig. 3.14 further reports the evolution of $d_{\min}$ with Pe for the droplet-wall and droplet-droplet collisions. Once again, the evolutions are similar, although the rebound distance is systematically smaller in the case of two droplets (or of a free surface) than for a droplet and a no-slip wall.

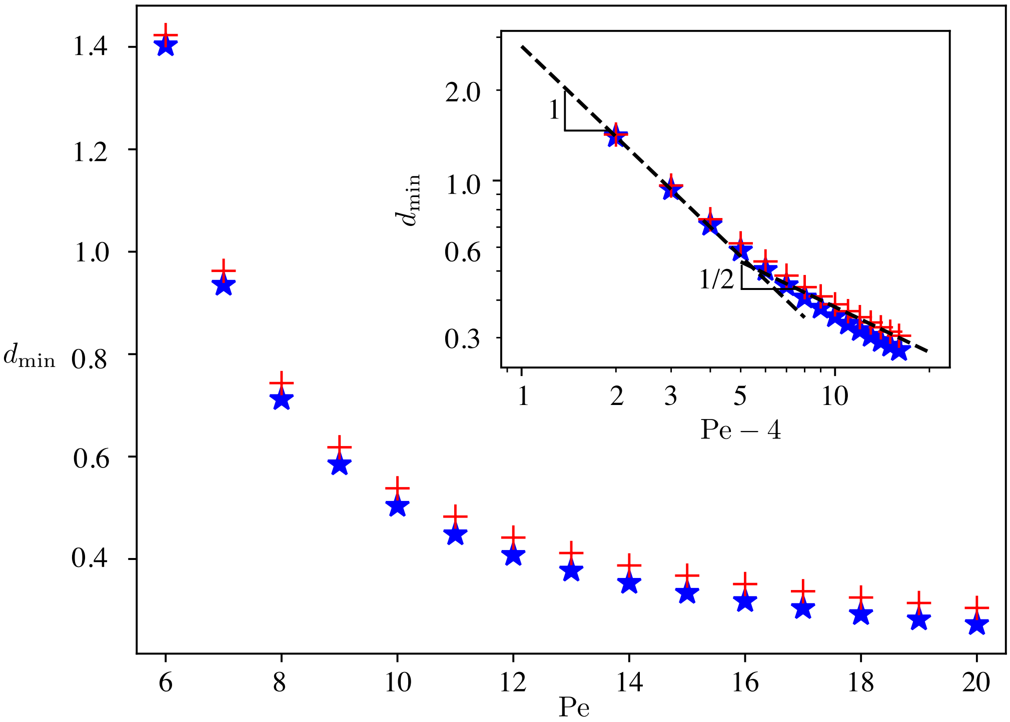

Figure 3.14: Evolution of the rebound distance $d_{\min}$ (measured when $v = 0$) for the droplet-wall collision (red crosses) and two-droplet collision (blue stars). The inset reproduces the same data in log-log scales to identify the asymptotic scaling for near critical and large Pe

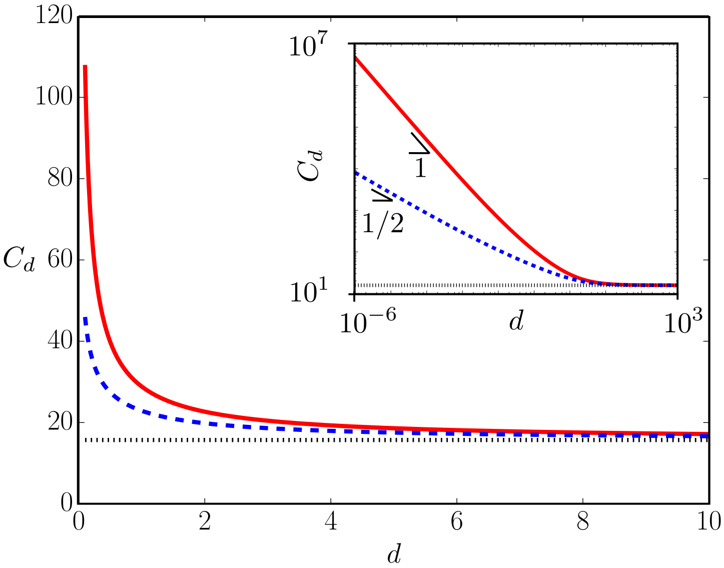

Figure 3.15: Evolution of the drag coefficient C_d experienced by a droplet as it moves closer to a rigid wall (red solide line) or another droplet of same size which swims in a symmetrical manner (blue dashed line). The drag coefficient $C_d = 5\pi$ experienced by a single droplet is also reported (black dotted line). All situations are computed for the particular case $\tilde{\eta} = 1$.

3.7 Asymptotic calculations

The asymptotic computations of this section have been carried out by Matvey Morozov, a former postdoctoral researcher at LadHyX. So far we have accrued a general understanding of the droplet-wall and droplet-droplet interactions in the presence of advection. In this section, we employ asymptotic methods to explain some of the findings in more detail for the symmetric collision of two identical droplets (although most of the reasoning below will be shown to be straightforwardly applicable to the collision of a single droplet with a no-slip wall). Since explicit analytical treatment of advection-diffusion in bi-spherical coordinates is exceedingly complex, we consider a pair of identical active droplets separated by a large center-to-center distance $2d_c \equiv 2D_c/\epsilon$, where $\epsilon \ll 1$. We postulate that the system remains symmetric at all times, i.e., droplets either approach each other with velocity $-2v$ or part ways with velocity $2v$. We also assume that the Péclet number is close to the critical value $\mathrm{Pe}_c = 4$ corresponding to the spontaneous onset of self-propulsion,

$$\mathrm{Pe} = \mathrm{Pe}_c + \epsilon\delta, \tag{3.34}$$

where $\delta = O(1)$ is the supercriticality parameter. In this case, a weakly-nonlinear theory of droplet interaction may be constructed using only axisymmetric spherical coordinates in the vicinity of each droplet. In particular, we will obtain an asymptotic solution to the problem formulated by Eqs. (3.2)–(3.9) by considering each of the droplets separately using axisymmetric spherical coordinates co-moving with the corresponding droplet. In the vicinity of the self-propulsion threshold (i.e. for $\epsilon \ll 1$), the droplet velocity is expected to be small,

$$\boldsymbol{v}_i = \epsilon \boldsymbol{v}_i^{(1)} + \epsilon^2 \boldsymbol{v}_i^{(2)} + \dots \quad \text{for } i = 1, 2, \tag{3.35}$$

and, thus, advection is weak [108, 101]. In the limit of weak advection, the chemical footprint of an individual droplet is known to consist of a near-field part, $N(\mathbf{r})$, valid for $r \ll 1/\epsilon$, and a far-field contribution, $F(\mathbf{r})$, valid for $r \gg 1$ [105, 108, 101]. Accordingly, we seek for a quasi-steady solution of the problem and expand the near- and far-field components of the concentration field of each droplet in powers of ϵ,

$$N_i(\mathbf{r}_i) = N_i^{(0)}(\mathbf{r}_i) + \epsilon N_i^{(1)}(\mathbf{r}_i) + \epsilon^2 N_i^{(2)}(\mathbf{r}_i) + \dots \quad \text{for } i = 1, 2, \tag{3.36}$$

$$F_i(\boldsymbol{\rho}_i) = \epsilon F_i^{(1)}(\boldsymbol{\rho}_i) + \epsilon^2 F_i^{(2)}(\boldsymbol{\rho}_i) + \dots \quad \text{for } i = 1, 2, \tag{3.37}$$

where $\mathbf{r}_i \equiv (r_i, \theta_i)$ and $\boldsymbol{\rho}_i \equiv (\rho_i, \theta_i) = (\epsilon r_i, \theta_i)$ are unstretched and stretched radius vectors in the frame of reference co-moving with the i-th drop, respectively (Fig. 3.16). In what follows we will show that interaction of a pair of distant droplets is encapsulated within $N_i^{(2)}$, while terms $N_i^{(0)}$, $N_i^{(1)}$, $F_i^{(1)}$, and $F_i^{(2)}$ may be computed for each droplet individually.

3.7.1 Problems at ϵ^0 and ϵ^1: isolated drops

To compute the terms $N_i^{(0)}$, $N_i^{(1)}$, and $F_i^{(1)}$ of expansions (3.36)–(3.37), we consider each of the droplets separately. That is, we substitute Eqs. (3.36)–(3.37) into the problem formulated by Eqs. (3.2)–(3.9) in the case of a solitary spherical active drop. We then collect $O(1)$ terms and recover the isotropic solution,

$$N_i^{(0)}(\mathbf{r}_i) = 1/r_i, \tag{3.38}$$

that corresponds to a motionless droplet and quiescent fluid.

We proceed with the solution of the problem formulated by the $O(\epsilon)$ terms. Since the flow field does not vanish at ϵ^1, we need to write a solution to Stokes equations (3.5) within and around a spherical drop. In contrast to advection-diffusion equation that requires a

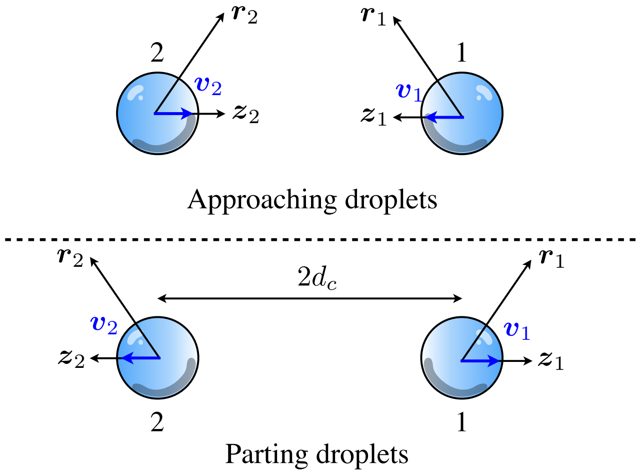

Figure 3.16: Asymptotic analysis and notations for the case of two approaching (top) or departing (bottom) active droplets. The direction of reference of each system of spherical coordinates (i.e. $\theta_i = 0$) is given by the swimming direction of the corresponding droplet, and is therefore opposite for the two droplets.

composite solution, Eqs. (3.36)–(3.37), Stokes equations are linear and admit a solution that is uniformly valid. At each order in ϵ, the axisymmetric solution of the Stokes problem, Eq. (3.5), within and outside of the spherical droplet is given by a superposition of orthogonal modes [109, 23, 110],

$$\psi_n^{(i)}(\mathbf{r}) = r^{n+1}\left(1-r^2\right)\left(1-\mu^2\right)L_n'(\mu), \tag{3.39}$$

$$\psi_n^{(o)}(\mathbf{r}) = \begin{cases} \left(1-r^3\right)\left(1-\mu^2\right)/r & n=1 \\ \left(1-r^2\right)\left(1-\mu^2\right)L_n'(\mu)/r^n & n>1 \end{cases}, \tag{3.40}$$

where $\psi_n^{(i,o)}$ denote the streamfunctions corresponding to the n-th mode of the flow decomposition within and outside of the drop, respectively.

Eq. (3.40) implies that in the reference frame co-moving with the drop, the far-field flow at $O(\epsilon)$ is unidirectional and the far-field advection-diffusion equation for each droplet may thus be rewritten as,

$$-\,\mathrm{Pe}\boldsymbol{v}_i^{(1)}\cdot\boldsymbol{\nabla}_{\boldsymbol{\rho}}F_i^{(1)}(\boldsymbol{\rho}_i) = \nabla^2_{\boldsymbol{\rho}}F_i^{(1)}(\boldsymbol{\rho}_i), \tag{3.41}$$

where $\boldsymbol{\nabla}_{\boldsymbol{\rho}}$ denotes the gradient in stretched coordinates. Since we disregard the droplet interactions at this order, we may adopt the corresponding solutions for $N_i^{(1)}$, and $F_i^{(1)}$ obtained by Ref. [101, 61],

$$N_i^{(1)}(\mathbf{r}_i) = -2v_i^{(1)}\left(1+\mu_i+\mu_i\frac{2-3r_i}{4r_i^3}\right), \qquad F_i^{(1)}(\boldsymbol{\rho}_i) = \frac{e^{-2v_i^{(1)}\rho_i(1+\mu_i)}}{\rho_i}, \tag{3.42}$$

where $v_i^{(1)} = \left|\boldsymbol{v}_i^{(1)}\right|$ and $\mu_i \equiv \cos\theta_i$. Note this effectively implies that $v_i^{(1)} > 0$ and that we define θ_i (and therefore μ_i) from an axis of reference that is oriented along the direction of propulsion of each droplet, i.e. toward (resp. away from) the second droplet for the approaching (resp. departing) case (Fig. 3.16).

Also note that Eqs. (3.36), (3.40) and (3.38) indicate that in the lab frame the leading order flow at a distance $1/\epsilon$ from an active droplet is $O(\epsilon^4)$ (recall that at ϵ^0 the fluid is motionless), while the droplet's chemical footprint is $O(\epsilon)$. That is, at a distance $1/\epsilon$ from both droplets, the advection diffusion equation, Eq. (3.2), reduces to an unsteady diffusion equation in the lab frame,

$$\mathrm{Pe}\frac{\partial F}{\partial t} = \nabla^2 F + O(\epsilon^4), \tag{3.43}$$

where F denotes the combined far-field concentration footprint of a pair of active drops, time derivative accounts for the displacement of the droplets in the lab frame, and $O(\epsilon^4)$ corresponds to the contribution of the flow field. Eq. (3.43) is linear, therefore F can be found as a superposition of the contributions from the individual droplets,

$$F = F_1 + F_2 = \epsilon\left(F_1^{(1)} + F_2^{(1)}\right) + \epsilon^2\left(F_1^{(2)} + F_2^{(2)}\right) + \dots. \tag{3.44}$$

Finally, we demonstrate that interaction between the droplets appears only in the problem at $O(\epsilon^2)$. To this end, we write the concentration field of droplet 2 in the coordinate system of droplet 1 and expand the result in powers of ϵ in the cases of approaching and departing drops, respectively,

$$F_{2,\text{approach}} = \epsilon\frac{e^{-8D_c v^{(1)}}}{2D_c} - \epsilon^2\frac{e^{-8D_c v^{(1)}}\left(1+8D_c v^{(1)}\right)}{4D_c^2} r_1\mu_1 + O(\epsilon^3), \tag{3.45}$$

$$F_{2,\text{departure}} = \epsilon\frac{1}{2D_c} + \epsilon^2\frac{r_1\mu_1}{4D_c^2} + O(\epsilon^3), \tag{3.46}$$

where $v^{(1)} \equiv v_1^{(1)} = v_2^{(1)}$. Note that the first term in the right-hand side of Eqs. (3.45)–(3.46) is constant and, thus, can not produce any Marangoni stresses. In turn, the second term in the right-hand side of Eq. (3.45) constitutes a unidirectional concentration gradient that implements the effect of droplet 2 onto droplet 1. This term is quadratic in ϵ, which justifies that the droplets may be considered separately at $O(\epsilon^0)$ and $O(\epsilon^1)$.

3.7.2 Problem at ϵ^2: droplet interaction

Section 3.7.1 established that the interaction of a pair of distant droplets is implemented by a linear concentration gradient in (3.45). On the other hand, in the reference frame co-moving with the drop, the near-field advection-diffusion, Eq. (3.2), reduces to an inhomogeneous steady diffusion equation [101, 61] that admits Eq. (3.45) as a solution. Therefore, the influence of the concentration gradient imposed by droplet 2 in the vicinity of droplet 1 only appears in the boundary conditions for droplet 1 and vice versa. As a result, general solutions for $N_i^{(2)}$, and $F_i^{(2)}$ may be adapted directly from Ref. [101, 61],

$$\begin{aligned}
N_i^{(2)}(\mathbf{r}_i) = \frac{C_{0,i}}{r_i} &+ \frac{(v^{(1)})^2}{30r_i^5}\left(8 - 15r_i + 20r_i^3 + 80r_i^6\right) - \frac{1}{2}\left(\delta v^{(1)} + 8A_{1,i}\right) \\
&+ L_1(\mu_i)\left(\frac{C_{1,i}}{r_i^2} + 4r_i(v^{(1)})^2 - \frac{1+2r_i^3}{4r_i^3}\left(\delta v^{(1)} + 8A_{1,i}\right)\right) \\
+ L_2(\mu_i)&\left(\frac{C_{2,i}}{r_i^3} + \frac{(v^{(1)})^2}{21r_i^5}\left(10 - 21r_i + 70r_i^3 - 42r_i^4 + 28r_i^6\right) - \frac{4+6r_i^2}{r_i^4}A_{2,i}\right),
\end{aligned} \tag{3.47}$$

$$F_i^{(2)}(\boldsymbol{\rho}_i) = -\frac{1+\mu_i}{2}e^{-2v^{(1)}\rho_i(1+\mu_i)}\left(\delta v^{(1)} + 8A_{1,i}\right), \tag{3.48}$$

where $A_{1,i}$, $A_{2,i}$, $C_{0,i}$, $C_{1,i}$, and $C_{2,i}$ are unknown coefficients to be determined from the boundary conditions. Following the procedure described by Ref. [101], we substitute $N_i^{(2)}(\mathbf{r}_i)$ and $F_i^{(2)}(\boldsymbol{\rho}_i)$ into the boundary conditions at ϵ^2 and obtain a set of algebraic equations in terms of the coefficients $A_{1,i}$, $A_{2,i}$, $C_{0,i}$, $C_{1,i}$, and $C_{2,i}$. Solvability condition of this set of

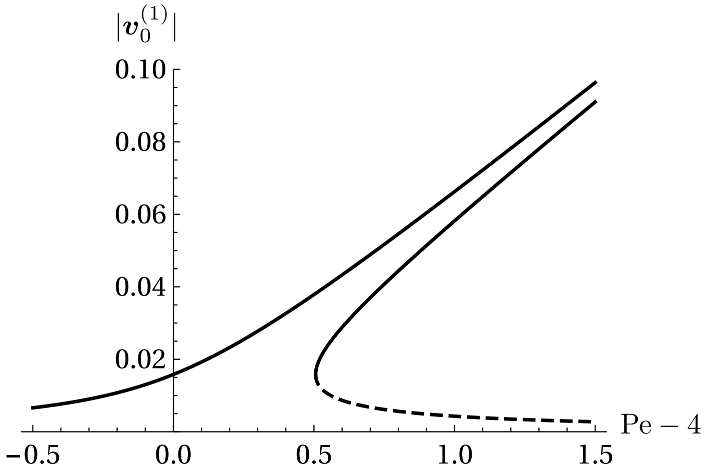

Figure 3.17: Bifurcation diagram (3.49): leading-order self-propulsion velocities of a pair of identical active droplets located at a distance $2d = 2D_c/\epsilon$ with $D_c = 10$. Top and bottom branches correspond to departing and approaching drops, respectively. A solid (resp. dashed) line denotes a stable (resp. unstable) propulsion regime.

equations yields the leading-order self-propulsion velocity of the droplet exposed to a weak concentration field,

$$v^{(1)} = \frac{\delta \pm \sqrt{\delta^2 + 256G}}{32}, \tag{3.49}$$

where

$$G = G_{\text{approach}} \equiv -\frac{e^{-8D_c v^{(1)}}\left(1 + 8D_c v^{(1)}\right)}{4D_c^2} \quad \text{or} \quad G = G_{\text{departure}} \equiv \frac{1}{4D_c^2} \tag{3.50}$$

for approaching and departing drops, respectively. We emphasise that $v^{(1)} \geq 0$ by definition. As a result, the departing configuration for which $G > 0$ is used in Eq. (3.49)), always admits a single solution while the approaching configuration for which $G < 0$ may have zero or two solutions depending on the magnitude of the concentration gradient.

Reconstructing the absolute relative velocity of the droplets is achieved as $v = -\epsilon v^{(1)}_{\text{approach}}$ (resp. $v = \epsilon v^{(1)}_{\text{departure}}$) for the approaching (resp. departing) case. In the numerical analysis, droplet approach corresponds to negative velocity (as shown in Fig. 3.7, Fig. 3.9 and Fig. 3.13), and the bifurcation diagram (3.49) is plotted in Fig. 3.17 to match this convention. Eq. (3.49) corresponds to an imperfect transcritical bifurcation implying that not all of the branches of the bifurcation diagram (3.49) are stable, as shown in Fig. 3.17. Also note that the bifurcation diagram corresponding to Eq. (3.49) is quasistatic, i.e., it depends on time through the separation distance between the droplets D_c only.

In essence, Eq. (3.49) establishes that the regime of steadily approaching droplets does not exist when $G_{\text{approach}} < G_c \equiv -\delta^2/256 < 0$. As the droplets approach each other, G is negative and increases in magnitude as D_c decreases, up to a point where the quasi-steady approach branch ceases to exist, which is identified to the droplet's velocity reversal and rebound dynamics. This event is associated with a critical center-to-center distance $\tilde{D}_c/\epsilon = \tilde{d}_c$ which provides an estimate for the rebound distance d_{min} and satisfies

$$\left(\tilde{D}_c\delta/4\right)^2 = 4\left(1 + \tilde{D}_c\delta/4\right)e^{-\tilde{D}_c\delta/4} \tag{3.51}$$

and

$$\tilde{d}_c \approx \frac{5.98}{\mathrm{Pe}-4}. \tag{3.52}$$

Estimation of the droplet rebound distance (3.52) reproduces the scaling obtained from the numerical simulations (section 3.6). This asymptotic estimate d_c of the rebound distance differs however slightly from the value estimated form the numerical results in Fig. 3.14. Such discrepancy is to be expected, since in numerical simulations rearrangement of the concentration field in the course of the rebound is not immediate, and in fact even in the quasi-steady framework presented here, $|v| = v_0/2 \neq 0$ when the approaching branch ceases to exist (Fig. 3.17). Instead, droplets take some time to slow down. This regime of transitory approach is beyond reach of the asymptotic analysis and, thus, the real rebound distance is shorter, compared to the theoretical prediction, Eq. (3.52).

The analysis presented here is focused on the case of two symmetric droplets. Yet, as emphasised throughout the analysis the coupling between the droplets is purely chemical. Indeed, the flow field contribution is limited to the near-field dynamics of the flow field and does not influence the far-field signature (only the displacement of the droplet does). This further validates that, near the self-propulsion threshold, hydrodynamic interactions play a subdominant role. While chemical interactions are mediated through chemical gradients which decay as $1/d^2$, direct hydrodynamic interactions (i.e. the drift of a droplet in the flow field of the second one) would be dominated by the stresslet flow created by each droplet, which also decays as $1/d^2$. However, the intensity of the stresslet itself is weak for $\mathrm{Pe} \approx \mathrm{Pe}_c$, namely scaling as ϵ^2 [101], so that hydrodynamic interactions are $O(\epsilon^4)$ in contrast with $O(\epsilon^2)$ chemical interactions. As a consequence, the present asymptotic analysis applies exactly to the case of a droplet collision with a no-slip wall.

Finally, we note that the present approach and bifurcation diagram in Eq. (3.49) applies to any active droplet exposed to a concentration field, c_e, that allows for an expansion in powers of ϵ as shown in Eqs. (3.45)–(3.46). The physical meaning of this mathematical requirement is twofold: (i) the evolution of c_e must be slow, that is, in the lab frame c_e should satisfy the steady diffusion equation up to $O(\epsilon^3)$,

$$\nabla^2 c_e = O(\epsilon^3), \tag{3.53}$$

and (ii) the gradient of c_e must be weak, namely, c_e may only contribute to $N_i^{(2)}$, that is,

$$\boldsymbol{\nabla} c_e = O(\epsilon^2). \tag{3.54}$$

Any c_e that satisfies these requirements, Eqs. (3.53)-(3.54), may be seamlessly included in the superposition in Eq. (3.44) and subsequently expanded in powers of ϵ to obtain the corresponding value of G for the bifurcation diagram (3.49).

3.8 Effective model of the collision dynamics

The results of § 3.5 emphasised the complexity of the interaction of the droplet with the confining wall (or with a second droplet) and the diversity of detailed behaviour when varying Pe. These results provide significant insight into such interactions and collisions that we may wish to implement in the modelling of more complex systems where full treatment of the coupled chemical and hydrodynamic problems is not achievable anymore. This includes, for example, the dynamics of a large number of droplets as observed experimentally, where the dynamics of each droplet can be seen as the succession of self-propelling stages (i.e. isolated dynamics) and collisions with neighbours and/or boundaries.

The purpose of the present section is therefore to provide a global effective characterisation of the rebound. The results of § 3.5 show that each collision is not simply the sequence of a self-propulsion with $\boldsymbol{v} = -v_0\boldsymbol{e}_z$ toward the wall followed by a propulsion one at $\boldsymbol{v} = v_0\boldsymbol{e}_z$ away from it. Indeed, the droplet may experience gradual slowdowns or a velocity plateau and may rebound at a different distance $d_{\min}$ depending on the exact ratio of diffusion and advection of the solute as quantified by Pe. However, the initial and final stages of the sequence are always the same, namely propulsion with velocity $\pm v_0\boldsymbol{e}_z$, so that the main quantity of interest when looking at the long-term dynamics is the total duration of the collision, or equivalently the excess time taken in comparison with an elastic shock (i.e. where a droplet would self-propel constantly at $\pm v_0\boldsymbol{e}_z$ and rebound on the wall).

We attempt to characterise here this quantity, and therefore the collision, using the following protocol: considering a (large) reference distance d_m away from the wall, we measure the corresponding time Δt needed for an active droplet to travel from $d = d_m$ towards the wall, rebound and come back at the same location. This lapse of time is then compared to $2d_m/v_0$, which is the time taken by a particle moving at the constant velocity $-v_0\boldsymbol{e}_z$ and experiencing a rigid collision *on the wall* before returning to its original position with constant velocity $V_0\boldsymbol{e}_z$. Their difference is the delay introduced by the full hydro-chemical dynamics with respect to a simple elastic shock, and we thus define the *relative excess collision time* as

$$T = \frac{V_0\Delta t - 2d_m}{R}. \tag{3.55}$$

The variations of $T(\mathrm{Pe})$ are shown on Fig. 3.18(a). First, one should observe that, within the range of Pe explored here, the relative collision time, T, is positive, meaning that the collision of a self-propelled droplet takes always more time than the rigid particle collision. This is a result of two competing effects, the rebound of the droplet at a finite distance away from the wall (i.e. it actually travels a distance shorter than $2d_m$) and its slowed-down dynamics in the vicinity of the wall, and $T > 0$ suggests that the latter is dominant. Secondly, two different regimes can be identified: for moderate Pe and up to $\mathrm{Pe} \approx 12$ the relative collision time T evolves concavely whereas it is mostly linear for higher Pe.

A better understanding of the origin of these two regimes stems from two main phenomena that cause an increase of Δt (and T) with Pe. As Pe increases away from Pe_c, the rebound distance $d_{\min}$ decreases and the droplet travels a longer distance before coming back. A particle propelling at velocity $\pm v_0$ and bouncing back at a distance $d_{\min}$ from the wall would take a time $2(d_m - d_{\min})/v_0$ before returning to its initial position, and the corresponding relative excess collision time would be $-2d_{\min}/R$. The asymptotic linear dependence between T and $d_{\min}$, observed in Fig. 3.18(b), therefore suggests that the increase in relative collision time T for the active droplet is caused by the change of $d_{\min}$ with Pe. This argument only explains the increase with Pe rather than the absolute variations:

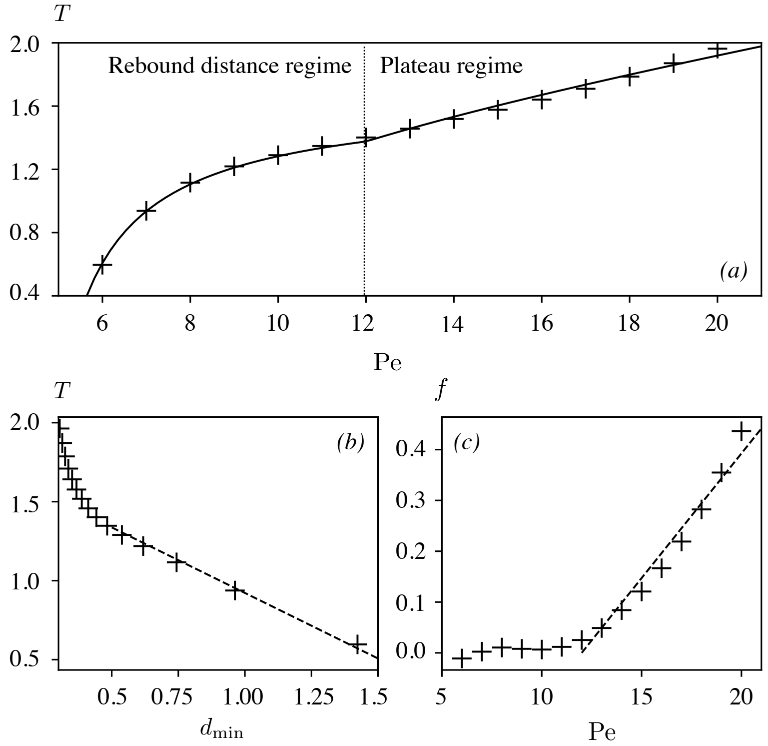

Figure 3.18: Time needed for the droplet to travel from a distance $d = d_m$ from the wall and coming back after collision at the same distance. (a): Ratio of the time travel Δt to the time $2d_m/v_0$ corresponding to the time taken by a particle travelling at velocity v_0 from $d = d_m$ to the same point after a rigid collision with the wall. (b): Extra time taken by the droplet compared to the rigid collision case as function of the rebound distance $d_{\min}$. (c): f evolution as function of Pe.

indeed, the droplet's velocity magnitude is smaller than v_0 for a significant part of the sequence so that $T > 0$ while $T < 0$ for the particle rigid collision at $d_{\min}$. Nevertheless, these observations suggest variations of T for moderate Pe of the form:

$$T = \frac{\Delta t v_0 - 2d_m}{R} = K_1 + K_2 d_{\mathrm{rb}}, \tag{3.56}$$

Using a Gauss-Newton method, the best least-square fit for K_1 and K_2 is obtained as $K_1 = 1.75$ and $K_2 = -0.83$.

Fig. 3.12 shows that the decrease of $d_{\min}$ is less pronounced for higher Pe, which suggests that a second phenomenon is responsible for the increase in relative collision time T at higher Pe. As emphasised in section 3.5, a distinctive feature of the larger Pe collisions is the development of a velocity plateau during which the droplet maintains a rather constant velocity smaller than v_0 after rebounding on the wall. This plateau is Pe-dependent and Fig. 3.18(c) shows the evolution of the function f defined by the difference at larger Pe between the actual value of T and its prediction of Eq. (3.56):

$$f = T - K_1 - K_2 \frac{d_{\min}}{R}. \tag{3.57}$$

Fig. 3.18(c) shows that f is reasonably well approximated by a linear function of Pe, so that a global effective model for the relative collision time is obtained as:

$$T = \frac{\Delta t v_0 - 2d_m}{R} = \; = \; K_1 + K_2 \frac{d_{\min}(\mathrm{Pe})}{R} + K_3, \max(0, \mathrm{Pe} - 12), \tag{3.58}$$

where the coefficient $K_3 = 0.05$ is fitted through Gauss-Newton non-linear regression method. Obtaining an effective model finally requires an expression of $d_{\min}$ as a function of Pe. Inspired by the asymptotic approach of section 3.7, a simple model is chosen of the form:

$$d_{\min}(\mathrm{Pe}) \;=\; \frac{K_4}{\mathrm{Pe} - 4} + \frac{K_5}{\sqrt{\mathrm{Pe} - 4}}, \tag{3.59}$$

with fitted constants $K_4 = 1.89$ and $K_5 = 0.61$ determined from the data of Fig. 3.12.

The resulting effective model for the excess relative collision time T is shown on Fig. 3.18(a) as a solid black line, and appears to provide a reasonable estimate of the collision time T for the range of Pe investigated here (i.e. Pe $\in [6\,,\,20]$). It includes the two main physical features of the collision dynamics for varying Pe, namely the change in rebound distance and the existence of a velocity plateau.

3.9 Conclusion

The present chapter provides a unique insight into the interaction and rebound dynamics of a chemically-active droplet with a rigid confining wall (as well as the related problem of the symmetric collision of two such droplets). In contrast with most existing studies that rely on some assumptions regarding either the simplified solute transport or the relative distance to the wall, the unsteady dynamics of the solute concentration and its coupling to the hydrodynamic here are fully resolved here for any relative distance. This provides a quantitative analysis of the detailed solute transport around the droplet during its rebound.

In particular, we show that for moderate Pe, namely the ratio of convective and diffusive solute transport, the rebound dynamics is well-captured by neglecting the hydrodynamic effect of the wall and can be understood as the slowdown, reversal and re-acceleration of the droplet in an adverse chemical gradient whose magnitude increases as the relative distance is decreased. In contrast, when advection becomes more dominant, the complex hydrodynamic flow around the confined droplet imposes a reorganisation of the chemical field that profoundly alters its swimming and rebound dynamics, with a significant reduction in the minimum distance to the wall and the emergence of a velocity plateau after the rebound, during which the droplet maintains a reduced and somewhat constant velocity before accelerating again to its nominal value as it escapes the region of influence of the wall. This phenomenon can be related to the self-sustained gradients in surface solute concentration by the Marangoni flows they generate, even when the droplet is forced to slow down and stop by the hydrodynamic effect of the wall.

To retain the relative simplicity of an axisymmetric problem, the configuration considered here is highly symmetric as only the normal approach of a single droplet to a flat wall is considered. Yet, this provides an important physical insight into the interaction and rebound dynamics, which could contribute significantly to a better understanding of experimental studies involving confined active droplets: several recent contributions have indeed suggested that the collective behaviour of many self-propelled droplets is greatly influenced by the role of confinement on their interactions [64, 62]. The present analysis also provides a critically-valuable benchmark analysis for the validation of simpler models (e.g. relying on far-field approximations or simplified interactions) that could be used for more complex problems (non-normal rebound or interactions of many droplets).

In the vicinity of the self-propulsion threshold, $\mathrm{Pe} \sim \mathrm{Pe}_c$, weakly-nonlinear theory of the droplet-droplet interaction confirms that the flow field created around a given droplet by the presence of the wall or another droplet is negligible and that the coupling is purely chemical (§ 3.7). Thereby, it rigorously establishes that the symmetric collision of two droplets and the rebound on a rigid wall or free-surface are equivalent at leading order in that limit. The slowdown, and eventual rebound dynamics, are then interpreted in the framework of imperfect transcritical bifurcations as the disappearing of one of the stable solution branches, corresponding to the propulsion of the droplet against a steepening chemical gradient (Fig. 3.17). Such an event occurs for distances that scale as $d \sim 1/(\mathrm{Pe} - \mathrm{Pe}_c)$, which is validated against the numerical solution of the full problem (Fig. 3.14). We further demonstrate that due to the purely chemical nature of weak droplet-droplet interactions, this framework and the resulting bifurcation diagram, Fig. 3.17, applies to any active droplet exposed to an externally-imposed spatially-evolving solute concentration $c_e(\mathrm{r})$, provided the variations of c_e are slow enough on the scale of the droplet, Eqs. (3.53)–(3.54). As such, the conclusions of the weakly-nonlinear analysis capture a universal feature of active droplet dynamics.

From a more technical point of view, the numerical approach followed here provides a novel framework for the simulation and spectral analysis of time-dependent problems in a bi-spherical geometry. At each instant, a coordinate system is used that fits the natural boundaries of the problem which is particularly well-suited for time-dependent multi-physics problems where two different dynamics are coupled on the moving boundary (here the hydrodynamic flow field and the solute concentration). In this chapter, we use this framework to analyse two geometrically-simple problems (i.e. a single droplet and a flat wall or two identical droplets), yet, it can be straightforwardly used to treat more complex situations such as the rebound on a curved wall or droplets of different sizes (see chapter 4). In particular, phoretic particles are known to exhibit non-reciprocal interactions [103, 111, 99] which stem from the coupling of two distinct physicochemical properties (activity and mobility) to generate self-propulsion and that can result in complex dynamics when coupling particles of different nature or sizes. A similar property can thus be expected for active droplets since their self-propulsion also rely on this activity-mobility combination.

While bi-spherical coordinates system have been already used in the past to solve diffusion or viscous flow problems, it was always limited to quasi-steady problems where Laplace or Stokes equations are solved independently at each instant [77, 102, 103, 112]. In contrast here, the advection-diffusion dynamics requires accounting for the non-trivial evolution of the grid. This is particularly useful for active droplets whose underlying physics critically relies on the non-linearity introduced by the advection-diffusion of the solute. Yet, it may also prove particularly useful to analyse a variety of other time-dependent problems such as the unsteady mass transfer and viscous growth/dissolution of gas bubbles (e.g. near catalytic surfaces or during boiling), or the collective dynamics of such bubbles or droplets [113].

Take home message of Chapter 3

1. Numerical approach using moving bi-spherical coordinates: Using a spectral decomposition method based on moving bi-spherical coordinates, we are able to compute the exact hydro-chemical interactions involved in the frontal collision of an active droplet against a rigid wall (as well as symmetric head-on collisions of two active droplets).

2. Interactions at moderate Péclet: The presence of a rigid wall in the path of an active droplet has two main consequences: (i) it increases the drag force experienced by the droplet and (ii) it increases the solute concentration in the confined area. As a result, the droplet slows down and eventually rebounds. At moderate Pe, we find that hydrodynamic interactions are subdominant. It is worth to recall that in this situation, the droplet's velocity can be reasonably approximated by using the polarity relation $\boldsymbol{v} = \mathbf{\Pi}$.

3. Interactions at higher Péclet: At higher Pe, advection flows transport more solute at the back of the droplet and thus decrease the solute concentration at its front. Therefore, in comparison to the moderate Pe case, an active droplet must go closer to the wall in order to rebound. Unlike the case at moderate Pe, both chemical and hydrodynamic interactions are significant. In particular, the solute wake at the back of an active droplet takes some time to diffuse and slows down the droplet in the second half of its rebound.

4

Size sensitivity in the collision of active droplets

Chemically-active droplets exhibit complex avoiding trajectories. While heterogeneity is inevitable in active matter experiments, it is mostly overlooked in their modelling. In this chapter, exploiting its geometric simplicity, we fully-resolve the head-on collision of two swimming droplets of different radii and demonstrate that even a small contrast in size critically conditions their collision and subsequent dynamics. We identify three fundamentally different regimes. The resulting high sensitivity of pairwise collisions is expected to affect their collective dynamics profoundly. The results of this chapter were published in Physical Review Fluids [114]

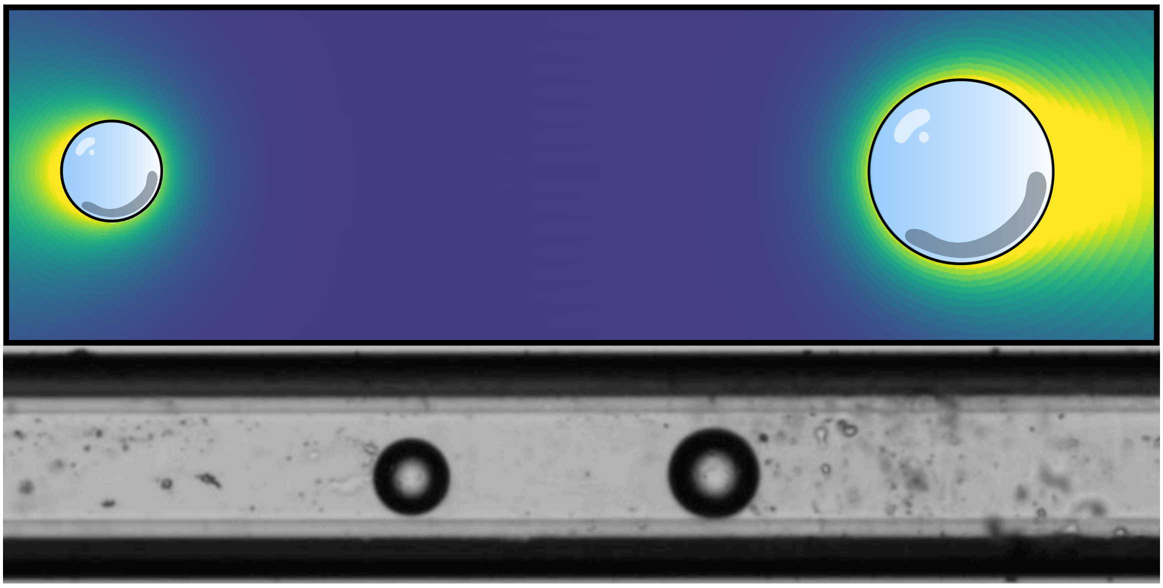

A collision of active droplets of different sizes. Top: concentration field resulting from the head-on collision of two active droplets obtained from bi-spherical simulations [114]. Bottom: picture of the collision of active droplets in a microfluidic capillary drawn from the experimental results of Charlotte de Blois during her PhD at Gulliver under the supervision of Olivier Dauchot and Mathilde Reyssat.

Contents

4.1 Experimental motivations

In chapter 1, we introduced active droplets that swim as a result of a solubilisation process. Recent studies then reported that due to micellar interactions at their surface, such active droplets would shrink and slow down over time [36, 57, 38, 37]. Fig. 4.1 reports the evolution of the velocities and radii of several active droplets drawn from Ref. [36]. In particular, the panel (*b*) of Fig. 4.1 informs that the shrinking rate might be different between two droplets. Therefore, even if two active droplets are initially identical, they might not be after a while. As a consequence, in experiments involving several active droplets: either in a circular arena [36], a Hele-shaw cell [37, 62, 115] or a large reservoir [64], we then expect interactions between active droplets of distinct sizes to occur. Hence we may thus wonder if a size difference between two active droplets has any influence on their interaction.

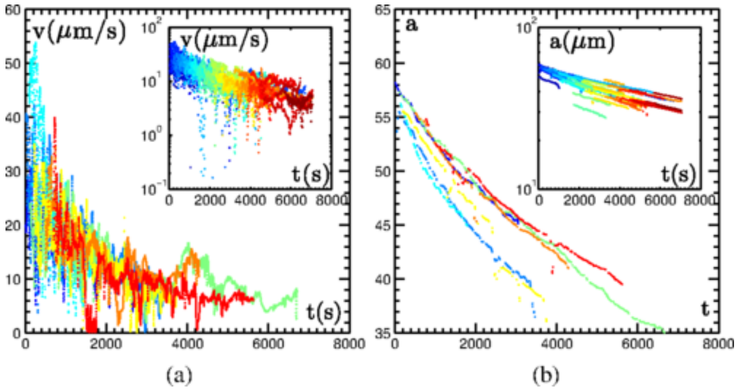

(a) (b)

Figure 4.1: Size and velocity evolution for a pure water droplets (*a*) Velocity and (*b*) diameter versus time for a selection of eight trajectories. Insets: Linear-log plot for a selection of 35 trajectory parts. Both panels are drawn from Ref. [36].

Besides, we may also consider the one-dimensional collective behaviour already mentioned in section 1.6 as an additional motivation to study size heterogeneity in active droplets. Indeed, Ref. [63] reported spontaneous formations of lines of droplets that swim in the same direction and at a fix separation distance from each other (called *trains* by the authors, see Fig. 4.2). At the origin of such a collective dynamics, the results of Ref. [63] suggest that the velocity difference between two colliding droplets is essential to notice a chasing state between the droplets. Keeping in mind that droplets of distinct sizes also have distinct velocities, it appears then natural to study the interactions between active droplets of various radii.

Adopting a more theoretical point of view, we remind that interactions between active systems of distinct sizes may result in complex behaviours. Indeed, even in the purely diffusive situation (Pe = 0), where the solute transport equation is linear, the results of Ref. [103] show non-trivial dynamics of two rigidly-bound active particles of different sizes. In particular, the considered active dumbbell self-propels in a direction that depends on the separation distance between the particles. We may then wonder about the resulting outcome following a collision between two self-propelled active droplets of distinct sizes, whose propulsion and interactions depend on a non-linear solute transport dynamics.

Inspired by the theoretical and experimental motivations described above, we focus on the interactions between two active droplets of different sizes. In particular, we study how the results of the head-on collisions presented in chapter 3 are affected by a difference in size.

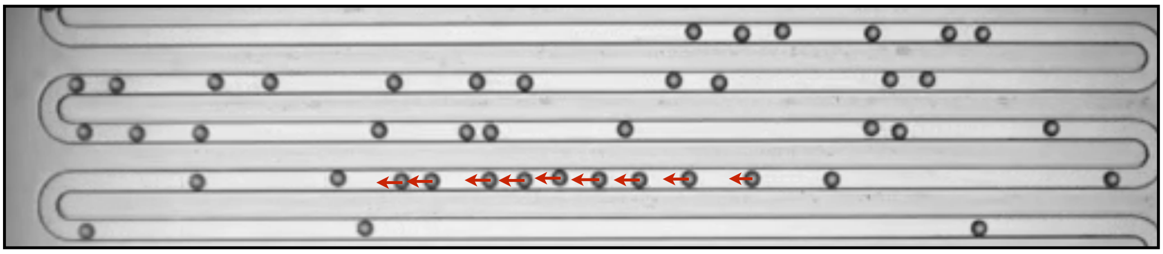

Figure 4.2: One-dimensional collective dynamics of swimming active droplets in a microfluidic serpentine from Ref. [63]. The red arrows illustrate the droplets' direction of motion.

4.2 Mathematical modelling of the collision

We consider the axisymmetric dynamics of two droplets of fixed radii R_1 and R_2, and of identical chemical properties and separated by a distance d (Fig. 4.3). We name droplet 1 (resp. droplet 2) the large droplet (resp. the small droplet) and thus impose that $R_1 \geq R_2$. Since droplets of distinct sizes are involved, a choice should be made regarding the characteristic quantities of the problem. First let us remind the characteristic drift velocity of a droplet of radius R_i in an externally-imposed gradient $\mathcal{A}/D$ [48]: $V_i^* = \mathcal{A}\gamma_1 R_i/[D(2\eta^{(o)} + 3\eta^{(i)})]$ (see section 1.5). Without loss of generality we consider R_2, V_2^* and $\mathcal{A}R_2/D$ as reference length, velocity and concentration respectively. Besides, the viscosity ratio $\tilde{\eta} = \eta^{(i)}/\eta^{(o)}$ is again set to unity for simplicity. The problem is fully-determined by two independent non-dimensional parameters, namely the specific Péclet number $\mathrm{Pe}_i = R_i V_i^*/D$ of each droplet in addition to their size ratio $\xi = R_1/R_2 = \sqrt{\mathrm{Pe}_1/\mathrm{Pe}_2} \geq 1$.

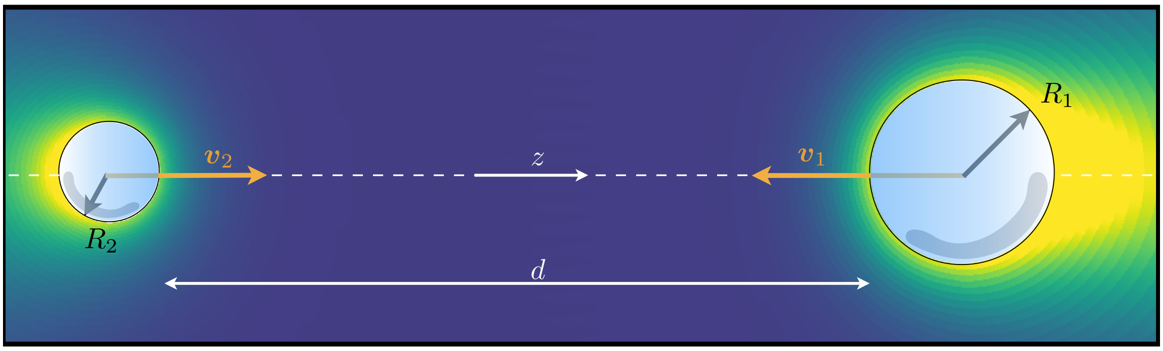

Figure 4.3: Collision of two chemically-active self-propelled droplets. The colour shades show typical solute concentration distributions around the moving droplets.

The Péclet number plays a key role for an individual droplet's dynamics, and we remind that for $\mathrm{Pe}_i \geq \mathrm{Pe}_c = 4$, a droplet of radius R_i starts swimming spontaneously as a result of a transcritical bifurcation [36, 101]. Above this threshold, the active droplets i self-propels at a velocity $v_0(\mathrm{Pe}_i)$ in units of V_i^*, where the evolution of v_0 is reported on Fig. 2.2. The previous choice regarding the characteristic quantities of the problem implies that the speed of each droplet is expressed in units of V_2^*. As a result, the self-propulsion velocity of droplet 1 (resp. of droplet 2) in units of V_2^* follows $v_{0,1} = v_0(\mathrm{Pe}_1)V_1^*/V_2^* = \xi v_0(\mathrm{Pe}_1)$ (resp. $v_{0,2} = v_0(\mathrm{Pe}_2)$). Firstly because Pe_1 evolves quadratically with ξ and also because of the factor ξ in the expression of $v_{0,1}$, we realise that droplet 1 and droplet 2 do not have identical self-propulsion velocities in units of V_2^*. For that reason, we find useful to provide on Fig. 4.4 the evolution of the self-propulsion velocity $v_{0,1}$ in units of V_2^* as function of Pe_2 and the size ratio ξ.

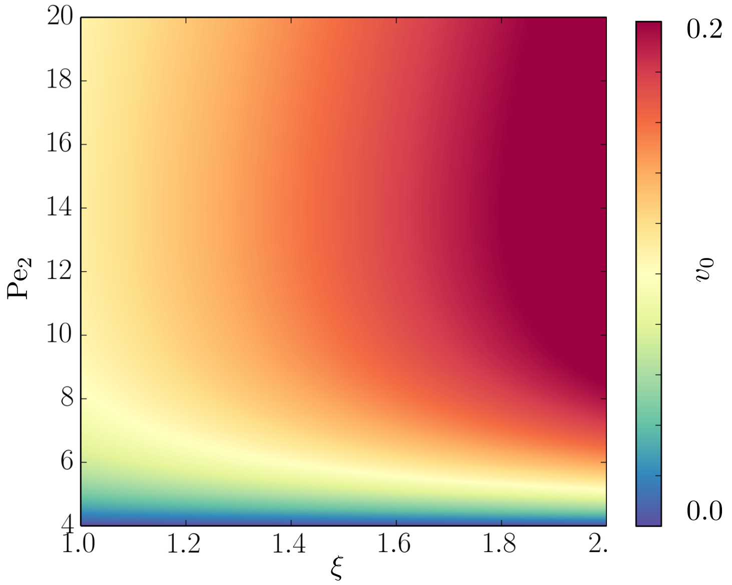

Figure 4.4: Self-propulsion velocity magnitude $v_{0,1}$ of droplet 1 (in units of V_2^*) as function of the size ratio ξ and Pe_2

4.2.1 Chemical problem

Using the previously introduced characteristic quantities, the resulting dimensionless concentration field c satisfies the following advection-diffusion problem in the outer phase:

$$\mathrm{Pe}_2\left(\frac{\partial c}{\partial t} + \boldsymbol{u}^{(o)}\cdot\boldsymbol{\nabla} c\right) = \nabla^2 c, \qquad \boldsymbol{\nabla} c|_{\mathcal{S}_i}\cdot\boldsymbol{n} = -1, \qquad c|_{\boldsymbol{r}\to\infty} = 0, \tag{4.1}$$

where $\mathcal{S}_i$ denotes the surface of droplet i and $\boldsymbol{u}^{(o)}$ denotes the outer Eulerian velocity field.

4.2.2 Hydrodynamic problem

Due to the microscopic droplet's size inertial effects are negligible and the velocity of the fluid is found by solving Stokes' equations in each phase, coupled through the Marangoni and continuity conditions (4.3) and (4.4):

$$\boldsymbol{\nabla}^2\boldsymbol{u}^{(i,o)} = \boldsymbol{\nabla} p^{(i,o)}, \qquad \boldsymbol{\nabla}\cdot\boldsymbol{u}^{(i,o)} = 0, \tag{4.2}$$

$$(\boldsymbol{I}-\boldsymbol{nn})\cdot(\boldsymbol{\sigma}^{(o)} - \tilde{\eta}\boldsymbol{\sigma}^{(i)})\Big|_{\mathcal{S}_i}\cdot\boldsymbol{n} = -(\boldsymbol{I}-\boldsymbol{nn})\cdot(2+3\tilde{\eta})\,\boldsymbol{\nabla} c|_{\mathcal{S}_i}, \tag{4.3}$$

$$\boldsymbol{u}^{(o)}\Big|_{\mathcal{S}_i} = \boldsymbol{u}^{(i)}\Big|_{\mathcal{S}_i}, \qquad \boldsymbol{u}^{(o)}\Big|_{r\to\infty} = \boldsymbol{0}, \qquad \left(\boldsymbol{u}^{(o)}\cdot\boldsymbol{n}\right)\Big|_{\mathcal{S}_i} = \boldsymbol{v}_i\cdot\boldsymbol{n}. \tag{4.4}$$

Finally, the droplets being force-free, Eq. (2.6) is satisfied at each droplet's surface, which enables to determine the droplets' velocities v_1 and v_2 through the relation:

$$\begin{bmatrix} v_1 \\ v_2 \end{bmatrix} = -\boldsymbol{R}_d^{-1}\cdot\begin{bmatrix} F_m^1 \\ F_m^2 \end{bmatrix}, \tag{4.5}$$

where $\boldsymbol{R}_d$ is the resistance matrix known from Ref. [77] and F_m^i the Marangoni forces applied on droplet i, measured positively along the axis of symmetry z. The Marangoni forces F_m^i are computed in the same way as in chapter 3, in evaluating the hydrodynamic forces experienced by each droplet that comes only from the solute distribution around its surface. The full nonlinear coupling of the Stokes and chemical transport problems is solved semi-analytically for arbitrary distance using the efficient scheme based on a time-dependent bi-spherical grid presented in detail in chapter 3.

4.2.3 Three identified regimes

To identify the effect of the size ratio, ξ, the results are reported in the following chapter in terms of $\xi \geq 1$ and of the Péclet number of droplet 2, $\mathrm{Pe}_2 \geq 4$, for the time-dependent dynamics of two droplets initially located far apart ($d \gg 1$) and swimming towards each other ($v_2 > 0$ and $v_1 < 0$).

Depending on the value of (ξ, Pe_2), three different collision regimes are observed and reported in the phase diagram of Fig. 4.5. First, a *rebound regime* (blue square) is observed for droplets of almost the same size ($\xi \approx 1$), which self-propel in opposed direction after the collision. Secondly, a *chasing regime* (green triangle) arises at moderate Pe and above a critical size ratio (which depends on Pe), for which droplet 1 swims behind droplet 2 and in the same direction. Finally, a *pausing regime* at higher Pe and above a critical size ratio (that depends also on Pe) is observed, for which droplet 1 is stopped after the collision with droplet 2 and remains at the same location for a long time (in comparison to the time scales involved in the collision dynamics). Each regime is analysed in details in the following sections.

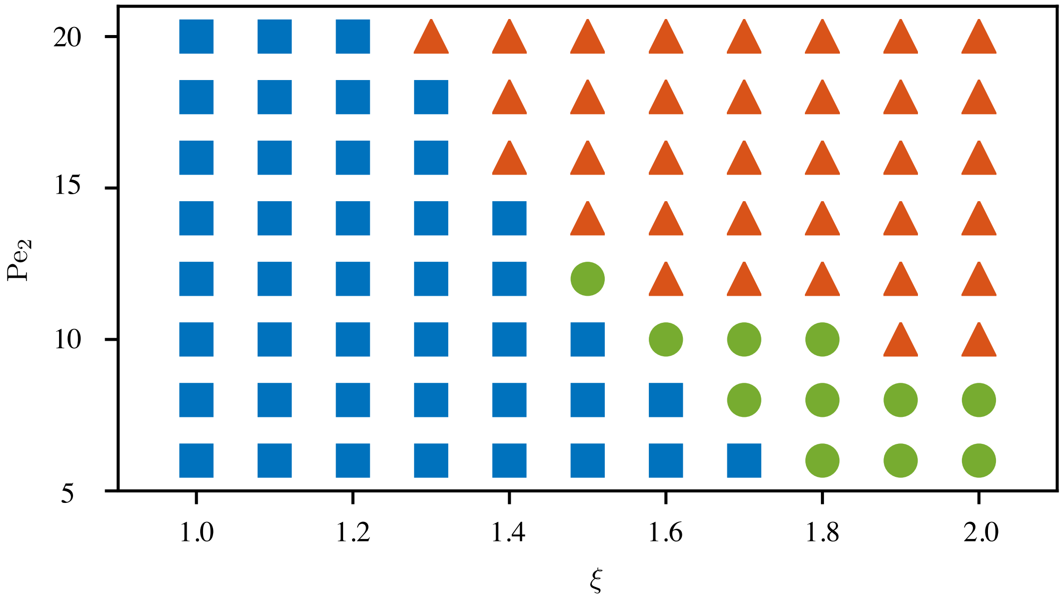

Figure 4.5: Regime selection for the axisymmetric dynamic collision of two droplets for varying (ξ, Pe_2): rebound (blue squares), chasing (green disks) and pausing regimes (red triangles).

4.3 Rebound regime

Regardless of the advection-to-diffusion ratio associated to the small droplet, Pe_2, and for sufficiently small contrast in size ($\xi - 1 \ll 1$), the collision always lead to a reversal of the swimming direction of both droplets (Fig. 4.5, blue).

The general dynamics associated with this regime is similar to that identified for symmetric collisions of chapter 3: at sufficiently large distances, both droplets swim at their self-propulsion velocities and the flow field around each one has a dipolar structure, as depicted on the panel A of Fig. 4.6. As the droplets get closer, the solute accumulates between them, reducing the polarity of their surface concentration and effectively acting as a chemical repulsion.

It should be however noted that the variations of each droplet's axial velocity are not symmetric with respect to the collision. Specifically, the droplets temporarily swim away more slowly than in their approach phase. This effect is even more pronounced for droplet 1. The delayed dynamic reversal of the concentration asymmetry is likely explained by a slower diffusion ($\mathrm{Pe}_1 \geq \mathrm{Pe}_2$) as it is the case in chapter 3 regarding symmetric collisions at high Pe. Such a "chemical inertia" regarding droplet 1 indeed results from the presence of two concentration spots: (*i*) the one at the back of droplet 1 coming from its former wake which takes time to diffuse, and (*ii*) the one at its front, carried by droplet 2. Such spots generate a quadrupolar flow field in the vicinity of droplet 1, as shown on the panels B and C of Fig. 4.6.

After a sufficient time, both droplets recover their self-propelling state and swim away from each other (panel C of Fig. 4.6). In addition, the minimal separation distance reached by the droplets decreases with Pe_2, a tendency consistent with the results obtained in chapter 3 for symmetric rebounds.

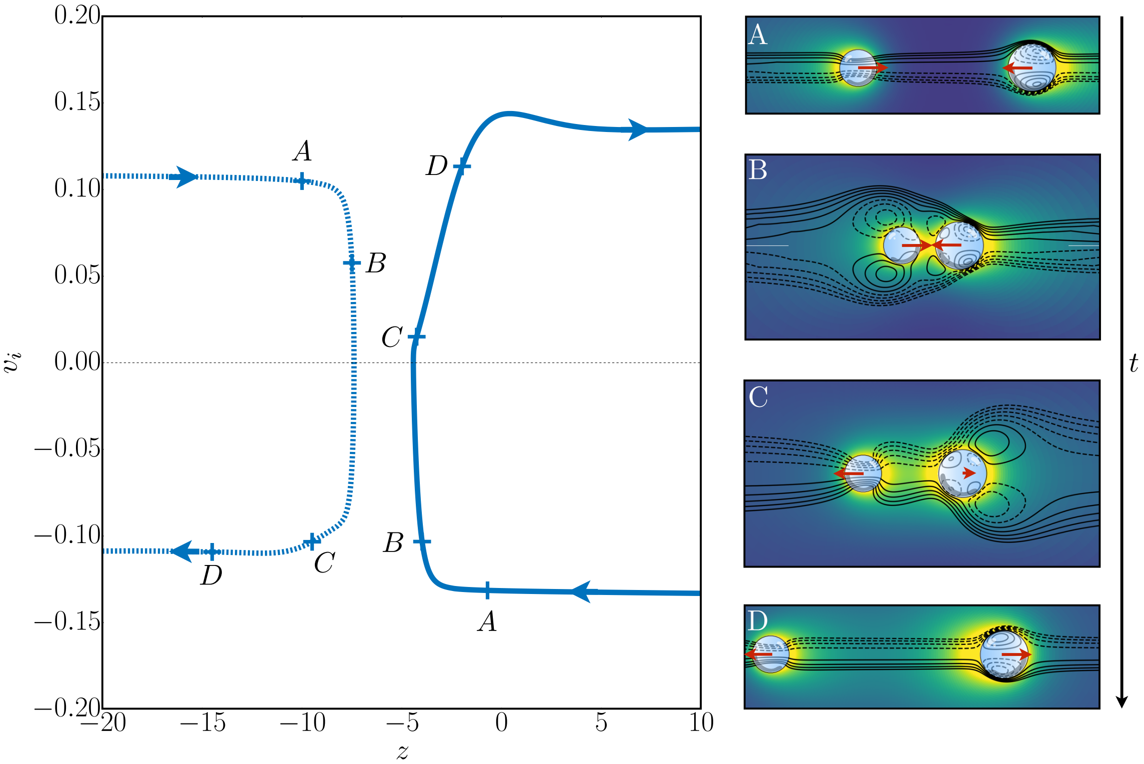

Figure 4.6: Rebound regime dynamics. Left panel reports the v_1 (solid blue) and v_2 (dashed blue) velocities as function of the position of each droplets on the z axis. Right panel shows snap-shots of the concentration field and streamlines in the frame of reference of droplet 1 at different instants along the collision: A long before the collision, B just before the collision, C just after the collision and D long after the collision.

4.4 Chasing regime

For moderate Pe_2 and larger size ratio ξ, a chasing regime is observed rather than an asymmetric collision one. While droplet 2 still experiences a similar repulsion and rebound dynamics, the effective repulsion it exerts on droplet 1 is not sufficient to reverse its swimming direction (Fig. 4.7, green solid line). As droplet 2 swims away, the polarity of droplet 1 still allows it to accelerate and recover its original direction, effectively chasing droplet 2. Because the absolute self-propulsion velocity increases with the droplet's size, droplet 1 is able to catch up and a bound state arises, where the two droplets maintain a fixed distance d_{eq} and swim together. Their velocity results from the balance of their self-propulsion and mutual chemical repulsion.

For a given Pe_2, the rebound to chasing transition illustrated in Fig. 4.8 depends on the detailed dynamics of the collision and occurs above a precise value $\xi_c(\mathrm{Pe}_2)$. Since the Péclet number associated to droplet 1 increases with ξ ($\mathrm{Pe}_1 = \xi^2\mathrm{Pe}_2$), the wake of the larger droplet is more persistent, and as a result the same is true for its chemical polarity and self-propulsion. In addition, the small droplet faces an even bigger gradient. The former reduces the effective interaction time with the smaller droplet which is quickly repelled away, while the latter increases the larger droplet's resistance to the chemical perturbations undergone during the collision.

The conditions of the emergence of a stationary chasing regime is further analysed here. In this bound state, both droplets have the same swimming velocity $v_{0,2} < v_b < v_{0,1}$ with

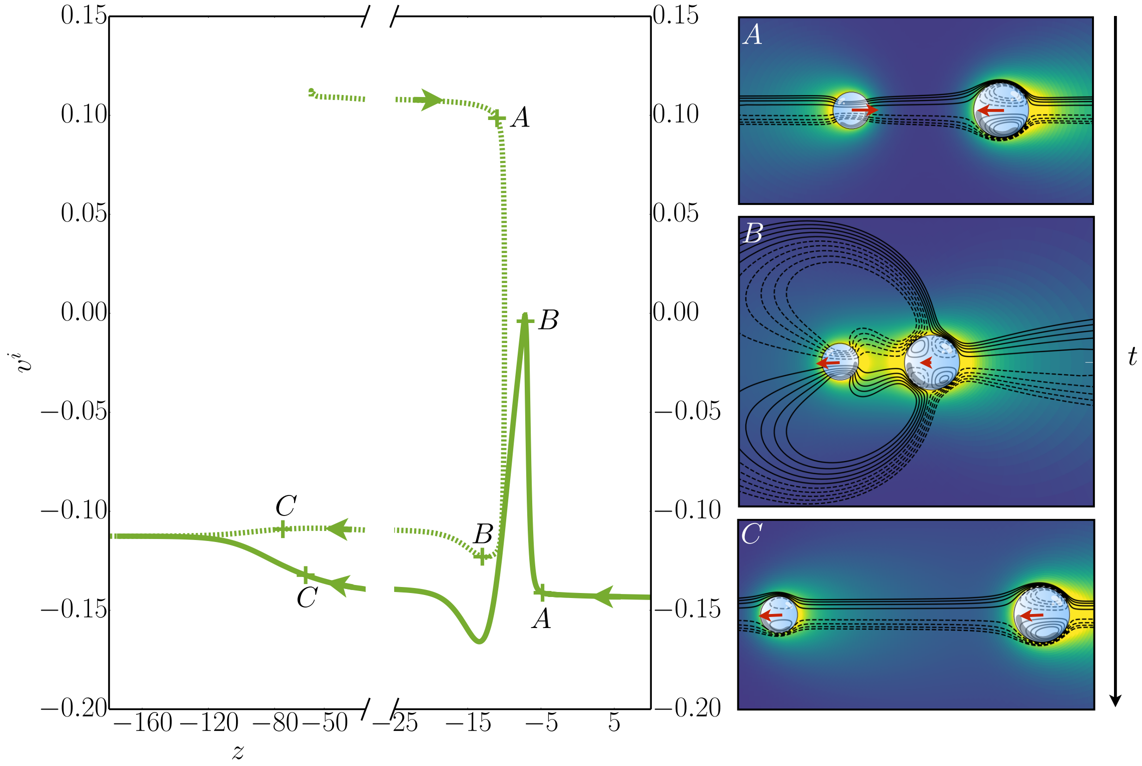

Figure 4.7: Chasing regime dynamics. Left panel reports the v_1 (solid green) and v_2 (dashed green) velocities as function of the position of each droplets on the z axis. Right panel shows snap-shots of the concentration field and streamlines in the frame of reference of droplet 1 at different instants along the collision

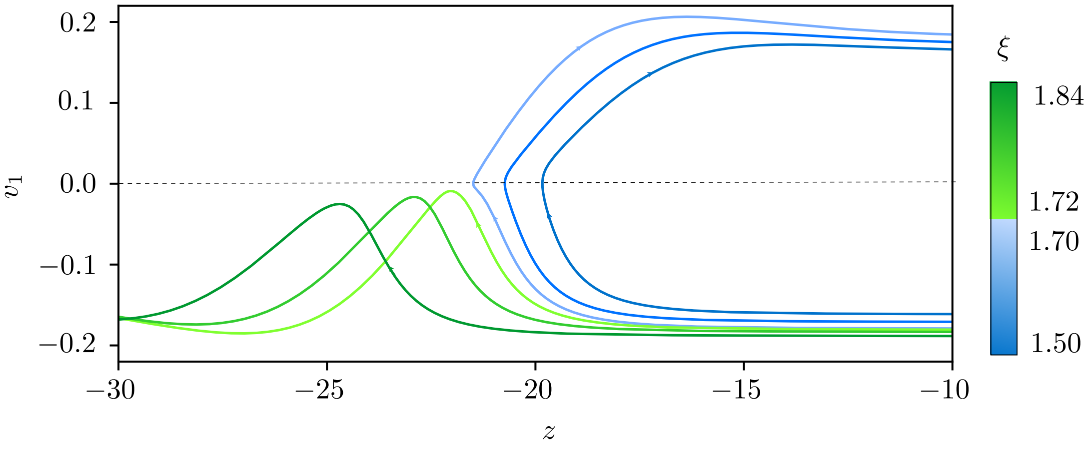

Figure 4.8: Rebound-to-chasing transition: influence of the size ratio ξ on the evolution of the larger droplet velocity, v_1, parameterized by the droplet position.

$v_{0,i}$ the steady velocity of each droplet when isolated. First the smaller droplet is pushed forward by the increase in solute concentration in its wake due to the presence of the larger droplet. Meanwhile, the larger droplet is slowed down by the adverse chemical gradient created by the wake of the smaller one at its front. Increasing the distance between the droplets reduces both effects leading to the larger droplet swimming faster than, and chasing, the smaller droplet. Conversely, a decrease in d induces larger chemical repulsions and thus the acceleration (resp. deceleration) of the smaller (resp. larger) droplet. This provides the physical ingredients to understand the existence of a stable equilibrium distance d_{eq} whose evolution with ξ for fixed Pe_2 is shown on Fig. 4.10.

Following the asymptotic approach of chapter 3, these arguments can be formulated quantitatively in the asymptotic limit of small supercriticality, i.e. when $\Delta\text{Pe}_i = \text{Pe}_i - \text{Pe}_c$ is small for $i = 1, 2$ (which imposes $\xi - 1 \ll 1$). The velocity of droplet i is then obtained at leading order as a function of the leading chemical gradient generated by droplet j,

$$|v_i| = \frac{v_{0,i}}{2}\left(1 + \sqrt{1 + \text{sgn}(v_i)\frac{256 G_{j\to i}}{(\Delta\text{Pe}_i)^2 d^2}}\right), \tag{4.6}$$

where $v_{0,i} = \Delta\text{Pe}_i/16$ denotes the reference velocity of each droplet for small ΔPe_i and small $\xi - 1$ [101]. In Eq. (4.6), $G_{j\to i}$ is proportional to the chemical repulsion exerted by droplet j on droplet i (which satisfies either Eq. (4.7) or Eq. (4.8) depending on the droplet one is looking at) and may either slow down or speed up the motion of droplet i depending on the relative signs of v_i and $G_{j\to i}$. Its exact expression depends on the swimming direction of j, as the decay of concentration in the vicinity of the droplet j is either exponential, in front of the it, or algebraic, behind it:

$$G_{1\to 2} = \begin{cases} -1 & \text{if } v_1 > 0, \quad \text{(see Fig. 4.9}c\text{)}, \\ -e^{-4d|v_1|}(1 + 4d|v_1|) & \text{if } v_1 < 0 \quad \text{(see Fig. 4.9}a - b\text{)}, \end{cases} \tag{4.7}$$

$$G_{2\to 1} = \begin{cases} 1 & \text{if } v_2 < 0, \quad \text{(see Fig. 4.9}b - c\text{)}, \\ e^{-4d|v_2|}(1 + 4d|v_2|) & \text{if } v_2 > 0, \quad \text{(see Fig. 4.9}a\text{)}. \end{cases} \tag{4.8}$$

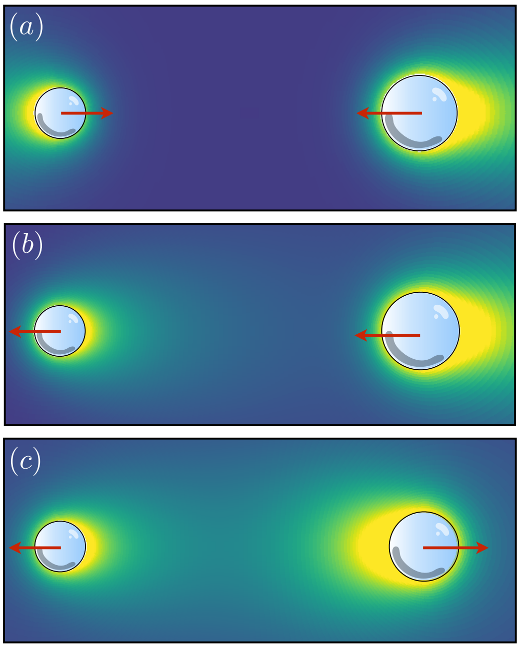

Figure 4.9: Three possible configurations for the active droplet's pair. (a): Droplets swimming towards each other, both exerting a chemical repulsion that decays exponentially with the distance. (b): Droplets chasing each other, with the small droplet feeling an exponentially decaying repulsion coming from the bigger one, while its wake exerts an algebraic repulsion on it. (c): Droplets swimming away from each other and exerting a chemical repulsion forces that decay algebraically with the distance.

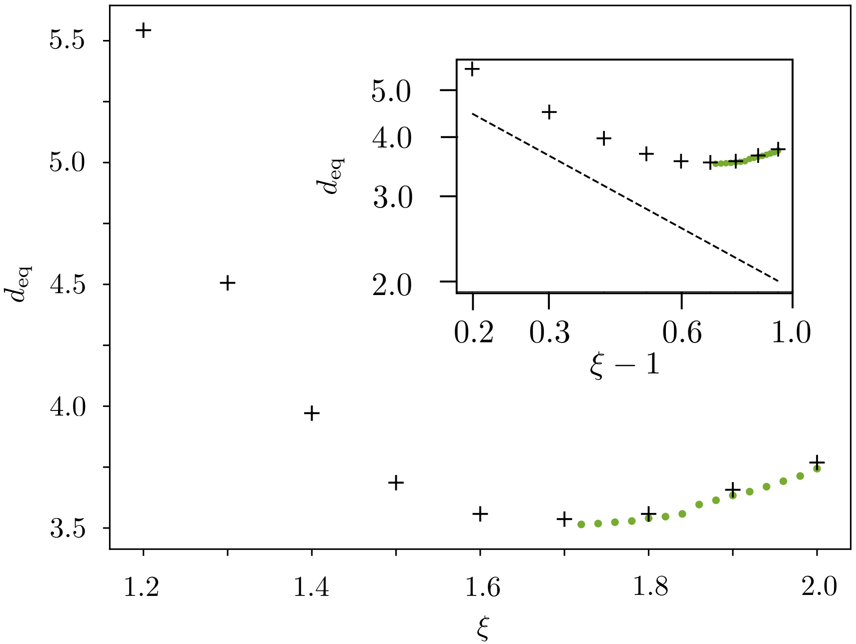

Figure 4.10: Evolution with the size ratio ξ of the equilibrium distance d_{eq} between the droplets in the bound state for $\text{Pe}_2 = 6$. The inset is in log-log scale. Results are obtained from the time-dependent dynamics of two droplets initially swimming in the same direction (black crosses) or towards each other (green dots).

Using these results and considering the situation where the leading droplet is the smaller one and $\xi - 1 \ll 1$, the leading order value of the equilibrium distance d_{eq} for which $v_1 = v_2 < 0$ is obtained as (see Appendix A.6 for more details):

$$d_{\text{eq}} = \frac{2\sqrt{2}}{\sqrt{(\xi - 1)(\text{Pe}_2 - 4)}}. \tag{4.9}$$

This result quantifies the physical divergence of d_{eq} when both droplets have the same size or swim near the critical threshold: in both cases, the swimming velocities are small so that their difference can only be compensated by a weak chemical repulsion (or large inter-droplet distance). The results of the full model, Fig. 4.10, show a good agreement with the $(\xi - 1)^{-1/2}$ scaling despite the large value of ΔPe_2, which is the most likely origin of any difference in prefactor. It should be further noted from Fig. 4.10 that d_{eq} presents a minimum for intermediate ξ, which is consistent with its divergence for small ξ.

For very large ξ, the influence of the chemical repulsion on the velocity of the larger droplet is negligeable and the whole assembly swims at a velocity $v_1^\infty \gg v_2^\infty$ which scales in non-dimensional units as ξ. For the smaller droplet, this must now be the magnitude of the gradient of concentration experienced from its larger neighbour, which scales as ξ^2/d^2 so that $d_{\text{eq}} \sim \xi^{1/2}$.

Fig. 4.10 in fact reports two sets of results for the long-time dynamics of two droplets that are initially swimming in the same direction (black crosses) or towards each other (green dots). While the bound states emerging from this chasing regime exist for any ξ, they can not follow a collision when ξ is too small ($\xi \leq 1.7$ when $\text{Pe}_2 = 6$). The exact history of the droplets' motion therefore appears critical in setting their long-term dynamics, thus underlining the nonlinearity and complexity of the transition to such bound states.

To conclude this section, we provide some pictures drawn from unpublished experiments carried out by Charlotte De Blois during her PhD at the Gulliver's lab under the supervision of Olivier Dauchot and Mathilde Reyssat for illustrative purpose only. Fig. 4.11 shows two active droplets made of water which swim inside a microfluidic capillary full of oil and surfactants. Both droplets initially swim in opposed directions, and while a rebound occurs when the droplets are almost the same size ($\xi \approx 1.05$), we notice that a sufficient increase of the size ratio ($\xi \approx 1.1$) leads to a situation where the bigger droplet chases the smaller one.

If we are tempted to compare directly the theoretical approach introduced above with the results of the experiments, several remarks deserve to be made. First, the very confined geometry of the experimental set up differs with the system considered in the theoretical approach in two important ways: (*i*) we expect hydrodynamic interactions to play a significant role, even regarding the dynamics of a single droplet; (*ii*) the lateral sides of the capillary prevent the solute (i.e swollen micelles in this particular case) to diffuse freely unlike the unbounded case of the theoretical model. As a direct consequence of the latter, we expect the droplets to be even more slowed down right after a rebound since the diffusion of their wake is limited by the lateral sides of the capillary.

Nevertheless, the situation where a large droplet chases a smaller one implies that the large droplet must have overcome the chemical repulsion from the smaller one. This phenomenon is similar in the theoretical model. In conclusion, even if we do not expect either the critical size ratio at the transition or the equilibrium distance value d_{eq} to match exactly between such experiments and the theoretical results of this chapter, they are a good illustration of a rebound to chasing transition caused by a sufficiently high size ratio difference.

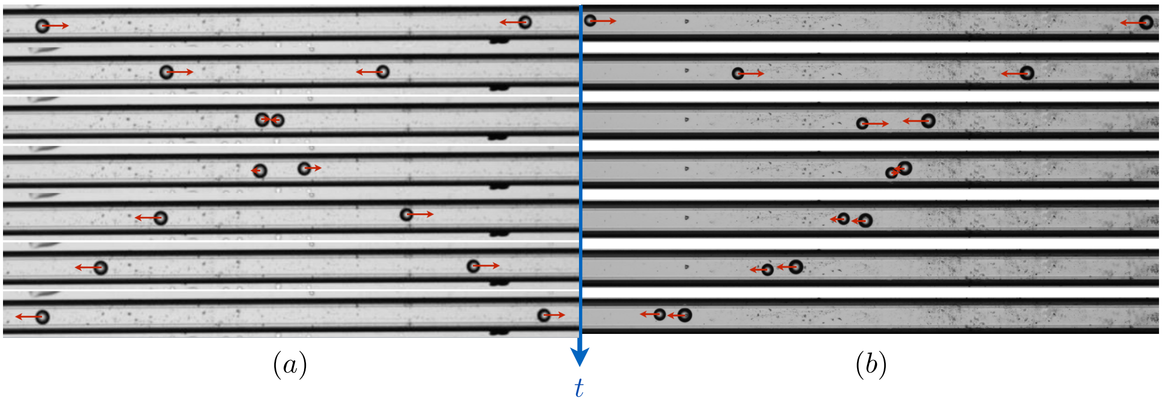

Figure 4.11: Collisions of two active droplets of distinct sizes in a microfluidic capillary. (*a*): $R_1 = 94\mu\text{m}$, $R_2 = 89\mu\text{m}$ ($\xi = 1.05$), (*b*): $R_1 = 103\mu\text{m}$, $R_2 = 93\mu\text{m}$ ($\xi = 1.1$). The pictures are drawn from unpublished experimental results of Charlotte de Blois during her PhD at Gulliver under the supervision of Olivier Dauchot and Mathilde Reyssat.

4.5 Pausing regime

For larger Pe_2, and even for relatively small contrasts in size, a rather surprising regime arises. Indeed, droplet 1 is slowed down by the excess concentration generated by the approach with droplet 2. Very much like for the other regimes, droplet 2 quickly reverses direction and propels away from the collision site. However, the chemical repulsion experienced by droplet 1 during this brief encounter is neither sufficiently large nor long to reverse its chemical polarity and provoke its rebound. Instead, some solute accumulates at its front, resulting in a symmetric but non-uniform surface concentration, driving pusher-like Marangoni flows from the equatorial plane towards its poles. Such quadrupolar flow is able to balance diffusion and maintain this stationary regime where the droplet acts as a symmetric pump (see Fig. 4.12).

This quadrupolar structure cannot avoid reminding the situation encountered in the recent experimental results of Ref. [58], which reveal that higher modes of the hydrodynamic field emerge spontaneously at sufficiently high Pe even regarding the dynamics of a single droplet in the bulk. Besides, the specific Péclet number of droplet 1 in this regime, $\mathrm{Pe}_1 = \xi^2 \mathrm{Pe}_2$, is greater than the critical instability threshold of the quadrupolar mode for a non-deformable active droplet computed in Refs. [101, 49]. The emergence of the pausing regime can therefore be interpreted as the non-linear transition between two solution branches of the single droplet dynamics, in response to the finite perturbation induced by the collision.

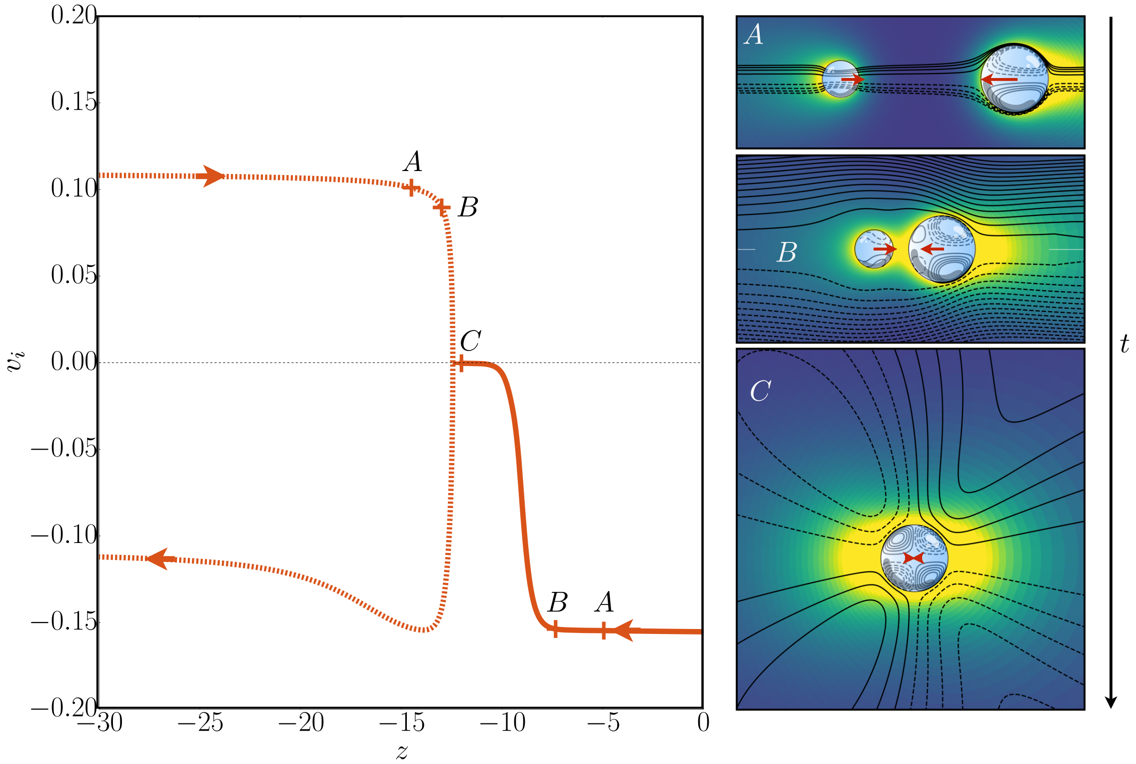

Figure 4.12: Pausing regime dynamics. Left panel reports the v_1 (solid orange) and v_2 (dashed orange) velocities as function of the position of each droplets on the z axis. Right panel shows snap-shots of the concentration field and streamlines in the frame of reference of droplet 1 at different instants along the collision.

The stability analysis of this pumping state lies beyond the scope of this chapter and is left for future research. Yet, regardless of the detailed stability properties, the dominance of the dipolar propelling mode in the dynamics of a single non-deformable droplet [66, 101, 116], suggests that sufficiently large perturbations of the concentration or flow fields (e.g. by another droplet) would likely provoke a new mode switching and self-propulsion of the larger droplet. This may however occur long after the first collision so that memory of the initial propulsion direction will be lost, reminiscent of the run-and-tumble motion of swimming bacteria [117, 118]. This is in stark contrast with the bouncing and chasing regimes, which do preserve the collision's directionality. Such memory loss is expected to significantly affect the collective long-term dynamics of droplets, by introducing an effective rotational diffusion. If such reorientation phenomenon is already noticed both in experiment [37, 58] and theory [60] in the case of a single droplet at sufficiently high Pe, it may thus arise at more reasonable ones in the case of an assembly of active droplets.

4.6 Conclusion

In summary, this chapter has shown how variability in the size of active droplets profoundly affects their collision dynamics. Although not considered here explicitly, variability in chemical properties likely has a similar effect, since regime selection results mainly from the droplet's chemical signature intensity and specific Péclet number. Once again, the strength of the advective coupling is a key factor: for moderate advection, the dynamics are only weakly modified by the symmetric collision, and large size contrast is required for more complex regimes. However, for large advective effects, non-symmetric bouncing, chasing or scattering may develop, even for droplets of comparable sizes, stressing the extreme sensitivity of the interaction.

If this chapter aims to provide the reader with three possible dynamics that may arise after a perfect head-on collision of two active droplets, it would be insightful to broach the issue of oblique collisions. Indeed, the main limitation of the current approach lies in the imposed axial-symmetry, which prevents the droplets to leave the z axis. On the contrary, the experiments show that active droplets do not swim in a perfect straight line, even at small Pe when their behaviour is still ballistic [58, 119, 57]. Therefore, there is only a small chance that perfect head-on collisions occur in experiments. For that reason, the issue of oblique collisions together with the influence of the droplets' wake in the interaction are tackled in the following chapter.

Take home message of Chapter 4

1. Rebound regime: A head-on collision between two active droplets always lead to a rebound for sufficiently small size contrasts ξ. While the smaller droplet promptly reverses its direction, the larger one takes more time to recover its self-propulsion velocity in the opposite direction.

2. Chasing regime: For a given Pe, there is a critical size ratio ξ_c, above which the bigger droplet keeps its initial swimming direction and chases the smaller one. After a time, the droplets reach an equilibrium state where they are separated by a fixed distance and swim at the same velocity.

3. Pausing regime: At high Pe, a pausing regime can arise as the result of a collision between two active droplets of different radii. In this regime, the larger droplet is trapped by a symmetric but non uniform solute distribution on its surface. As a result, it is immobile and behaves as an active pump by generating a quadrupolar flow field.

5

Oblique collisions of active droplets

In this chapter, we aim to extent the framework of the two previous ones by studying more generic collisions of two co-planar active droplets. The first goal of this study is to quantify the influence of the relative initial angle on the collision dynamics. Besides, recent experiments reported the significant influence of the solute trace left by active droplets on their swimming dynamics. For that reason, in this chapter, we also study asymmetric initial conditions and the resulting wake influence on the collision dynamics. The results of this chapter are currently in review.

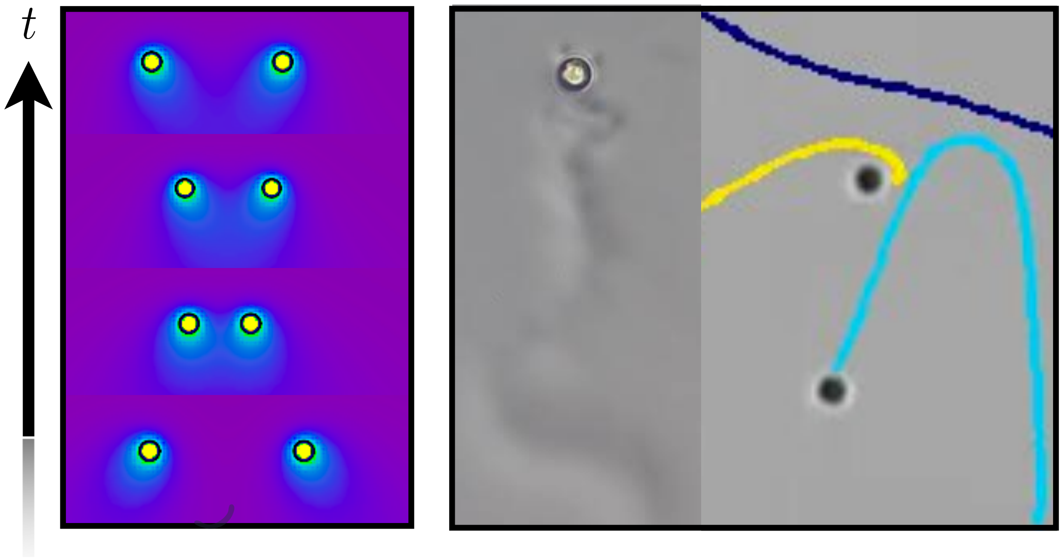

Left panel: concentration field snapshots along the oblique collision of two active droplets (numerics). Right panel: phase contrast microscopy picture from Ref. [120] of a droplet swimmer that leaves a trail on its path (left part). Picture of three droplet swimmers from Ref. [120] being repelled from each other's trails (trajectories represented by solid color lines)

Contents

5.1 Motivations to study oblique collisions of active droplets

We have learnt from chapter 1 that active droplets do not swim in a perfect straight line even at low Pe where they still exhibit a ballistic regime [58]. As a consequence, if the exact results of chapters 3 and 4 provide a better understanding of the complex hydro-chemical interactions between two active droplets that collide frontally, they have only little chance to occur in experiments. For that reason, in this chapter we open the question of oblique collisions between two self-propelled droplets.

Let us first consider the experiments of Ref. [56], which provide interesting results regarding the oblique collision of two active droplets of radius $R \approx 20\mu$m and velocity $V \approx 30\mu$m/s. The Péclet number in this experiment may then be estimated to Pe ~ 6 when estimating the diffusivity $D \approx 10^{-10}$ for typical surfactant molecules. As expected, the chemical repulsion felt by each droplet leads to a rebound. Nevertheless, a further look on the trajectories depicted on the panel (*a*) of Fig. 5.1 enables us to realise that the collision is not symmetric but one droplet appears ahead of a distance $\ell \approx 6$ radii. If the solute transport at finite Pe is expected to play a role on the collision dynamics, we may also wonder about the effect of a collision asymmetry.

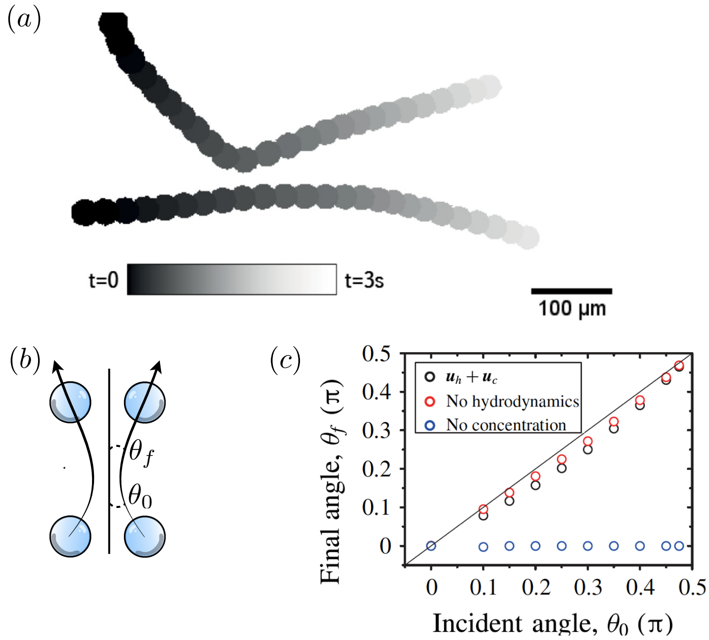

Figure 5.1: (*a*): Two oil droplets swimming in given initial directions repel one another as a result of their concentration gradients. Circles map their trajectories over time. Figure taken from Ref. [56]. (*b*): Schematic representing of a symmetric collision between two active droplets with θ_0 (resp. θ_f) the initial (resp. final) collision angle. (*c*): evolution taken from Ref. [87] of the final collision angle (θ_f) as function of the initial one (θ_0), without the hydrodynamic interaction (red), without the concentration-mediated interaction (blue) and with both contribution (black).

A first attempt to characterise oblique collision dynamics between two active droplets is provided in Ref. [87], in the particular case of far-field interactions, where both hydrodynamic and chemical problems may be decoupled. Such a decoupling between the solute dynamics and the flow field enables to study each of their contribution in the collision separately. Besides, the droplets are considered to be slightly above the instability threshold, so that (*i*) their velocities are very small and (*ii*) the concentration field around each of them is almost isotropic. Denoting by θ_0 (resp. θ_f) the initial (resp. final) collision angle (see the panel (*b*) of Fig. 5.1), Ref. [87] provides the evolution of θ_f as function of θ_0 in the particular case of symmetric collisions (see the panel (*c*) of Fig. 5.1). This results in a perfect alignment of the droplets when only hydrodynamics interactions are considered, while a rebound with a weak alignment is noticed in the situation with chemical interactions only. Finally, summing both contributions only slightly modify the results from the case of purely chemical interactions and always lead to a rebound, which tends to slightly align the droplets ($\theta_0 - \theta_f \approx 10°$ for $\theta_0 \approx 45°$). However, in the experiments presented in Ref. [56], the velocity of each droplet is not negligible and we expect the concentration field around each droplet to be anisotropic. Since the solute distribution around each droplet significantly influence the chemical interactions (see chapter 3), we may thus wonder about the outcome of two self-propelling active droplets that collide each other at a finite speed.

Finally, active droplets are known to modify the physico-chemical properties of the medium on their path and recent experiments have highlighted such a “pollution” may influence the motion of other droplets [120, 121]. The trajectories of active droplets depicted on Fig. 5.2 show how active droplets may be deviated or even experience a rebound from the presence of the solute trace left by another active droplet [120]. As a result, not only the collision angle but also the wake relaxation is expected to have direct consequences in the collision dynamics.

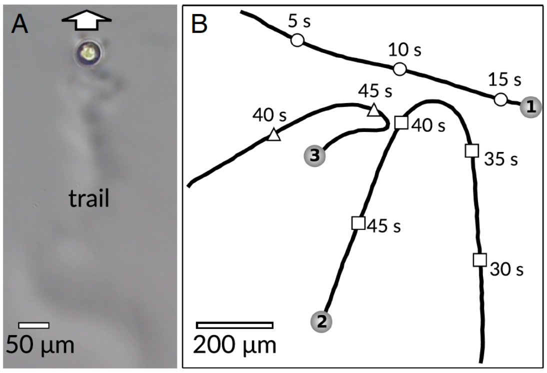

Figure 5.2: (A) A droplet swimmer leaves a trail that can be seen under phase-contrast microscopy from the slightly different refractive index from Ref. [120]. (B) Free swimmers avoiding each other’s trails from Ref. [120]. Sphere drawings (to scale) mark the trajectory end points, timing marks on trajectories time points in the experiment.

Adapting the bi-spherical framework developed in chapter 3 to deal with generic collisions is expected to be quite a feat since it would require the use of the full bi-spherical coordinates system (see the section conclusion and perspectives in chapter 6). In this chapter, inspired by the model of Ref. [82] and Ref. [87], we instead suggest an approximate model for self-propelled active droplets. Such a model enables us to investigate generic collisions (in the plane) while still providing a reasonable head-on collision dynamics when compared to the exact results of chapter 3. First, we will introduce the physical framework and adopted numerical method. In a second part we will present the results obtained for oblique symmetric collisions. Finally we will focus on asymmetric collisions, for which one of the droplets is initially delayed.

5.2 Modelling droplet collisions

In the following, the physical properties of the droplets are not different from the previous chapters but we place ourselves in the case of droplets of the same radius R. We remind that both droplets emit a chemical solute of diffusivity D with a constant total flux $4\pi R^2 D\mathcal{A} > 0$. The solute of concentration C interacts with the droplets' surface so that surface chemical gradients induce local Marangoni stresses, $\boldsymbol{\nabla}_{\|}\gamma = \gamma_1 \boldsymbol{\nabla}_{\|} c$ where γ_1 is a positive constant [89, 101, 36]. Keeping the same notations as in the previous chapters, we choose R, $C^* = \mathcal{A}R/D$ and $V^* = \mathcal{A}R\gamma_1/(D(2\eta^{(o)} + 3\eta^{(i)}))$ as characteristic length, concentration and velocity scales.

5.2.1 Interactions of swimming droplets

As seen in the previous chapters, droplets influence each other both hydrodynamically and chemically by emitting solute and driving a fluid flow. Yet, the complete modelling of two-droplet head-on collisions of chapter 3 demonstrated that the hydrodynamic interactions only have a subdominant contribution to the collision dynamics, at least for moderate Pe, providing quantitative arguments for the simplified model detailed below, where direct hydrodynamic coupling between droplets is neglected. It can however be noted that nonlinear convective solute transport around each droplet, and the emergence of a chemical wake, are the essence of the self-propulsion mechanism, and should necessarily be retained at the individual droplet level, in particular their positive feedback on the polarity of the concentration distribution around the droplet.

As a consequence, using the Lorentz Reciprocal Theorem for Stokes flow (see section 2.1.3), the dimensionless swimming velocity of each isolated droplet $\boldsymbol{v}_i$ can be obtained from the mean Marangoni stress at its surface or equivalently the chemical polarity of its surface $\mathcal{S}_i$ equation (2.40) reminded here for convenience:

$$\boldsymbol{v}_i = -\frac{1}{2\pi}\int_{\mathcal{S}_i} c\boldsymbol{n}\,\mathrm{d}\mathcal{S} = \boldsymbol{\Pi}_i, \tag{5.1}$$

where c denotes the dimensionless concentration field and $\boldsymbol{n}$ the outward-pointing normal on the surface $\mathcal{S}_i$.

5.2.2 Moving singularity model

The *moving singularity model* introduced in this section approximates the effect of each droplet on the concentration distribution by a moving singularity. The chemical transport dynamics is therefore governed by an unsteady diffusion equation:

$$\mathrm{Pe}\frac{\partial c(\boldsymbol{r},t)}{\partial t} = \nabla^2 c(\boldsymbol{r},t) + 4\pi\sum_{i=1}^{N}\left(\mathbf{I} + \zeta(v_i)\boldsymbol{v}_i\cdot\boldsymbol{\nabla}\right)\delta(\boldsymbol{r}-\boldsymbol{x}_i(t)), \tag{5.2}$$

where $\boldsymbol{x}_i(t)$ denotes the instantaneous position of droplet i, whose velocity $\dot{\boldsymbol{x}}_i = \boldsymbol{v}_i$ is obtained from Eq. (5.1), thus accounting indirectly for the interfacial stress balance and the nonzero size of the droplet.

The advantage of this formulation is to retain the effect of the droplet motion on the polarity of the distribution (a chemical "wake" can form behind the moving point source) while allowing for linear superposition (since equation Eq. (5.2) is linear) of the chemical fields created by each droplet independently. Each droplet is represented as (i) a moving source of known intensity (i.e. total activity) and (ii) a moving source dipole oriented along the swimming direction, that accounts empirically for the convective transport associated with near-field flows around each moving droplet. The intensity of the moving source dipole, $\zeta(v)$, depends on the velocity magnitude, and is set so that the present moving singularity model applied to a single isolated droplet matches the exact result obtained from the full advection-diffusion problem for all Pe [36].

It can be noted that Eqs. (5.1) and (5.2) are linear so that the concentration field is the superposition of the concentration emitted by each droplet independently, $c = \sum_j c_j$ where c_j is the solution of Eq. (5.2) forced by droplet j only. As a result, the velocity $\boldsymbol{v}_j$ of droplet j is obtained from Eq. (5.1) as the superposition of the contributions of:

1. the polarity at its surface $\mathcal{S}_j$ of its own concentration footprint, i.e. the asymmetry of its “wake”, $\boldsymbol{\Pi}_j = -(1/2\pi)\int_{\mathcal{S}_j} c_j \boldsymbol{n} \mathrm{d}S$,
2. the polarity at its surface $\mathcal{S}_j$ of the concentration emitted by other droplets, $-(1/2\pi)\int_{\mathcal{S}_j} c_k \boldsymbol{n} \mathrm{d}\mathcal{S}$ with $k \neq j$.

In the case of a single isolated droplet in steady self-propulsion with velocity $\boldsymbol{v}$, the dimensionless concentration field writes:

$$\begin{aligned} c &= (\mathbf{I} + \zeta(v)\boldsymbol{v}\cdot\boldsymbol{\nabla})\cdot\left\{\frac{1}{r}\exp\left[-\mathrm{Pe}\frac{(vr+\boldsymbol{v}\cdot\boldsymbol{r})}{2}\right]\right\} \\ &= \frac{1}{r}\left[1-\zeta(v)\left(\frac{\boldsymbol{v}\cdot\boldsymbol{r}}{r^2}+\mathrm{Pe}\frac{v(vr+\boldsymbol{v}\cdot\boldsymbol{r})}{2r}\right)\right]\exp\left[-\mathrm{Pe}\frac{(vr+\boldsymbol{v}\cdot\boldsymbol{r})}{2}\right], \end{aligned} \tag{5.3}$$

where $\boldsymbol{r}$ is the radial vector taken from the droplet's center. Using this result of Eq. (5.1), and defining $\lambda = v\mathrm{Pe}/2$, provides the dipole intensity ζ uniquely in terms of the exact result for the non-dimensional velocity $v_0(\mathrm{Pe})$ [36]:

$$\zeta(\lambda) = \frac{\mathrm{Pe}}{2}\left[\frac{\lambda^2 e^{\lambda} v_0/2 - \lambda\cosh\lambda + \sinh\lambda}{2\sinh\lambda - (2\lambda + 2\lambda^2 + \lambda^3)e^{-\lambda}}\right]. \tag{5.4}$$

It can be noted that in its non-dimensional form and for a fixed viscosity ratio (which will affect $v_0(\lambda)$), the dipole intensity only depends on λ. In the following, $\eta^{(i)} = \eta^{(o)}$ is assumed.

Eq. (5.1), Eq. (5.2) and Eq. (5.4) together with the definition of the droplets' velocity $\dot{\boldsymbol{x}}_i = \boldsymbol{v}_i$ provide a closed set of equations for the droplets' dynamics and concentration distribution. These equations are solved spectrally (see Appendix B.2). In the following, we apply this moving singularity model to analyse collision dynamics of $N = 2$ droplets. Initially, the droplets are located at a dimensionless center-to-center distance d_c that is large enough that they essentially behave as isolated and have a steady self-propulsion velocity of magnitude $v_0(\mathrm{Pe})$. After the encounter with the second droplet, each droplet recovers a steady self-propulsion regime albeit with a modified orientation. Note that the model proposed here is fully three-dimensional. Yet, motivated in part by the quasi-2D motion of active droplets in experiments, we restrict our discussion of the collision problem to planar trajectories of both droplets (the chemical dynamics remains however three-dimensional).

5.3 Validation of the numerics

Here we provide several tests aiming to check the validity and relevance of the numerical model introduced in the last section. First, in order to verify the implementation of the solute diffusive dynamics, we compare the concentration field generated by a single fixed source of solute with analytical computations. The obtained results provided in Appendix B.3 confirm the good numerical solving of Eq. (5.2). Secondly, aiming to check the expression of the dipole intensity provided by Eq. (5.4) as well as its implementation in the code, we have confronted the self-propulsion dynamics of a single active droplets for various Pe obtained by the moving singularity model with the exact dynamics given in chapter 3 (see Appendix B.3). As expected by the choice of the dipole intensity, the self-propulsion velocities in the steady state provide a good match with the analytical ones. The slight difference is a direct consequence of the finite resolution in the code, which provides solutions at a reasonable numerical cost. Besides, considering the significant modelling simplification in comparison to the approach suggested in chapter 3, the transitory regime in the self-propulsion obtained using this reduced model appears reasonably close to the exact ones.

Furthermore, aiming to assess the relevance of the moving singularity model, we focus on the axisymmetric collision of two active droplets, for which the exact dynamics have been solved completely for various Pe in chapter 3. Active swimming droplets are anti-chemotactic, and thus swim away from the zones of higher concentration, e.g. their own wake or the proximity with other emitting droplets [36, 119, 120]. In a head-on collision, the droplets thus slow down and stop at a minimum distance d_{min} from each other. The confinement-induced accumulation of the emitted solute between the droplets reverses the chemical polarity of the droplets which start swimming in the opposite direction and rebound. This dynamics is clearly visible in the evolution of the droplets' axial velocity with their relative distance (see Fig. 5.3), and the moving singularity model provides a good approximation of the exact rebound dynamics provided by the chapter 3. The rebound distance d_{min} is slightly underestimated in the moving singularity model, which is consistent with the modelling of the droplet as point singularities for the chemical field which reduces the confinement-induced accumulation of solute between the droplets.

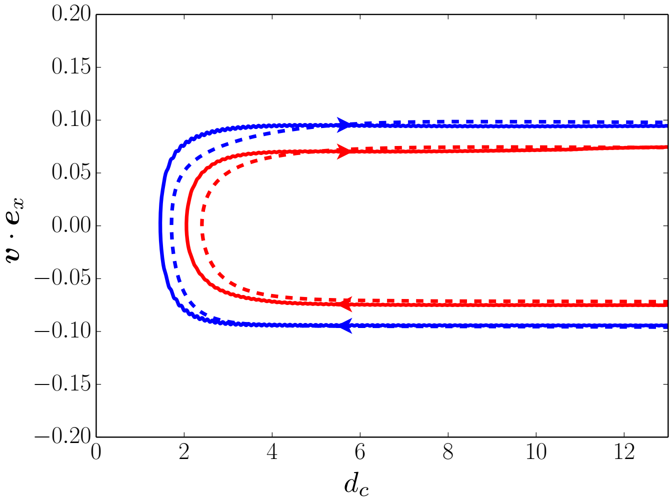

Figure 5.3: Droplet axial velocity in an axisymmetric head-on collision with a second identical droplet for Pe=6 (red) and Pe = 8 (blue) as obtained using the moving singularity model, Eqs. (5.1)–(5.2) (solid) and the exact result [89] (dashed).

Finally, the Fourier spectral method used to solve the droplets' dynamics (see Appendix B.3) imposes the boundaries to be periodic (such a choice would be in particular useful in the study of an assembly of active droplets, tackled in the chapter 6.2.1). As a result, the solute cannot escape from the box and its absolute concentration keeps increasing over time. After having checked the amount of solute present in the box satisfies well the conservation law imposed by Eq. (5.2) (see Appendix B.3 for more details), we have analysed the robustness of the interaction dynamics for several Pe. Indeed, the spatial periodicity of the problem infers the droplets also interact with their periodic counterpart. As a consequence, two droplets involved in a symmetric head-on collision experience a periodic collision dynamics as illustrated by the schematic on the panel (a) of Fig. 5.4. Besides, for a sufficiently large box, the droplets recover their self-propelled regime between each collision. This tells the only difference between the several collisions is the presence of the solute "pollution" generated by the active droplets which increases the average concentration level.

Considering the framework of the head-on collision between two identical active droplets, Fig. 5.4-b provides the evolution of the axial velocity $v_x = \boldsymbol{v} \cdot \boldsymbol{e}_x$ of the droplet located on the right part of the box as function of its x position. Besides, sufficient time is let so that each droplet experiences 20 collisions (10 cycles). We therefore notice the periodic velocity evolution reported on the panel (b) of Fig. 5.4 remains unchanged even in the presence of the pollution and resulting increase of the average solute concentration. We may thus confirm the interaction dynamic provided by the present numerical approach appears robust even in the presence of periodic boundary conditions.

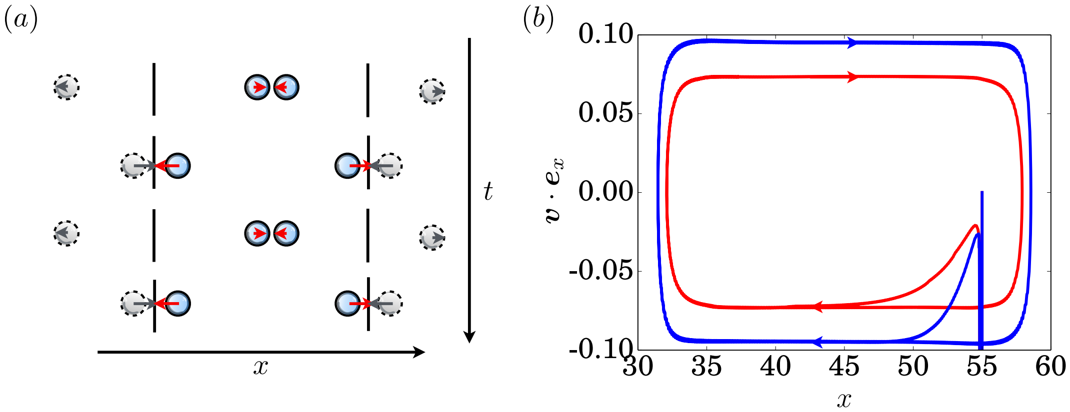

Figure 5.4: Periodic boundary conditions impose the collision to occur also at the boundary, leading to an oscillatory collision dynamics. (a): Schematic of the looped collision dynamics. (b): Evolution the right droplet velocity $v_x = \boldsymbol{v} \cdot \boldsymbol{e}_x$ as function of its position x at Pe=6 (red) and Pe $= 8$ (blue). In each case, the droplet performs 10 cycles.

Active swimming droplets are anti-chemotactic, and thus swim away from the zones of higher concentration, e.g. their own wake or the proximity with other emitting droplets [36, 119, 120]. During the encounter of two droplets, the confinement-induced accumulation of the emitted solute between them modifies the orientation of their chemical polarity and velocity: after a transient interaction, the droplets swim away from each other in different and modified directions (Fig. 5.7). In a head-on collision, the axisymmetry of the problem imposes that the droplet velocity is strictly zero when they are closest to each other.

This is however not necessarily the case in oblique collisions, for which the droplets can maintain a non-zero velocity at all time, and the location of the chemical wake can rotate around the droplet as a result of the change in swimming direction (see Fig. 5.7). The outcome of such oblique collisions is therefore not obvious, in particular for the final direction of the droplets as they swim away from each other. In particular, it is intimately linked to the detailed unsteady dynamics of the droplets' chemical wake. This is the main focus of the present chapter and in the following, we analyse in detail the influence of generic droplet-droplet interactions on their directional dynamics. Symmetric oblique collisions are first analysed, where the two droplets are initially exactly on a collision course: by this terminology, we mean that the droplets are initially at the same distance of the crossing point of their incoming trajectory. In this situation, the problem maintains therefore a reflection symmetry at all times. In a second step, the general case is considered, where one of the droplets (termed droplet 2 by convention) is lagging by a finite distance.

5.4 Symmetric oblique collisions

We first consider the symmetric collision of two active droplets, initially separated by a large distance $d_c \gg 1$ and swimming towards each other (Fig. 5.5). The droplets' motion is completely symmetric and we thus focus exclusively on the dynamics of the left-most droplet (droplet 1). When the two droplets are sufficiently far from each other the concentration field they create does not influence the other's swimming motion. As a result, long before and after the collision, each droplet swims as if it was isolated, with a constant velocity v_0 along a straight trajectory.

5.4.1 Collision-induced alignment

Defining $(\boldsymbol{v}_1^0, \boldsymbol{v}_2^0)$ and $(\boldsymbol{v}_1^\mathrm{f}, \boldsymbol{v}_2^\mathrm{f})$ the initial and final droplets' velocities (Fig. 5.5 and Fig. 5.9), as well as their relative direction sines and cosines

$$\chi = \frac{\boldsymbol{v}_1 \cdot \boldsymbol{v}_2}{|\boldsymbol{v}_1||\boldsymbol{v}_2|}, \quad \zeta = \frac{\boldsymbol{e}_z \cdot (\boldsymbol{v}_1 \times \boldsymbol{v}_2)}{|\boldsymbol{v}_1||\boldsymbol{v}_2|}, \tag{5.5}$$

the effect of the collision on the droplets' alignment can be quantified by relating their relative direction cosine before (χ_0) and after (χ_f) the collision (Fig. 5.6).

In sharp contrast with a perfect elastic shock of rigid passive spheres (for which $\chi_0 = \chi_f$), the symmetric collision of active droplets results in a systematic alignment of the droplets regardless of their initial relative angle $(\chi_f > \chi_0)$. This alignment is most striking for rather frontal collisions for which $\chi_0 \in]-1, 0]$, which corresponds to droplets initially heading mostly toward each other. Qualitatively, we understand this as the result of the droplets coming closer to each other in such configurations (smaller d_min): the chemical repulsion induced by the other droplet, at the origin of the droplet's reorientation and rebound, is a decreasing function of their relative distance.

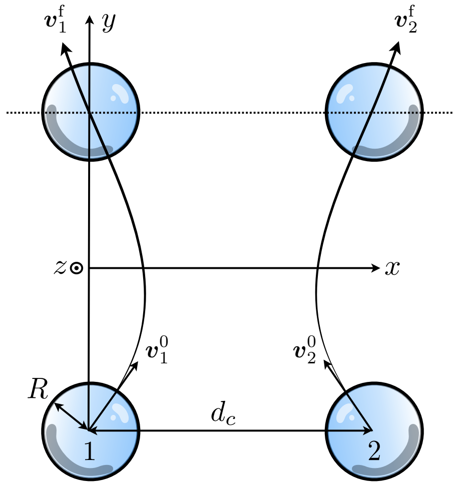

Figure 5.5: Symmetric collision of two active droplets. d_c denotes the center-to-center separation distance and $(\boldsymbol{v}_1^0, \boldsymbol{v}_2^0)$ (resp. $(\boldsymbol{v}_1^{\mathrm{f}}, \boldsymbol{v}_2^{\mathrm{f}})$) denote the initial (resp. final) droplets' velocities.

Furthermore, a plateau can clearly be seen for $\chi_0 \in [-0.9, 0.5]$: within that range, the droplets swim away from each other with a relative angle corresponding to $\chi_f \approx 0.5$ that is essentially independent of their incoming orientation. For greater χ_0 (i.e. almost parallel incoming trajectories), the elastic rebound dynamics is recovered $\chi_f \approx \chi_0$ as a result of the weak interaction of the droplets which remain far from each other at all times. For almost head-on collisions ($\chi_0 < -0.9$), the final direction of the droplets is extremely sensitive to the exact impinging angle. Perfect head-on collisions ($\chi_0 = -1$) result in a normal rebound ($\chi_f = -1$) by complete reversal of the chemical wake and of their swimming velocity; but a small departure from this situation (e.g. $\chi_0 = -0.93$) results in a sharp alignment of the droplets ($\chi_f = 0.5$). This sensitivity is intimately linked to the complex reorganisation of the chemical polarity in this type of collisions and suggests furthermore that purely head-on collisions are unstable.

Greater physical insight into the collision dynamics is provided by the dynamic evolution of the chemical wake which is represented at different stages of a collision with $\chi_0 = 0.5$ and Pe = 6 on Fig. 5.7. The unsteady nature of solute diffusion is retained in the moving singularity model, and it should thus be noted that the direction of the wake created by a droplet's own chemical footprint $\boldsymbol{p}_i$ does not align instantaneously to its velocity $\boldsymbol{v}_i$, but instead takes a finite time to adjust to changes in the swimming direction induced by the additional drift created by the other droplet's chemical footprint.

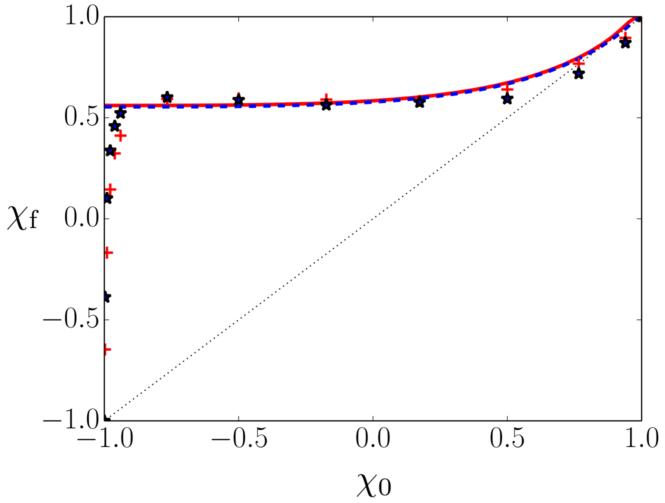

Figure 5.6: Reorientation of the droplets' dynamics in a symmetric collision for Pe = 6 (red) and Pe = 8 (blue). The cosine of the velocity relative orientation is compared in the initial and final steady propulsion regimes when the droplets are far away from each other. The results of the moving singularity model (symbols) are compared to the prediction of the reduced model (lines).

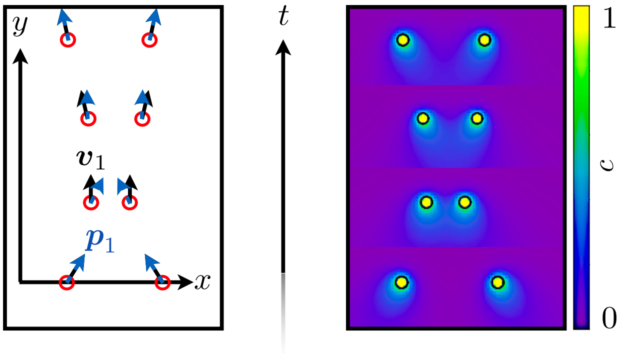

Figure 5.7: (Left) Oblique symmetric collision of two active droplets in exact collision course. Schematic snapshots of the polarity direction $\boldsymbol{p}_1 = \boldsymbol{\Pi}_1/\Pi_1$ and velocity $\boldsymbol{v}_1$ are provided along the collision (left) as well as the corresponding concentration fields (right) $\chi_0 = 0.5$ and Pe = 6.

5.4.2 Minimal collision model

These observations provide the basic ingredients of an even simpler dynamic model for the collision, which is referred to in the following as *minimal collision model*, with only two degrees of freedom: the separation distance d_c between the droplets and the direction, $\boldsymbol{p}_1$, of the chemical wake of the left-most droplet, i.e. the polarity of its own concentration footprint c_1 at its surface $\mathcal{S}_1$. When the droplet is isolated, its velocity is aligned with $\boldsymbol{p}_1$, i.e. $\boldsymbol{v}_1 = \boldsymbol{\Pi}_1 = v_0\boldsymbol{p}_1$. In a more general situation, invoking (5.1) and (5.2), its total velocity $\boldsymbol{v}_1$ is obtained as the sum of two contributions:

$$\boldsymbol{v}_1 \quad = \quad \boldsymbol{\Pi}_1 + \boldsymbol{v}_1^r, \qquad (5.6)$$

with $\boldsymbol{v}_1^r$ the chemical repulsive drift induced on droplet 1 by droplet 2. For simplicity, this repulsion velocity $\boldsymbol{v}_1^r$ is modelled here as resulting from the chemical gradient generated by a fixed source of dimensionless intensity 4π at the location of a second droplet, which allows us to retain only the slowest decaying singularity signature of the moving singularity model:

$$\boldsymbol{v}_1^r = M\frac{\boldsymbol{x}_1 - \boldsymbol{x}_2}{|\boldsymbol{x}_1 - \boldsymbol{x}_2|^3} = -\frac{M}{d_c^2}\boldsymbol{e}_x, \tag{5.7}$$

where M is a positive constant characterising the mobility of a passive droplet in a chemical gradient. In the full moving singularity model, the evolution of a droplet's wake in response to changes in its total velocity is a complex process and involves both changes of direction and magnitude in the chemical self-polarity (i.e. corresponding to its own chemical footprint) under the effect of diffusion and of the droplet's translation. The simplified model considered here is based on two important physical properties of the droplets' polarity, namely that (i) it evolves in response to changes in the droplet's velocity and (ii) relaxes with a finite delay τ to the droplet's swimming direction in steady state. As a result, and further assuming that the magnitude of the self-polarity Π_1 does not change in time, the evolution equation for the velocity $\boldsymbol{v}_1$ and wake direction $\boldsymbol{p}_1$ become (see Appendix B.4)

$$\boldsymbol{v}_1 = v_0\boldsymbol{p}_1 + \boldsymbol{v}_1^r, \tag{5.8}$$

$$\frac{d\boldsymbol{p}_1}{dt} = \frac{1}{\tau v_0}(\boldsymbol{p}_1 \times \boldsymbol{v}_1) \times \boldsymbol{p}_1 = \frac{\kappa(\boldsymbol{p}_1 \cdot \boldsymbol{e}_y)}{d_c^2}\boldsymbol{e}_z \times \boldsymbol{p}_1, \tag{5.9}$$

where $\kappa = M/(\tau v_0)$ is a positive constant. The reorientation of the polarity is then solely the result of the chemical repulsion by the other droplet, Eq. (5.9).

The essence of the collision dynamics observed for the full system is well captured by this simplified model: as the droplets get closer to each other, the chemical repulsion reduces the magnitude of their relative velocity (i.e. the velocity component along the x-axis on Fig. 5.7) which eventually vanishes at a distance $d_{\min}$; at that instant, the component of self-propulsion in the x direction balances the chemical repulsion exactly. However, $\boldsymbol{p}_1$ is not yet aligned with $\boldsymbol{v}_1$ as a result of the finite time delay τ: the wake continues rotating for a finite time, reducing (and eventually reversing) the self-propulsion component along $\boldsymbol{e}_x$ which cannot balance the chemical repulsion $\boldsymbol{v}_1^r \parallel -\boldsymbol{e}_x$: this generates the rebound of droplet 1 away from its neighbour.

The results of the minimal collision model can now be compared with those of the original dynamics obtained from the moving singularity description. In the simplified model, the self-propulsion velocity v_0 is directly imposed by the choice of Péclet number [36]; for fixed Pe, the minimal model, Eqs. (5.8)–(5.9), therefore includes a single fitting parameter κ. Fig. 5.6 confronts the final relative angle characterised by χ_f, plotted against χ_0 and predicted by the simplified model (solid lines). The complete numerical results obtained for Pe $= 6$ and Pe $= 8$ (respectively red crosses and blue stars) are also reported. We note that for $\chi_0 > -0.93$ the simplified model captures the emergence of the constant χ_f plateau for a large range of approaching angles.

In head-on collisions, the norm of the droplets' polarity vanishes to zero at the moment they are closest (see Fig. 5.3). This is expected as the *minimal collision model* only describes the direction of polarity and not its magnitude, and is thus naturally unable to reproduce the physics of such specific configurations.

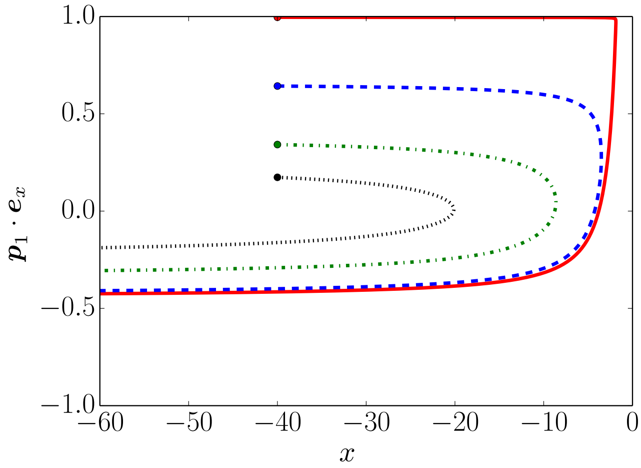

Figure 5.8: Evolution of $\boldsymbol{p}_1 \cdot \boldsymbol{e}_x$ as function of the droplet's position x for different initial angles: solid red line $\chi_0 = -0.98$, dashed blue line $\chi_0 = 0.17$, dashed dotted green line $\chi_0 = 0.77$ and black dotted line $\chi_0 = 0.94$.

The problem is invariant by translation along y, and the simplified model provides a two-degree-of-freedom description of the collision dynamics, namely the x position of droplet 1 and the angle of its polarity direction $\boldsymbol{p}_1$ with the y-axis. The dynamics can therefore be fully characterised by the system trajectories in the $(x, \boldsymbol{p}_1 \cdot \boldsymbol{e}_x)$-plane (Fig. 5.8). We note an accumulation of the trajectories near the minimum distance and onto the trajectory emerging from a perturbation of the head-on collision ($\chi_0 \approx -1$), which is indeed consistent with the emergence of the plateau-behaviour of the outgoing relative angle, regardless of the initial orientation of the droplets.

5.5 Delayed collisions: several collisions regimes

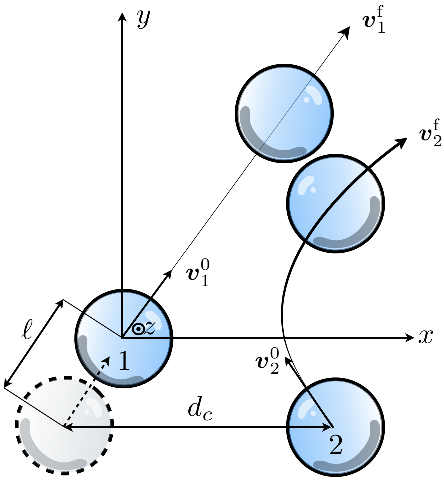

Figure 5.9: Generic collisions of two active droplets where $(\boldsymbol{v}_1^0, \boldsymbol{v}_2^0)$ (resp. $(\boldsymbol{v}_1^{\mathrm{f}}, \boldsymbol{v}_2^{\mathrm{f}})$) denote the initial (resp. final) droplets' velocities. If d_c would have been the droplet-droplet distance in the symmetric case, ℓ further denotes the lead distance of droplet 1 on the second droplet. The final velocity directions of droplets 1 and 2 are not symmetric anymore.

We now turn to the general problem of asymmetric or delayed collisions, which are characterised in this paragraph using the full moving singularity model introduced in section 5.2. In such collisions, droplet 2 is initially located further than droplet 1 by a "delay" distance ℓ from the virtual crossing point of the initial trajectories (Fig. 5.9). In contrast with many active particle systems, active droplets leave a chemical "trail" that extends over several tens of radii and is known to influence critically their collective dynamics and trajectories [120, 121]: when crossing another droplet's trail, a second droplet is expected to be deviated away or repelled by the slowly-diffusing solute left by the first droplet when it went by. This interaction and deviation is obviously stronger for close interactions, i.e. when ℓ is small.

In the following paragraphs, we analyse the possible outcome of such general encounter of two droplets and impact on their subsequent relative dynamics. By convention, and without any loss of generality, droplets 1 (resp. 2) is initially located on the left (resp. right) and both droplets are heading toward each other, so that $\zeta > 0$, see Eq. (5.5). Depending both on their initial relative alignment, χ, and on the delay length ℓ, the droplets can either *cross paths* ($\zeta_0\zeta_f > 0$) or *rebound* ($\zeta_0\zeta_f < 0$).

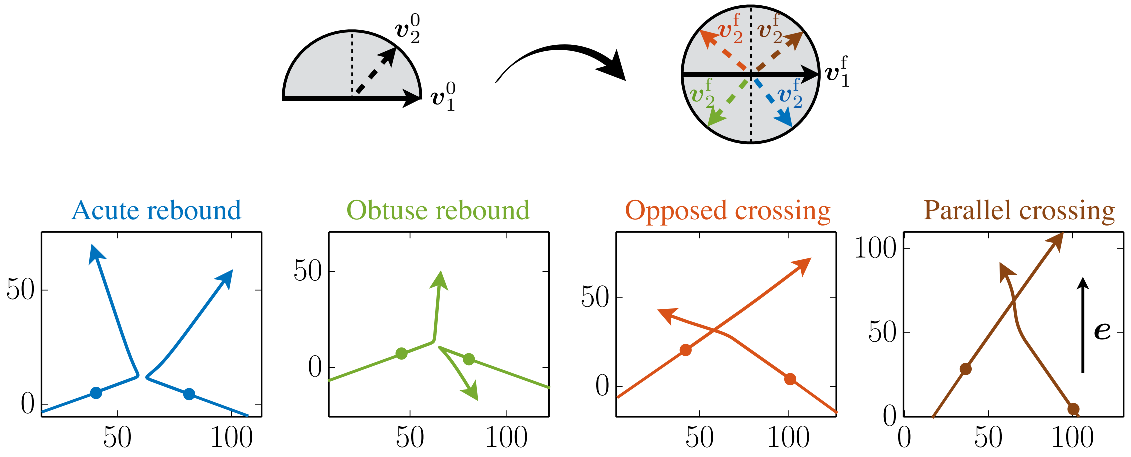

Figure 5.10: Four possible regimes following asymmetric (delayed) collisions of two droplets. Top: Initial and final relative orientations of the droplets in each regime. Bottom: Illustration of each regime. Acute rebound (blue, $\chi_0 = -0.77, \ell = 2$), obtuse rebound (green, $\chi_0 = -0.34, \ell = 30$), opposed crossing (red, $\chi_0 = -0.77, \ell = 8$) and parallel crossing (brown, $\chi_0 = 0.34, \ell = 30$). In each case, the droplets' trajectories are provided together with their position at a given time before the collision.

Each of these two general behaviours is further divided into two different regimes depending on the sign of their final relative alignment, χ_f (Fig. 5.10):

- In the *crossing regimes*, $\zeta_f < 0$, droplet 2 passes through the chemical wake of droplet 1. In their final state, the droplets can either swim in opposite direction (*opposed crossings*, $\chi_f < 0$, red color on Fig. 5.10), or in the same direction (*aligned crossings*, $\chi_f > 0$, brown color on Fig. 5.10).
- In the *rebound regimes*, $\zeta_f > 0$, droplet 2 is repelled by droplet 1 and its chemical trail and is deviated away before crossing its path (for sufficiently small ℓ, droplet 1 may also be deviated by the oncoming droplet 2). Again, the final relative orientation

of the droplets provides a distinction between *acute rebounds* ($\chi_f > 0$, blue color on Fig. 5.10) and *obtuse rebounds* ($\chi_f < 0$, green color on Fig. 5.10).

These four different regimes are illustrated on Fig. 5.10 and the influence of the delay length ℓ and the initial alignment χ_0 on the regime type following a collision is fully characterised below.

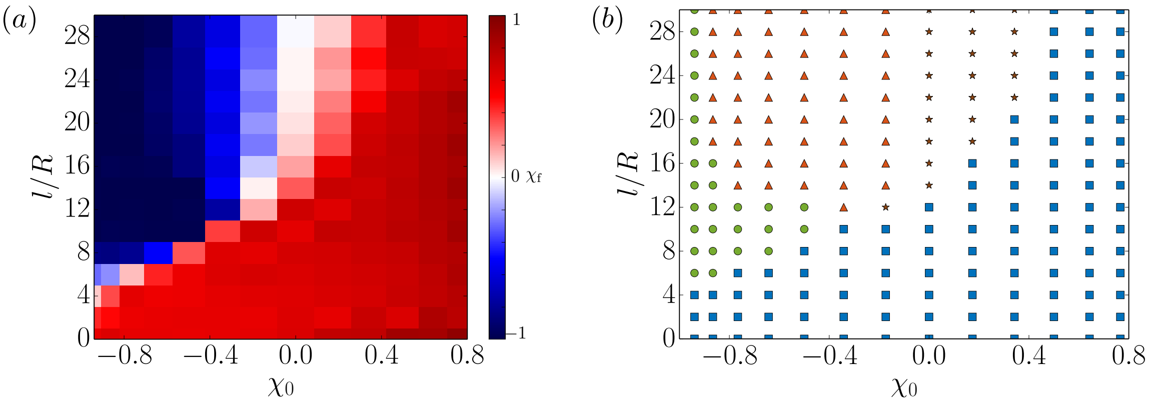

Figure 5.11: (*a*): Final alignment, χ_f, as a function of the initial alignment χ_0 and delay length ℓ. (*b*): Phase diagram of the collision outcome depending on the initial relative alignment, χ_0, and delay length, ℓ: Acute rebound (blue), obtuse rebound (green), opposed crossing (red) and parallel crossing (brown)

When ℓ is small, the problem is almost symmetric so that both droplets rebound around the same time under the effect of their repulsive interaction, oriented along $\boldsymbol{e}$, defined as the unit vector orthogonal to the average initial direction of both droplets. This symmetry is broken when ℓ is increased; as a result, when the droplets are closest, the repulsive interactions experienced by each of them point along distinct directions, and can lead to completely different dynamics for the leading and trailing droplets.

Section 5.4 demonstrated that symmetric collisions ($\ell = 0$) systematically lead to acute rebounds provided $\chi_0 > -0.98$, while obtuse rebound are observed for strictly head-on collisions ($\chi_0 = -1$). It is therefore no surprise that such observations are maintained for small enough delay length ℓ. Note that Fig. 5.11 does not include strict head-on and parallel collisions, for which $\chi_0 = \pm 1$ and ℓ cannot be defined.

In fact, acute rebounds are observed for most initial relative orientations when $\ell/R < 5$, and for even larger delay lengths when the droplets are initially swimming in rather parallel directions ($\chi_0 > 0$). For more frontal collisions ($\chi_0 < -0.3$), alignment of the droplets and acute rebounds are still observed for small ℓ, but the second (delayed) droplet follows a drastically different dynamics emerges when a critical delay length ℓ_c is exceeded, leading to obtuse rebounds. To understand this acute-to-obtuse rebound transition, the detailed dynamics of the droplets must be analysed in the *closest interaction region*, loosely defined here as the region where their relative distance is at its minimum.

We noted previously the asymmetry of the chemical footprint of a swimming droplet: most of the chemical released by a droplet is left in its wake. As a result, the interaction region is almost solute-free as the first (leading) droplet crosses it, and for larger delay length, droplet 1 is therefore only weakly deviated. In contrast, when it finally crosses the interaction region, droplet 2 is repelled by the wake of droplet 1 in a direction that depends both on ℓ (i.e. how long ago droplet 1 went by) and χ_0. For large enough ℓ and small χ_0 (droplets heading toward each other), this repulsion includes a component along $-\boldsymbol{e}$. This justifies the existence of a critical delay length ℓ_c for the acute-to-obtuse rebound transition observed on Fig. 5.11: for $\ell \approx \ell_c$, the repulsion of droplet 2 along $-\boldsymbol{e}$ compensates its initial velocity component along $+\boldsymbol{e}$, which increases with χ_0. As the interaction strength decreases with the droplet separation, ℓ_c is an increasing function of χ_0, which is consistent with the positive slope of the separation between acute and obtuse rebound regimes on the panel (a) of Fig. 5.11.

For larger ℓ (typically $\ell \gtrsim 5$–10), the sign of the droplets' alignment, χ, is conserved between the initial and final configurations: droplets initially swimming along rather parallel directions ($\chi_0 > 0$)) experience an *acute rebound* or a *parallel crossing* while droplets heading more directly toward each other ($\chi_0 < 0$), experience an *obtuse rebound* or an *opposed crossing*. In both cases, a rebound-to-crossing transition is observed when the delay ℓ is large enough (Panel (a) of Fig. 5.11). This is consistent with the physical intuition that the droplets essentially do not interact and maintain a straight trajectory for sufficiently large ℓ, as the wake of the leading droplet has diffused away by the time the second droplet crosses the interaction region.

It can be noted that the critical delay length ℓ_c^* required for this rebound-to-crossing transition varies non-monotonically with χ_0: it is minimum for $\chi_0 \approx 0$ and diverges for rather parallel or head-on configurations ($\chi_0 \to \pm 1$). This feature results from the combined effect of (i) the sensitivity of initial trajectory to a rebound-to-crossing transition and (ii) the non-trivial variations of the minimum distance of the two droplets with ℓ and χ_0.

The minimum distance observed between the droplets generally increases with χ_0 (see Fig. 5.8 for the case of symmetric collisions, $\ell = 0$), and diverges for parallel configurations ($\chi_0 \to 1$). To experience a rebound, the repulsive interaction between the droplets must exceed the component of their relative velocity normal to $\boldsymbol{e}$, which is proportional to $\sqrt{1-\chi_0}$. For greater initial alignment (larger χ_0), this happens at greater distances (the chemical repulsion decreases as $1/d^2$). Furthermore, the interaction of the droplets is stronger as their alignment increases due to the angular asymmetry of their chemical wake (see Eq. (5.3)). As a result, a much greater delay length ℓ is required to avoid a rebound when the droplets are initially swimming parallel to each other, which is consistent with the critical delay ℓ_c^* for a rebound-to-crossing transition being an increasing function of χ_0 when $\chi_0 > 0$ (Fig. 5.11-a).

Additionally, a first estimate of the minimum distance of the two droplets is provided by the minimum distance reached by two non interacting droplets $d^*_{\text{min}} \sim \ell\sqrt{1+\chi_0}$, which is always small for head-on configurations, even for large ℓ. As a result, a rebound is observed for larger delay ℓ when $\chi_0 \to -1$ (head-on collisions), which is consistent with ℓ_c^* being a decreasing function of χ_0 for $\chi_0 < 0$ (Fig. 5.11-a).

Finally, in addition to the phase diagram provided on the panel (a) of Fig. 5.11, the panel (b) of Fig. 5.11 provides the evolution of the final relative alignment of the droplets, χ_f, in the (χ_0, ℓ)-parameter space. Two regions can be distinguished in this figure. Acute rebounds (small ℓ or large χ_0) are characterised, as for symmetric collisions, by a rather fixed directional outcome which corresponds to a general alignment of the droplets (χ_f is almost constant and greater than χ_0). This region is separated by a sharp transition from the rest of the map in which the relative direction is mostly conserved ($\chi_f \approx \chi_0$) and depends only weakly on ℓ. This sharp transition stems from sudden changes in the reorientation direction of the trailing droplet under the effect of the chemical wake left behind the leading droplet. It emphasizes the sensitivity of the collision outcome to ℓ and the scattering ability of such collisions on the collective behaviour of the droplets.

5.6 Conclusion

Swimming droplets influence each other's dynamics through the wake of chemical solute they generate in order to self-propel. These chemical interactions are repulsive and have been identified as the dominant contribution to the droplets' collective dynamics, both in experiments [120] and from a complete modelling of the two-droplet dynamics as seen in chapters 3 and 4. Based on this observation, this chapter proposed a general simplified framework in terms of moving singularities to analyse the collisions of N-droplet collisions. This model was then exploited to characterise in detail the generic (oblique) planar collisions of two droplets.

Our results show that symmetric collisions systematically align the droplets' after their encounter ($\chi_f \geq \chi_0$), leading to a surprisingly constant relative final alignment χ_f, regardless of the incoming orientation χ_0. This phenomenon was proved to result essentially from the reorientation dynamics of each droplets' own wake during the collision, and was rationalised using a simple two-degree-of-freedom model in terms of the wake orientation and inter-droplet distance. This alignment ability of the droplet interactions is maintained for significant asymmetry in the droplets' oncoming dynamics, at least for effective delay length of a few droplet radii. When the asymmetry of the droplet interaction is greater (i.e. when the trailing droplet crosses the interaction region long enough after the leading droplet did), the interaction outcomes are much more diverse, and both rebound regimes (where the droplets' relative velocity is reversed) and crossing regimes (where the droplets are only deviated away from their original trajectory) were observed. Two sharp transitions between fundamentally different outcomes were observed as a result of the strong sensitivity of the trailing droplet's trajectory and final heading to the exact timing of its crossing of the solute-rich region left behind the first droplet.

The relative alignment resulting from droplets interaction is expected to favour a certain collective coherence of the droplets' trajectory at large scales. On the other hand, sharp transitions in the final dynamic regime denote the scattering ability of such collisions, which provide the droplets with the ability to explore new spatial directions.

Building upon a detailed understanding of the axisymmetric configuration, for which a full solution of the chemo-hydrodynamic system is available [89, 114], this chapter provides an analysis of the generic oblique collisions, which is more relevant to experimental conditions. It is shown that such axisymmetric or head-on collisions are very specific in terms of the droplets' wake dynamics whose polarity must vanish in a rebound, while it is able to rotate around the droplet in a more generic setting. As a result, mostly (but not strictly) head-on collisions lead to a significant scattering. Similarly, introducing a small delay in the oncoming dynamics of the two droplets in an oblique symmetric collision triggers the emergence of a large variety of different dynamic regimes.

For simplicity, we specifically focused here on the planar dynamics of the two droplets, still accounting for the fully-3D diffusion of the chemical solute. The stability of such planar collisions remain however to be studied. Yet, in experimental situations, an external mechanism (in general confinement or buoyancy-induced trapping close to a boundary) maintains such planar configurations and we therefore expect the present findings to be relevant to such situations. It can be also noted, that the present framework could be generalised to include the effect of confinement on the solute dynamics, e.g. exploiting the linearity of the chemical problem through the method of images.

Take home message of Chapter 5

2. Moving singularity model: At moderate Pe, we approximate an active droplet by the superposition of a source and source-dipole located at its centre. In particular, this reduced model provides consistent results of head-on collisions in comparison to the exact ones provided in chapter 3.

2. Symmetric oblique collisions: We find that oblique symmetric collisions of active droplets tend to induce a relative alignment of their swimming direction. Besides, the final relative angle between each droplet's direction is almost the same for a large range of incoming angles. This last feature results from the particular dynamics of the solute wake around each droplet.

3. Delayed oblique collisions: We find that introducing a delay on one droplet during an oblique collision can lead to the emergence of four different regimes. In particular, for almost head-on collisions, the system can exhibit scattering events with the introduction of a misalignment in the droplets' initial conditions.

6

Conclusion and perspectives

In this last chapter, we will conclude this manuscript by first of all providing a summary of the results introduced in the previous chapters. Besides, we suggest four possible future projects that may help gain insight into the interactions and collective dynamics among active droplets.

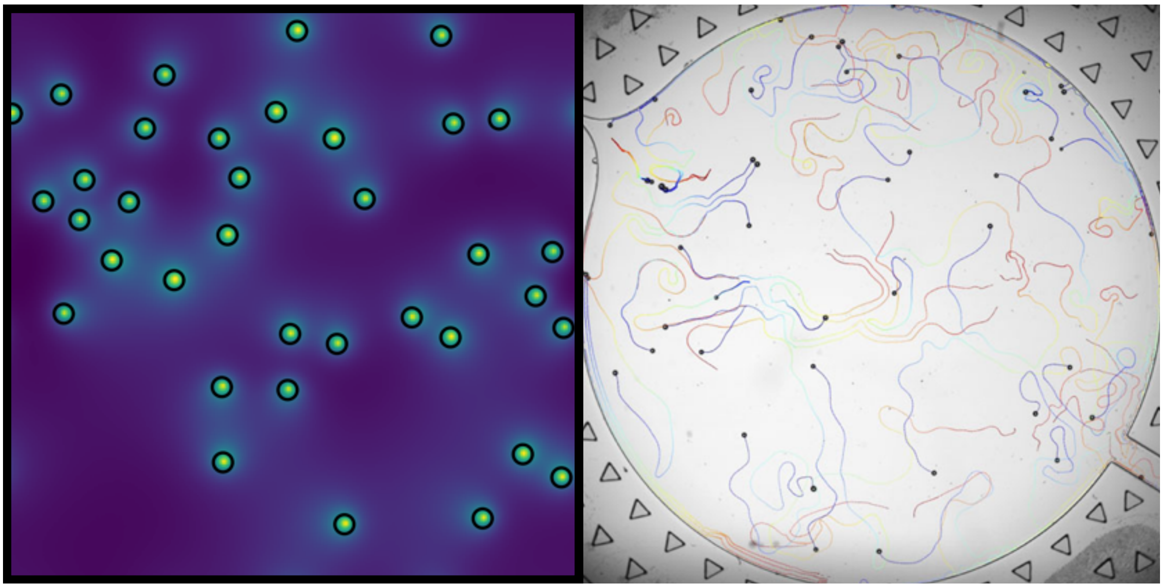

Left panel: concentration field of several active droplets driven according to the moving singularity model. Right panel: assembly of active water droplets in a circular arena from Ref. [36]

Contents

The central objective of this PhD has been to characterise the interactions between self-propelling *active droplets* by the mean of theoretical and numerical tools. Before this PhD started, an extensive amount of work had already been done regarding the theoretical modelling of the single active droplet's self-propulsion enabling to gain insight into the involved mechanisms. If knowledge of single droplet dynamics was advanced, the number of studies that examined their interactions remained small. Several attempts have been performed to characterise the collision of two self-propelled active droplets. First, an interaction model in the purely diffusive limit (Pe = 0) and with no hydrodynamic interactions has been developed by Ref. [56]. Besides, the numerical simulations from Ref. [86] tackle the collision problem by focusing on the hydrodynamic interactions between two active droplets. Finally, the far-field model from Ref. [87] consider the influence of both chemical and hydrodynamic interactions during the collision of two self-propelled droplets. It should be noted that the latter model remains valid for far-appart active droplets close to the self-propulsion threshold. When this PhD started, the effect of the hydro-chemical coupling on the interaction remained thus unclear. Therefore, the first objective of this thesis has been to provide an exact interaction model between active droplets, to characterise their interactions and determine which of the hydrodynamical or the chemical contribution is the most important during a collision. Another objective has been to provide a benchmark for more effective models and understand the behaviours of active droplets observed in the experiments.

6.1 Summary

In the first chapter of this manuscript, we analysed the study of interactions between active individuals (birds, ants, active emulsions), which can help understand the physical origin of some of their intriguing collective dynamics. We then realised that at a microscale, in the absence of inertia, a swimmer needs to break spatio-temporal symmetry to achieve propulsion. In using the example of the paramecium, we saw that generating a slip velocity at the surface of a body appears to be a convenient swimming strategy at those small scales. The latter inspired a wide range of artificial microswimmers that use interfacial stresses to propel. In particular, we focused on microdroplets that experience a solubilisation process when immersed in a liquid saturated with surfactant molecules. After briefly presenting the activity mechanism at the droplet surface, we provided a qualitative explanation of the instability phenomenon at the origin of the self-propulsion of the droplet. We specifically stressed the importance of the coupling between solute dynamics and flow field, which appears essential for a droplet to swim. Finally, we concluded this first chapter by providing some observed exotic behaviour adopted by a single active droplet at high Pe, in addition to some collective motion that can appear in specific geometries.

In the second chapter, we presented a spectral decomposition approach [66, 36], which helps compute the exact dynamics of a single self-propelled active droplet. Then, we provided some qualitative descriptions of the hydrodynamic and chemical interactions that arise in the presence of several droplets or boundaries. Moreover, in order to better grasp the fundamental difficulty to determine these hydro-chemical interactions, we briefly mentioned the case of interacting active particles in a purely diffusive limit. Consequently, this second chapter opened the question of the modelling of those interactions, which seems not possible with the current models of the literature.

The third chapter of the manuscript provided a new semi-analytical method that computes the exact interactions between an active droplet which frontally collides with a rigid wall . To solve this problem, we adapted the bi-spherical coordinates system to solve both Stokes and advection-diffusion equations in a situation where the droplet moves. The latter imposes the grid to experience inconvenient distortions. If bi-spherical coordinates have been used for a long time to deal with quasi-steady problems (where Stokes and Laplace equations are decoupled), the developed framework may be used and rather easily adapted to deal with any axisymmetric boundary value problem between two spheres of any radius (where a sphere for which $R \to \infty$ appears as a plane), involving unsteady transport dynamics coupled to low Reynolds flows and for which the involved boundaries may move and deform over time (as soon as the surfaces remain either spherical or flat). Such a situation may, for instance, be encountered in the growth or dissolution of gas bubbles near a heating plate or to study the effect of shrinkage in the dynamics of active dumbbells [103]. The first result of this chapter regards the case of moderate Pe (illustrated by $\mathrm{Pe} = 6$), where chemical effects turn out to be predominant in the interactions. Within this limit, a reasonable approximation of the head-on collision involving two active droplets may thus be imagined in neglecting any hydrodynamical influence on their velocities. However, when increasing Pe, the enhanced advection leads to a decrease of the solute concentration at the front of the droplet, which therefore needs to get closer to the wall before experiencing a rebound. In particular, for higher Pe (illustrated by $\mathrm{Pe} = 20$) and during the second half of the collision, the droplet is held back by the trace of its former wake which needs some time to diffuse. As a result, the droplet experiences a velocity plateau during which it spends some time with an average speed before re-accelerating up to its self-propulsion velocity. Chapter 3 then provides a useful benchmark against which the single active droplet dynamics obtained from reduced models may be confronted. In the same manner, the results regarding the collision durations and rebound distances of sections 3.6.2 and 3.8 may be used to check the validity of a reduced model regarding pairwise interactions.

In the fourth chapter, we applied the same mathematical framework to study head-on collisions between active droplets of distinct sizes. Surprisingly, even a slight difference in size may lead to significantly distinct behaviours: first a rebound regime for almost identical droplets and second a chasing regime achieved at moderate Pe for droplets above a critical size ratio and for which both droplets eventually swim in the same direction and at the same speed. In the third regime, called *pausing*, the bigger droplet is stopped right after the collision and behaves as an active pump. While the second regime may be a possible track to follow to learn more about the one-dimensional collective dynamics observed experimentally [63], the pausing regime depicts somehow a situation where the big droplet loses its memory. Regarding the latter regime, in a situation involving more than two droplets, we can imagine the bigger droplet would eventually recover a propulsion state after experiencing a second collision with another small one. Then, after some time, the big droplet may be once more stopped due to a third frontal collision with another active droplet. Such pattern reminds somewhat of the run-and-tumble behaviour experienced notably by E.Coli bacteria [122], which makes this regime an interesting issue to deepen.

Finally, in the fifth chapter, we examined oblique collisions of active droplets by considering an approximate model based on moving singularities. This model, checked beforehand with the exact interaction results of chapter 3, enabled to find out that symmetric oblique collisions between active droplets induce an alignment of their directions. Besides, for a large range of incoming angles, both droplets leave with almost the same final angle after the rebound. This identified plateau for the relative direction can be explained by the particular wake dynamics around each droplet, which adjusts its direction in a finite time as the droplet deviates. While such an alignment phenomenon would give some hope in observing collective dynamics [123], we realise the great sensitivity of the collision outcome to the delay between the droplets. Indeed, as a droplet leaves a trace of solute on its path, it influences the motion of the other one, even a relatively long time after the first droplet has left. We demonstrated that within the range of near head-on collisions, a delay between the droplets may lead to significantly different regimes, in which the droplets either bounce back or are deviated as a result of the collision.

6.2 Perspectives and future work

In this section, we suggest four different paths that we may follow to better understand the behaviour of active droplets. In the first, we focus on the behaviour of an assembly of active droplets, by specifically providing preliminary results of the effect of the number of droplets on the assembly dynamics. In the second, we open the question of multi-body interactions, which appear to generate ephemeral alignment events. In the third, we tackle the issue of the effect of size heterogeneity in polydisperse assemblies of active droplets. Finally, in the fourth part, inspired by recent sliding behaviours empirically observed, we suggest a generalisation of the exact model provided in chapter 3.

6.2.1 Interactions of several active droplets: diffusion properties and transition

The experiments of Ref. [124] provide interesting results regarding the dynamics of an assembly of active droplets. The active water droplets considered evolve in an oil medium saturated with surfactant molecules and are confined by two hydrophobic glass plates separated by a distance of about one droplet in diameter. Consequently, the assembly is a 2-D monolayer of active droplets (see Fig. 6.1), for which we define the density of droplets $\phi = N_d/N_d^{\max}$ as the ratio of the number of active droplets N_d involved in the experiment to the one reached for a maximal 2D hexagonal packing $N_d^{\max}$ provided by Lagrange in 1773 [125].

As shown by the mean square displacement time evolution (MSD) of Fig. 6.1, we notice that the behaviour of the assembly is ballistic at the short time scale and becomes eventually diffusive at a larger time scale. In the particular case of dilute assemblies ($0.005 < \phi < 0.08$), we notice that the diffusivity of the assembly decreases as ϕ grows. This result may be interpreted as the consequence of more frequent interactions between the droplets when increasing ϕ [124]. However, at higher ϕ, the rope of the MSD instead slightly increases (see panel (*b*) of Fig. 6.1). Such a diffusivity enhancement may be attributed to collective swimming events among the assembly [62, 115, 126].

In the following, we present very preliminary numerical results and on-going work regarding the effect of the density of droplets on the assembly dynamics. Let us consider $N_d > 2$ active droplets of equal radius R evolving in the same plane (x, y). Each droplet is described by the *moving singularity model* introduced in chapter 5. Keeping the same notations as in chapter 5, we deal with dimensionless quantities, where the time t is expressed in units of the advective time R/V^*. We consider that each active droplet emits a total flux of solute 4π inside a box of dimensions (L_x, L_y, L_z) with imposed periodic boundary conditions (see Fig. 6.2). In the following, we keep the same definition of the density of droplets as in Ref. [62]: $\phi = N_d/N_d^{\max}$, where $N_d^{\max}$ denotes the maximum number of droplets, arranged in a hexagonal lattice, that could fit inside the rectangle of dimensions (L_x, L_y) ($N_d = 1039$ for $L_x = L_y = 60$). We note that ϕ may be multiplied by $\pi/\sqrt{12}$ to recover a density in terms of area fraction.

First, we randomly assign the initial positions of the droplets one by one. If the position of the first droplet is rigorously random inside the box, the positions of the next ones are

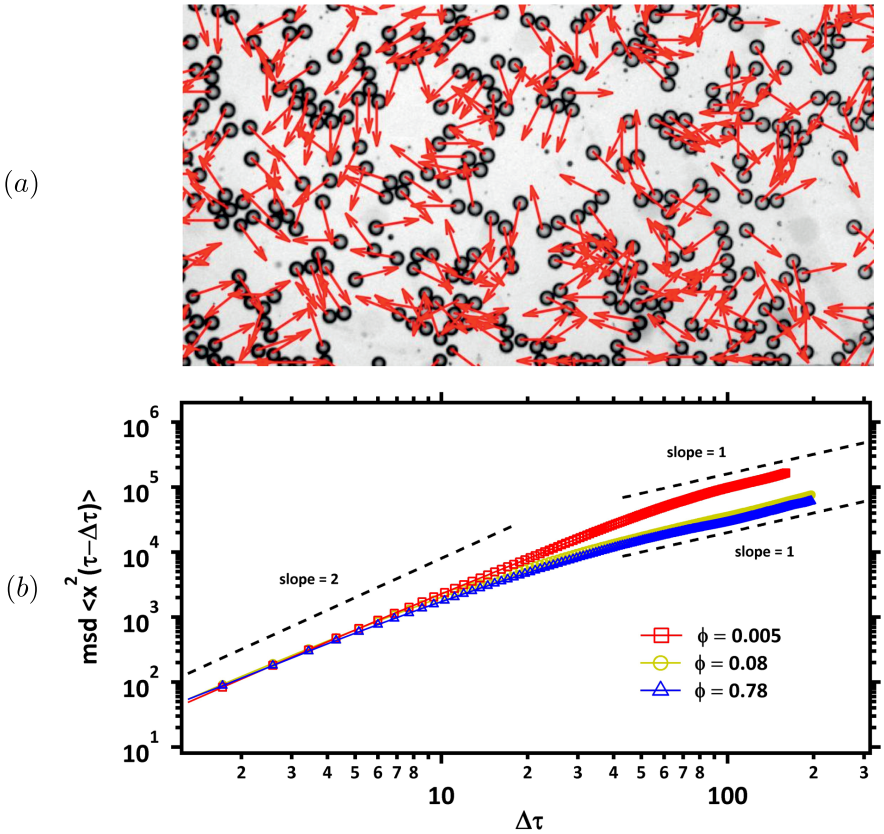

Figure 6.1: (*a*): Top view of a typical experiment involving an assembly of active droplets. The droplet diameter is 80μm. The red arrows indicate the momentary direction of the droplet motion. (*b*) Ensemble averaged mean square displacement (MSD) for a 2-dimensional monolayer of squirmer population at different area fractions. Each population has between 50-500 squirmer droplets. (*a*) and (*b*) panels are drawn from Ref. [115] and Ref. [124] respectively.

chosen randomly in the available space so that their fictitious surfaces do not overlap. The dynamics of the assembly is described (*i*) by the unsteady diffusion equation Eq. (5.2), (*ii*) by the polarity relation Eq. (5.1) (providing the speed of each droplet) and (*iii*) by the value of the dipole intensity for each droplet given by Eq. (5.4). The following system of equations thus describes the global dynamics:

$$\begin{aligned}
\mathrm{Pe}\frac{\partial c(\boldsymbol{r},t)}{\partial t} &= \nabla^2 c(\boldsymbol{r},t) + 4\pi\sum_{i=1}^{N_d}\left(\mathbf{I} + \zeta(v_i)\boldsymbol{v}_i\cdot\boldsymbol{\nabla}\right)\delta(\boldsymbol{r}-\boldsymbol{x}_i(t)), \quad c(\boldsymbol{r},0)=0, && (6.1)\\
\boldsymbol{v}_i &= -\frac{1}{2\pi}\int_{\mathcal{S}_i} c\boldsymbol{n}\mathrm{d}S = \boldsymbol{\Pi}^i, && (6.2)\\
\zeta(\lambda_i) &= \frac{\mathrm{Pe}}{2}\left[\frac{\lambda_i^2 e^{\lambda_i} v_0/2 - \lambda_i\cosh\lambda_i + \sinh\lambda_i}{2\sinh\lambda_i - (2\lambda_i + 2\lambda_i^2 + \lambda_i^3)e^{-\lambda_i}}\right], \quad \lambda_i = |\boldsymbol{v}_i|\mathrm{Pe}/2, && (6.3)
\end{aligned}$$

where $\mathrm{Pe} = 6$ in the simulations.

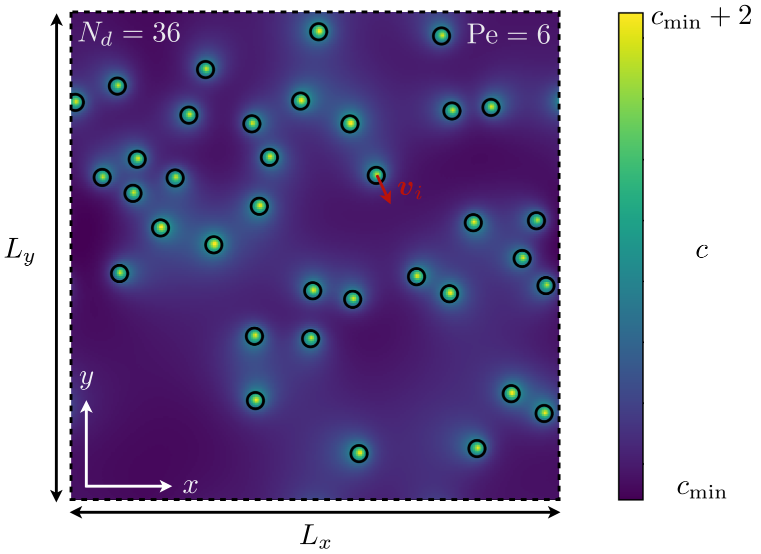

Figure 6.2: Plot of the concentration field in the plane $z = L_z/2$ generated by $N_d = 36$ active droplets ($\phi = 0.035$) at $\mathrm{Pe} = 6$. The velocity of each droplet is denoted by $\boldsymbol{v}_i$ ($i \in [1, 36]$). Since the solute concentration keeps increasing inside the box we choose the color-bar to range from the current minimal concentration $c_{\min}$ to $c_{\min} + 2$ for readability convenience

Interested in the influence of the density of droplets on the assembly dynamics, Fig. 6.3 reports the results obtained for four different densities: $\phi \in \{0.010, 0.029, 0.115, 0.338\}$. For each panel, the upper part represents the concentration field generated by the assembly, where the colour-bar range between the minimal solute concentration $c_{\min}$ (which increases with time due to the periodicity of the boundaries as seen in chapter 5) and $c_{\min} + 2$. Such a choice enables each situation to keep the same colour contrast between high and low concentration zones even if the total amount of solute inside the box varies.

Considering that periodic boundary conditions are equivalent to the situation where an infinite number of identical boxes are juxtaposed, the lower part of each panel of figure Fig. 6.3 represents the droplets' trajectories as if each droplet were able to travel through the boxes. Importantly, even if we may have the impression that the droplets move far away from each other, the periodic boundary conditions maintain the same density of droplets over time.

First, let us qualitatively describe the numerical results reported on Fig. 6.3. At a first glance, increasing ϕ seems to lead to more frequent interactions within the droplet assembly. Let us compare the trajectories provided by the lower part of each panel. We notice that for most of the droplets, the separation distances between their initial positions and the ones after $\Delta t = 9500$ (in units of R/V^*) seem to decrease when ϕ increases. Furthermore, for $\phi = 0.115$ (panel (c) of Fig. 6.3), the droplets perform fast oscillations due to frequent interactions with their neighbours, whereas their net displacement appears significantly reduced. Finally, for $\phi = 0.338$, the droplets become immobile after a short transitory regime, in which they arrange in a hexagonal lattice. Willing to get a more quantitative analysis of the assembly dynamics, we remind the definition of the mean square displacement:

$$\langle \Delta r^2 \rangle = \frac{1}{N_d} \sum_{i=1}^{N_d} |\boldsymbol{x}_i(t) - \boldsymbol{x}_i(0)|^2, \tag{6.4}$$

where $\boldsymbol{x}_i(t)$ denotes the absolute position of the droplet i at the time t.

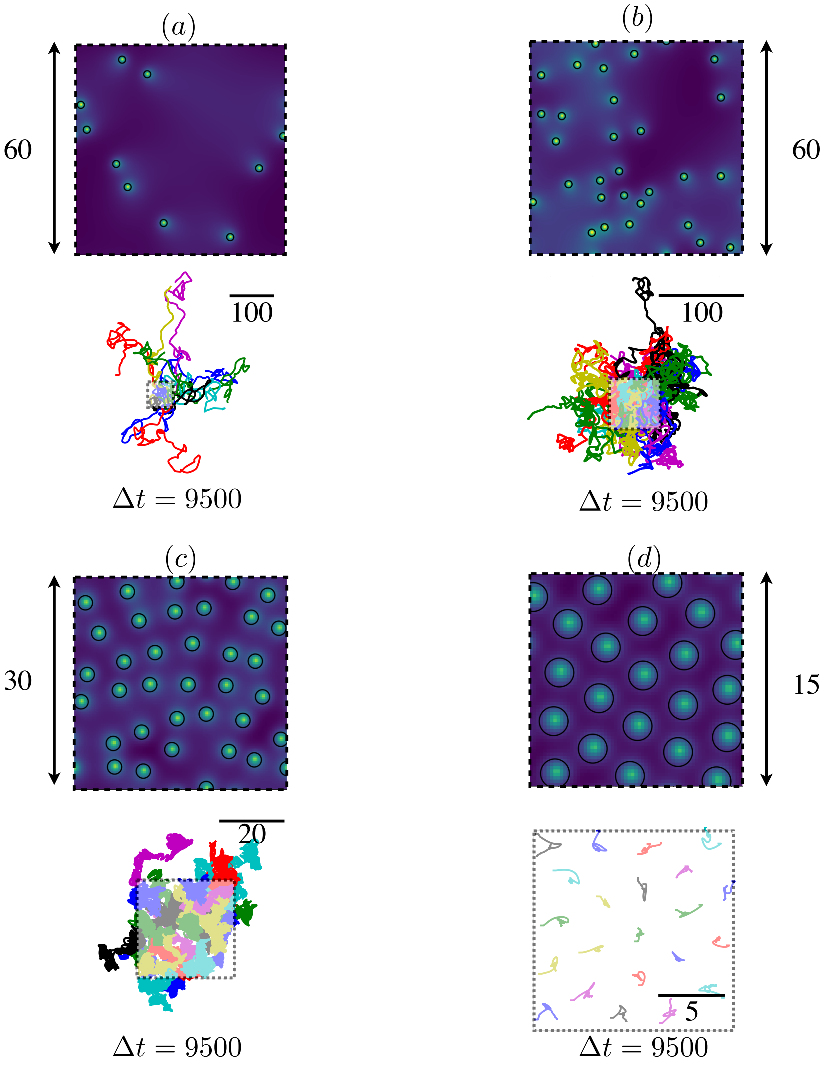

Figure 6.3: Concentration field (top) and droplets' trajectories after at time $\Delta t = 9500$ in units of R/V^* (down) for different densities. (a): $\phi = 0.010$,(b): $\phi = 0.029$, (c): $\phi = 0.115$, (d): $\phi = 0.338$. In each panel, the gray zone delimited by black dashed lines represent a the periodic box dimensions.

The time evolution of the mean square displacement for several ϕ informs that after a transitory ballistic regime, the droplets among a dilute assembly ($\phi < 0.115$) have a global diffusive behaviour. We then define the self-diffusivity [127, 128]:

$$D_{\text{eff}} = \lim_{t \to \infty} \frac{\langle \Delta r^2 \rangle}{4t}, \tag{6.5}$$

which is reported for several ϕ on the panel (b) of Fig. 6.4 by fitting the long-time behaviour of the average mean-square displacement. As expected from the previous paragraph, increasing ϕ reduces D_{eff}. Besides, it seems that D_{eff} decreases exponentially as ϕ increases.

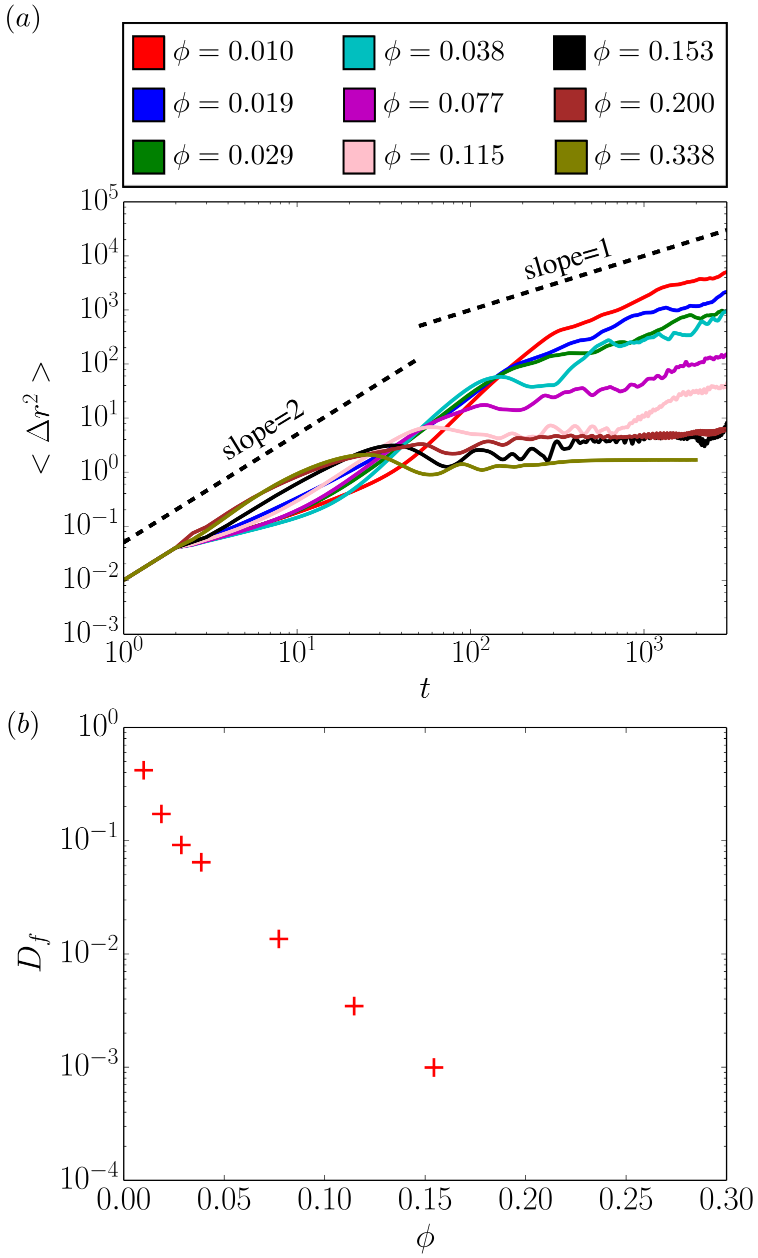

Figure 6.4: (a) Log-log time evolution of the mean square displacement $\langle \Delta r^2 \rangle$ for various densities (b): Semi-log evolution of the self-diffusivity D_{eff} as function of the density of droplets ϕ.

Finally, curious about the spatial structure of the droplet assembly, we introduce the time-averaged density correlation function:

$$g(r) = \left\langle \frac{1}{N_d} \sum_{i=1}^{N_d} \frac{\mathcal{N}^i_{r,dr}(t)}{2\pi r dr \phi} \right\rangle_t , \tag{6.6}$$

where $\mathcal{N}^i_{r,dr}$ denotes the number of droplets that lie between the circles of radii r and $r + dr$ both centred on the location of droplet i (where $dr = L_Y / N_y$ with N_y the number of grid points used along the y axis). This function is a useful tool to describe the structure of a system, and especially to detect if the assembly shares similarities with a dilute gas, a liquid or a crystalline structure [129, 130]. The panel (b) of Fig. 6.5 provides an example of typical evolutions of g for three states of argon at different temperatures (solid for

$T = 50K$, liquid for $T = 80K$, and gaseous for $T = 300K$). In the crystalline state, g to exhibit a series of peaks that suggest the presence of a regular lattice among the particles. Secondly, due to their ability to flow, liquids do not have such a periodic evolution and loose their long-range structure. Consequently, the function g for typical liquids performs damped oscillations over r and tends to 1 at large distances. Finally, the gas phase involves particles that do not have any regular structure and for which g decays rapidly to 1.

We report on the panel (a) of Fig. 6.5 the evolution of g for three different active droplet densities ($\phi = 0.029$, $\phi = 0.12$ and $\phi = 0.34$). The evolution of the spatial structure among the droplet assembly seems to share some similarities with the gas, liquid and crystalline phases. More time should be devoted to the study of the spatial structure of active droplet assemblies. In particular, we expect that considering much more droplets and larger boxes would enable to obtain a smoother g function and a more regular hexagonal lattice in the case of denser assemblies.

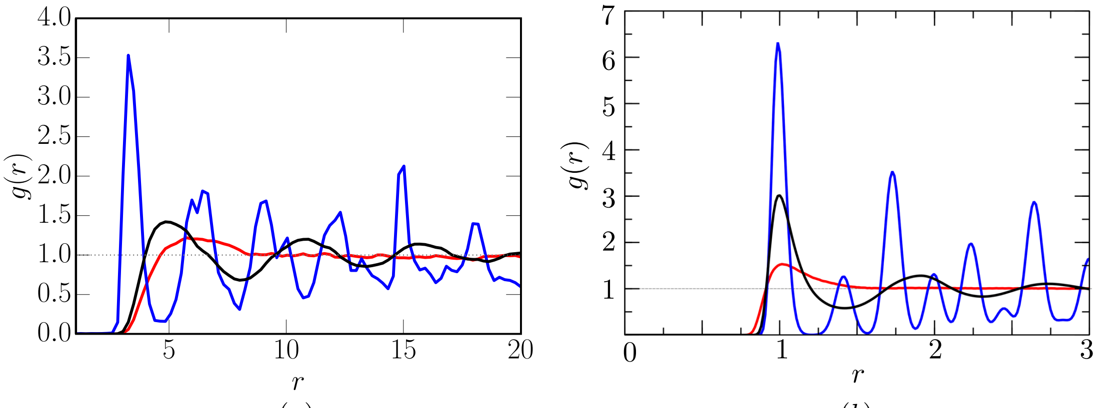

(a) (b)

Figure 6.5: Evolution of the time averaged radial correlation function g for (a) an assembly of active droplets at $\phi = 0.029$ in red, $\phi = 0.12$ in black and $\phi = 0.34$ in blue, and (b) molecules of argon at the gas state ($T = 300K$) in red, at the liquid state ($T = 80K$) in black and at the solid-state ($T = 50K$) in blue. While in (a), r is the radial distance per unit of the droplets' radii, in (b), r is expressed in terms of the molecular diameter $d_{\text{mol}} = 3.822Å$.

6.2.2 Ephemeral alignment and multi-body interactions

Recently, the results of Ref. [62] showed that groups of droplets confined in a Hele-Shaw cell may exhibit ephemeral collective dynamics. Indeed, several droplets are observed to swim side-by-side and form a small unstable line that breaks after having travelled a distance of few radii. If far-field hydrodynamic interactions were considered in Ref. [62], we may wonder if such lines can still be observed considering the influence of chemical interactions only. Since an active droplet is a pusher kind of swimmer (see chapter 2), we thus expect the hydrodynamic interactions between two side by side droplets to be attractive. On the contrary, due to its antichemotactic nature, we expect chemical interactions to be repulsive and not favour the formation of lines.

However, a diluted assembly of active droplets described by the moving singularity model introduced in chapter 5 appears to exhibit short periods of alignment. The panel (a) of Fig. 6.6 provides snapshots of the concentration field at $\mathrm{Pe} = 6$ involving $N_d = 6$ active droplets of unit radius which swim in the same plane of a periodic cubic box of side $L = 60$. We notice the formation of small groups (indicated by red and yellow circles) that swim side by side and in the same direction for a distance a few radii before being scattered. Within a group, the droplet in the middle feels the chemical repulsion which comes from the ones on its sides and appears somehow to be chemically guided. Furthermore, when increasing the number of active droplets inside the box, such temporal alignment seems to result in complex multi-body interactions as illustrated on the panel (b) of Fig. 6.6. Multi-body interactions thus deserve to be studied more carefully and is identified as a possible future project.

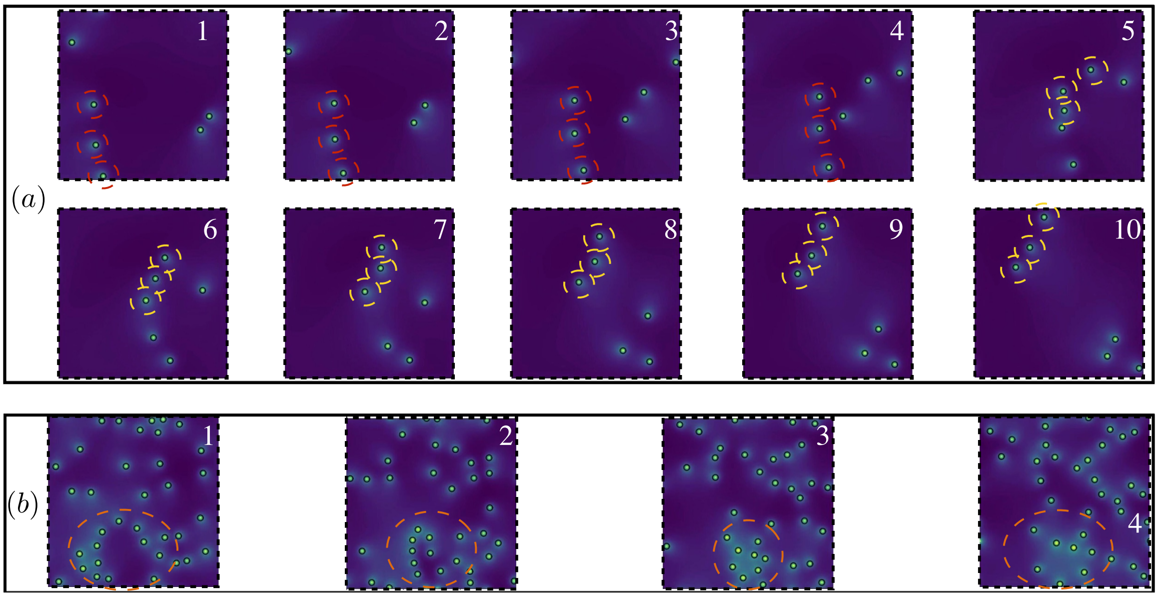

Figure 6.6: (a): Snapshots of the concentration field obtained from numerical simulations (*moving singularity model*) involving $N_d = 6$ active droplets that swim in a cubic periodic box of size $L = 60$ (in units of radius) at $\mathrm{Pe} = 6$. The red and yellow dashed circles identify two groups of three active droplets that swim together for a distance of few radii. (b): Snapshots of the concentration field obtained at $\mathrm{Pe} = 6$ with the same numerical approach as in (a) for $N_d = 36$ active droplets in a cubic and periodic box of size $L = 60$. The droplets involved in a complex multi-body interaction are surrounded by a dashed orange line. In both panels, the time between each snapshot is constant and taken to 30 (in units of R/V^*).

6.2.3 Poly-disperse assembly of active droplets

As mentioned at the end of chapter 4, the recent experiments of Ref. [63] enable us to identify that velocity differences among interacting droplets, when placed in a microfluidic capillary beforehand, can lead to one-dimensional collective dynamics. The physical origin of such train formations still remains an open question. As the droplets solubilise, they shrink and thus slow down over time. Size heterogeneity appears therefore as a possible route to observe interacting droplets at various velocities. As a consequence, we may hope to notice such collective dynamics in studying a poly-disperse assembly of active droplets.

If the full hydro-chemical interactions between an assembly of active droplets in a capillary appear intractable, we may use the exact results of chapters 3 and 4 as benchmarks to develop more reduced models. First, we may think of using the moving singularity model of chapter 5, which may be easily adapted to deal with droplets of various sizes. Indeed, active droplets are modelled by a superimposition of chemical singularities, whose intensities may be tuned to represent either smaller or larger droplets. Then, we may first focus on collisions between identical droplets at a higher Pe to assess the ability of the reduced model to reproduce the velocity plateau phenomenon which occurs as the result of their apparent "chemical inertia". If the moving singularity model fails to describe a similar behaviour, we can think of adding higher-order chemical singularities, whose intensities may be chosen to reproduce at best the effective collision dynamics provided at the end of chapter 3. If conclusive, such an enhanced model may thus be used (*i*) to see if the regimes identified in chapter 4 may be reproduced by a significantly simpler model and (*ii*) to study an assembly of active droplets of various radii, evolving along the same axis, to see if the minimal ingredients introduced in the model are sufficient to notice the one-dimensional collective motion observed experimentally in Ref. [63].

Finally, such an enhanced version of the reduced model may thus be used to investigate the situation of poly-disperse assemblies of droplets that are free to move in the entire plane or volume. Even if an assembly of active droplets is always poly-dispersed in the experiments, the situation of significant size difference has not yet been broached. Such a numerical study would be a way to identify possible new regimes of interest that are worth exploring. In effect, it is not an easy task to predict the behaviour of the assembly, which would likely depend on the packing fraction, on the proportion of large droplets and finally on the Péclet number. We may, for instance, witness a situation where the big droplets, being faster and more chemically active, dominate the global motion and drive the trajectory of the small ones, as herding dogs would do with a group of sheep. On the contrary, it would also be possible to see the large droplets, ceaselessly disturbed in their motion by frequent collisions with smaller ones, remain almost at the same location as the result of their larger 'chemical inertia". In such a case, we may observe two existing phases, where the large droplets would appear as a rigid matrix, inside which the smaller droplets swim.

Inspired (*i*) by the collective motion observed in the experiments of Ref. [63] and (*ii*) by yet unexplored poly-disperse regimes, studying the influence of the size heterogeneity in an assembly of active droplets appears thus as a promising subject.

6.2.4 Generic collisions in bi-spherical coordinates

Let us consider the experiments of Ref. [36] that considers an assembly of active droplets inside a circular arena. In this situation, we may sometimes notice an active droplet that slides on the curved wall of the arena. Besides, experiments of Ref. [121] noticed such a sliding behaviour when an active droplet collides against a circular pillar. An apparent balance between a hydrodynamic attraction and a chemical repulsion enables the droplet to orbit around the pillar.

An accurate description of oblique collisions involving both hydrodynamic and chemical interactions appears then essential to properly describe such a subtle phenomenon. Adapting the approach of chapter 3 using generic bi-spherical coordinates system would enable first to obtain exact results between a droplet sliding on a wall and also examine the influence of the hydrodynamic interactions in the oblique collision dynamics presented in chapter 5.

First, let us remind the experimental results of Ref. [58], which have shown that a single droplet may perform perpendicular reorientations as a result of the spontaneous emergence of a quadrupolar flow field. In this particular situation, the flow transports the solute on one side of the droplet, leading to its lateral propulsion. On the other hand, chapter 3 tells us that at sufficiently high Pe, a significant quadrupolar flow field emerges when the droplets are about to rebound.

Secondly, let us thus consider a small deviation from the perfect head-on collision model of chapter 3. In this case, the droplets collide almost frontally. Similarly to the axisymmetric collision, we expect the bigger droplet to be, at least temporarily, trapped by the chemical repulsion from the small one and its own solute wake. However, because the collision is not perfectly frontal, advection may transport the solute from the front and back of the bigger droplet towards one of its sides. As a result, the bigger droplet would swim in a direction orthogonal to its initial one. This situation is not expected to differ much from the case of an active droplet that collides almost frontally with rigid wall (as seen in chapter 3 for head-on collision). Consequently, a droplet that ends up swimming orthogonally to its initial direction would then appear to slide over the wall.

Moreover, it would be interesting to compare the theoretical flow field induced by an active droplet swimming parallel to a rigid wall with the one noticed in the recent experiments of Ref. [75]. It would provide a theoretical insight regarding the origin of the monopolar flow field that emerges from chemical interaction with the wall. Finally, such a model would enable to examine the robustness of the behaviours identified in chapter 4 when the droplets are not involved in a head-on collision.

APPENDICES

A

EXACT INTERACTION MODEL: MATHEMATICAL FRAMEWORK AND BI-SPHERICAL COORDINATES

In this appendix, we provide the mathematical framework necessary for the use of bi-spherical coordinates applied to the axi-symmetric collision of two self-propelled active droplets. After a brief introduction of the Legendre polynomials, we introduce the adapted bi-spherical coordinates in the generic problem of two spheres of different radii. The following parts are dedicated to the projection of the advection-diffusion equation together with the hydrodynamical problem. Finally, we provide some asymptotic computations regarding the equilibrium state between two active droplets of distincts sizes.

Contents

A.1 Legendre polynomials

In this section we provide some useful properties of the Legendre polynomials which have been used in the bi-spherical approach as a decomposition basis for both hydrodynamical and concentration fields. The Legendre polynomials are named after Adrien-Marie Legendre, who discovered them in 1782 and are a system of orthogonal polynomials. If several manners exist to define them, one can consider they are solution of the Legendre's differential equation:

$$\frac{d}{dx}\left[(1-x^2)\frac{dL_n(x)}{dx}\right] + n(n+1)L_n(x) = 0. \tag{A.1}$$

Furthermore, they satisfy the following orthogonal property for $n, m \in \mathbb{Z}$:

$$\int_{-1}^{1} L_m(x)L_n(x)\mathrm{d}x = \frac{2}{2n+1}\delta_{nm}, \tag{A.2}$$

where δ_{nm} is the Kronecker delta function. For illustration purposes, we provide the first six Legendre polynomials which are plotted on Fig. A.2:

$$\begin{aligned} L_0(x) = 1, \quad L_1(x) = x, \quad L_2(x) = \frac{3x^2-1}{2}, \quad L_3(x) = \frac{5x^3-3x}{2} \\ L_4(x) = \frac{35x^4-30x^2+3}{8}, \quad L_5(x) = \frac{63x^5-70x^3+15x}{8}. \end{aligned} \tag{A.3}$$

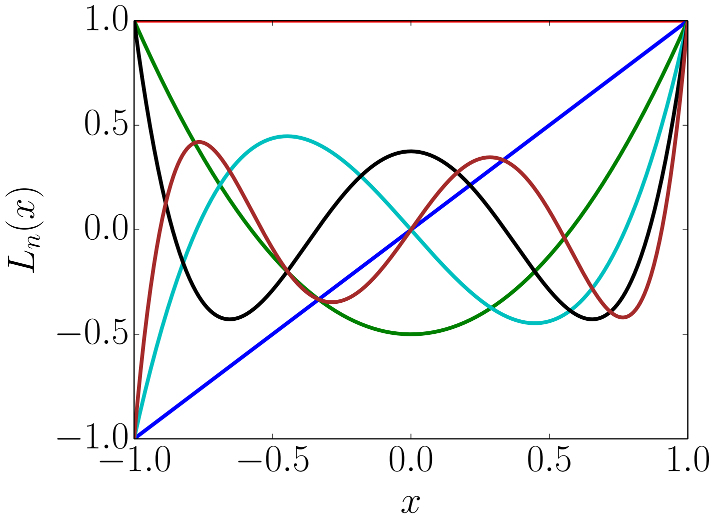

Figure A.1: Legendre polynomials L_n for $n \in \{0, 1, 2, 3, 4, 5\}$ (respectively red, blue, green, cyan, black and brown) as function of $x \in [-1, 1]$

An additional useful property of the Legendre polynomials is called the multipole expansion:

$$\frac{1}{\sqrt{1+\eta^2-2\eta x}} = \sum_{k=0}^{\infty} \eta^k L_k(x), \tag{A.4}$$

used repeatedly in the projection computations of the diffusion-advection equation in the bi-spherical coordinates system, for the particular case of $\eta = 1$. Finally, we conclude this section with some useful properties satisfied by the Legendre polynomials:

$$L_n(-x) = (-1)^n L_n(x), \tag{A.5}$$

in addition to the Bonnet's recursion formulas:

$$\begin{aligned} (n+1)L_{n+1}(x) &= (2n+1)xL_n(x) - nL_{n-1}(x), & \text{(A.6)} \\ \frac{x^2-1}{n}\frac{dL_n(x)}{dx} &= xL_n(x) - L_{n-1}(x). & \text{(A.7)} \end{aligned}$$

A.2 Adapted bi-spherical coordinates system

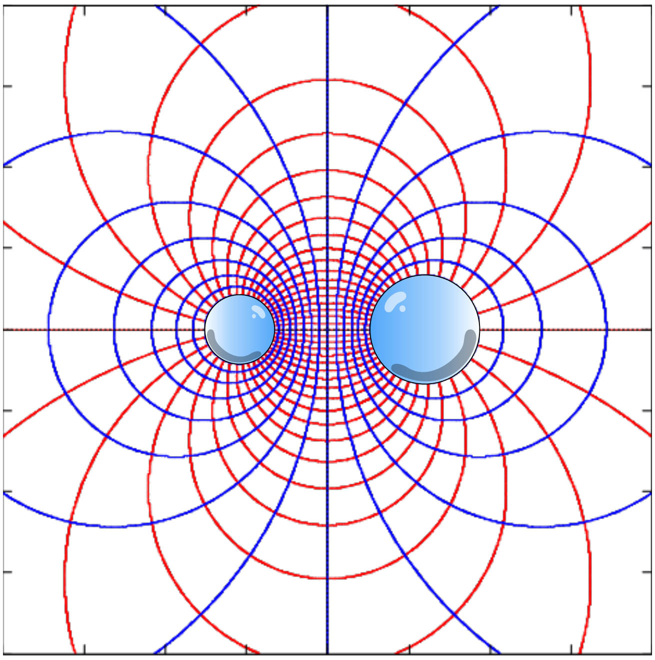

Figure A.2: Bi-spherical grid where both droplets correspond to τ_1 and τ_2, where iso-τ are plotted in blue and iso-μ in red.

In the general situation of two spheres of radii R_1 and R_2 located at a distance respectively $d_1 = R_1 \cosh \tau_1$ and $d_2 = R_2 \cosh \tau_2$ from the origin of the bi-spherical coordinates, the relations between the cylindrical coordinates system and the bi-spherical one read:

$$\begin{aligned} \rho &= \frac{a(t)\sqrt{1-\mu^2}}{\cosh(\alpha(t)\xi + \beta(t)) - \mu}, & \text{(A.8)} \\ z &= z_0 + \frac{a(t)\sinh(\alpha(t)\xi + \beta(t))}{\cosh(\alpha(t)\xi + \beta(t)) - \mu}, & \text{(A.9)} \end{aligned}$$

for which

$$\begin{aligned}
\alpha(t) &= \frac{\tau_1(t)-\tau_2(t)}{2}, && \text{(A.10)}\\
\beta(t) &= \frac{\tau_1(t)+\tau_2(t)}{2}, && \text{(A.11)}\\
a(t) &= R_1 \sinh\tau_1(t) = -R_2\sinh\tau_2(t), && \text{(A.12)}
\end{aligned}$$

where $\xi \in [-1,1]$ and $z_0(t)$ is the position of the origin of the bi-spherical system. The concentration field $c(\xi,\mu,t)$ in the new fitting grid coordinates system is linked to the concentration field $C(\rho,z,t)$ in the cylindrical one through:

$$\begin{bmatrix} \partial_\xi c|_{t,\mu} \\ \partial_\mu c|_{\tau,t} \\ \partial_t c|_{\tau,\mu} \end{bmatrix} = \begin{bmatrix} A_\xi & B_\xi & 0 \\ A_\mu & B_\mu & 0 \\ A_t & B_t & 1 \end{bmatrix} \cdot \begin{bmatrix} \partial_\rho C|_{t,z} \\ \partial_z C|_{t,\rho} \\ \partial_t C|_{\rho,z} \end{bmatrix} \tag{A.13}$$

With

$$\begin{aligned}
A_i &= \frac{\partial \rho}{\partial i} = \frac{\partial}{\partial i}\Big(\frac{a(t)\sqrt{1-\mu^2}}{\cosh(\alpha(t)\xi+\beta(t))-\mu}\Big) && \text{(A.14)}\\
B_i &= \frac{\partial z}{\partial i} = \frac{\partial}{\partial i}\Big(z_0(t) + \frac{a(t)\sinh(\alpha(t)\xi+\beta(t))}{\cosh(\alpha(t)\xi+\beta(t))-\mu}\Big), && \text{(A.15)}
\end{aligned}$$

where $i = \xi, \mu, t$. Inverting the previous relation we get:

$$\begin{bmatrix} \partial_\rho C|_{t,z} \\ \partial_z C|_{t,\rho} \\ \partial_t C|_{\rho,z} \end{bmatrix} = \frac{1}{A_\xi B_\mu - B_\xi A_\mu} \begin{bmatrix} B_\mu & -B_\xi & 0 \\ -A_\mu & A_\xi & 0 \\ A_\mu B_t - B_\mu A_t & -(A_\xi B_t - B_\xi A_t) & A_\xi B_\mu - B_\xi A_\mu \end{bmatrix} \cdot \begin{bmatrix} \partial_\xi c|_{t,\mu} \\ \partial_\mu c|_{\xi,t} \\ \partial_t c|_{\xi,\mu} \end{bmatrix} \tag{A.16}$$

$$\begin{aligned}
A_\xi &= -\frac{a(t)\sqrt{1-\mu^2}\sinh(\alpha(t)\xi+\beta(t))\alpha(t)}{(\cosh(\alpha(t)\xi+\beta(t))-\mu)^2} && \text{(A.17)}\\
B_\xi &= -\frac{a(t)\alpha(t)(\mu\cosh(\alpha(t)\xi+\beta(t))-1)}{(\cosh(\alpha(t)\xi+\beta(t))-\mu)^2} && \text{(A.18)}\\
A_\mu &= -\frac{a(t)(\mu\cosh(\alpha(t)\xi+\beta(t))-1)}{\sqrt{1-\mu^2}(\cosh(\alpha(t)\xi+\beta(t))-\mu)^2} && \text{(A.19)}\\
B_\mu &= \frac{a(t)\sinh(\alpha(t)\xi+\beta(t))}{(\cosh(\alpha(t)\xi+\beta(t))-\mu)^2} && \text{(A.20)}\\
A_t &= \frac{\sqrt{1-\mu^2}(\dot{a}(t)(\cosh(\alpha(t)\xi+\beta(t))-\mu) - a(t)\left(\dot{\alpha}\xi+\dot{\beta}\right)\sinh(\alpha(t)\xi+\beta(t)))}{(\cosh(\alpha(t)\xi+\beta(t))-\mu)^2} && \text{(A.21)}\\
B_t &= \dot{z}_0(t)\\
&+ \frac{\dot{a}(t)\sinh(\alpha(t)\xi+\beta(t))(\cosh(\alpha(t)\xi+\beta(t))-\mu) + a(t)\left(\dot{\alpha}\xi+\dot{\beta}\right)(1-\cosh(\alpha(t)\xi+\beta(t))\mu)}{(\cosh(\alpha(t)\xi+\beta(t))-\mu)^2} && \text{(A.22)}
\end{aligned}$$

Those relations lead to:

$$\begin{aligned}
\frac{A_\mu B_t - A_t B_\mu}{A_\xi B_\mu - A_\mu B_\xi} &= \frac{\dot{a}\mu\sinh(\alpha\xi+\beta)}{\alpha a} - \frac{(\dot{\alpha}\xi+\dot{\beta})}{\alpha} - \dot{z}_0(t)\frac{1-\mu\cosh(\alpha\xi+\beta)}{\alpha a} && \text{(A.23)}\\
\frac{A_\xi B_t - A_t B_\xi}{A_\xi B_\mu - A_\mu B_\xi} &= \dot{z}_0(t)\frac{(1-\mu^2)\sinh(\alpha\xi+\beta)}{a} + \frac{\dot{a}}{a}(1-\mu^2)\cosh(\alpha\xi+\beta) && \text{(A.24)}
\end{aligned}$$

Finally we get the relation:

$$\begin{aligned}\partial_t C|_{\rho,z} &= \left.\frac{\partial c}{\partial t}\right|_{\xi,\mu} + \left(\frac{\dot a\mu\sinh(\alpha\xi+\beta)}{\alpha a} - \frac{(\dot\alpha\xi+\dot\beta)}{\alpha} - \dot z_0(t)\frac{1-\mu\cosh(\alpha\xi+\beta)}{\alpha a}\right)\left.\frac{\partial c}{\partial\xi}\right|_{t,\mu} \\ &- \left(\dot z_0(t)\frac{(1-\mu^2)\sinh(\alpha\xi+\beta)}{a} + \frac{\dot a}{a}(1-\mu^2)\cosh(\alpha\xi+\beta)\right)\left.\frac{\partial c}{\partial\mu}\right|_{\xi,t} \qquad (\text{A.25})\end{aligned}$$

In the particular case of a droplet that collide with a wall we get $z_0(t) = 0$, $\xi \in [0,1]$, $\alpha = \lambda$ and $\beta = 0$ and thus the previous expression simplifies to:

$$\partial_t C|_{\rho,z} = \left.\frac{\partial c}{\partial t}\right|_{\xi,\mu} + \left(\frac{\dot a\mu\sinh(\lambda\xi)}{\lambda a} - \frac{\dot\lambda\xi}{\lambda}\right)\left.\frac{\partial c}{\partial\xi}\right|_{t,\mu} - \frac{\dot a}{a}(1-\mu^2)\cosh(\lambda\xi)\left.\frac{\partial c}{\partial\mu}\right|_{\xi,t} \qquad (\text{A.26})$$

which provides the relation:

$$\boldsymbol{\chi}\cdot\boldsymbol{\nabla}c = \left(\frac{\dot\lambda\xi}{\lambda} - \frac{\dot a\mu\sinh(\lambda\xi)}{\lambda a}\right)\frac{\partial c}{\partial\xi} + \frac{\dot a}{a}(1-\mu^2)\cosh(\lambda\xi)\frac{\partial c}{\partial\mu}. \qquad (\text{A.27})$$

A.3 Projection of the advection-diffusion equation

In the following, for simplicity, we consider the particular case of the collision of an active droplet against a wall. As a result, $\xi \in [0,1]$, $\alpha = \lambda = \cosh^{-1}\left(\frac{d(t)}{R}+1\right)$, $a(t) = R\sqrt{d(t)(d(t)+2R)}$ and $\beta = 0$. We remind that the expression of the diffusion-advection equation in such specific coordinates system reads:

$$\begin{aligned}&\sum_{n=0}^{\infty}\Bigg\{\frac{L_n}{\Gamma^{1/2}}\frac{\partial c_n}{\partial t} + \frac{\dot a}{a}\left[\frac{(1+\mu\cosh(\lambda\xi))L_n - 2\cosh(\lambda\xi)(1-\mu^2)L_n'}{2\Gamma^{1/2}}\right]c_n \\ &+ \left(\frac{\dot a\mu\sinh(\lambda\xi) - \dot\lambda\xi a}{\lambda a}\right)\frac{L_n}{\Gamma^{1/2}}\frac{\partial c_n}{\partial\xi} + \frac{1}{\lambda a^3}\sum_{k=1}^{\infty}\left[\left(\frac{3}{2}(1-\mu^2)L_k'L_n - k(k+1)\Gamma L_k L_n\right)U_k\frac{\partial c_n}{\partial\xi}\right. \\ &\left.+ \frac{\lambda\sinh(\lambda\xi)}{2}\left[3(1-\mu^2)L_k'L_n' - k(k+1)L_nL_k\right]U_kc_n + (1-\mu^2)L_k'\left(\frac{L_n}{2} - \Gamma L_n'\right)\frac{\partial U_k}{\partial\xi}c_n\right] \\ &\quad = \frac{\Gamma^{3/2}}{a^2\mathrm{Pe}}\sum_{n=0}^{\infty}\left(\frac{1}{\lambda^2}\frac{\partial^2 c_n}{\partial\xi^2} - \left(n+\frac{1}{2}\right)^2 c_n\right)L_n, \qquad (\text{A.28})\end{aligned}$$

where c_n and U_k are the modes relative to the concentration field and the streamfunction respectively. Using the multipole expansion (A.4) in the particular case of $\eta = 1$ we get:

$$\frac{1}{\Gamma^{1/2}} = \frac{1}{\sqrt{\cosh(\lambda\xi)-\mu}} = \sqrt{2}\sum_{k=0}^{\infty}L_k(\mu)\mathrm{e}^{-(p+1/2)|\lambda\xi|}, \qquad (\text{A.29})$$

enabling to compute the projection of (A.28) on the Legendre basis, which provides the following partial differential equation:

$$\begin{aligned}&\boldsymbol{H}\cdot\frac{\partial\tilde{\boldsymbol{C}}}{\partial t} + \left(\boldsymbol{B}^1\cdot\boldsymbol{U} + \boldsymbol{B}^2\cdot\frac{\partial\boldsymbol{U}}{\partial\xi} + \boldsymbol{G}^1\right)\cdot\tilde{\boldsymbol{C}} \\ &\qquad + \left(\boldsymbol{B}^3\cdot\boldsymbol{U} + \boldsymbol{G}^2\right)\cdot\frac{\partial\tilde{\boldsymbol{C}}}{\partial\xi} = \frac{1}{\mathrm{Pe}}\left(\boldsymbol{A}^1\cdot\tilde{\boldsymbol{C}} + \boldsymbol{A}^2\cdot\frac{\partial^2\tilde{\boldsymbol{C}}}{\partial\xi^2}\right), \qquad (\text{A.30})\end{aligned}$$

for which $\tilde{\boldsymbol{C}}(\xi,t) = [c_0(\xi,t), c_1(\xi,t), ..., c_N(\xi,t)]$, and the others terms can be obtained as:

$$H_{pn} = \sqrt{2}\sum_{k=0}^{\infty} Q^0_{knp} e^{-(k+1/2)|\lambda\xi|}, \tag{A.31}$$

$$G^1_{pn} = \frac{\dot{a}}{a\sqrt{2}}\sum_{k=0}^{\infty}\left(Q^0_{knp} + \cosh(\lambda\xi)Q^1_{knp} - 2\cosh(\lambda\xi)R^0_{knp}\right) e^{-(k+1/2)|\lambda\xi|}, \tag{A.32}$$

$$G^2_{pn} = \sqrt{2}\sum_{k=0}^{\infty}\left(\frac{\dot{a}\sinh(\lambda\xi)}{a\lambda}Q^1_{knp} - \frac{\dot{\lambda}\xi}{\lambda}Q^0_{knp}\right) e^{-(k+1/2)|\lambda\xi|}, \tag{A.33}$$

$$B^1_{pnk} = \frac{1}{a^3}\left(\frac{3\sinh(\lambda\xi)}{2}S^0_{knp} - \frac{k(k+1)}{2}\sinh(\lambda\xi)Q^0_{knp}\right), \tag{A.34}$$

$$B^2_{pnk} = \frac{1}{\lambda a^3}\left(-\cosh(\lambda\xi)S^0_{knp} + S^1_{knp} + \frac{1}{2}R^0_{nkp}\right), \tag{A.35}$$

$$B^3_{pnk} = \frac{1}{\lambda a^3}\left(\frac{3}{2}R^0_{nkp} - k(k+1)\left(\cosh(\lambda\xi)Q^0_{knp} - Q^1_{knp}\right)\right), \tag{A.36}$$

$$A^2_{pn} = \frac{\sqrt{2}}{\lambda^2 a^2}\sum_{k=0}^{\infty}\left(\cosh^2(\lambda\xi)Q^0_{knp} - 2\cosh(\lambda\xi)Q^1_{knp} + Q^2_{knp}\right) e^{-(k+1/2)|\lambda\xi|}, \tag{A.37}$$

$$A^1_{pn} = -\lambda^2\left(n+\frac{1}{2}\right)^2 A^2_{pn}. \tag{A.38}$$

where Q^i_{knp}, R^i_{knp} and S^i_{knp} are the following integrals of Legendre polynomials:

$$Q^i_{knp} = \int_{-1}^{1}\mu^i L_n L_k L_p \mathrm{d}\mu, \tag{A.39}$$

$$R^i_{knp} = \int_{-1}^{1}\mu^i(1-\mu^2)L'_n L_k L_p \mathrm{d}\mu = \frac{n(n+1)}{2n+1}\left(Q^i_{k,n-1,p} - Q^i_{k,n+1,p}\right), \tag{A.40}$$

$$S^i_{knp} = \int_{-1}^{1}\mu^i(1-\mu^2)L'_n L'_k L_p \mathrm{d}\mu, \tag{A.41}$$

and can be obtained recursively using classical relations between Legendre polynomials [131]:

$$Q^0_{0,n,p} = \frac{2}{2p+1}\delta_{n,p}, \qquad Q^0_{1,n,p} = \frac{n+1}{2n+1}\delta_{p,n+1} + \frac{n}{2n+1}\delta_{p,n-1}, \tag{A.42}$$

$$Q^0_{k,n,p} = \frac{2k-1}{k}\left(\frac{n+1}{2n+1}Q^0_{k-1,n+1,p} + \frac{n}{2n+1}Q^0_{k-1,n-1,p}\right) - \frac{k-1}{k}Q^0_{k-2,n,p}, \tag{A.43}$$

$$Q^i_{0,n,p} = Q^{i-1}_{1np}, \qquad Q^i_{k,n,p} = \frac{k+1}{2k+1}Q^{i-1}_{k+1,n,p} + \frac{k}{2k+1}Q^{i-1}_{k-1,n,p}, \tag{A.44}$$

$$S^i_{0,n,p} = S^i_{n,0,p} = 0, \qquad S^0_{k,n,p} = S^0_{k-1,n,p} + (2k-1)R^0_{k-1,n,p}, \tag{A.45}$$

$$S^i_{k,n,p} = S^{i-1}_{k+1,n,p} - (k+1)R^{i-1}_{k,n,p}. \tag{A.46}$$

A.4 Projection of the hydrodynamic boundary conditions

In order to solve Eq. (A.30) one should compute the modes U_k which determine the streamfunction $\psi^{(i,o)}$, and thus the flow field around the droplets. Substituting the definition of $\psi^{(i,o)}$, Eq. (3.20), as well as Eq. (A.29) into Eqs. (3.24) and (3.25) leads after projection onto $(1-\mu^2)L'_n$ to:

$$U^i_n\big|_{\xi=1} = U^o_n\big|_{\xi=1} = \frac{\sqrt{2}va^2}{2}\left(\frac{e^{-(n-1/2)|\lambda|}}{2n-1} - \frac{e^{-(n+3/2)|\lambda|}}{2n+3}\right), \tag{A.47}$$

$$\left.\frac{\partial U^o_n}{\partial \xi}\right|_{\xi=1} = \left.\frac{\partial U^i_n}{\partial \xi}\right|_{\xi=1}. \tag{A.48}$$

Similarly, at the wall surface, the no-slip conditions simply reads:

$$U_{n,o}\big|_{\xi=0} = 0, \tag{A.49}$$

$$\left.\frac{\partial U_{n,o}}{\partial \xi}\right|_{\xi=0} = 0. \tag{A.50}$$

The tangential shear stress at the surface of the droplet is obtained as:

$$\sigma^{i,o}_{\xi\mu}\Big|_S = -\frac{\Gamma^{3/2}}{a^3}\sum_{n=1}^{\infty}\sqrt{1-\mu^2}L'_n\left[\frac{1}{\lambda^2}\frac{\partial^2 U^{i,o}_n}{\partial \xi^2} + \left(n(n+1) - \frac{3}{4}\left(1+\frac{2\sinh(\lambda\xi)^2}{\Gamma^2}\right)\right)U^{i,o}_n\right] \tag{A.51}$$

and substitution into the Marangoni condition, Eq. (3.26), provides the following condition at the droplet surface ($\xi = 1$):

$$\sum_{n=1}^{\infty} L'_n\left\{\frac{\Gamma^2}{\lambda^2}\left(\frac{\partial^2 U^o_n}{\partial \xi^2} - \tilde{\eta}\frac{\partial^2 U^i_n}{\partial \xi^2}\right) + \left[\left(n^2+n-\frac{3}{4}\right)\Gamma^2 - \frac{3}{2}\sinh^2(\lambda\xi)\right]\left(U^o_n - \tilde{\eta}U^i_n\right)\right\}\Bigg|_{\xi=1}$$
$$= -(2+3\tilde{\eta})a^2\sum_{n=0}^{\infty}\left[c_n\left(-\frac{\Gamma L_n}{2} + \Gamma^2 L'_n\right)\right]\Bigg|_{\xi=1} \tag{A.52}$$

Projecting the previous equation onto $(1-\mu^2)L'_p(\mu)$ finally leads to:

$$\sum_{n=1}^{\infty}\frac{\bar{S}_{np}(\lambda)}{\lambda^2}\left[\frac{\partial^2 U^o_n}{\partial \xi^2} - \tilde{\eta}\frac{\partial^2 U^i_n}{\partial \xi^2} + \lambda^2\left(n^2+n-\frac{3}{4}\right)\left(U^o_n - \tilde{\eta}U^i_n\right)\right]\Bigg|_{\xi=1}$$
$$-\frac{3p(p+1)\sinh^2\lambda}{2p+1}\left(U^o_p - \tilde{\eta}U^i_p\right)\big|_{\xi=1} = (2+3\tilde{\eta})a^2\sum_{n=0}^{\infty}\left[\frac{\bar{R}_{np}(\lambda)}{2} - \bar{S}_{np}(\lambda)\right]c_n\big|_{\xi=1}, \tag{A.53}$$

where the functions $\bar{S}_{np}(\lambda)$ and $\bar{R}_{np}(\lambda)$ are computed from the different integrals in Eqs. (A.39)–(A.46) as:

$$\bar{S}_{np}(\lambda) = S^0_{np0}\cosh^2\lambda - 2S^1_{np0}\cosh\lambda + S^2_{np0}, \qquad \bar{R}_{np}(\lambda) = R^0_{np0}\cosh\lambda - R^1_{np0}. \tag{A.54}$$

A.5 Projection of the concentration boundary conditions

While the vanishing property of the concentration field at infinity is ensured by its chosen form Eq. (3.28), the constant emission rate of solute (resp. no flux) at the surface of the droplet (resp. at the wall) equation (3.3) are expressed in the bi-spherical coordinates system:

$$\frac{\cosh(\lambda\xi)-\mu}{\lambda a}\frac{\partial c}{\partial \xi}=-1, \quad \frac{\partial c}{\partial \xi}=0, \tag{A.55}$$

which are also projected on the Legendre modes, providing the following additional relations for the c_p modes:

$$\lambda\sinh(\lambda)c_p(1)+2\cosh(\lambda)c_p'(1)-\frac{2(p+1)}{2p+3}c_{p+1}'(1)-\frac{2p}{2p-1}c_{p-1}'(1) = -2a\lambda\sqrt{2}e^{-(p+1/2)|\lambda|} \tag{A.56}$$

$$2c_p'(0)-\frac{2(p+1)}{2p+3}c_{p+1}'(0)-\frac{2p}{2p-1}c_{p-1}'(0) = 0. \tag{A.57}$$

A.6 Equilibrium distance between active droplets of distinct sizes

In this section we provide more details about the equilibrium distance given by Eq. (4.9) while keeping the same notation of chapter 4. First, we remind the leading order velocity of each droplet in the particular case where droplet 1 is chasing the droplet 2:

$$v_1 = \frac{v_{0,1}}{2}\left(1+\sqrt{1-\frac{256}{(\Delta\mathrm{Pe}_1)^2 d^2}}\right), \tag{A.58}$$

$$v_2 = \frac{v_{0,2}}{2}\left(1+\sqrt{1+\frac{256e^{-4d|v_1|}(1+4d|v_1|)}{(\Delta\mathrm{Pe}_2)^2 d^2}}\right), \tag{A.59}$$

where $v_{0,1} = (\mathrm{Pe}_i - \mathrm{Pe}_c)/16$. When the equilibrium state is reached, both droplets swim at the same velocity v_b, which provides the relation $v_1 = v_2 = v_b$. In the limit of almost same size droplets ($\xi - 1 \ll 1$) close to the self-propulsion threshold ($\mathrm{Pe}_2 - \mathrm{Pe}_c \ll 1$) we expect $d \gg 1$. At the leading order, Eqs. (A.58)–(A.59) become:

$$v_1 = \frac{v_{0,1}}{2}\left(1+\sqrt{1-\frac{256}{(\Delta\mathrm{Pe}_1)^2 d^2}}\right), \tag{A.60}$$

$$v_2 = v_{0,2}. \tag{A.61}$$

From the equilibrium condition $v_1 = v_2$, one obtains the following equation:

$$\frac{\xi^2\mathrm{Pe}_2 - \mathrm{Pe}_c}{32}\left(1+\sqrt{1-\frac{256}{(\xi^2\mathrm{Pe}_2 - \mathrm{Pe}_c)^2 d^2}}\right) = \frac{\mathrm{Pe}_2 - \mathrm{Pe}_c}{16}. \tag{A.62}$$

Solving Eq. (A.62) provides an unique positive solution of the separation distance, d_{eq}, which reads:

$$d_{\mathrm{eq}} = \frac{2\sqrt{2}}{\sqrt{(\mathrm{Pe}_2 - 4)(\xi - 1)}}, \tag{A.63}$$

where $\mathrm{Pe}_c = 4$ has been used.

B

MOVING SINGULARITY MODEL FOR SELF-PROPELLED ACTIVE DROPLETS

This appendix provides some calculation details of the reduced model of chapter 5. The first section aims to compute the concentration field generated by a point source-dipole, the second introduces the numerical approach, based on Fourier decomposition, used to compute the droplets' dynamics while imposing periodic boundary conditions. Finally, some details about the two degrees of freedom dynamics are given.

Contents

B.1 Point source-dipole concentration field

In this section we aim to compute the concentration field induced by the superposition at the location of the droplet $\boldsymbol{x}(t)$ of a source of unit intensity (total flux equals 4π) and a dipolar contribution whose intensity a_1 is chosen so that the self-propulsion velocity of the droplet matches the analytical one of [36]. Denoting by $\boldsymbol{v} = v\boldsymbol{p}$ the velocity of the droplet, the unsteady and dimensionless transport problem reads:

$$\mathrm{Pe}\frac{\partial c}{\partial t} = \nabla^2 c + 4\pi\Big(\delta_{\boldsymbol{x}(t)} + a_1 \boldsymbol{\nabla}\delta_{\boldsymbol{x}(t)} \cdot \boldsymbol{p}\Big). \tag{B.1}$$

As a result, the concentration field is a sum of all the contributions of the point source on its path, meaning:

$$\frac{c(\boldsymbol{r})}{4\pi} = \int_{-\infty}^{0} \Big(\boldsymbol{I} + a_1 \boldsymbol{p}\cdot\boldsymbol{\nabla}\Big) G(\boldsymbol{r} - \boldsymbol{x}(t), -t)\mathrm{d}t \tag{B.2}$$

$$G(\boldsymbol{r}, t) = \frac{1}{(4\pi D t)^{3/2}} e^{-\frac{r^2}{4Dt}}. \tag{B.3}$$

Interested in the steady state regime, the droplet's velocity is considered constant and thus $\boldsymbol{x}(t) = \boldsymbol{v}t$, which enables to compute the integral (B.2) [82]:

$$c(\boldsymbol{r}) = \frac{1}{r}\left[1 - a_1\left(\lambda + \left(\frac{1}{r} + \lambda\right)\frac{\boldsymbol{r}\cdot\boldsymbol{p}}{r}\right)\right] e^{-\lambda r\left(1 + \frac{\boldsymbol{r}\cdot\boldsymbol{p}}{r}\right)}, \tag{B.4}$$

where $\lambda = v\mathrm{Pe}/2$.

B.2 Numerical solution of the moving source model

The dynamics of N_d active droplets is obtained by solving Eqs. (5.1), (5.2) and (5.4) in a large periodic domain of dimensions (L_x, L_y, L_z). We therefore use a spectral decomposition of the concentration field in Fourier modes:

$$c(\boldsymbol{r}, t) = \sum_{l,m,n} \hat{c}_{l,m,n}(t) e^{2\pi i \boldsymbol{k}\cdot\boldsymbol{r}}, \tag{B.5}$$

where $\boldsymbol{k} = l/L_x \boldsymbol{e}_x + m/L_y \boldsymbol{e}_y + n/L_z \boldsymbol{e}_z$ with $(l, m, n) \in \mathbb{N}$. The velocity $\boldsymbol{v}_i$ of droplet i is then computed by substitution of Eq. (B.5) into Eq. (5.1), as:

$$\boldsymbol{v}_i = \sum_{l,m,n} \frac{\hat{c}_{l,m,n} e^{2\pi i \boldsymbol{k}\cdot\boldsymbol{x}_i}}{\pi k^2}\Big(\cos(2\pi k) - \mathrm{sinc}(2\pi k)\Big)\boldsymbol{k}. \tag{B.6}$$

B.3 Additional validations of the numerical method

Aiming to compare the diffusion dynamics numerically solved on chapters 5 and 6.2.1, we consider the canonic problem of a single source of intensity 4π located at the center $\boldsymbol{x}_0$ of a box of dimensions $L_x = L_y = L_z = 60$. The box is taken sufficiently large so that the influence of the boundary is negligible on the time scale considered. Consequently, the numerical solution may be compared with the case of a single source in an infinite medium. Keeping the same notations introduced on chapter 5, the solute dynamics satisfies:

$$\mathrm{Pe}\frac{\partial c(\boldsymbol{r},t)}{\partial t} = \nabla^2 c + 4\pi\delta(\boldsymbol{r} - \boldsymbol{x}_0). \tag{B.7}$$

Initially the box is empty ($c(\boldsymbol{r},0) = 0$), and we compare the evolution of the concentration field towards the steady state of a single source in an infinite medium. The solution of the latter may be computed analytically using Fourier transforms:

$$c_{\text{steady}}(\boldsymbol{r}) = \frac{1}{|\boldsymbol{r} - \boldsymbol{x}_0|}. \tag{B.8}$$

Concentration fields and intensity profiles are provided on Fig. B.1 at three different instants $t = 5, 50, 250$. The resulting good match between numerics with analytics thus confirms the validity of this part of the code.

Secondly, as mentioned on chapter 5, the total amount of solute keeps increasing due to the periodicity of the boundaries. In order to check the conservation of the amount of solute inside the box, we remind the unsteady diffusion equation satisfied by the c:

$$\mathrm{Pe}\frac{\partial c(\boldsymbol{r},t)}{\partial t} = \nabla^2 c(\boldsymbol{r},t) + 4\pi \sum_{i=1}^{N} \left(\mathbf{I} + \zeta(v_i)\boldsymbol{v}_i \cdot \boldsymbol{\nabla}\right) \delta(\boldsymbol{r} - \boldsymbol{x}_i(t)), \tag{B.9}$$

where $\boldsymbol{x}_i$ are the locations of the N_d active droplets. Integrating Eq. (B.9) on the whole box (of volume $\mathcal{V}$) and denoting by $\langle c\rangle_{\mathcal{V}} = (1/\mathcal{V}) \int_{\mathcal{V}} c(\boldsymbol{r},t)\mathrm{d}\mathcal{V}$ the volume averaged concentration, one can write:

$$\frac{d\langle c\rangle_{\mathcal{V}}(t)}{dt} = \frac{4\pi N_d}{\mathrm{Pe}\mathcal{V}}. \tag{B.10}$$

To obtain Eq. (B.10), we have used the problem's periodicity, which imposes a no-flux boundary condition for c on the boundaries. Since the right hand side of Eq. (B.10) is constant and reminding that $c(t = 0) = 0$, the average solute concentration reads:

$$\langle c\rangle_{\mathcal{V}}(t) = \frac{4\pi N_d}{\mathrm{Pe}\mathcal{V}} t. \tag{B.11}$$

The spectral method used in the numerics enables directly to identify the mode relative to the volume average. Fig. B.2 enables us to confront the time evolution of the latter with the analytical result of Eq. (B.11). The perfect matching thus directly ensures the amount of solute conservation in the simulations.

Finally, in order to check the validity of both computation and implementation of the dipole intensity, one compares the self-propulsion dynamics of a single active droplet in a periodic box ($L_x = L_z = 15$ an $L_y = 120$) obtained numerically with the exact dynamics provided on chapter 3. In particular, a fine balance between accuracy and numerical cost is reached for the following set of parameters:

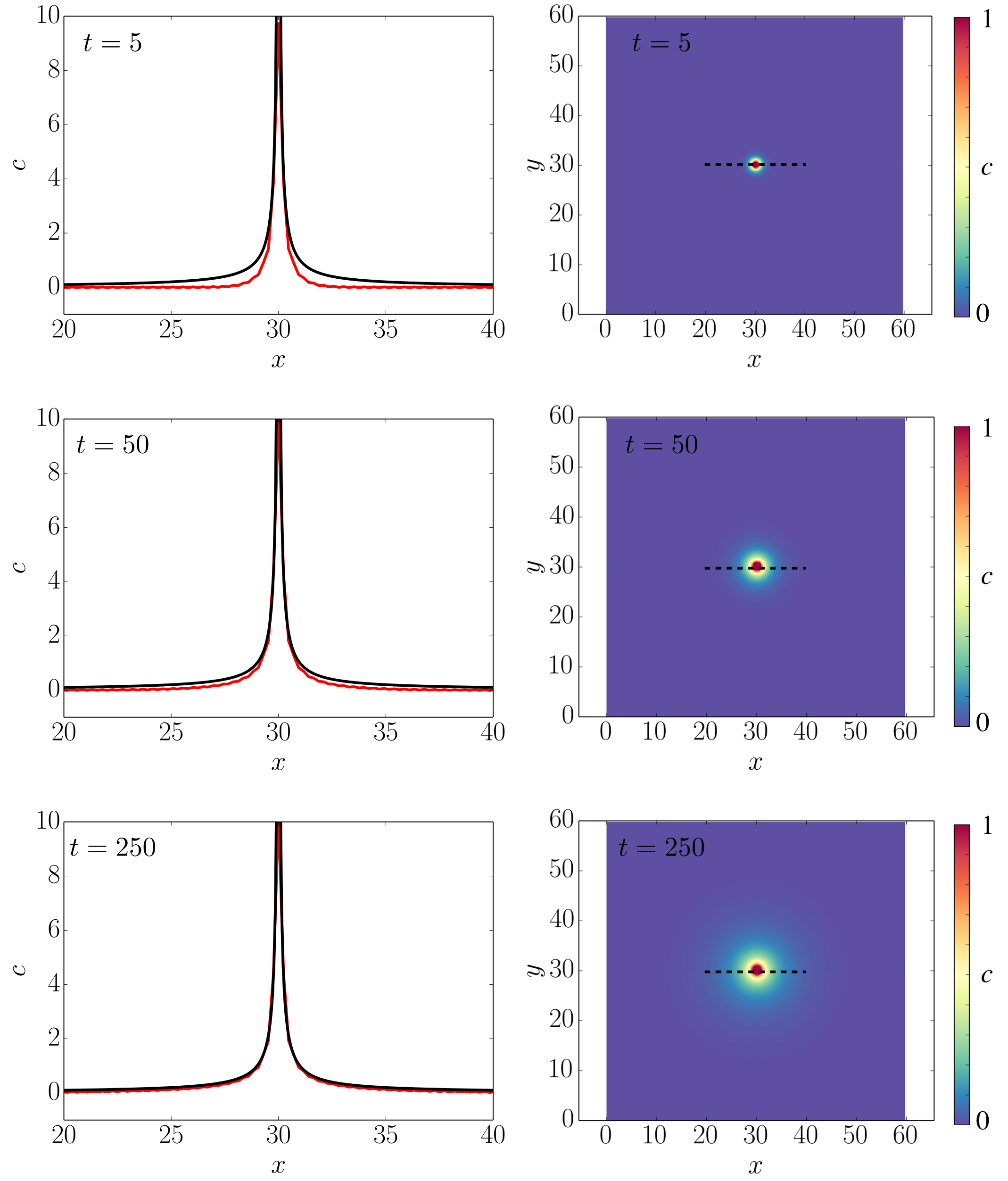

Figure B.1: Diffusion dynamics of a single and fixed point source. Right: concentration field generated by the source at three different instants $t = 5, 50, 250$. Left: Concentration profile on the regions marked by the black dashed on the concentration plots for the same respective instants $t = 5, 50, 250$.

- Number of grid points $N_x = N_z = 2^7$ and $N_y = 2^{10}$
- Time step $dt = 0.2$

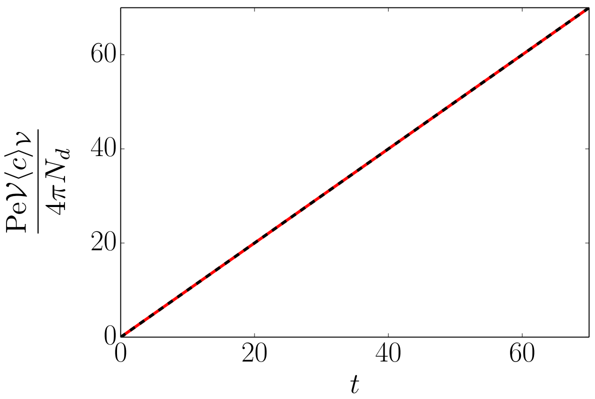

Figure B.2: Evolution of the solute concentration volume average $\langle c\rangle_{\mathcal{V}}$ as function of time. $N_d = 4$, $L_x = L_y = L_z = 60$ and $\mathrm{Pe} = 6$. Solid red line: numerics. Dashed blue line: analytical results of Eq. (B.11).

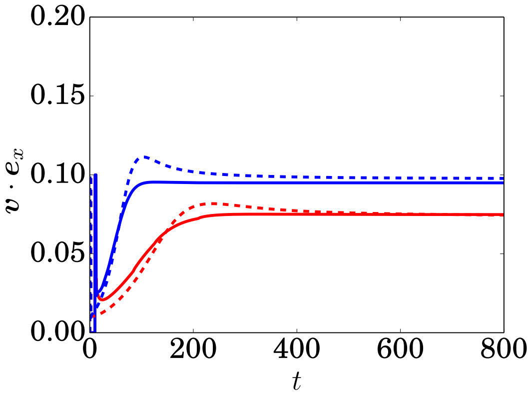

Figure B.3: Self-propulsion dynamics of a single active droplets at $\mathrm{Pe} = 6$ (red) and $\mathrm{Pe} = 8$ (blue). One compares the dynamics obtained with the reduced model (solid lines) and the exact one provided on chapter 3 (dashed lines).

First, the steady self-propulsion velocity, imposed by the choice of the dipole intensity, has a good match with the analytical results. Secondly, considering the significant simplifications introduced in the point source-dipole model, the transitory regime appears reasonably close to the exact one.

B.4 Simplified model for the evolution of the polarity evolution

For an isolated droplet in steady self-propulsion, we remind its velocity $\boldsymbol{v}$ and polarity $\boldsymbol{\Pi}$ are equal. Along the oblique collision with a second droplet, the self-propulsion still adjusts instantaneously to the chemical distribution in the Stokes regime, but the chemical polarity now results from the translation of the droplet and the unsteady diffusion of the chemical trail it leaves behind it. This introduces a finite relaxation time τ of the self-polarity, or wake, towards $\boldsymbol{v}$ (or to zero if the droplet stops moving). One can thus establish a simple model for the polarity dynamics as an overdamped relaxation:

$$\frac{d\boldsymbol{\Pi}_i}{dt} = \frac{1}{\tau}\left(\boldsymbol{v}_i - \boldsymbol{\Pi}_i\right). \tag{B.12}$$

As a result, the polarity magnitude $\Pi_i = |\boldsymbol{\Pi}_i|$ and direction $\boldsymbol{p}_i = \boldsymbol{\Pi}_i/\Pi_i$ satisfy:

$$\frac{d\Pi_i}{dt} = \frac{1}{\tau}\left(\boldsymbol{v}_i \cdot \boldsymbol{p}_i - \Pi_i\right) \tag{B.13}$$

$$\frac{d\boldsymbol{p}_i}{dt} = \frac{1}{\tau\Pi_i}(\boldsymbol{p}_i \times \boldsymbol{v}_i) \times \boldsymbol{p}_i. \tag{B.14}$$

In the following, we further neglect changes in magnitude of the polarity; as a consequence, the self-induced propulsion velocity (i.e. that due to the solute released by the droplet itself) has constant magnitude v_0 and $\Pi_i \approx v_0$, and the wake's orientational dynamics simplifies into:

$$\frac{d\boldsymbol{p}_i}{dt} = \frac{(\boldsymbol{p}_i \times \boldsymbol{v}_i) \times \boldsymbol{p}_i}{\tau v_0}. \tag{B.15}$$

Note that neglecting changes in the polarity magnitude is only valid when the wake reorganization is dominated by its reorientation (as in Fig. 5.7) and certainly does not hold for purely head-on collisions where the polarity must vanish in magnitude in order to reverse direction [89].

C

No net motion for oscillating near-spheres at low Reynolds numbers

We investigate the flow around an oscillating nearly-spherical particle at low, yet non-vanishing, Reynolds numbers, and the potential resulting locomotion. We analytically demonstrate that no net motion can arise up to order one in Re and order one in the asphericity parameter, regardless of the particle's shape. Therefore, geometry-induced acoustic streaming propulsion, if any, must arise at higher order [132]

This project initially started during my Master internship between Ecole des Ponts et Chaussées and the Imperial College of London under the supervision of Olivier Dauchot and Michael Benzaquen. Then, we decided to pursue it during the first 6 months of my PhD where Sébastien Michelin took part in the project. During this one-year project, I have discovered the non-intuitive beauty of low Reynolds fluid mechanics. For that reason, I wish to include this work in my thesis while thanking Olivier Dauchot, Michael Benzaquen and Sébastien Michelin for their great help, their patience and finally their implication on this project.

J. Fluid Mech. (2019), *vol.* 866, R1, doi:10.1017/jfm.2019.130

JFM RAPIDS
journals.cambridge.org/rapids

No net motion for oscillating near-spheres at low Reynolds numbers

K. Lippera[1], **O. Dauchot**[2], **S. Michelin**[1] **and M. Benzaquen**[1,†]

[1]LadHyX, UMR CNRS 7646, Ecole polytechnique, 91128 Palaiseau, France
[2]EC2M, UMR CNRS 7083 Gulliver, ESPCI ParisTech, 10 rue Vauquelin, 75005 Paris, France

(Received 19 November 2018; revised 30 January 2019; accepted 10 February 2019)

We investigate the flow around an oscillating nearly spherical particle at low, yet non-vanishing, Reynolds numbers (*Re*), and the potential resulting locomotion. We analytically demonstrate that no net motion can arise up to order one in *Re* and order one in the asphericity parameter, regardless of the particle's shape. Therefore, geometry-induced acoustic streaming propulsion, if any, must arise at higher order.

Key words: flow–structure interactions, propulsion

1. Introduction

Solid bodies forced to oscillate in a fluid may, as a result, undergo a net motion, provided their shape breaks an appropriate symmetry. Yet, in the absence of inertia (i.e. when the Reynolds number *Re* is strictly zero), no net motion can arise from time-reciprocal actuation due to the linearity of Stokes' equations (Purcell 1977). Above a critical $Re_c = O(1)$, a symmetric rigid body can achieve unidirectional locomotion as a result of symmetry-breaking instability resulting from the nonlinear inertial contribution to the Navier–Stokes equations (Alben & Shelley 2005). The purpose of the present work is to analyse the emergence of self-propulsion at small but finite *Re* (i.e. the effect of inertia is weak but non-negligible) for oscillating asymmetric particles. Indeed one could expect that asymmetric flows, resulting from asymmetric boundary conditions, will push the particle, thereby inducing non-zero average motion (Nadal & Lauga 2014).

Artificial microswimmers have received much recent attention, thanks to their potential application to drug delivery or water treatment (Sundararajan *et al.* 2008; Tiwari, Behari & Sen 2008; Martinez-Pedrero & Tierno 2015), or their fundamental interest in the study of active matter (see, for example Buttinoni *et al.* 2013; Palacci *et al.* 2013; Bechinger *et al.* 2016). Among the many possible routes to self-propulsion, swimming in self-generated physico-chemical gradients, i.e.

---

† Email address for correspondence: michael.benzaquen@polytechnique.edu

autophoresis (Moran & Posner 2017), as well as bubble-generating (Wang & Wu 2014; Li, Rozen & Wang 2016) or magnetically actuated microswimmers (Dreyfus *et al.* 2005) have received particular attention. In these examples, a front–back asymmetry in the design of the system is necessary. Yet, symmetry-breaking and self-propulsion can also be achieved by exploiting an instability (Bricard *et al.* 2013; Michelin, Lauga & Bartolo 2013; Izri *et al.* 2014) or flexibility (Wiggins & Goldstein 1998).

Recently, passive rigid particles levitating in the nodal planes of an acoustic stationary wave have been observed to self-propel in a plane orthogonal to their direction of excitation (Wang *et al.* 2012). To explain such findings, Nadal & Lauga (2014) proposed an acoustic streaming mechanism, suggesting that near-spherical particles with asphericity parameter ϵ can achieve a net $O(\epsilon Re)$ propulsion, in the low-frequency limit. Several studies have since stood upon the results of Nadal & Lauga to account for their observations (see, for example Ahmed *et al.* 2016; Soto *et al.* 2016; Sabrina *et al.* 2018).

In contrast, we here demonstrate analytically that no net motion can arise at $O(\epsilon Re)$ from a time-reciprocal oscillation and that self-propulsion, if any, must arise at higher order. In § 2, the governing equations for an oscillating particle are presented. In § 3, we introduce the particle geometry and the Taylor expansions of the velocity fields in Re and ϵ. In §§ 4 and 5, we compute the net motion of the particle at the first two orders in Re. In § 6, we discuss our results and conclude.

2. Governing equations

We consider here a rigid and homogeneous particle of typical size R oscillating with frequency ω and amplitude a in an incompressible and Newtonian fluid of kinematic viscosity ν. Using R, $a\omega$ and $1/\omega$, respectively, as reference length, velocity and time scales, the dimensionless Navier–Stokes and continuity equations read (Zhang & Stone 1998)

$$\lambda^2 \partial_t \boldsymbol{u} + Re \nabla \boldsymbol{u} \boldsymbol{\cdot} \boldsymbol{u} = \nabla \boldsymbol{\cdot} \boldsymbol{\sigma}, \quad \nabla \boldsymbol{\cdot} \boldsymbol{u} = 0, \tag{2.1a,b}$$

with $\boldsymbol{\sigma} = -p\boldsymbol{I} + (\nabla \boldsymbol{u} + \nabla^\top \boldsymbol{u})$, the dimensionless stress tensor. The Reynolds number and reduced frequency are respectively defined as $Re = a\omega R/\nu$ and $\lambda^2 = (R/\delta)^2$, with $\delta = \sqrt{\nu/\omega}$ the viscous penetration depth. More precisely, a translational oscillation is imposed to the particle along the $\boldsymbol{e}_x$ direction, $\tilde{\boldsymbol{U}} = \mathrm{e}^{\mathrm{i}t}\boldsymbol{e}_x$, and the particle is free to move along the other directions, and is thus force-free along the yz plane and torque-free about any axis. The longitudinal and angular velocities of the particle resulting from its imposed oscillation are $\boldsymbol{U} = U_y \boldsymbol{e}_y + U_z \boldsymbol{e}_z$ and $\boldsymbol{\Omega} = \Omega_x \boldsymbol{e}_x + \Omega_y \boldsymbol{e}_y + \Omega_z \boldsymbol{e}_z$. In the frame of reference of the laboratory, the boundary conditions read

$$\boldsymbol{u}|_S = \tilde{\boldsymbol{U}} + \boldsymbol{U} + \boldsymbol{\Omega} \times \boldsymbol{r}, \quad \boldsymbol{u}|_{r\to\infty} = \boldsymbol{0}. \tag{2.2a,b}$$

In order to determine $\boldsymbol{U}$ and $\boldsymbol{\Omega}$ following an approach analogous to that of Lorentz' reciprocal theorem (Happel & Brenner 1965), the auxiliary problem of a particle of the same *instantaneous* geometry in a steady Stokes flow is considered:

$$\nabla \boldsymbol{\cdot} \widehat{\boldsymbol{\sigma}} = \boldsymbol{0}, \quad \nabla \boldsymbol{\cdot} \widehat{\boldsymbol{u}} = 0, \tag{2.3a,b}$$

with boundary conditions

$$\widehat{\boldsymbol{u}}|_S = \widehat{\boldsymbol{U}} + \widehat{\boldsymbol{\Omega}} \times \boldsymbol{r}, \quad \widehat{\boldsymbol{u}}|_{r\to\infty} = \boldsymbol{0}. \tag{2.4a,b}$$

Let us stress that the particle is rigid so that by instantaneous geometry one should understand that the surface boundary of the auxiliary problem matches that of its real counterpart at each time. Using (2.1) and (2.3), one obtains

$$\int_V [\widehat{\boldsymbol{u}}\boldsymbol{\cdot}(\nabla\boldsymbol{\cdot}\boldsymbol{\sigma}) - \boldsymbol{u}\boldsymbol{\cdot}(\nabla\boldsymbol{\cdot}\widehat{\boldsymbol{\sigma}})]\,\mathrm{d}V = Re\int_V \widehat{\boldsymbol{u}}\boldsymbol{\cdot}\nabla\boldsymbol{u}\boldsymbol{\cdot}\boldsymbol{u}\,\mathrm{d}V + \lambda^2\int_V \widehat{\boldsymbol{u}}\boldsymbol{\cdot}\partial_t\boldsymbol{u}\,\mathrm{d}V. \tag{2.5}$$

Using the divergence theorem together with the continuity equations, equation (2.5) reduces to

$$\int_{S_\infty - S}(\widehat{\boldsymbol{u}}\boldsymbol{\cdot}\boldsymbol{\sigma} - \boldsymbol{u}\boldsymbol{\cdot}\widehat{\boldsymbol{\sigma}})\boldsymbol{\cdot}\boldsymbol{n}\,\mathrm{d}S = Re\int_V \widehat{\boldsymbol{u}}\boldsymbol{\cdot}\nabla\boldsymbol{u}\boldsymbol{\cdot}\boldsymbol{u}\,\mathrm{d}V + \lambda^2\int_V \widehat{\boldsymbol{u}}\boldsymbol{\cdot}\partial_t\boldsymbol{u}\,\mathrm{d}V. \tag{2.6}$$

Because $\boldsymbol{u}, \widehat{\boldsymbol{u}} \sim 1/r$ and $\boldsymbol{\sigma}, \widehat{\boldsymbol{\sigma}} \sim 1/r^2$ when $r \rightarrow \infty$ (see e.g. Happel & Brenner 1965), the surface integral at infinity in (2.6) vanishes. The boundary conditions (2.2) and (2.4) then yield

$$(\tilde{\boldsymbol{U}} + \boldsymbol{U})\boldsymbol{\cdot}\widehat{\boldsymbol{F}} + \boldsymbol{\varOmega}\boldsymbol{\cdot}\widehat{\boldsymbol{L}} - \widehat{\boldsymbol{U}}\boldsymbol{\cdot}\boldsymbol{F} - \widehat{\boldsymbol{\varOmega}}\boldsymbol{\cdot}\boldsymbol{L} = Re\int_V \widehat{\boldsymbol{u}}\boldsymbol{\cdot}\nabla\boldsymbol{u}\boldsymbol{\cdot}\boldsymbol{u}\,\mathrm{d}V + \lambda^2\int_V \widehat{\boldsymbol{u}}\boldsymbol{\cdot}\partial_t\boldsymbol{u}\,\mathrm{d}V, \tag{2.7}$$

with $\boldsymbol{F} = \int_S \boldsymbol{\sigma}\boldsymbol{\cdot}\boldsymbol{n}\,\mathrm{d}S$ and $\boldsymbol{L} = \int_S (\boldsymbol{r}\times\boldsymbol{\sigma})\boldsymbol{\cdot}\boldsymbol{n}\,\mathrm{d}S$ (respectively $\hat{\boldsymbol{F}}$ and $\hat{\boldsymbol{L}}$), the force and torque in the real (respectively auxiliary) problem. For the real problem, $\boldsymbol{F}$ and $\boldsymbol{L}$ derive from Newton's laws:

$$\boldsymbol{F} = \bar{\rho}\partial_t\boldsymbol{U}, \quad \boldsymbol{L} = \partial_t(\boldsymbol{J}\boldsymbol{\cdot}\boldsymbol{\varOmega}), \tag{2.8a,b}$$

with $\bar{\rho}$ the particle-to-fluid density ratio and $\boldsymbol{J}$ the particle's inertia tensor. For the auxiliary problem, $\hat{\boldsymbol{F}}$ and $\hat{\boldsymbol{L}}$ are linearly related to $\hat{\boldsymbol{U}}$ and $\hat{\boldsymbol{\varOmega}}$ through the possibly non-diagonal resistance matrix (Kim & Karrila 1991). In order to compute the particle motion $(\boldsymbol{U}, \boldsymbol{\varOmega})$, we shall consider in (2.7) either (i) an auxiliary steady propulsion $(\hat{\boldsymbol{U}}, \boldsymbol{0})$ with $\hat{\boldsymbol{U}} \parallel \boldsymbol{U}$ to determine $\boldsymbol{U}$, or (ii) an auxiliary steady rotation $(\boldsymbol{0}, \hat{\boldsymbol{\varOmega}})$ with $\hat{\boldsymbol{\varOmega}} \parallel \boldsymbol{\varOmega}$ to determine $\boldsymbol{\varOmega}$. Note that finding the contribution at $O(Re^n)$ of the first term on the right-hand side of (2.7) relies on the knowledge of the velocity field $\boldsymbol{u}$ at $O(Re^{n-1})$ only, hence the possibility of a recursive calculation order by order in Re. Conversely, computing the second term will rely on peculiar symmetry and time-average considerations to be made explicit below. Note that for a homogeneous particle, the above formulation also applies to the motion of a particle exposed to a uniform oscillating flow $-\tilde{\boldsymbol{U}}$, once inertial forces are accounted for as a modified pressure.

3. Nearly spherical particles in low-*Re* flows

We consider a nearly spherical particle of volume $\mathcal{V}$ and centre of mass O. By choosing $R = (3\mathcal{V}/4\pi)^{1/3}$ and taking O as the origin of the system of axes, one can define the particle's geometry through $r = 1 + \epsilon f(\boldsymbol{n})$ with $\epsilon \ll 1$. By construction f satisfies

$$\int_S f(\boldsymbol{n})\,\mathrm{d}S = 0, \quad \int_S f(\boldsymbol{n})\boldsymbol{n}\,\mathrm{d}S = \boldsymbol{0}. \tag{3.1a,b}$$

The governing equations are first linearised with respect to $Re \ll 1$, e.g. defining $\boldsymbol{u} = \boldsymbol{u}_0 + Re\boldsymbol{u}_1 + O(Re^2)$, and each order is further expanded as a regular perturbation problem in $\epsilon \ll 1$, e.g. $\boldsymbol{u}_k = \boldsymbol{u}_k^0 + \epsilon \boldsymbol{u}_k^\epsilon + O(\epsilon^2)$ with $k = 0, 1$. Note that ϵ must remain small compared to all other dimensionless length scales, i.e. $\epsilon \ll 1$ (particle radius) and $\epsilon \ll 1/\lambda$ (viscous boundary layer thickness). In the following sections, we shall consider the problems at $O(Re^k \epsilon^\ell)$, and successively look into the two leading orders in Re.

4. Zeroth order in Re

At leading order $O(Re^0)$, equations (2.1) and (2.2) become

$$\lambda^2 \partial_t \boldsymbol{u}_0 = -\nabla p_0 + \nabla^2 \boldsymbol{u}_0, \quad \nabla \boldsymbol{\cdot} \boldsymbol{u}_0 = 0, \tag{4.1a,b}$$

$$\boldsymbol{u}_0|_S = \tilde{\boldsymbol{U}} + \boldsymbol{U}_0 + \boldsymbol{\Omega}_0 \times \boldsymbol{r}, \quad \boldsymbol{u}_0|_{r\to\infty} = \boldsymbol{0}, \tag{4.2a,b}$$

and (2.7) reduces to

$$(\tilde{\boldsymbol{U}} + \boldsymbol{U}_0) \boldsymbol{\cdot} \widehat{\boldsymbol{F}} + \boldsymbol{\Omega}_0 \boldsymbol{\cdot} \widehat{\boldsymbol{L}} - \widehat{\boldsymbol{U}} \boldsymbol{\cdot} \boldsymbol{F}_0 - \widehat{\boldsymbol{\Omega}} \boldsymbol{\cdot} \boldsymbol{L}_0 = \lambda^2 \int_V \widehat{\boldsymbol{u}} \boldsymbol{\cdot} \partial_t \boldsymbol{u}_0 \,\mathrm{d}V, \tag{4.3}$$

and this result is expanded as a linear perturbation in ϵ below.

4.1. *Perfect sphere* – $O(Re^0\epsilon^0)$

While it is quite clear that no net motion can arise at $O(\epsilon^0 Re^0)$ (i.e. unsteady Stokes flow around a spherical particle), we briefly rederive this result to provide the reader with the general methodology. At leading order $O(\epsilon^0)$, equation (4.3) becomes

$$(\tilde{\boldsymbol{U}} + \boldsymbol{U}_0^0) \boldsymbol{\cdot} \widehat{\boldsymbol{F}}^0 + \boldsymbol{\Omega}_0^0 \boldsymbol{\cdot} \widehat{\boldsymbol{L}}^0 - \widehat{\boldsymbol{U}} \boldsymbol{\cdot} \boldsymbol{F}_0^0 - \widehat{\boldsymbol{\Omega}} \boldsymbol{\cdot} \boldsymbol{L}_0^0 = \lambda^2 \int_{V_0} \widehat{\boldsymbol{u}}^0 \boldsymbol{\cdot} \partial_t \boldsymbol{u}_0^0 \,\mathrm{d}V, \tag{4.4}$$

where V_0 denotes the volume of fluid outside the reference unit sphere. First, recalling $\widehat{\boldsymbol{U}} \parallel \boldsymbol{U}_0^0$ provides $\widehat{\boldsymbol{U}} \boldsymbol{\cdot} \tilde{\boldsymbol{U}} = 0$. Second, the velocity field $\widehat{\boldsymbol{u}}^0$ (respectively $\boldsymbol{u}_0^0$) is linear with respect to $\widehat{\boldsymbol{U}}$ (respectively $\tilde{\boldsymbol{U}}$), and axisymmetric about the axis holding the vector $\widehat{\boldsymbol{U}}$ (respectively $\tilde{\boldsymbol{U}}$) and passing through the centre of mass of the particle. As a result, using the expression of $\widehat{\boldsymbol{u}}^0$ and $\boldsymbol{u}_0^0$ (appendix A) shows that the RHS of (4.4) does not include any contribution from the forcing $\tilde{\boldsymbol{U}}$. There is therefore no net motion at this order, i.e. $\boldsymbol{U}_0^0 = \boldsymbol{0}$. A similar reasoning shows that $\boldsymbol{\Omega}_0^0 = \boldsymbol{0}$ as well. This last result imposes the rotation velocity of the particle to be at least first order (either in ϵ or Re). The forcing and induced rotation act therefore on two separate time scales. As a consequence, at leading order, the geometry of the particle, f, can be considered constant over the $O(1)$ period of the forcing (fast time scale).

4.2. *Near-sphere correction* – $O(Re^0\epsilon^1)$

At $O(\epsilon^1)$, equation (4.3) becomes

$$\begin{aligned} &\boldsymbol{U}_0^\epsilon \boldsymbol{\cdot} \widehat{\boldsymbol{F}}^0 + \boldsymbol{\Omega}_0^\epsilon \boldsymbol{\cdot} \widehat{\boldsymbol{L}}^0 + \tilde{\boldsymbol{U}} \boldsymbol{\cdot} \widehat{\boldsymbol{F}}^\epsilon - \widehat{\boldsymbol{U}} \boldsymbol{\cdot} \boldsymbol{F}_0^\epsilon - \widehat{\boldsymbol{\Omega}} \boldsymbol{\cdot} \boldsymbol{L}_0^\epsilon \\ &\quad = \lambda^2 \int_{V_0} (\widehat{\boldsymbol{u}}^\epsilon \boldsymbol{\cdot} \partial_t \boldsymbol{u}_0^0 + \widehat{\boldsymbol{u}}^0 \boldsymbol{\cdot} \partial_t \boldsymbol{u}_0^\epsilon) \,\mathrm{d}V - \lambda^2 \int_{S_0} f \widehat{\boldsymbol{u}}^0 \boldsymbol{\cdot} \partial_t \boldsymbol{u}_0^0 \,\mathrm{d}S, \end{aligned} \tag{4.5}$$

where the surface integral is the $O(\epsilon)$ contribution from the difference of the volume integrals on V and V_0 (e.g. Zhang & Stone 1998). The analysis of Zhang & Stone (1998) shows that the rotation of a torque-free homogeneous near-sphere resulting from an $O(1)$ imposed translation is $O(\epsilon^2)$ and thus $\boldsymbol{\Omega}_0^{\epsilon} = \boldsymbol{0}$. Consequently the torque $\boldsymbol{L}_0^{\epsilon}$ linked to $\boldsymbol{\Omega}_0^{\epsilon}$ through Newton's law (2.8) vanishes as well. Using (2.4) and (3.1), the last term in (4.5) vanishes exactly:

$$\int_{S_0} f\widehat{\boldsymbol{u}}^0 \boldsymbol{\cdot} \partial_t \boldsymbol{u}_0^0 \, \mathrm{d}S = (\dot{\tilde{\boldsymbol{U}}} \times \widehat{\boldsymbol{\Omega}}) \boldsymbol{\cdot} \int_{S_0} f\boldsymbol{n} \, \mathrm{d}S = 0. \tag{4.6}$$

Since we are interested in the net motion of the particle, we take the time-average over the fast time scale (forcing period) of (4.5). The $\langle \mathrm{RHS} \rangle_t$ can be shown to vanish because $\boldsymbol{u}_0^{\epsilon}$ and $\boldsymbol{u}_0^0$ are periodic in time, and the integration domains are time-independent. Therefore

$$\langle \boldsymbol{U}_0^{\epsilon} \rangle_t \boldsymbol{\cdot} \widehat{\boldsymbol{F}}^0 - \widehat{\boldsymbol{U}} \boldsymbol{\cdot} \langle \boldsymbol{F}_0^{\epsilon} \rangle_t = 0. \tag{4.7}$$

Equation (4.7) is linear with no net contribution of the forcing $\tilde{\boldsymbol{U}}$: no net motion can occur at $O(Re^0 \epsilon^1)$, $\langle \boldsymbol{U}_0^{\epsilon} \rangle_t = \boldsymbol{0}$.

5. First order in *Re*

At $O(Re^1)$, equations (2.1) and (2.2) become

$$\lambda^2 \partial_t \boldsymbol{u}_1 + \boldsymbol{\nabla} \boldsymbol{u}_0 \boldsymbol{\cdot} \boldsymbol{u}_0 = -\boldsymbol{\nabla} p_1 + \nabla^2 \boldsymbol{u}_1, \quad \boldsymbol{\nabla} \boldsymbol{\cdot} \boldsymbol{u}_1 = 0, \tag{5.1a,b}$$

$$\boldsymbol{u}_1|_S = \boldsymbol{U}_1 + \boldsymbol{\Omega}_1 \times \boldsymbol{r}, \quad \boldsymbol{u}_1|_{r\to\infty} = \boldsymbol{0}, \tag{5.2a,b}$$

and (2.7) reduces to

$$\boldsymbol{U}_1 \boldsymbol{\cdot} \widehat{\boldsymbol{F}} + \boldsymbol{\Omega}_1 \boldsymbol{\cdot} \widehat{\boldsymbol{L}} - \widehat{\boldsymbol{U}} \boldsymbol{\cdot} \boldsymbol{F}_1 - \widehat{\boldsymbol{\Omega}} \boldsymbol{\cdot} \boldsymbol{L}_1 = \int_V \widehat{\boldsymbol{u}} \boldsymbol{\cdot} \boldsymbol{\nabla} \boldsymbol{u}_0 \boldsymbol{\cdot} \boldsymbol{u}_0 \, \mathrm{d}V + \lambda^2 \int_V \widehat{\boldsymbol{u}} \boldsymbol{\cdot} \partial_t \boldsymbol{u}_1 \, \mathrm{d}V. \tag{5.3}$$

Note that here, in addition to the unsteady forcing, the nonlinear convective term acts as a source term in (5.3). Because it is quadratic in velocity, one might expect that its average in time is non-zero, which could in turn yield net particle motion.

5.1. *Perfect sphere – $O(Re^1\epsilon^0)$*

At leading order $O(\epsilon^0)$ (5.3) becomes

$$\boldsymbol{U}_1^0 \boldsymbol{\cdot} \widehat{\boldsymbol{F}}^0 + \boldsymbol{\Omega}_1^0 \boldsymbol{\cdot} \widehat{\boldsymbol{L}}^0 - \widehat{\boldsymbol{U}} \boldsymbol{\cdot} \boldsymbol{F}_1^0 - \widehat{\boldsymbol{\Omega}} \boldsymbol{\cdot} \boldsymbol{L}_1^0 = \int_{V_0} \widehat{\boldsymbol{u}}^0 \boldsymbol{\cdot} \boldsymbol{\nabla} \boldsymbol{u}_0^0 \boldsymbol{\cdot} \boldsymbol{u}_0^0 \, \mathrm{d}V + \lambda^2 \int_{V_0} \widehat{\boldsymbol{u}}^0 \boldsymbol{\cdot} \partial_t \boldsymbol{u}_1^0 \, \mathrm{d}V. \tag{5.4}$$

The symmetry properties of $\widehat{\boldsymbol{u}}^0$ and $\boldsymbol{u}_0^0$ (appendix A) impose that the first term on the RHS of (5.4) vanishes. The second term on the RHS vanishes as well because it is the integral of the scalar product between two axisymmetric fields about orthogonal principal directions. Therefore (5.4) becomes

$$\boldsymbol{U}_1^0 \boldsymbol{\cdot} \widehat{\boldsymbol{F}}^0 + \boldsymbol{\Omega}_1^0 \boldsymbol{\cdot} \widehat{\boldsymbol{L}}^0 - \widehat{\boldsymbol{U}} \boldsymbol{\cdot} \boldsymbol{F}_1^0 - \widehat{\boldsymbol{\Omega}} \boldsymbol{\cdot} \boldsymbol{L}_1^0 = \boldsymbol{0}, \tag{5.5}$$

implying that, very much like for $O(Re^0\epsilon^0)$, $\boldsymbol{U}_1^0 = \boldsymbol{0}$ and $\boldsymbol{\Omega}_1^0 = \boldsymbol{0}$.

5.2. *Near-sphere correction – $O(Re^1\epsilon^1)$*

At $O(\epsilon^1)$, and using (2.8) together with (5.5), (5.3) becomes

$$\begin{aligned}\boldsymbol{U}_1^\epsilon\boldsymbol{\cdot}\widehat{\boldsymbol{F}}^0+\boldsymbol{\Omega}_1^\epsilon\boldsymbol{\cdot}\widehat{\boldsymbol{L}}^0-\widehat{\boldsymbol{U}}\boldsymbol{\cdot}\boldsymbol{F}_1^\epsilon-\widehat{\boldsymbol{\Omega}}\boldsymbol{\cdot}\boldsymbol{L}_1^\epsilon&=-\int_{S_0} f\,\widehat{\boldsymbol{u}}^0\boldsymbol{\cdot}\boldsymbol{\nabla}\boldsymbol{u}_0^0\boldsymbol{\cdot}\boldsymbol{u}_0^0\,\mathrm{d}S\\ &+\int_{V_0}(\widehat{\boldsymbol{u}}^\epsilon\boldsymbol{\cdot}\boldsymbol{\nabla}\boldsymbol{u}_0^0\boldsymbol{\cdot}\boldsymbol{u}_0^0+\widehat{\boldsymbol{u}}^0\boldsymbol{\cdot}[\boldsymbol{\nabla}\boldsymbol{u}_0^0\boldsymbol{\cdot}\boldsymbol{u}_0^\epsilon+\boldsymbol{\nabla}\boldsymbol{u}_0^\epsilon\boldsymbol{\cdot}\boldsymbol{u}_0^0])\,\mathrm{d}V\\ &+\lambda^2\int_{V_0}(\widehat{\boldsymbol{u}}^0\boldsymbol{\cdot}\partial_t\boldsymbol{u}_1^\epsilon+\widehat{\boldsymbol{u}}^\epsilon\boldsymbol{\cdot}\partial_t\boldsymbol{u}_1^0)\,\mathrm{d}V-\lambda^2\int_{S_0} f\widehat{\boldsymbol{u}}^0\boldsymbol{\cdot}\partial_t\boldsymbol{u}_1^0\,\mathrm{d}S.\end{aligned}\tag{5.6}$$

Taking the average in time of (5.6) over the forcing period, and using that $\boldsymbol{u}_1^\epsilon$ and $\boldsymbol{u}_1^0$ are periodic and that $\boldsymbol{F}_1^\epsilon$ and $\boldsymbol{L}_1^\epsilon$ are temporal derivatives of periodic functions (2.8), one finally obtains

$$6\pi\langle\boldsymbol{U}_1^\epsilon\rangle_t\boldsymbol{\cdot}\widehat{\boldsymbol{U}}+8\pi\langle\boldsymbol{\Omega}_1^\epsilon\rangle_t\boldsymbol{\cdot}\widehat{\boldsymbol{\Omega}}=-v_1^\epsilon,\quad\text{with}\tag{5.7}$$

$$v_1^\epsilon=\left\langle\int_{V_0}(\widehat{\boldsymbol{u}}^\epsilon\boldsymbol{\cdot}\boldsymbol{\nabla}\boldsymbol{u}_0^0\boldsymbol{\cdot}\boldsymbol{u}_0^0+\widehat{\boldsymbol{u}}^0\boldsymbol{\cdot}[\boldsymbol{\nabla}\boldsymbol{u}_0^0\boldsymbol{\cdot}\boldsymbol{u}_0^\epsilon+\boldsymbol{\nabla}\boldsymbol{u}_0^\epsilon\boldsymbol{\cdot}\boldsymbol{u}_0^0])\,\mathrm{d}V-\int_{S_0} f\widehat{\boldsymbol{u}}^0\boldsymbol{\cdot}\boldsymbol{\nabla}\boldsymbol{u}_0^0\boldsymbol{\cdot}\boldsymbol{u}_0^0\,\mathrm{d}S\right\rangle_t\tag{5.8}$$

where we have used $\widehat{\boldsymbol{F}}^0=-6\pi\widehat{\boldsymbol{U}}$ and $\widehat{\boldsymbol{L}}^0=-8\pi\widehat{\boldsymbol{\Omega}}$. Integrating by parts, and using the expressions of $\widehat{\boldsymbol{u}}^0$ and $\boldsymbol{u}_0^0$ (appendix A), one obtains

$$v_1^\epsilon=\int_{V_0}(\widehat{\boldsymbol{u}}^\epsilon\boldsymbol{\cdot}\boldsymbol{G}_1(\boldsymbol{r})-\langle\boldsymbol{u}_0^\epsilon\boldsymbol{\cdot}\boldsymbol{G}_2(\boldsymbol{r})\rangle_t)\,\mathrm{d}V,\tag{5.9}$$

with the vector fields $\boldsymbol{G}_1$ and $\boldsymbol{G}_2$ defined as $\boldsymbol{G}_1=\langle\boldsymbol{\nabla}\boldsymbol{u}_0^0\boldsymbol{\cdot}\boldsymbol{u}_0^0\rangle_t$ and $\boldsymbol{G}_2=[\boldsymbol{\nabla}\widehat{\boldsymbol{u}}^0+(\boldsymbol{\nabla}\widehat{\boldsymbol{u}}^0)^T]\boldsymbol{\cdot}\boldsymbol{u}_0^0$, whose expressions are provided in appendix A.

Using domain perturbation, the velocity field $\boldsymbol{u}_0^\epsilon$ (respectively $\widehat{\boldsymbol{u}}^\epsilon$) is solution of (4.1) (respectively (2.3)) with the following boundary conditions on the unit sphere (see appendix B):

$$\boldsymbol{u}_0^\epsilon|_{r=1}=-f(\boldsymbol{n})\partial_r\boldsymbol{u}_0^0|_{r=1}+\boldsymbol{U}_0^\epsilon+\boldsymbol{\Omega}_0^\epsilon\times\boldsymbol{r},\tag{5.10a}$$

$$\widehat{\boldsymbol{u}}^\epsilon|_{r=1}=-f(\boldsymbol{n})\partial_r\widehat{\boldsymbol{u}}^0|_{r=1}.\tag{5.10b}$$

A first simplification comes from recalling that $\boldsymbol{\Omega}_0^\epsilon=\boldsymbol{0}$. A second one arises from the fact that the Stokes problem with the uniform boundary condition $\boldsymbol{U}_0^\epsilon$ on the unit sphere does not contribute to particle motion, as demonstrated in § 5.1. As a consequence, only the first contribution to $\boldsymbol{u}_0^\epsilon|_{r=1}$ in (5.10a) provides a net contribution to v_1^ϵ.

For clarity, we now distinguish the cases of pure translation and pure rotation.

5.2.1. *Translation*

Setting $\widehat{\boldsymbol{\Omega}}=\boldsymbol{0}$, equation (5.9) simplifies after some algebraic calculations using the definitions of $\boldsymbol{G}_1$, $\boldsymbol{G}_2$, $\widehat{\boldsymbol{u}}^\varepsilon$ and $\boldsymbol{u}_0^\varepsilon$ (appendices A and B):

$$v_1^\epsilon=\mathcal{K}(\lambda)[f\boldsymbol{nnn}]_{\boldsymbol{n}}\,\vdots\,\boldsymbol{e}_x\boldsymbol{e}_x\widehat{\boldsymbol{U}},\tag{5.11}$$

where $[\bullet]_{\boldsymbol{n}}$ denotes the average over the unit sphere: $[\bullet]_{\boldsymbol{n}}=\int_{S_0}\bullet(\boldsymbol{n})\,\mathrm{d}S$, and $\vdots$ denotes the three-fold tensorial contraction. Quite remarkably, equation (5.11) provides the expression of the net translational velocity as a product of a function of λ and a functional of f. The tensorial contraction, together with the angular symmetry properties of the inertial forcing, ensure that only a limited set of the spherical harmonic components of the shape function f can contribute to a net motion. Further algebraic calculations show that $\mathcal{K}(\lambda)$ conveniently reduces to $\mathcal{K}(\lambda)=\int_{r=1}^{\infty}(\mathrm{d}\mathcal{J}_\lambda(r)/\mathrm{d}r)\,\mathrm{d}r$ with

$$\begin{aligned}\mathcal{J}_\lambda(r) \;=\; -\frac{1}{4}\mathrm{Re}\Bigg[&\frac{27(1-r^2)}{16\lambda_0^4r^8}\,(-3|\Lambda_0|^2+2\overline{\Lambda_0}(3+3\lambda_0 r-\lambda_0^2r^2)\mathrm{e}^{\lambda_0(1-r)}\\ &-(3+3\lambda_0 r+(\lambda_0 r)^2)(\overline{1+\lambda_0 r-\lambda_0^2r^2})\mathrm{e}^{2\mathrm{Re}[\lambda_0](1-r)})\Bigg],\end{aligned} \tag{5.12}$$

where an overbar denotes the complex conjugate, Re$[z]$ is the real part operator of z and $\Lambda_0=1+\lambda_0+\lambda_0^2/3$ with $\lambda_0=\lambda\mathrm{e}^{-i\pi/4}$. Therefore, using $\mathcal{J}_\lambda(\infty)=\mathcal{J}_\lambda(1)=0$, one finds the central result of the present communication:

$$\langle \boldsymbol{U}_1^\epsilon\rangle_t=\boldsymbol{0}. \tag{5.13}$$

No translational net motion can arise at first order (both in *Re* and non-sphericity ϵ) from geometric asymmetry. This result stems from the fact that the near-field ($r=O(1)$) and far-field ($r\gg 1$) contributions to the inertial forcing compensate exactly.

5.2.2. *Rotation*

Considering now $\widehat{\boldsymbol{U}}=\boldsymbol{0}$, the same method provides

$$v_1^\epsilon=\mathcal{L}(\lambda)[f\boldsymbol{nn}]_{\boldsymbol{n}}:\boldsymbol{e}_x(\boldsymbol{e}_x\times\widehat{\boldsymbol{\Omega}}), \tag{5.14}$$

with

$$\begin{aligned}\mathcal{L}(\lambda) \;=\; \frac{1}{256}\mathrm{Im}\Bigg\{&\frac{1}{\Lambda_0}\,[-48(\lambda_0(\lambda_0(\lambda_0(\lambda_0+6)+18)+30)+24)|\lambda_0|^2F(2\mathrm{Re}(\lambda_0))\\ &+3\mathrm{i}(\lambda_0(\lambda_0(\lambda_0(\lambda_0+9)+27)+42)+30)\lambda_0^2\bar{\Lambda}_0F(\lambda_0)\\ &+3\mathrm{i}(\lambda_0(\lambda_0(\lambda_0(\lambda_0+3)+33)+78)+66)\lambda_0^2\Lambda_0F(\mathrm{i}\lambda_0)\\ &+(1-\mathrm{i})\lambda_0^7+(3-7\mathrm{i})\lambda_0^6-(5+35\mathrm{i})\lambda_0^5-(6+108\mathrm{i})\lambda_0^4-(60+210\mathrm{i})\lambda_0^3\\ &-(264+306\mathrm{i})\lambda_0^2-(348+360\mathrm{i})\lambda_0-132\mathrm{i}]\Bigg\},\end{aligned} \tag{5.15}$$

with $F(z)=[\mathrm{Chi}(z)-\mathrm{Shi}(z)]\mathrm{e}^z$ where Chi/Shi are the hyperbolic cosine/sine integral functions respectively (Abramowitz & Stegun 1965). We note from (5.8) and (5.14) that (i) no rotation is obtained along the direction of oscillation (i.e. $\langle\boldsymbol{\Omega}_1^\epsilon\rangle_t\cdot\tilde{\boldsymbol{U}}=0$) and that (ii) the particle dynamics is an overdamped rotation towards an equilibrium position. The oscillation direction $\tilde{\boldsymbol{U}}$ is aligned with a principal direction of the symmetric and traceless second-order tensor $[f\boldsymbol{nn}]_{\boldsymbol{n}}$ with positive or negative eigenvalue depending on the sign of $\mathcal{L}$. Further, the function $\langle\mathcal{L}\rangle_t$ changes sign for $\lambda_c\approx 3.6$, resulting in a shift in the equilibrium orientation between $\lambda<\lambda_c$ and $\lambda>\lambda_c$. This transition confirms fundamental differences in the streaming flow and associated forcing between small and large frequencies, as already observed by Collis, Chakraborty & Sader (2017) when studying numerically the propulsion of an oscillating asymmetric dumbbell.

6. Conclusion

In this work, we analysed the translation and rotation resulting from the oscillation of a homogeneous near-sphere up to $O(\epsilon Re)$, showing analytically that no net translation occurs regardless of the oscillation frequency and despite the geometric asymmetry of the particle. This result, which contradicts the conclusions of Nadal & Lauga (2014), stems from the exact cancellation of the streaming flow forcing in the immediate vicinity of the particle and far away from it, making it difficult to capture numerically, as any discretisation introduces necessarily a truncation error. We also show that a transient rotation can stir back the particle towards one of its equilibrium positions.

Notwithstanding, our results do not contradict the numerical observations of Collis *et al.* (2017) for which a weak front–back asymmetry of a dumbbell was sufficient to produce a net motion at that order: in that case, the elongated shape of the particle combined with the small asymmetry of the two spheres leads to an $O(1)$ periodic rotation of the system, which is at the heart of the self-propulsion, when coupled to the oscillating translation – in contrast, such rotation is absent at $O(\epsilon Re)$ in the case of a near-sphere. All together, developing net motion around an asymmetric particle appears to require an $O(\epsilon)$ rotation/translation coupling, as obtained for instance using density inhomogeneities.

Acknowledgements

We are grateful to F. Nadal and E. Lauga for insightful discussions on this problem. This project has received funding from the European Research Council (ERC) under the European Union's Horizon 2020 research and innovation programme under Grant Agreement 714027 (SM).

Appendix A. Unsteady Stokes flow past a spherical particle

A.1. *Oscillating flow*

The complex velocity field around a sphere oscillating at velocity $\tilde{\boldsymbol{U}}$ reads (Kim & Karrila 1991) $\boldsymbol{u}_0^0 = A\tilde{\boldsymbol{U}} + B(\tilde{\boldsymbol{U}}\boldsymbol{\cdot}\boldsymbol{n})\boldsymbol{n}$ where

$$A(r,\lambda) = \frac{3}{2\lambda_0^2 r^3}[-\Lambda_0 + (1+\lambda_0 r + \lambda_0^2 r^2)\mathrm{e}^{\lambda_0(1-r)}], \tag{A 1}$$

$$B(r,\lambda) = \frac{3}{2\lambda_0^2 r^3}[3\Lambda_0 - (3+3\lambda_0 r + \lambda_0^2 r^2)\mathrm{e}^{\lambda_0(1-r)}], \tag{A 2}$$

and where $\lambda_0 = \lambda \mathrm{e}^{-\mathrm{i}\pi/4}$ and $\Lambda_0 = 1 + \lambda_0 + \lambda_0^2/3$. Recalling that

$$\nabla \boldsymbol{u}_0^0 = A'\tilde{\boldsymbol{U}}\boldsymbol{n} + B'(\tilde{\boldsymbol{U}}\boldsymbol{\cdot}\boldsymbol{n})\boldsymbol{n}\boldsymbol{n} + \frac{B}{r}(\boldsymbol{I}-\boldsymbol{n}\boldsymbol{n})(\tilde{\boldsymbol{U}}\boldsymbol{\cdot}\boldsymbol{n}) + \frac{B}{r}\boldsymbol{n}(\boldsymbol{I}-\boldsymbol{n}\boldsymbol{n})\boldsymbol{\cdot}\tilde{\boldsymbol{U}}, \tag{A 3}$$

one may compute $\boldsymbol{G}_1 = \langle \nabla \boldsymbol{u}_0^0 \boldsymbol{\cdot} \boldsymbol{u}_0^0 \rangle_t$, that is,

$$\boldsymbol{G}_1 = \frac{1}{2}\mathrm{Re}[(A+B)\overline{[A'\boldsymbol{I}\boldsymbol{n} + B'\boldsymbol{n}\boldsymbol{n}\boldsymbol{n}]} + \frac{A\overline{B}}{r}[\boldsymbol{n}(\boldsymbol{I}-\boldsymbol{n}\boldsymbol{n}) + (\boldsymbol{I}-\boldsymbol{n}\boldsymbol{n})\boldsymbol{n}]]:\boldsymbol{e}_x\boldsymbol{e}_x. \tag{A 4}$$

A.2. *Steady translation*

The particular case of a steady translating sphere ($\lambda = 0$) at velocity $\widehat{\boldsymbol{U}}$ is given by $\widehat{\boldsymbol{u}}^0 = \widehat{A}\widehat{\boldsymbol{U}} + \widehat{B}(\widehat{\boldsymbol{U}} \boldsymbol{\cdot} \boldsymbol{n})\boldsymbol{n}$, where

$$\widehat{A}(r) = \frac{3}{4r} + \frac{1}{4r^3}, \quad \widehat{B}(r) = \frac{3}{4}\left(\frac{1}{r} - \frac{1}{r^3}\right). \tag{A 5a,b}$$

One may compute $\boldsymbol{G}_2 = \boldsymbol{\nabla}\widehat{\boldsymbol{u}}_0^0 \boldsymbol{\cdot} \boldsymbol{u}_0^0 + \boldsymbol{u}_0^0 \boldsymbol{\cdot} \boldsymbol{\nabla}\widehat{\boldsymbol{u}}_0^0$, that is,

$$\begin{aligned} \boldsymbol{G}_2 \ &= \ \widehat{A}'A\boldsymbol{n}\boldsymbol{I} : \widehat{\boldsymbol{U}}\tilde{\boldsymbol{U}} + \widehat{A}'(A+B)\boldsymbol{I}\boldsymbol{n} : \tilde{\boldsymbol{U}}\widehat{\boldsymbol{U}} + (\widehat{A}'B + 2\widehat{B}'(A+B))\boldsymbol{n}\boldsymbol{n}\boldsymbol{n} : \tilde{\boldsymbol{U}}\widehat{\boldsymbol{U}} \\ &\quad + \frac{\widehat{B}A}{r}[\boldsymbol{n}(\boldsymbol{I} - \boldsymbol{n}\boldsymbol{n}) : \tilde{\boldsymbol{U}}\widehat{\boldsymbol{U}} + 2(\boldsymbol{I} - \boldsymbol{n}\boldsymbol{n})\boldsymbol{n} : \widehat{\boldsymbol{U}}\tilde{\boldsymbol{U}}] + \frac{\widehat{B}(A+B)}{r}(\boldsymbol{I} - \boldsymbol{n}\boldsymbol{n})\boldsymbol{n} : \tilde{\boldsymbol{U}}\widehat{\boldsymbol{U}}. \end{aligned} \tag{A 6}$$

A.3. *Steady rotation*

The velocity field around a steady rotating sphere reads $\widehat{\boldsymbol{u}}^0 = \widehat{\boldsymbol{\Omega}} \times \boldsymbol{n}/r^2$. Computing

$$\boldsymbol{\nabla}\widehat{\boldsymbol{u}}^0 \boldsymbol{\cdot} \boldsymbol{u}_0^0 = \frac{1}{r^3}[\widehat{\boldsymbol{\Omega}} \times \boldsymbol{u}_0^0 - 3(\boldsymbol{u}_0^0 \boldsymbol{\cdot} \boldsymbol{n})(\widehat{\boldsymbol{\Omega}} \times \boldsymbol{n})], \tag{A 7}$$

$$\boldsymbol{u}_0^0 \boldsymbol{\cdot} \boldsymbol{\nabla}\widehat{\boldsymbol{u}}^0 = \frac{1}{r^3}[\boldsymbol{u}_0^0 \times \widehat{\boldsymbol{\Omega}} - 3\boldsymbol{u}_0^0 \boldsymbol{\cdot} (\widehat{\boldsymbol{\Omega}} \times \boldsymbol{n})\boldsymbol{n}], \tag{A 8}$$

one obtains the expression of $\boldsymbol{G}_2 = \boldsymbol{\nabla}\widehat{\boldsymbol{u}}_0^0 \boldsymbol{\cdot} \boldsymbol{u}_0^0 + \boldsymbol{u}_0^0 \boldsymbol{\cdot} \boldsymbol{\nabla}\widehat{\boldsymbol{u}}_0^0$ as

$$\boldsymbol{G}_2 = -\frac{3A}{r^3}(\tilde{\boldsymbol{U}} \times \widehat{\boldsymbol{\Omega}}) \boldsymbol{\cdot} \boldsymbol{n}\boldsymbol{n} - \frac{3(A+B)}{r^3}(\tilde{\boldsymbol{U}} \boldsymbol{\cdot} \boldsymbol{n})(\widehat{\boldsymbol{\Omega}} \times \boldsymbol{n}). \tag{A 9}$$

Appendix B. Unsteady Stokes flow past a nearly spherical particle

Here we compute the velocity field solution of the unsteady Stokes problem around a nearly spherical particle:

$$\lambda^2 \partial_t \boldsymbol{u}_0^\epsilon = -\boldsymbol{\nabla} p_0^\epsilon + \nabla^2 \boldsymbol{u}_0^\epsilon, \quad \boldsymbol{\nabla} \boldsymbol{\cdot} \boldsymbol{u}_0^\epsilon = 0, \tag{B 1a,b}$$

$$\boldsymbol{u}_0^\epsilon|_{r=1} = -f(\boldsymbol{n})\partial_r \boldsymbol{u}_0^0|_{r=1}, \quad \boldsymbol{u}_0|_{r\to\infty} = \boldsymbol{0}. \tag{B 2a,b}$$

In Fourier space the boundary condition on the surface of the particle (B 2) takes the form (Zhang & Stone 1998)

$$\boldsymbol{u}_0^\epsilon|_{r=1} = \frac{3f(\boldsymbol{n})}{2}(1 + \lambda_0)(\boldsymbol{I} - \boldsymbol{n}\boldsymbol{n}) \boldsymbol{\cdot} \tilde{\boldsymbol{U}}. \tag{B 3}$$

Following Sani (1963), we perform a reconstruction of the velocity field from its radial component and associated vorticity:

$$\boldsymbol{u}_0^\epsilon = u_{0,r}^\epsilon \boldsymbol{n} + r^2 \sum_{n=1}^{\infty} \frac{1}{n(n+1)}[\boldsymbol{\nabla}_s(\nabla^2 u_{r,n}) - \boldsymbol{n} \times \boldsymbol{\nabla}_s \chi_{r,n}], \tag{B 4}$$

where $\boldsymbol{\nabla}_s = \boldsymbol{\nabla} - \boldsymbol{n}\partial_r$ and where $u_{r,n}$ denotes the nth mode in the spherical harmonics basis of the radial component of $\boldsymbol{u}_0^\epsilon$. The latter satisfies in time-Fourier space the equation $\nabla^2(\mathrm{i}\lambda^2 + \nabla^2)(ru^{\epsilon}_{0,r}) = 0$. The function $\chi_{r,n}$ is the nth mode of the radial component of $\nabla \times \boldsymbol{u}^{\epsilon}_0$, satisfying $(\nabla^2 + \mathrm{i}\lambda^2)(r\chi^{\epsilon}_r) = 0$. Defining p and q through

$$p = -\frac{2\nabla_s \cdot \boldsymbol{u}^{\epsilon}_0|_{r=1}}{3(1+\lambda_0)}, \quad q = \frac{2\boldsymbol{n} \cdot \nabla_s \times \boldsymbol{u}^{\epsilon}_0|_{r=1}}{3(1+\lambda_0)}, \tag{B 5a,b}$$

one finally obtains

$$\boldsymbol{u}^{\epsilon}_0 = \frac{1}{r}\sum_{n=1}^{\infty}\sum_{m=-n}^{n} U_n p^m_n Y^m_n \boldsymbol{n} + \sum_{n=1}^{\infty}\sum_{m=-n}^{n} \frac{r^2 V_n p^m_n}{n(n+1)} \nabla Y^m_n - \sum_{n=1}^{\infty}\sum_{m=-n}^{n} \frac{r X_n q^m_n}{n(n+1)} \boldsymbol{n} \times \nabla Y^m_n, \tag{B 6}$$

where p^m_n and q^m_n denote respectively the modes of p and q in the spherical harmonics basis (Y^m_n), and U_n, V_n and X_n follow:

$$U_n(r,\lambda) = \frac{3}{2}(1+\lambda_0)\frac{h^{(1)}_n(\overline{\lambda_0}r) - \dfrac{h^{(1)}_n(\overline{\lambda_0})}{r^{n+1}}}{(2n+1)h^{(1)}_n(\overline{\lambda_0}) - \overline{\lambda_0}h^{(1)}_{n+1}(\overline{\lambda_0})}, \tag{B 7}$$

$$V_n(r,\lambda) = \frac{U_n(r,\lambda)}{r^2} + \frac{\partial_r U_n(r,\lambda)}{r}, \tag{B 8}$$

$$X_n(r,\lambda) = \frac{3}{2}(1+\lambda_0)\frac{h^{(1)}_n(\overline{\lambda_0}r)}{h^{(1)}_n(\overline{\lambda_0})}, \tag{B 9}$$

with h_n the spherical Hankel function of the first kind and order n (Abramowitz & Stegun 1965). In (B 5), the functions p and q defined on the surface of the unit sphere are directly related to the shape function f through (B 2). Using (3.1), they further satisfy

$$[p]_{\boldsymbol{n}} = [q]_{\boldsymbol{n}} = 0, \quad [q\boldsymbol{n}]_{\boldsymbol{n}} = 0, \tag{B 10a,b}$$

$$[\nabla p\boldsymbol{n}]_{\boldsymbol{n}} = [\boldsymbol{n}\nabla p]_{\boldsymbol{n}} = [p\boldsymbol{n}\boldsymbol{n}]_{\boldsymbol{n}} = -2[f\boldsymbol{n}\boldsymbol{n}\boldsymbol{n}]_{\boldsymbol{n}} \cdot \tilde{\boldsymbol{U}}. \tag{B 11}$$

Note that these results can be transposed to obtain $\widehat{\boldsymbol{u}}^{\epsilon}$ taking $\lambda = 0$ for the translation problem. And a similar approach can be used in the rotating case.

References

Abramowitz, M. & Stegun, I. A. 1965 *Handbook of Mathematical Functions: With Formulas, Graphs, and Mathematical Tables*. Courier Corporation.

Ahmed, S., Wang, W., Bai, L., Gentekos, D. T., Hoyos, M. & Mallouk, T. E. 2016 Density and shape effects in the acoustic propulsion of bimetallic nanorod motors. *ACS Nano* **10** (4), 4763–4769.

Alben, S. & Shelley, M. 2005 Coherent locomotion as an attracting state for a free flapping body. *Proc. Natl Acad. Sci. USA* **102** (32), 11163–11166.

Bechinger, C., Di Leonardo, R., Löwen, H., Reichhardt, C., Volpe, G. & Volpe, G. 2016 Active particles in complex and crowded environments. *Rev. Mod. Phys.* **88** (4), 1–50.

Bricard, A., Caussin, J.-B., Desreumaux, N., Dauchot, O. & Bartolo, D. 2013 Emergence of macroscopic directed motion in populations of motile colloids. *Nature* **503** (7474), 95.

Buttinoni, I., Bialké, J., Kümmel, F., Löwen, H., Bechinger, C. & Speck, T. 2013 Dynamical clustering and phase separation in suspensions of self-propelled colloidal particles. *Phys. Rev. Lett.* **110** (23), 238301.

Collis, J. F., Chakraborty, D. & Sader, J. E. 2017 Autonomous propulsion of nanorods trapped in an acoustic field. *J. Fluid Mech.* **825**, 29–48.

Dreyfus, R., Baudry, J., Roper, M. L., Fermigier, M., Stone, H. A. & Bibette, J. 2005 Microscopic artificial swimmers. *Nature* **437** (7060), 862–865.

Happel, J. & Brenner, H. 1965 *Low Reynolds Number Hydrodynamics: With Special Applications to Particulate Media*. Prentice Hall.

Izri, Z., Van Der Linden, M. N., Michelin, S. & Dauchot, O. 2014 Self-propulsion of pure water droplets by spontaneous Marangoni-stress-driven motion. *Phys. Rev. Lett.* **113** (24), 248302.

Kim, S. & Karrila, S. J. 1991 *Microhydrodynamics: Principles and Selected Applications*. Butterworth-Heinemann.

Li, J., Rozen, I. & Wang, J. 2016 Rocket science at the nanoscale. *ACS Nano* **10**, 5619–5634.

Martinez-Pedrero, F. & Tierno, P. 2015 Magnetic propulsion of self-assembled colloidal carpets: efficient cargo transport via a conveyor-belt effect. *Phys. Rev. Appl.* **3** (5), 051003.

Michelin, S., Lauga, E. & Bartolo, D. 2013 Spontaneous autophoretic motion of isotropic particles. *Phys. Fluids* **25** (6), 061701.

Moran, J. L. & Posner, J. D. 2017 Phoretic self-propulsion. *Annu. Rev. Fluid Mech.* **49**, 511–540.

Nadal, F. & Lauga, E. 2014 Asymmetric steady streaming as a mechanism for acoustic propulsion of rigid bodies. *Phys. Fluids* **26** (8), 082001.

Palacci, J., Sacanna, S., Steinberg, A. P., Pine, D. J. & Chaikin, P. M. 2013 Living crystals of light-activated colloidal surfers. *Science* **339** (6122), 936–940.

Purcell, E. M. 1977 Life at low-Reynolds number. *Am. J. Phys.* **45**, 3–11.

Sabrina, S., Tasinkevych, M., Ahmed, S., Brooks, A. M., Olivera de la Cruz, M., Mallouk, T. E. & Bishop, K. J. M. 2018 Shape-directed microspinners powered by ultrasound. *ACS Nano* **12** (3), 2939–2947.

Sani, R. L. 1963 Convective instability. PhD thesis, University of Minnesota.

Soto, F., Wagner, G. L., Garcia-Gradilla, V., Gillespie, K. T., Lakshmipathy, D. R., Karshalev, E., Angell, C., Chen, Y. & Wang, J. 2016 Acoustically propelled nanoshells. *Nanoscale* **8** (41), 17788–17793.

Sundararajan, S., Lammert, P. E., Zudans, A. W., Crespi, V. H. & Sen, A. 2008 Catalytic motors for transport of colloidal cargo. *Nano Lett.* **8** (5), 1271–1276.

Tiwari, D. K., Behari, J. & Sen, P. 2008 Application of nanoparticles in waste water treatment. *World Appl. Sci. J.* **3** (3), 417–433.

Wang, S. & Wu, N. 2014 Selecting the swimming mechanisms of colloidal particles: bubble propulsion versus self-diffusiophoresis. *Langmuir* **30**, 3477–3486.

Wang, W., Castro, L. A., Hoyos, M. & Mallouk, T. E. 2012 Autonomous motion of metallic microrods propelled by ultrasound. *ACS Nano* **6** (7), 6122–6132.

Wiggins, C. H. & Goldstein, R. E. 1998 Flexive and propulsive dynamics of elastica at low Reynolds number. *Phys. Rev. Lett.* **80** (17), 3879.

Zhang, W. & Stone, H. A. 1998 Oscillatory motions of circular disks and nearly spherical particles in viscous flows. *J. Fluid Mech.* **367**, 329–358.

Bibliography

[1] V. Schaller, C. Weber, C. Semmrich, E. Frey, and A.R. Bausch. Polar patterns of driven filaments. *Nature*, 467(7311):73–77, September 2010.

[2] T. C. Schneirla. *A unique case of circular milling in ants, considered in relation to trail following and the general problem of orientation.* American Museum of Natural History, 1944.

[3] T. Vicsek and A. Zafeiris. Collective motion. *Physics Reports*, 517(3-4):71–140, August 2012.

[4] D.V. Radakov. *Schooling in the Ecology of Fish.* A Halsted Press book. J. Wiley, 1973.

[5] A. Filella, T. Nadal, C. Sire, E. Kanso, and C. Eloy. Model of collective fish behavior with hydrodynamic interactions. *Physical Review Letters*, 120(19), May 2018.

[6] D. Weihs. Hydromechanics of fish schooling. *Nature*, 241(5387):290–291, January 1973.

[7] F. Ginelli, F. Peruani, M. Pillot, H. Chaté, G. Theraulaz, and Bon. Intermittent collective dynamics emerge from conflicting imperatives in sheep herds. *Proceedings of the National Academy of Sciences*, 112(41):12729–12734, September 2015.

[8] A. Garcimartín, I. Zuriguel, J.M. Pastor, C. Martín-Gómez, and D.R. Parisi. Experimental evidence of the “faster is slower” effect. *Transportation Research Procedia*, 2:760–767, 2014.

[9] Y. Wu, Y. Jiang, D. Kaiser, and M. Alber. Social interactions in myxobacterial swarming. *PLoS Computational Biology*, 3(12):e253, December 2007.

[10] D.A.I. Mavridou, D. Gonzalez, W. Kim, S.A. West, and K.R. Foster. Bacteria use collective behavior to generate diverse combat strategies. *Current Biology*, 28(3):345–355.e4, February 2018.

[11] H.C. Berg and D.A. Brown. Chemotaxis in escherichia coli analysed by three-dimensional tracking. *Nature*, 239(5374):500–504, October 1972.

[12] J. Gray and G.J. Hancock. The propulsion of sea-urchin spermatozoa. *Journal of Experimental Biology*, 32(4):802–814, 1955.

[13] P.V. Bayly, B.L. Lewis, E.C. Ranz, R.J. Okamoto, R.B. Pless, and S.K. Dutcher. Propulsive forces on the flagellum during locomotion of chlamydomonas reinhardtii. *Biophysical Journal*, 100(11):2716–2725, June 2011.

[14] S.L. Tamm. ciliary motion in paramecium. *The Journal of Cell Biology*, 55(1):250–255, October 1972.

[15] M. J. Lighthill. Aquatic animal propulsion of high hydromechanical efficiency. *Journal of Fluid Mechanics*, 44(02):265, November 1970.

[16] N. Osterman and A. Vilfan. Finding the ciliary beating pattern with optimal efficiency. *Proceedings of the National Academy of Sciences*, 108(38):15727–15732, September 2011.

[17] S. Chattopadhyay, R. Moldovan, C. Yeung, and X.L. Wu. Swimming efficiency of bacterium escherichia coli. *Proceedings of the National Academy of Sciences*, 103(37):13712–13717, September 2006.

[18] W.J. Zhu. Preparation and observation methods can produce misleading artefacts in human sperm ultrastructural morphology. *Andrologia*, 50(7):e13043, May 2018.

[19] J.R. Blake. A spherical envelope approach to ciliary propulsion. *Journal of Fluid Mechanics*, 46(1):199–208, March 1971.

[20] E. Lauga and T.R. Powers. The hydrodynamics of swimming microorganisms. *Reports on Progress in Physics*, 72(9):096601, August 2009.

[21] G.G. Stokes. *On the effect of the internal friction of fluids on the motion of pendulums*, volume 9. Pitt Press Cambridge, 1851.

[22] S. Kim and S. J. (2013). Karrila. *Microhydrodynamics: principles and selected applications.* Courier Corporation, 2013.

[23] J. Happel and H. Brenner. *Low Reynolds number hydrodynamics: with special applications to particulate media (Mechanics of Fluids and Transport Processes)*. Springer, 1983.

[24] E.M. Purcell. Life at low reynolds number. *American Journal of Physics*, 45(1):3–11, January 1977.

[25] H.A. Stone and A.D.T. Samuel. Propulsion of microorganisms by surface distortions. *Physical Review Letters*, 77(19):4102–4104, November 1996.

[26] G.J. Elfring and E. Lauga. Synchronization of flexible sheets. *Journal of Fluid Mechanics*, 674:163–173, March 2011.

[27] P. Zhang, S. Jana, M. Giarra, P.P. Vlachos, and S. Jung. Paramecia swimming in viscous flow. *The European Physical Journal Special Topics*, 224(17-18):3199–3210, December 2015.

[28] S. Palagi, E.W.H. Jager, B. Mazzolai, and L. Beccai. Propulsion of swimming microrobots inspired by metachronal waves in ciliates: from biology to material specifications. *Bioinspiration & Biomimetics*, 8(4):046004, October 2013.

[29] A. Dauptain, J. Favier, and A. Bottaro. Hydrodynamics of ciliary propulsion. *Journal of Fluids and Structures*, 24(8):1156–1165, November 2008.

[30] M.J. Lighthill. On the squirming motion of nearly spherical deformable bodies through liquids at very small reynolds numbers. *Communications on Pure and Applied Mathematics*, 5(2):109–118, May 1952.

[31] Y. Sumino, H. Kitahata, K. Yoshikawa, M. Nagayama, N. Nomura, S.M. andx Magome, and Y. Mori. Chemosensitive running droplet. *Physical Review E*, 72(4), October 2005.

[32] F.D. Dos Santos and T. Ondarçuhu. Free-running droplets. *Physical Review Letters*, 75(16):2972–2975, October 1995.

[33] T. Toyota, H. Tsuha, K. Yamada, K. Takakura, T. Ikegami, and T. Sugawara. Listeria-like motion of oil droplets. *Chemistry Letters*, 35(7):708–709, July 2006.

[34] T. Toyota, N. Maru, M.M. Hanczyc, T. Ikegami, and T. Sugawara. Self-propelled oil droplets consuming “fuel” surfactant. *Journal of the American Chemical Society*, 131(14):5012–5013, April 2009.

[35] M.M. Hanczyc, T. Toyota, T. Ikegami, N. Packard, and T. Sugawara. Fatty acid chemistry at the oil-water interface: self-propelled oil droplets. *Journal of the American Chemical Society*, 129(30):9386–9391, August 2007.

[36] Z. Izri, M.N. van der Linden, S. Michelin, and O. Dauchot. Self-propulsion of pure water droplets by spontaneous marangoni-stress-driven motion. *Physical Review Letters*, 113(24), December 2014.

[37] A. Izzet, P.G Moerman, P. Gross, J. Groenewold, A.D. Hollingsworth, J. Bibette, and J. Brujic. Tunable persistent random walk in swimming droplets. *Physical Review X*, 10(2), May 2020.

[38] S. Herminghaus, C.C. Maass, C. Krüger, S. Thutupalli, L. Goehring, and C. Bahr. Interfacial mechanisms in active emulsions. *Soft Matter*, 10(36):7008–7022, 2014.

[39] C. Krüger, G. Klös, C. Bahr, and C.C. Maass. Curling liquid crystal microswimmers: A cascade of spontaneous symmetry breaking. *Physical Review Letters*, 117(4), July 2016.

[40] D. Vella and L. Mahadevan. The “cheerios effect”. *American Journal of Physics*, 73(9):817–825, September 2005.

[41] J. Thomson. On certain curious motions observable at the surfaces of wine and other alcoholic liquors. *The London, Edinburgh, and Dublin Philosophical Magazine and Journal of Science*, 10(67):330–333, 1855.

[42] CGM Marangoni. *Sull’espansione delle gocce liquide*. PhD thesis, Doctoral Dissertation, University of Pavia, Pavia, Italy (in Italian), 1865.

[43] T. Young. III. an essay on the cohesion of fluids. *Philosophical Transactions of the Royal Society of London*, 95:65–87, December 1805.

[44] D.C. Venerus and D.N. Simavilla. Tears of wine: new insights on an old phenomenon. *Scientific Reports*, 5(1), November 2015.

[45] H. Manikantan and T.M. Squires. Surfactant dynamics: hidden variables controlling fluid flows. *Journal of Fluid Mechanics*, 892, April 2020.

[46] J.S. Hadamard. Mouvement permanent lent d’une sphère liquide et visqueuse dans un liquide visqueux. *Comptes rendus hebdomadaires des séances de l’Académie des sciences*, 152:1735–1738, 1911.

[47] N.O. Young, J.S. Goldstein, and M.J. Block. The motion of bubbles in a vertical temperature gradient. *Journal of Fluid Mechanics*, 6(03):350, October 1959.

[48] J.L. Anderson. Colloid transport by interfacial forces. *Annual Review of Fluid Mechanics*, 21(1):61–99, January 1989.

[49] M. Morozov. Adsorption inhibition by swollen micelles may cause multistability in active droplets. *Soft Matter*, 16(24):5624–5632, 2020.

[50] R. Brown. *A Brief Account of Microscopical Observations made in the Months of June, July, and August, 1827, on the Particles contained in the Pollen of Plants and on the General Existence of Active Molecules in Organic and Inorganic Bodies*. John Joseph Bennett, 1827.

[51] A. Einstein. Über die von der molekularkinetischen theorie der wärme geforderte bewegung von in ruhenden flüssigkeiten suspendierten teilchen. *Annalen der Physik*, 322(8):549–560, 1905.

[52] W. Sutherland. LXXV. a dynamical theory of diffusion for non-electrolytes and the molecular mass of albumin. *The London, Edinburgh, and Dublin Philosophical Magazine and Journal of Science*, 9(54):781–785, June 1905.

[53] M. Von Smoluchowski. Zur kinetischen theorie der brownschen molekularbewegung und der suspensionen. *Annalen der Physik*, 326(14):756–780, 1906.

[54] J. Perrin. Mouvement brownien et grandeurs moléculaires. *Le Radium*, 6(12):353–360, 1909.

[55] A. Fick. Ueber diffusion. *Annalen der Physik und Chemie*, 170(1):59–86, 1855.

[56] P.G. Moerman, H.W. Moyses, E.B. Van der Wee, D.G. Grier, A. Van Blaaderen, W.K. Kegel, J. Groenewold, and J. Brujic. Solute-mediated interactions between active droplets. *Physical Review E*, 96(3), September 2017.

[57] M. Suga, S. Suda, M. Ichikawa, and Y. Kimura. Self-propelled motion switching in nematic liquid crystal droplets in aqueous surfactant solutions. *Physical Review E*, 97:062703, 2018.

[58] B. V. Hokmabad, R. Dey, M. Jalaal, D. Mohanty, M. Almukambetova, K. A Baldwin, D. Lohse, and C.C. Maass. Stop-and-go droplet swimmers. *arXiv preprint arXiv:2005.12721*, 2020.

[59] M. Morozov and S. Michelin. Orientational instability and spontaneous rotation of active nematic droplets. *Soft Matter*, 15(39):7814–7822, 2019.

[60] W. Hu, T. Lin, S. Rafai, and C. Misbah. Chaotic swimming of phoretic particles. *Physical Review Letters*, 123(23), December 2019.

[61] M. Morozov and S. Michelin. Nonlinear dynamics of a chemically-active drop: from steady to chaotic self-propulsion. *The Journal of Chemical Physics*, 150:044110, 2019.

[62] S. Thutupalli, D. Geyer, R. Singh, R. Adhikari, and H.A. Stone. Flow-induced phase separation of active particles is controlled by boundary conditions. *Proceedings of the National Academy of Sciences*, 115(21):5403–5408, May 2018.

[63] Pierre Illien, Charlotte de Blois, Yang Liu, Marjolein N. van der Linden, and Olivier Dauchot. Speed-dispersion-induced alignment: A one-dimensional model inspired by swimming droplets experiments. *Physical Review E*, 101:040602, Apr 2020.

[64] C. Krüger, C. Bahr, S. Herminghaus, and C.C. Maass. Dimensionality matters in the collective behaviour of active emulsions. *The European Physical Journal E*, 39(6), June 2016.

[65] A. Walther and A.H.E. Müller. Janus particles. *Soft Matter*, 4(4):663, 2008.

[66] S. Michelin, E. Lauga, and D. Bartolo. Spontaneous autophoretic motion of isotropic particles. *Physics of Fluids*, 25(6):061701, June 2013.

[67] A.T. Chwang and T.Y. Wu. Hydromechanics of low-reynolds-number flow. part 2. singularity method for stokes flows. *Journal of Fluid Mechanics*, 67(4):787–815, February 1975.

[68] G.J. Hancock. The self-propulsion of microscopic organisms through liquids. *Proceedings of the Royal Society of London. Series A. Mathematical and Physical Sciences*, 217(1128):96–121, March 1953.

[69] S.E. Spagnolie and E. Lauga. Hydrodynamics of self-propulsion near a boundary: predictions and accuracy of far-field approximations. *Journal of Fluid Mechanics*, 700:105–147, April 2012.

[70] William Bailey Russel, WB Russel, Dudley A Saville, and William Raymond Schowalter. *Colloidal dispersions*. Cambridge university press, 1991.

[71] M. Schmitt and H. Stark. Swimming active droplet: A theoretical analysis. *Europhysics Letters*, 101(4):44008, February 2013.

[72] T. Ishikawa and T.J. Pedley. Diffusion of swimming model micro-organisms in a semi-dilute suspension. *Journal of Fluid Mechanics*, 588:437–462, September 2007.

[73] N.G. Chisholm, D. Legendre, E. Lauga, and A.S. Khair. A squirmer across reynolds numbers. *Journal of Fluid Mechanics*, 796:233–256, April 2016.

[74] I. Llopis and I. Pagonabarraga. Hydrodynamic interactions in squirmer motion: Swimming with a neighbour and close to a wall. *Journal of Non-Newtonian Fluid Mechanics*, 165(17-18):946–952, September 2010.

[75] C. de Blois, M. Reyssat, M. Michelin, and D. Dauchot. Flow field around a confined active droplet. *Physical Review Fluids*, 4(5), May 2019.

[76] M. Smoluchowski. *Über die Wechselwirkung von Kugeln die sich in einer zähen Flüssigkeit bewegen*. Akad. Umiejketnośći, 1911.

[77] M. Stimson and G. B. Jeffery. The motion of two spheres in a viscous fluid. *Proceedings of the Royal Society*, 111(757):110–116, 1926.

[78] J.R. Blake and A.T. Chwang. Fundamental singularities of viscous flow. *Journal of Engineering Mathematics*, 8(1):23–29, January 1974.

[79] A. Varma and S. Michelin. Modeling chemo-hydrodynamic interactions of phoretic particles: A unified framework. *Physical Review Fluids*, 4(12), December 2019.

[80] Gad Hetsroni and Shimon Haber. The flow in and around a droplet or bubble submerged in an unbound arbitrary velocity field. *Rheologica Acta*, 9(4):488–496, 1970.

[81] B.J. Kirby. *Micro-and nanoscale fluid mechanics: transport in microfluidic devices*. Cambridge university press, 2010.

[82] D. Boniface, C. Cottin-Bizonne, R. Kervil, C. Ybert, and F. Detcheverry. Self-propulsion of symmetric chemically active particles: Point-source model and experiments on camphor disks. *Physical Review E*, 99(6):062605, 2019.

[83] N. Yoshinaga, K. H. Nagai, Y. Sumino, and H. Kitahata. Drift instability in the motion of a fluid droplet with a chemically reactive surface driven by marangoni flow. *Physical Review E*, 86(1):016108, 2012.

[84] R. Golestanian, T.B. Liverpool, and A. Ajdari. Designing phoretic micro- and nano-swimmers. *New Journal of Physics*, 9(5):126–126, May 2007.

[85] Y. Ibrahim and T.B. Liverpool. How walls affect the dynamics of self-phoretic microswimmers. *The European Physical Journal Special Topics*, 225(8-9):1843–1874, October 2016.

[86] F. Fadda, G. Gonnella, A. Lamura, and A. Tiribocchi. Lattice boltzmann study of chemically-driven self-propelled droplets. *The European Physical Journal E*, 40(12), December 2017.

[87] S. Yabunaka and N. Yoshinaga. Collision between chemically driven self-propelled drops. *J. Fluid Mech.*, 806:205–233, 2016.

[88] N. Yoshinaga. Simple models of self-propelled colloids and liquid drops: From individual motion to collective behaviors. *Journal of the Physical Society of Japan*, 86(10):101009, October 2017.

[89] K. Lippera, M. Morozov, M. Benzaquen, and S. Michelin. Collisions and rebounds of chemically active droplets. *Journal of Fluid Mechanics*, 886, January 2020.

[90] I. Theurkauff, C. Cottin-Bizonne, J. Palacci, C. Ybert, and L. Bocquet. Dynamic clustering in active colloidal suspensions with chemical signaling. *Physical Review Letter*, 108:268303, 2012.

[91] J. Palacci, S. Sacanna, A.P. Steinberg, D.J. Pine, and P.M. Chaikin. Living crystals of light-activated colloidal surfers. *Science*, 339:936–940, 2013.

[92] S. Saha, R. Golestanian, and S. Ramaswamy. Clusters, asters, and collective oscillations in chemotactic colloids. *Physical Review E*, 89(6):062316, 2014.

[93] O. Pohl and H. Stark. Dynamic clustering and chemotactic collapse of self-phoretic active particles. *Physical Review Letter*, 112(23):238303, 2014.

[94] B. Liebchen and H. Löwen. Which interactions dominate in active colloids? *The Journal of Chemical Physics*, 150(6):061102, 2019.

[95] E. Kanso and S. Michelin. Phoretic and hydrodynamic interactions of weakly confined autophoretic particles. *The Journal of Chemical Physics*, 150:044902, 2019.

[96] D. G. Crowdy. Wall effects on self-diffusiophoretic janus particles: a theoretical study. *Journal of Fluid Mechanics*, 735:473–498, 2013.

[97] W.E. Uspal, M.N. Popescu, S. Dietrich, and M. Tasinkevych. Self-propulsion of a catalytically active particle near a planar wall: from reflection to sliding and hovering. *Soft Matter*, 11(3):434–438, 2015.

[98] E. Yariv. Wall-induced self-diffusiophoresis of active isotropic colloids. *Physical Review Fluids*, 1(3), July 2016.

[99] R. Soto and R. Golestanian. Self-assembly of active colloidal molecules with dynamic function. *Physical Review E*, 91(5):052304, 2015.

[100] A. Varma, T.D. Montenegro-Johnson, and S. Michelin. Clustering-induced self-propulsion of isotropic autophoretic particles. *Soft matter*, 14(35):7155–7173, 2018.

[101] M. Morozov and S. Michelin. Self-propulsion near the onset of marangoni instability of deformable active droplets. *Journal of Fluid Mechanics*, 860:711–738, 2019.

[102] M.N. Popescu, M. Tasinkevych, and S. Dietrich. Pulling and pushing a cargo with a catalytically active carrier. *Europhysics Letters*, 95:28004, 2011.

[103] S. Michelin and E. Lauga. Autophoretic locomotion from geometric asymmetry. *The European Physical Journal E*, 38(2):7, 2015.

[104] S.Y. Reigh and R. Kapral. Catalytic dimer nanomotors: continuum theory and microscopic dynamics. *Soft Matter*, 11:3149, 2015.

[105] A. Acrivos and T.D. Taylor. Heat and mass transfer form single spheres in stokes flow. *Physics of Fluids*, 5:387, 1962.

[106] S. Michelin and E. Lauga. Phoretic self-propulsion at finite péclet numbers. *Journal of Fluid Mechanics*, 747:572–604, 2014.

[107] R.H. Davis, J.A. Schonberg, and J.M. Rallison. The lubrication force between two viscous drops. *Physics of Fluids*, 1(1):77–81, 1989.

[108] A.Ye. Rednikov, Y.S. Ryazantsev, and M.G. Velarde. Drop motion with surfactant transfer in a homogeneous surrounding. *Physics of Fluids*, 6:451, 1994.

[109] H. Lamb. *Hydrodynamics*. Dover Books on Physics. Dover publications, 1945.

[110] L.G. Leal. *Advanced Transport Phenomena: Fluid Mechanics and Convective Transport Processes*. Cambridge Series in Chemical Engineering. Cambridge University Press, 2007.

[111] R. Soto and R. Golestanian. Self-assembly of catalytically active colloidal molecules: tailoring activity through surface chemistry. *Physical Review Letters*, 112:068301, 2014.

[112] S. Michelin, G. Gallino, F. Gallaire, and E. Lauga. Viscous growth and rebound or a bubble near a rigid surface. *Journal of Fluid Mechanics*, 860:172–199, 2019.

[113] S. Michelin, E. Guérin, and E. Lauga. Collective dissolution of microbubbles. *Physical Review Fluids*, 3:043601, 2018.

[114] K. Lippera, M. Benzaquen, and S. Michelin. Bouncing, chasing, or pausing: Asymmetric collisions of active droplets. *Physical Review Fluids*, 5(3), March 2020.

[115] S. Thutupalli, R. Seemann, and S. Herminghaus. Swarming behavior of simple model squirmers. *New Journal of Physics*, 13(7):073021, 2011.

[116] M. Morozov and S. Michelin. Nonlinear dynamics of a chemically-active drop: From steady to chaotic self-propulsion. *The Journal of Chemical Physics*, 150(4):044110, 2019.

[117] H.C. Berg. *Random walks in biology*. Princeton Univ Pr, 1993.

[118] E. Lauga. Bacterial hydrodynamics. *Annual Review of Fluid Mechanics*, 48(1):105–130, January 2016.

[119] C.C. Maass, C. Krüger, S. Herminghaus, and C. Bahr. Swimming droplets. *Annual Review of Condensed Matter Physics*, 7(1):171–193, March 2016.

[120] C. Jin, C. Krüger, and C.C. Maass. Chemotaxis and autochemotaxis of self-propelling droplet swimmers. *Proceedings of the National Academy of Sciences*, 114(20):5089–5094, May 2017.

[121] C. Jin, B.V. Hokmabad, K.A. Baldwin, and C.C. Maass. Chemotactic droplet swimmers in complex geometries. *Journal of Physics: Condensed Matter*, 30(5):054003, January 2018.

[122] A.E. Patteson, A. Gopinath, M. Goulian, and P.E. Arratia. Running and tumbling with e. coli in polymeric solutions. *Scientific reports*, 5:15761, 2015.

[123] K. N. T. Lam, M. Schindler, and O. Dauchot. Polar active liquids: a universal classification rooted in nonconservation of momentum. *Journal of Statistical Mechanics: Theory and Experiment*, 2015(10):P10017, 2015.

[124] S. Thutupalli. *Towards autonomous soft matter systems: experiments on membranes and active emulsions*. Springer Science & Business Media, 2013.

[125] C. Zong. Packing, covering and tiling in two-dimensional spaces. *Expositiones Mathematicae*, 32(4):297–364, 2014.

[126] J.P. Hernandez-Ortiz, C.G. Stoltz, and M.D. Graham. Transport and collective dynamics in suspensions of confined swimming particles. *Physical review letters*, 95(20):204501, 2005.

[127] D. Bi, X. Yang, M.C. Marchetti, and M.L. Manning. Motility-driven glass and jamming transitions in biological tissues. *Physical Review X*, 6(2), April 2016.

[128] J. Mittal, J.R. Errington, and T.M. Truskett. Relationships between self-diffusivity, packing fraction, and excess entropy in simple bulk and confined fluids. *The Journal of Physical Chemistry B*, 111(34):10054–10063, August 2007.

[129] J. G. Kirkwood and E.M. Boggs. The radial distribution function in liquids. *The Journal of Chemical Physics*, 10(6):394–402, 1942.

[130] G.H.A. Cole. *An introduction to the statistical theory of classical simple dense fluids*. Elsevier, 2014.

[131] M. Abramowitz. Handbook of mathematical functions, national bureau of standards. *Applied Mathematics Series*, (55), 1964.

[132] K. Lippera, O. Dauchot, S. Michelin, and M. Benzaquen. No net motion for oscillating near-spheres at low reynolds numbers. *Journal of Fluid Mechanics*, 866:R1, 2019.

ECOLE
DOCTORALE

Titre : Gouttes actives autopropulsées: une histoire d’intéractions.

Mots clés : Gouttes actives, Micro-nageurs, Mécanique des fluides bas Reynolds, Matière active

Résumé : Une fois immergées dans un liquide saturé en surfactants, une microgoutte composée d’eau ou d’huile peut s’auto-propulser à une vitesse de l’ordre de quelques rayons par seconde. Bien que l’origine physico-chimique exacte de ce phénomène reste encore débattue, de recents travaux ont permis de comprendre qu’il est lié à la solubilisation de ces gouttes dans leur milieu. Une goutte active apparaît alors comme émettant un ensemble d’espèces chimiques, appelé soluté, qui a pour effet d’augmenter la tension de surface. Par conséquent, une distribution inhomogène de soluté à l’interface de la goutte génère un écoulement dit de Marangoni qui propulse la goutte. L’autopropulsion s’explique alors par une instabilité issue du couplage entre la dynamique de transport du soluté et l’écoulement Marangoni qui en résulte. Cette thèse a pour but d’étudier les interactions entre plusieurs de ces gouttes ou en présence d’un confinement. Le premier chapitre introduit des notions générales de mécanique des fluides à bas Reynolds ainsi qu’une description des systèmes de gouttes actives utilisées expérimentalement. Le deuxième chapitre présente le cadre mathématique modélisant l’autopropulsion d’une goutte seule, puis fournit une discussion traitant des interactions hydro-chimiques attendues en présence de plusieurs gouttes ou d’un mur. Le troisième chapitre présente une dérivation exacte des interactions hydro-chimiques entre une goutte active et un mur dans le cas axisymétrique. Cette approche a permis de quantifier l’influence de l’advection du soluté sur la dynamique de collision et de soulever des effets de retard survenant à haut nombre de Péclet. Dans le quatrième chapitre, on étudie alors les conséquences sur la dynamique de collision d’une différence de taille entre deux gouttes actives. On montre alors que la dynamique de collision est très sensible à une différence de rayon et peut conduire à des régimes très différents et appelés rebond, poursuite et pause. Le cinquième chapitre introduit un modèle simplifié de la dynamique d’une goutte active, utilisé dans l’étude des collisions obliques. Si une collision symétrique tend à aligner les gouttes, des conditions initiales asymétriques peuvent à l’inverse les disperser. Enfin, le sixième chapitre apporte la conclusion de ce manuscrit et suggère diverses perspectives pour la suite de l’étude des interactions de gouttes actives.

Title : Self-propelled active droplets: a short story of their interactions

Keywords : Active droplets, Microswimmers, Low Reynolds fluid mechanics, Active matter

Abstract : When immersed in a surfactant-saturated fluid, droplets made out of oil or water can self-propel at velocities attaining several radii per second. While the exact physicochemical mechanisms underlying this behaviour are still under debate, recent studies have shown that they are related to the solubilisation of the droplet. Indeed, these active droplets release a mixture of chemical species, i.e. solute, locally modifying their surface tension. When a non-uniform solute distribution is attained at the droplet surface, the imbalance in surface tension induces Marangoni flows, producing a net fluid flow and the droplet’s swimming motion. Thus, a droplet’s self-propulsion results from the coupling of solute transport dynamics to the resulting Marangoni flows. In this thesis, we aim to study the behaviour of several active droplets interacting with each other, as well as with fixed boundaries. In the first chapter, we introduce some key aspects of low Reynolds number fluid mechanics and describe the physical system of interest, namely active droplets like those used in recent experiments. The mathematical framework employed to model the self-propulsion of active droplets is presented in chapter two, together with a preliminary discussion of the hydro-chemical interactions involved in the presence of multiple droplets and generic boundaries. In chapter three we provide the exact derivation of the hydro-chemical interactions involved for a droplet colliding against a rigid wall, or with another active droplet. In the fourth chapter, we study the influence of the size-ratio on head-on collisions of two droplets. Here we show that collision dynamics are highly dependent on the droplet’s size ratio, leading to three different regimes, i.e. rebound, chasing and pausing. In chapter five we introduce a simplified framework for modelling the behaviour of active droplets’ dynamics, which is then employed to study the general case of oblique collisions. While we notice a significant alignment of the droplets when initial conditions are symmetric, we show that the system can become highly asymmetric with the introduction of a misalignment in the drops’ initial conditions. In the sixth and final chapter, we provide several perspectives regarding the study of active droplet interactions.

Institut Polytechnique de Paris
91120 Palaiseau, France